University of Strathclyde

Department of Naval Architecture, Ocean and Marine
Engineering

BEMT and CFD-Based Unsteady Aerodynamic Analyses of Floating Offshore Wind Turbine

Lin Lin

A Thesis presented in fulfilment of the requirements for
the degree of Doctor of Philosophy

September 2016

Declaration

This thesis is the result of the author's original research. It has been composed by the author and has not been previously submitted for examination which has led to the award of a degree.

The copyright of this thesis belongs to the author under the terms of the United Kingdom Copyright Acts as qualified by University of Strathclyde Regulation 3.50. Due acknowledgement must always be made of the use of any material contained in, or derived from, this thesis.

Signed: Date:

Acknowledgements

Three years ago, when I first stepped into university of Strathclyde, Glasgow, I had no idea of research. However, now, I have almost finished my PhD. Recalling the past, I would like to express my gratitude to all those who helped me during the PhD.

First of all, I would like to express my sincere gratitude to my supervisor, Professor Dracos Vassalos, for his constant encouragement and guidance. He has walked me through all the stages of my PhD. Without his consistent and illuminating instruction, this thesis could not have reached its present form. What's more, I was most inspired by his professional work style and serious working attitude. Research needs all your attention. You cannot take easy when you work. Moreover, Professor Vassalos was very kind and helpful for my life.

Also, I would like to thank Dr Shan Huang who is in British Petrol now. He brought me from China and became my supervisor in my first year of PhD. He leaded me into the academic area and taught me how to be a real PhD. Without him, I would never have this opportunity to study in Glasgow. Though he left the university, I would never forget his help and instruction.

I am grateful to the support from my colleagues, Qi Qi, Saishuai Dai, Aijun Wang, and Dr Zhengqiang Xu. They always appeared timely when I need help. We shared experience and methods without any reservation. And I would like to thank my best friends in Glasgow, Haipeng Liu, Tong Cui, Xiao xiaoxi and Pengfei zhang. They often accompanied me when I feel lonely and homesick. We like a real family.

Table of Contents

List of Figures

List of Tables

Nomenclature

Roman symbols

$U_{platform}$ =   velocity of Platform motions

U_{surge} =   velocity of platform surge motion

U_{sway} =   velocity of platform sway motion

U_{heave} =   velocity of platform heave motion

$y+$ =   distance from the first layer of viscous wall to the airfoil surface

y_p =   distance from the first computational node to the wall

w =   wall properties

C_l =   lift coefficient

C_d =   drag coefficient

C_{lmax} =   maximum lift coefficient

C_{dmax} =   maximum drag coefficient

Re =   Reynolds number

u =   free stream velocity

C =   airfoil chord length

C_T =   thrust coefficient

C_P =   power coefficient

S_m =   a continuous quality

P =   static pressure

G =   gravity volume force

F =   external volume force

$\overline{u_\iota}$ =   time average velocity

u_i' =   turbulent fluctuation velocity

k =   turbulent energy

y_v	=	physical viscous sub-layer thickness
S	=	simulation results
T	=	truth results
U_{SN}	=	simulation numerical uncertainty
U_{ScN}	=	corrected uncertainty
S_C	=	numerical benchmark
U_{SM}	=	simulation modelling uncertainty
E	=	comparison error
D	=	difference in the data
U_V	=	validation uncertainty
m	=	mass
a	=	acceleration
k	=	reduced frequencies
h	=	amplitude
R	=	blade radius
F_L	=	lift force
F_D	=	drag force
f	=	oscillation frequency
w	=	angle velocity
P	=	power
T	=	axial force
V	=	velocity
A	=	rotor area
a_1	=	axial induction factors
u_a	=	axial induced velocity
a_2	=	angular induction factor

V_a	=	axial velocity
V_T	=	tangential velocity
W	=	actual airflow speed
F_n	=	normal force
F_t	=	tangential force
C_n	=	normal force coefficient
C_t	=	tangential force coefficient
N_b	=	number of blades
M	=	momentum
F_t	=	tip loss correction
F_r	=	hub loss correction
a_{skew}	=	skewed wake correction
K	=	skew angle
V_{ref}	=	reference wind speed
P_W	=	Weibull probability distribution
P_R	=	Rayleigh probability function
c	=	scale parameter of the Weibull function
V_{hub}	=	10-min mean of the wind speed at hub height
V_{ave}	=	annual average wind speed
z	=	height above the ground
V_{cg}	=	standard wind turbine classes
T	=	rise time
B	=	size reduction factor
U_{rel}	=	relative wind speed
Vr	=	rotation velocity
Vx	=	inflow velocity

AR	=	blade aspect ratio

Greek symbols

$\dot{\theta}_{pitch}$	=	angle velocity of pitch motion
$\dot{\theta}_{yaw}$	=	angle velocity of yaw motion
$\dot{\theta}_{roll}$	=	angle velocity of roll motion
ρ	=	freestream density
μ	=	dynamic viscosity
τ	=	Stress tensor
δ_S	=	simulation error
δ_{SM}	=	additive modelling errors
δ_{SN}	=	numerical errors
δ_{SN}^*	=	simulation numerical error
μ_t	=	turbulent viscosity coefficient
α_E	=	effective angle of attack
α	=	angles of attack
Ω	=	rotating angular velocity
λ	=	tip speed ratio
φ	=	inflow angle
θ	=	twist angle
Ψ	=	azimuth angle
Γ	=	gamma function
σ	=	power law exponent
σ_1	=	longitudinal wind velocity component

Abbreviations

EWEA	European Wind Energy Association
NREAP	National Renewable Energy Action Plan
EC	European Commission
HAWT	Horizontal Axis Wind Turbine
VAWT	Vertical Axis Wind Turbine
TLP	Tension-leg Platform
NMRI	National Maritime Research Institute
FOWT	Floating offshore wind turbine
BEMT	Blade Element Momentum Theory
VLM	Vortex Lattice Method
CFD	Computational Fluid Dynamics
ASE	Aero-servo-elasticity
OC3	Offshore Code Comparison Collaboration
IEA	International Energy Agency
DOF	Degree of Freedom
FAST	Fatigue, Aerodynamics, Structures, and Turbulence
ITTC	International Towing Tank Resistance Committees
GDW	Generalised Dynamic Wake
NREL	National Renewable Energy Laboratory
DLC	Design Load Cases
IEC	International Electrotechnical Commission
NACA	National Advisory Committee for Aeronautics
RANS	Reynolds-Average Navier-Stokes
DS	Dynamic Stall
BL	Beddoes–Leishman

LES	Large Eddy Simulation
EN	e^N Envelop
SST	Shear Stress Transport
NASA	National Aeronautics and Space Administration
ECN	Energy Research Centre of the Netherlands
DES	Detached Eddy Simulation
ECG	Extreme Coherent Gust
EOG	Extreme Operation Gust
AOA	Angle of Attack
ALE	Arbitrary-Lagrange-Eulerian
NURB	Non-Uniform Rational B-splines
PIV	Particle Image Velocimetry
MSWT	Marin Stock Wind Turbine
MARIN	Maritime Research Institution Netherlands
GA	Genetic Algorithm
GFRD	Geometrically Free Rotor Design
DEAP	Distributed Evolutionary Algorithms in Python
RAOs	Response Amplitude Operators
OWC	Oscillating Water Column
TWS	Turbulent Wake State
FVM	Free Vortex Models
WInDS	Wake Induced Dynamics Simulator
RNG	Re-Normalisation Group
EFD	Experimental Fluid Dynamics
RE	Richardson Extrapolation
GCI	Grid Convergence Index

S-A	Spalart–Allmaras
NWS	Normal Working State
VBS	Vortex Ring State
WBS	Windmill Braking State
MIT	Massachusetts Institute of Technology
ADAMS	Automatic Dynamic Analysis of Mechanical Systems
NFAC	Full- Scale Aerodynamic Complex
REM	Reference Frame Method
SIMPLE	Semi-Implicit Method to Solve the Pressure-Linked Equation
NWP	Normal Wind Profile
EWM	wind speed model
P-S	Pitch-Surge
TSR	Tip Speed Ratio
RPM	Revolutions Per Minute
MBS	Multibody system

Abstract

Nowadays the demands for floating offshore wind (FOWT) have exceeded 5MW with the rapidly growing wind market. The aerodynamic environment of FOWT is more complex than onshore or fixed offshore wind turbine due to the large motions of floating platforms. The platform motion, especially pitch and surge motions, increase aerodynamic unsteadiness, wake interactions and other complex flow phenomena. These conditions influence the velocities and accelerations at the rotor sections along the blade. However, a limited simulation and load estimation capability make aerodynamic analysis a challenge. It is questionable whether some industry aerodynamic analysis codes like conventional Blade Element Momentum (BEM) theory and Generalised Dynamic Wake theory are accurate. Results indicate that current methods for predicting the aerodynamic loads may be inadequate.

Aerodynamic flow effects cannot be accurately modelled using traditional BEM theory with common corrections in such a complex condition. So compared with traditional potential theory, CFD method provides more physically realistic simulation. The applying and validation of CFD method will be outlined in this dissertation. The commercial multi-purpose CFD solver STAR CCM+ 9.02 is employed for calculation of the flow using Reynolds-Average Navier-Stokes (RANS) equations in conjunction with different turbulent models. Finally, results from CFD simulations of various offshore floating wind turbines under different load conditions will be presented. CFD simulation is accurate, but time consuming. So, an optimization method will be detected to get a more accurate result and saving time. 2D CFD RANS data was instead of commonly 2D data. However, not result in the desired improvements when compared to BEM results. Therefore, a 2D airfoil data obtained by post-processing of 3D CFD computations was used. 3D results were used to estimate 2D airfoil characteristics to modify two important parameters in BEM codes: the axial and the tangential induction factors by applying the reduced axial velocity method by getting the local angle of attack from CFD solutions. This thesis will demonstrate that the aerodynamics of offshore floating wind turbines is sufficiently different from conventional offshore and onshore wind turbines, warranting the use of higher fidelity analysis approaches. It is obvious that the

platform motions will have a great effect on unsteady aerodynamic performance of the wind turbine rotor. This thesis will study and explain the rules and reasons of this phenomenon in detail.

Future offshore floating wind turbine designs should strive to either minimize platform motions or be complementarily optimized, via higher fidelity aerodynamic analysis techniques, to account for them. It is believed that this dissertation is the first in-depth study of offshore floating wind turbine aerodynamics and the applicability of various analysis methods.

1.   INTRODUCTION

Since 1970's when world broke out energy crisis, countries paid more attention to the energy issues. Environmental pollution, global warming and energy supply had become more and more prominent, so the development and utilization for the renewable energy has become an important issue in today's world, which can reduce the emission of greenhouse gases. Moreover, wind source is free and clean. According to the reasons above, wind turbine technology is growing fast. Part of that growth is to deploy wind turbines further offshore into deep water. This chapter gives a brief introduction of wind energy development, especially the offshore floating wind turbine. Research objectives and scopes outlined as well.

1.1   Overview of Wind Energy

Currently, the renewable energy mainly includes wind energy, solar energy, nuclear energy, tidal energy and biomass energy. Wind energy technology is the most potential and mature one in comparison with other renewable energy engineering. It is safer than nuclear energy, cheaper than solar energy, more mature than biomass energy and more industrial than tidal energy. So wind energy has become the most suitable renewable energy which can be exploited in large scale. The future competition in the global new energy industry will be mainly focused on the wind energy.

Figure 1.1 shows the increase in wind power capacity of the whole world from 1997 to 2014. Seen from the figure, the newly installed capacity for global wind power in 2014 was reported at nearly 51.5 GW with an annual growth of about 44%, while the cumulative was 35.7 GW of installed wind power globally at the end of 2013. It is reported that the total installed capacity at the end of 2014 was about 369 GW. So as the big demand for the wind energy, more and more countries are interested in this industry.
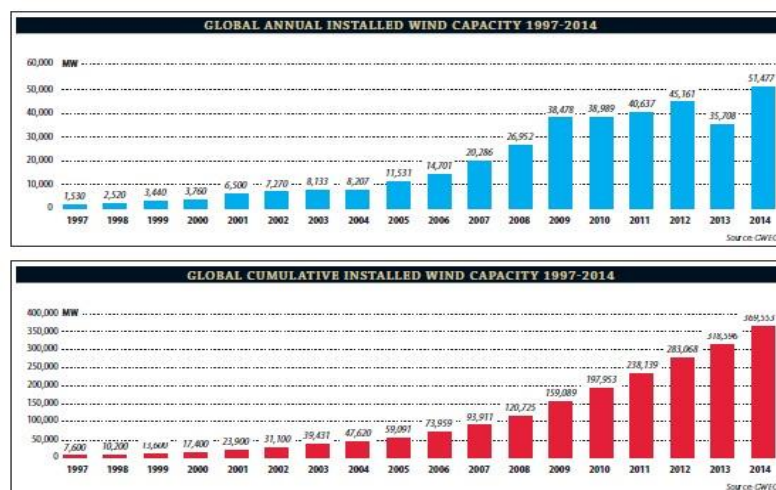
Figure 1.1 Global annual and cumulative installed wind capacity 1997-2014 (Global Wind Energy Council, 2015)

In 2014, China become world leader in installed wind energy capacity with 44.7GW of total installed capacity. Table 1.1 (Global Wind Energy Council, 2015) lists the top 10 countries that account for 84.2% of the global installed capacity as of December 2014. Though China and USA installed largest wind energy capacity, Europe also got a large capacity and become the leader in the world wind energy industry.

Table 1.1 Total installed wind energy capacity for the top 10 countries in 2014

	Country	Installed Capacity(MW)	% of Global Total
1	China	114763	31.0
2	USA	65879	17.8
3	Germany	39165	10.6
4	Spain	22987	6.2
5	India	22465	6.1
6	United Kingdom	12440	3.4
7	Italy	9694	2.6
8	France	9285	2.5
9	Italy	8663	2.3
10	Brazil	5935	1.6

1.2   Offshore Wind Energy

In the Early, wind energy development focused on land. However, as the wind power technology gradually extended from land to sea, offshore wind energy development has become the important direction of the global wind power industry. Offshore wind farm has many advantages compared with onshore wind farm. First, the annual average wind speed at sea is much higher than that on land. A study showed that as the sea roughness is smaller, the offshore wind speed which is 10 Km away from the land is 25% higher than on land. Table 1.2 shows the ratio of the average wind speed at sea and on land. Seen from the table, wind speed increases with the distance from the land enhancement. Second, it is in a more steady wind condition of lower wind shear and turbulence. What's more, as offshore wind farm is on the sea, it can save the valuable land recourse and has little impact on human life. Finally, for the wind turbine technology, it has a greater unit capacity and annual utilization hours. And the limitation of noise rule and transportation conditions is smaller. The offshore wind energy technology in Europe is very mature and step into the large-scale development phase.

Table 1.2 the ratio of the average wind speed at sea and on land

Distance from the land (km)	Ratio of Annual average wind speed	
	On land	At sea
0 (Standard wind speed)	4-6 (m/s)	7-9 (m/s)
25-30	1.4-1.5	1.2
30-50	1.5-1.6	1.4
>50	1.6-1.7	1.5

The concept of a floating wind turbine has existed since the early 1970s, but the industry only started researching it in the mid-1990s. From 1980 to 1990, Europe began to assess offshore wind resource and study related basic technology in large scale. Follow the route from development to demonstration and then to the commercial stage, a number of different sizes offshore wind power project have been developed and constructed according to different stages. First stage was offshore wind power development research and demonstration phase (from 1990 to 2000). Denmark, the Netherlands and Spain built 32,000 kilowatts small offshore wind

power projects for basic research and advanced demonstration together. Most projects built in the shallow coastal waters or waters with protective facilities and stand-alone wind turbine capacity was hundred kilowatts level. The most meaningful project was the first 250 kilowatts offshore wind turbine installation in Nogersund, Sweden in 1990. In 1991, Denmark established the world's first offshore wind farm near Vindeby on west coast of the Baltic sea. It installed 11450 kilowatts wind turbines and total energy capacity was 5MW. The wind farm was 1.5-3km from the shore and the water depth was 2.5-5m. In Europe, every year since 2000, new offshore wind turbines have been coming online. These projects are farther and larger. In 2000, Denmark installed 20 2MW offshore wind turbine in Copenhagen Bay and have been used by now which is the world's first commercial offshore wind farm. What's more, in 2003, the world's largest offshore wind farm was established in Lolland, Denmark so far. The total energy capacity was 165.6MW and it was 9km from the shore. The water depth was from 6 to 10 meters and the total number of the 2.3MW wind turbines was 72. In May 2007, the Beatrice wind farm in east costal of Scotland successfully installed the world's largest energy capacity wind turbine which reached 5MW.

Under the impetus of large offshore demonstration project, the global offshore wind power has increased steadily and reaches 1.08 million kilowatts, which accounts for 1.5 percent of the world wind power. Among them, the European Union is about 900,000 kilowatts, accounting for 90% of the world wind power. According to the newest statistics, the total wind power has arrived 1.48 million kilowatts by the end of 2008. In 2008, Blue H technologies installed the first test floating wind turbine off the Italian coast. The turbine had a rated capacity of 80 kW and after a year of testing and data collection, it was decommissioned. A year later the Poseidon 37 project followed a 37m- wide wave energy plant and floating wind turbine foundation tested at DONG's offshore wind farm at Onsevig. In 2009, Statoil installed the world's first large scale grid connected floating wind turbine, Hywind, in Norway, with a 2.3 MW Siemens turbine seen figure 1.2. The unit is located at a water depth of 200m, 10km off Norway's west coast. It has been thoroughly inspected after the first and second years in service, and no signs of deterioration, damage, or wear connected to being on a floater have been reported. Figure 1.3 shows the second largest scale floating

system, WindFloat, developed by Principle Power in partnership with EDP and Repsol, was installed off the Portuguese coast in 2011. Equipped with a 2 MW Vestas wind turbine, the installation started producing energy in 2012. In 2012, the average water depth of offshore wind farms was 22m. The average distance to shore was 29km. It is clear from projects under construction, consented or planned, that average water depth and distance to shore will increase. Projects announced are up to 200km from shore and in water depths of up to 215m. Alongside the trend towards deeper waters, the offshore wind sector is also developing larger turbines. The average size of the turbines grid connected during 2012 was 4 MW, up from 3.6 MW in 2011. 38 new offshore wind turbine models announced, only 9 (24%) had rated capacities of less than 5 MW. The remaining 29 (76%) were larger machines. Deep offshore designs will need to adapt to these increased turbine sizes to achieve the optimal balance between power production and cost. At the end of 2012 there were 1,662 turbines totalling 5 GW of installed offshore wind capacity spread across 55 wind farms in 10 European countries. They produced 18 TWh, enough electricity to power almost five million households. A further 4,460 MW were under construction and around 18,000 MW consented. Offshore wind represents 10% of the annual wind energy installations across Europe. This is only the beginning of major global industrial development, led by Europe. There were two full scale grid connected offshore wind turbines on floating substructures, Hywind and Windfloat. Both are located in Europe, one in the North Sea and one in the Atlantic.
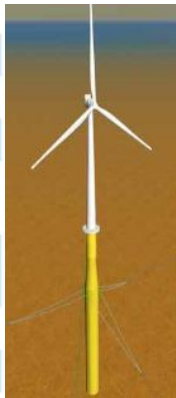
Design name	Hywind
Company	Statoil
Manufacturer	Siemens
Type of floater	Spar-buoy
Turbine capacity	2.3 MW (prototype) 3-7 MW (commercial)
Prototype installed	2009, West coast of Norway
Commercial installation	2015-2016
Origin	Norway

Figure 1.2 Hywind concept (European Wind Energy Association, 2013)

Design name	WindFloat
Company	Principle Power, EDP, Repsol
Manufacturer	Vestas
Substructure	Semi-submersible
Turbine capacity	2 MW (prototype) 5-7 MW (commercial)
Prototype installed	2011, Portugal
Commercial installation	2017
Origin	Portugal

Figure 1.3 Windfloat concept (European Wind Energy Association, 2013)

Seven experimental floating substructures (four in Europe, two in Japan and one in the US) are in a test phase: SeaTwirl, SWAY, Blue H and Poseidon in Europe, Kabashima Island concept and WindLens in Japan and DeepCwind floating turbine in the US. In addition FLiDAR is a floating Lidar, an offshore meteorological station designed for marine renewable energy technologies such as offshore wind, wave and tidal.

Figure 1.4 describes annual and cumulative installations of offshore wind in 2014. UK reaches the largest capacity about 45MW. There were 191.8 GW of installed wind energy capacity in the EU in 2014: 168.9 GW onshore and 23.5 GW offshore which can be seen in Table 1.3. Most of the offshore projects (3.2 GW or 65% of total capacity) are located in the North Sea. 16% of total capacity is located in the Baltic Sea and 19% in the Atlantic. There are currently no offshore wind farms in the Mediterranean, because the water is deep, and current commercial substructures are limited to 40m to 50m maximum depths. This restricts the potential to exploit offshore wind development in the Mediterranean.

Figure 1.4 Annual and cumulative installations of offshore wind (MW) (Global Wind Energy Council, 2015)

Table 1.3 Estimated EU wind power installations, production and share of EU consumption, and new EWEA low, central and high scenarios (Global Wind Energy Council, 2015)

	Wind energy installations GW			Wind energy production TWh			Share of wind energy in demand %		
	Onshore	Offshore	Total	Onshore	Offshore	Total	Onshore	Offshore	Total
EWEA 2014	168.9	23.5	191.8	355	86.4	441.7	12%	2.9%	14.9%
NREAPs	170	43	213	354.9	139.8	494.7	10%	4%	14%
EC 2013	156.5	47.6	204	343.2	142.9	486.3	11.6%	4.8%	16.4%

In addition, there are more and more countries having the developing experience of offshore wind turbine. Denmark, the Netherland, Sweden, UK and Ireland has established 22 commercial offshore wind farm which become currently the world leaders in wind energy technology. And German, France, Italy, Belgium and Japan has established or under construction as well. Recently, United States also began to attach importance to the development of offshore wind power and constructed the first one in 2010. For example, the Roscoe wind farm in Roscoe, Texas, United States has 627 wind turbines and covers over 100,000 acres of land. As Europe and other countries implement a large number of offshore wind power projects, offshore wind power has become a highlight causing investment boom and national attention. In 2010, new capacity has exceeded 1444MW. However, the European market is still dominant.
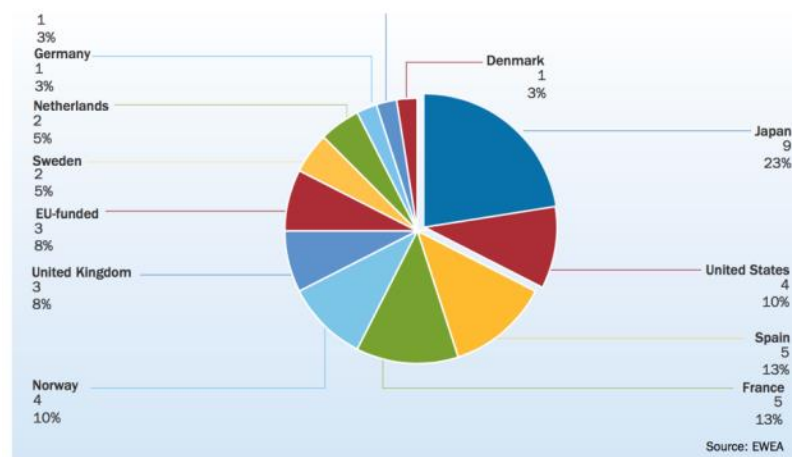
Figure 1.5 Location of deep water wind energy designs (based on number of projects announced) (Global Wind Energy Council, 2015)

By 2020, the EU must get 20% of its energy from renewables, have reduced its carbon emissions by 20% and its energy consumption by 20%. EWEA forecasts that by 2020, 40 GW offshore wind capacity could be operational in European waters,

producing 148 TWh provided that the right framework conditions are in place. By 2020 offshore wind will represent 30% of the new installation annual wind market. By 2030, EWEA forecasts 150 GW of installed offshore wind capacity, enough to power 145 million house- holds. Offshore wind will represent 60% of the new annual installations, exceeding the onshore market. Finally, by 2050 offshore wind could reach 460 GW, producing 1,813 TWh and contributing to a European power supply met 50% by wind. This exponential growth is only achievable through the deployment of deep offshore designs.
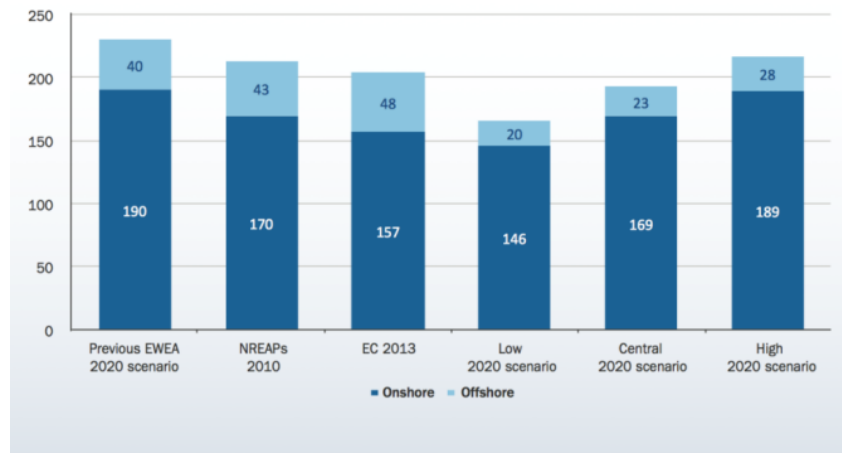
Figure 1.6 Previous EWEA, NREAP, EC primes and new EWEA 2020 EU wind power installation scenarios in GW (Global Wind Energy Council, 2015)

However, for this to happen, a supportive legislative framework is needed, and new offshore designs must be developed for deep water in order to tap the large wind potential of the Atlantic, Mediterranean and deep North Sea waters. Current commercial substructures are economically limited to maximum water depths of 40m to 50m. The 'deep offshore' environment starts at water depths greater than 50m.

Deep offshore designs are competitive in terms of the levelised cost of energy with bottom- fixed foundations in more than 50m water depth. The technology is still at a very early stage of development and in order to achieve commercial and large-scale deployment, the sector must overcome technical, economic and political challenges. If the challenges are overcome, the first deep off- shore wind farms could be installed and grid connected by 2017.

1.3 Wind Turbines

Wind turbines are the most important part of the wind energy industry. They are the machines which convert wind power to electrical energy. They are divided into two types: Horizontal Axis Wind Turbine (HAWT) and Vertical Axis Wind Turbine (VAWT) shown as figure 1.7 and 1.8, respectively. HAWTs are more commonly used because of their high efficiency in power production. Therefore, this dissertation just focuses HAWT.

Figure 1.7 HAWT type (GOOGLE)   Figure 1.8 VAWT type (GOOGLE)

Modern wind turbines use principles of aerodynamics to realize the full potential of rotating wind blades. Wind turbine blades are usually twisted with varying chord and thickness along the blade from root to tip. The cross section of a wind turbine blade is an airfoil as show in figure 1.9. The geometry of the airfoil has a direct effect on the coefficient of lift and drag. The lift force has a component that produces power on turbine rotation, whereas the drag force has a component that impacts negatively on power production.
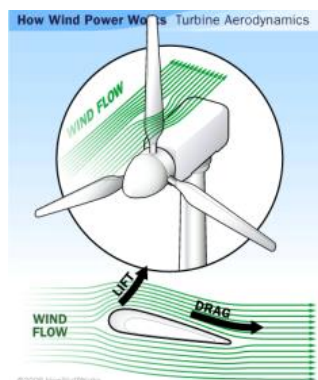
Figure 1.9 Aerodynamic performance of wind turbine blade (HowStuffWorks.com)

1.4 Floating Platform Configurations

Firstly, offshore wind turbines may be bottom founded or of the floating type.

Generally when the water depth is shallow or moderately deep (i.e. less than 50m), it is more economical to have bottom founded wind turbines. For large water depths and soft seabeds, floating wind turbines are attractive due to a cheaper anchor installation than the cost of a fixed foundation. Floating wind turbines can be used in water as deep as 700m. Drawing from the design classifications of floating offshore platforms for the offshore oil and gas industry, floating wind turbines can also be categorised into four main types. They are:

- Spar-buoy type
- Tension-leg platform (TLP) type
- Semi-submersible type (Column stabilised)
- Pontoon-type (Barge-type)

1.4.1 Spar-type floating wind turbine

As shown in figure 1.10, the spar wind turbine comprises the floating foundation (or some- times referred to as the floater), the tower and the rotor-nacelle assembly. The floating foundation (consisting of a steel and/or concrete cylinder filled with a ballast of water and gravels to keep the centre of gravity well below the centre of buoyancy) ensures the wind turbine floats in the sea and stays upright, since it creates a large righting moment arm and high inertial resistance to pitch and roll motions which will cause a free-yawing effect. The first full scale size spar floating turbine has been deployed off the south-west coast of Karmoy Island, Norway by Statoil in the Hywind demonstration project. The turbine has a 2.3 MW rating, a rotor diameter of 82.4 m, a hub- height of 65 m, a floating foundation draft of 100 m, weighs 5300 tons, and is moored by 3 taut mooring lines in deep water.

Figure 1.10 Spar-buoy type floating wind turbine (Utsunomiya et al., 2010)

1.4.2   TLP-type floating wind turbine

The TLP type comprises a floating platform structure to carry the wind turbine as shown in Figure 1.11 (a). In the offshore oil and gas industry, the conventional TLP platform comprises a square pontoon with columns on which the topside deck rests. A smaller version of this conventional hull form is the mini-TLP, which has been adopted by the TLP-type floating wind turbine (see Figure 1.11 (b)). Unlike the spar-type which needs to be assembled in water, this TLP wind turbine may be assembled and commissioned onshore thereby avoiding the logistical difficulties of offshore assembly. This type of floating wind turbine has a relatively less dynamic response to waves when compared to the spar-buoy type, the semi-submersible type or the pontoon type but is subject to a phenomenon known as 'pull down' which is an increase in draft as the platform is offset from its equilibrium position.
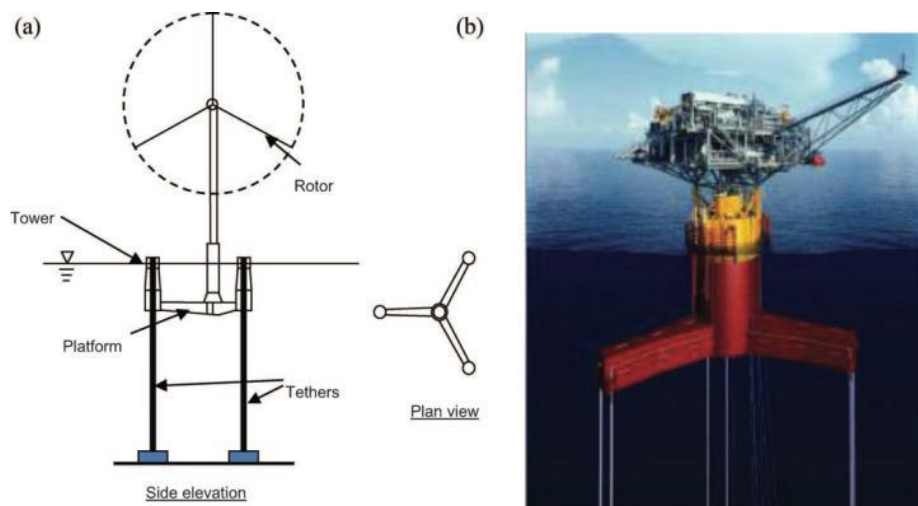
Figure 1.11 (a) TLP-type floating wind turbine and (b) offshore oil and gas mini-TLP (Suzuki et al. 2009)

1.4.3   Other types floating wind turbine

The semi-submersible type comprises a few large column tubes connected to each other by tubular members. A wind turbine may sit on one of the column tubes or there could be wind turbines sitting in all the columns. Alternatively, the wind turbine may be positioned at the geometric centre of the column tubes and supported by lateral bracing members. The column tubes provide the ballast and they are partially filled with water. Until now, there is no semi-submersible floating wind

turbine in operation. Principle Power Inc. is promoting the semi-submersible type which consists of three column tubes with patented horizontal water entrapment heave plates at the bases as shown in Figure 1.12. Figure 1.13 shows another concept design of semi-submersible type as proposed by Ishihara et al. (2007a,b). It has three wind turbines seated on three tubular columns.

Figure 1.12 Semi-submersible type floating wind turbine (Principle Power, Inc R5)

Figure 1.13 Semi-submersible type floating wind turbine (Ishihara et al. 2007)

The pontoon-type has a very large pontoon structure to carry a group of wind turbines. The large pontoon structure achieves stability via distributed buoyancy and by taking advantage of the weighted water plane area for righting moment. The pontoon type may be moored by conventional catenary anchor chains. However, the setback of the pontoon-type wind turbine is that it is susceptible to the roll and pitch motions in waves experienced by ocean-going ship- shaped vessels and may only be sited in calm seas, like in a harbour, sheltered cove or lagoon. The National Maritime Research Institute (NMRI) in Tokyo has made some studies on such pontoon-type

floating wind turbines. Design concepts of NMRI and that of Prof Ohta from Kyushu University are shown in Figures 1.14 and 1.15, respectively.

Figure 1.14 Prof Ohta's concept of pontoon-type wind turbine with rotor shroud nozzle
(Wang, 2010)

Figure 1.15 Prof Ohta's concept of pontoon-type wind turbine with rotor shroud nozzle
(Wang, 2010)

Also, there is an interesting concept of a sailing-type floating wind turbine (see Figure 1.16) that was studied at the National Institute for Environmental Studies, Japan (2007). The floating wind power plant has no mooring system but navigates with sails and azimuth thrusters. The self-sailing and self-propelled mobility allows the wind farm to move to a location that maximizes the generation of wind power as well as to weather route from storms.
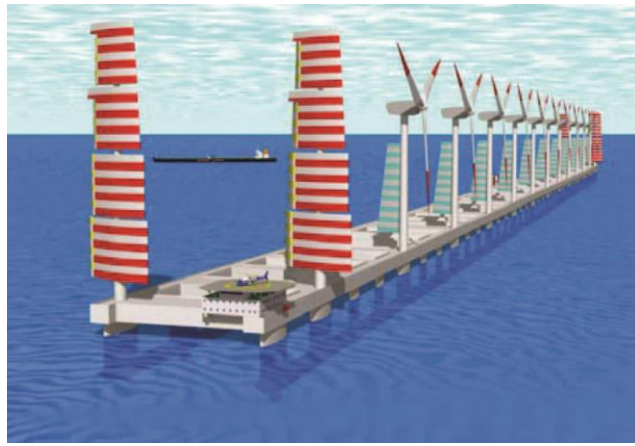
Figure 1.16 Sailing-type floating wind turbine (Picture courtesy of National Institute for Environmental Studies, Japan)

1.5   Methods to Predict the Aerodynamic Performance of a Rotor

The prediction of aerodynamic loads is fundamental to the design and simulation of wind turbine systems. A number of codes have been developed to model wind turbine behaviour. As there are not many FOWT experiments, majority of these codes are used by the wind industry to validate wind turbine designs. Currently three major approaches analysing aerodynamic performance of wind turbine are blade element momentum theory (BEMT), vortex lattice method (VLM) and computational fluid dynamics (CFD). Moreover, as the wind turbine blade is larger and larger, flexibility and addressed structural dynamics become more and more important. Aero-servo-elasticity (ASE) is a multidisciplinary technology dealing with the interaction of the aircraft's flexible structure, the steady and unsteady aerodynamic forces resulting from the aircraft motion, and the flight control systems. (Thomas,1990)

1.5.1   Blade Element Momentum (BEM) Method

Most wind turbine design codes are based on Blade Element Momentum method. Blade element momentum theory is a theory that combines both blade element theory and momentum theory. It is used to calculate the local forces on a propeller or wind-turbine blade. This theory is an extension of actuator disk theory, first proposed by the pioneering propeller work of Rankine and Froude in the late 19th century. The BEM theory, generally attributed to Betz and Glauert (1935), actually originates

from two different theories: blade element theory and momentum theory (see Leishman 2000).

In Blade Element Momentum theory, angular momentum is included in the model, meaning that the wake (the air after interaction with the rotor) has angular momentum. That is, the air begins to rotate about the z-axis immediately upon interaction with the rotor (see diagram below). Angular momentum must be taken into account since the rotor, which is the device that extracts the energy from the wind, is rotating as a result of the interaction with the wind.

1.5.2 Vortex Lattice Method

Vortex Lattice Method (VLM) is a method similar to the normal Panel Method. This method is based on the idea of a vortex singularity as the solution of Laplace's equation, and it is very easy to use and capable of providing remarkable insight into wing aerodynamics and component interaction. It was among the earliest methods utilizing computers to actually assist aerodynamicists in estimating aircraft aerodynamics.

1.5.3 Computational Fluid Dynamics (CFD)

Computational Fluid Dynamics (CFD) is a more accurate tool. It is a branch of fluid mechanics that uses numerical methods and algorithms to solve the governing equations of fluid flow and provide useful information for analysis and design of system involving fluid flow. The CFD analysis procedures are generally divided into three steps: pre-processing, simulation and post-processing. It can overcome many disadvantages of the potential theory, for example it can be used to solve very complex fluid flow problems. But it takes a lot of computation time, therefore, it is used only for analysis of specific problems which have uncertainties for potential theory method.

1.5.4 Aero-servo-elastic Method

In order to accurately predict the dynamic performance of wind turbines, aerodynamic models for determining wind loads and structural models for describing the dynamic response of the wind turbine have to be involved in the aeroelastic code.

In recent years, some of these codes have been expanded to include the additional dynamics pertinent to offshore installations, including the incident waves, sea current, hydrodynamics, and foundation dynamics of the support structure. The sophistication of these aero-hydro-servo-elastic codes, and the limited data available with which to validate them, underscore the need to verify their accuracy and correctness. The Offshore Code Comparison Collaboration (OC3), which operates under Subtask 2 of the International Energy Agency (IEA) Wind Task 23, was established to meet this need. To test the newly developed codes, the main activities of OC3 were to (1) discuss modelling strategies, (2) develop a suite of benchmark models and simulations, (3) run the simulations and process the simulation results, and (4) compare and discuss the results. (Jonkman, 2010) The OC3 project was performed through technical exchange among a group of international participants from universities, research institutions, and industry across the United States of America, Germany, Denmark, the United Kingdom, Spain, the Netherlands, Norway, Sweden, and Korea. Moreover, most of the aero-hydro-servo-elastic codes developed for modelling the dynamic response of offshore wind turbines were tested within OC3.

1.6   Research Objective and Dissertation Outline

The motions of an offshore floating wind turbine will result in significant cyclical loads on all major turbine components. In order to reduce this influence, the control system, like generator torque or independent blade pitch, maybe used to reduce the peak cyclical loads. However, tuning these systems needs an accurate aerodynamic simulation capability. Most design and dynamics study of floating offshore wind turbine is to assume that the aerodynamic analysis methods used in the onshore or conventional offshore wind turbine are also suitable for floating offshore wind turbine. But this hypothesis may be not accurate. They may violate the original formula assumes. For example, using the BEM theory and dynamic inflow method, it supposed potential energy conservation of blades. As the limitation of this method, this is may not valid for FOWT. So the rationality of the results obtained from these assumptions are doubtful.

Moreover, floating offshore wind turbine is always in a more complex environmental condition than onshore HAWT. The unsteady aerodynamic performance of floating

offshore wind turbine is associated with platform motions: surge, sway, heave, roll, pitch and yaw (shown in figure 1.17). The yaw and pitch platform motions will cause a larger skewed flows. Second, an effective wind shear or gradient across the rotor disk will be occurred due to angular motions. What's more, as a result of unsteady flows arising from a platform derived effective wind component, rapid local velocity changes. The platform motion DOFs produced an effective velocity contribution with respect to the rotor as shown in equation 1.1.

$$U_{platform} = \left(U_{surge} + \dot{\theta}_{pitch}z - \dot{\theta}_{yaw}y\right)\hat{\imath} + \left(U_{sway} + \dot{\theta}_{yaw}x - \dot{\theta}_{roll}z\right)\hat{\jmath} +$$
$$\left(U_{heave} + \dot{\theta}_{roll}y - \dot{\theta}_{pitch}x\right)\hat{k} \qquad (1.1)$$

This dissertation will study the aerodynamic operating environment of floating offshore wind turbine and identity the aerodynamically-significant platform modes and load cases. The most common aerodynamic characteristic analysis technology and limitation will be outlined. And some formulation assumption will be confirmed. CFD will be used to simulate the response of FOWT undergoing various platform motions with different operating conditions. These results are used to have a better understanding of the aerodynamic performance of floating offshore wind turbine and to determine when it may not be right to analyse these assumptions applying a simple method.
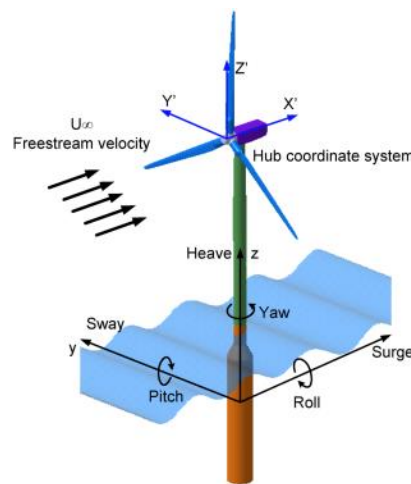
Figure 1.17 Platform motion of floating offshore wind turbine (GOOGLE)

The main research objective is to quantify the aerodynamic performance of multi-objective applied to the two main floating platform concepts: the tension leg and

spar-buoy platforms. The results and conclusions in this work are intended to be used by designers and developers of floating turbines. Simulations are carried out using FAST, a well-established wind turbine design and simulation tool, and CFD commercial software, STAR CCM+.

In addition to above objectives, it is important to define what the structure of this research is. This dissertation consists of 10 chapters.

Chapter 2 reviews previous work on aerodynamic calculation of wind turbines with three different methods as introduced above. The literature review of 2D airfoil and 3D blade aerodynamic analysis are both described respectively.

Chapter 3 is a simple introduction of CFD method. In addition, there is a description of the CFD commercial solver used in this dissertation, STAR CCM+. In CFD simulation, the uncertainty analysis in CFD verification and validation is very important to confirm the accuracy of CFD results. So, the ITTC rule is described in this chapter.

Begin to analyse the 3D blade, the 2D airfoil aerodynamic analysis is significant to study the flow phenomenon and dynamic characteristics. When the airfoil is in different oscillating motions like pitch, surge or pitch-surge combined motion, the aerodynamic performance is complex. The results are compared with the potential theory, Beddoes-Leishman model. The potential method cannot describe the complex flow. Chapter 4 has a detail description.

Chapter 5, the NREL 5MW offshore floating wind turbine is introduced and the selected simulation tool (FAST) is briefly described along with the assumption used to model wind turbines with floating platforms. Some test load cases are also formulated and the simulation is done in two potential methods, BEM and Generalised Dynamic Wake (GDW). The platform motions simulated by FAST will be used in the CFD simulation. Simulation results of aerodynamic performance for the onshore wind turbine, tension leg and spar-buoy platforms are analysed and discussed in chapter as well.

To confirm the accuracy of CFD method, it needs to validate with the experimental

results. However, there are not enough experiments about NREL 5MW wind turbine. This dissertation used the experimental results of NREL phase VI wind turbine to compare with the CFD simulation shown in Chapter 6. And then, using this numerical method calculates 5MW wind turbine at different load cases. The shear wind condition set up according to DLC1.2 of the IEC61400-3 standard and the performance metrics used to analyse the simulation results. The skewed flow phenomenon is occurred obviously as the dynamic condition. When compared with FAST results, the CFD method is more applicable in the dynamic condition. The results are also presented and discussed in chapter 7.

In next chapter, the dissertation is focused on the floating offshore wind turbine. Two different platforms are chosen as discussed in chapter 5. Given by FAST results, the pitch and surge motions are larger. Although yaw motion has a significant effect on aerodynamic performance of wind turbine, the numerical is too small. It is out of consideration in this paper. The platforms' simulation results are then compared relative to an onshore wind turbine in Chapter 8. Normalising the results relative to an onshore wind turbine allows for comparison between the floating platforms. In addition, the results are also compared with FAST results and 2D results to find that 3D effect is obvious. As the complexity of flow, the potential method may be not suitable to simulate the floating offshore wind turbine. A detective to an optimization of FAST method is very necessary.

Chapter 9 is combined the CFD results into the FAST source. It can describe the dynamic condition better and will get a better result when calculate the floating offshore wind turbine.

Conclusions of this work are presented in chapter 10. Some investigations which can be done in future are also discussed.

2. LITERATURE REVIEW OF AERODYNAMIC METHODS

Methods of various of levels of complexity have been developed to predict the aerodynamic behaviour of a wind turbine rotor. The review has been divided into three parts according to different analysis objects.

2.1 Review of Aerodynamic Method for Two-Dimensional Airfoil

The good aerodynamic performance of the airfoil is the key factor which affects the power coefficient of the wind turbine, so aerodynamic performance is fundamental for efficient rotor design. Aerodynamic lift is the force responsible for the power yield generated by the turbine and it is therefore essential to maximize this force using appropriate design. A resistant drag force which opposes the motion of the blade is also generated by friction which must be minimized. (Peter, 2012)

The aviation airfoils were often chosen to use in the traditional leaf blade of wind turbine. However, due to the different work environment and running conditions between wind turbine and airplane, the traditional aviation airfoils cannot meet the aerodynamic performance requirements of wind turbine. There are two methods to solve the problem. One is to add small height and length sheet-like lift devices which form a certain angle with the airfoil chord line in the lower surface of the trailing edge. Adding flaps in the wing tail of the wind turbine can indeed increase the maximum lift coefficient and an effective lift coefficient of the airfoil which is closely related to its height. When the height of the flag is 2 percentage of the chord, it can reach the best lift-to-drag ratio under steady state. Liebeck (1978) got a conclusion in the study of the Gurney flag that it would not bring obviously resistance increasing when the height of the flap was less than 2 percentage of the chord.

What's more, another way is to develop special airfoils. The choice of airfoils mainly included NACA series airfoils, NRELS series airfoils, SERI series airfoils, RISF-A series airfoils, FFAW series airfoils and DU series airfoils. National Advisory Committee for Aeronautics (NACA) four and five digit designs have been used for

early modern wind turbines (Hau, 2006). The classification shows the geometric profile of a NACA airfoil where the 1st digit refers to maximum chamber to chord ratio, 2nd digit is the camber position in tenths of the chord and the 3rd & 4th digits are the maximum thickness to chord ratio in percentage (Abbott, 1949). The emergence of wind turbine specific airfoils such as the Delft University (Timmer,2003), LS, SERI-NREL and FFA (Burton,2011) and RISO (Fuglsang, 2004) now provide alternatives specifically tailored to the needs of the wind turbine industry. Compared with the traditional airfoils, I found that the wind turbine airfoils are providing significant increases in annual energy production as a result of less sensitivity to roughness effects, better lift-to-drag ratios, and in the case of stall-regulated rotors, through the use of more swept area for a given generator size. The parameters of airfoils such as d-α, leading edge radius and so on will affect the aerodynamic (Franck, 2001). This section is a review of detecting aerodynamic performance of 2D wind turbine airfoil.

2.1.1   Wind tunnel experimental measurements and theoretical analysis

Early airfoil studies rely on theoretical analysis and wind tunnel experiments. Traditionally airfoils are tested experimentally with tables correlating lift and drag at given angles of attack and Reynolds numbers. Munk and Miller (1926) introduced wind tunnel experiments and measurement methods of boundary layer theory detailed. Historical wind turbine airfoil designs have been borrowed from aircraft technologies with similar Reynolds numbers and section thicknesses suitable for conditions at the blade tip. However, special considerations should be made for the design of wind turbine specific airfoil profiles due to the differences in operating conditions and mechanical loads. Since 20th centuries, National Renewable Energy Laboratory (Tangler, 1995), Risø National Laboratory, Roskilde, Denmark (Kristian, 1998) and Delft University of Technology, the Netherlands have done experiments for the aerodynamic performance and published the results. For example, Timmer and Schaffarczyk (2004) explored wind tunnel experiments results of DU97-W-300 airfoil in a high Reynolds number and studied the relationship between the trailing edge thickness and the maximum lift coefficient. However, the wind tunnel tests are time-consuming and expensive.

With the development of numerical simulation technology, more and more airfoil analysis using numerical methods, including surface element method, Boundary layer theory and CFD methods. Drefa (1969) developed the famous airfoil analysis and design software XFoIL based on potential flow theory and boundary layer integral equation coupling calculation method. During the same period, Eppler (1990) compiled the code for analysing and designing airfoils based on the panel method and the boundary layer equations. This code is widely used in wind turbine airfoil computing and made outstanding contribution to design and aerodynamic analysis of wind turbine airfoil. This approach can quickly get the calculating results, but the forecast of C_{lmax} is mainly dependent on the experienced modified formula of the boundary layer parameters (van Rooij, 1996). Timmer and van Rooij (2003) applied XFOIL software to enhance the prediction of the maximum lift coefficient, measure flutter effect and the influence of the vortex generators for different airfoils. They also studied the reason of why thick wind turbine airfoilsis sensitive to the roughness and how to determine the local angle of attack.

2.1.2 CFD methods

In recent years, with the advances of computer technology and turbulence model, the CFD methods for solving Navier - Stocks equations analysis play an increasingly important role in wind turbine airfoil aerodynamic due to the ability to accurately calculate the boundary layer parameters and flow separation, and to facilitate the analysis of the details of the flow field characteristics. And also, it can be completed early in the design of fast performance evaluation to improve the design, optimize design performance and save time, money and greatly reduce the risks of the new design. Therefore, more wind aerofoil aerodynamic performance tests apply CFD simulation. A.P. Schaffarczyk and B.Stahl (2004) applied an improved N-S equation solution method to study numerical simulation and wind tunnel experiment when the surface of airfoils were smooth or rough, as well as increasing Reynolds number.

However, several problems need to be addressed when testing wind turbine airfoil aerodynamic performance using the CFD numerical simulation. First, although the rapid development of computer technology has weakened the speed problem of the simulation of two-dimensional aerofoil, but the calculation accuracy has still been a

very prominent problem. The accuracy of the CFD simulation is not only related to the software itself, but also to the turbulence model factors associated with the users. It requires users to build the experience about how to use the software in order to play a better role of CFD numerical simulation.

Second, in the development of CFD, the turbulence problem has always failed to solve well. When you use numerical simulation methods to solve this problem, you need to make all kinds of assumptions of turbulent transport processes. The various physical quantities in the turbulent transport processes are linked to the flow field, which is the content of the turbulence model. Selecting the turbulent model should not only consider the reliability and accuracy of the simulation of complex flow, but also need to calculate the cost and determine the time to solve problems. Currently the most popular turbulent models are the Reynolds- Average model and the renormalization group model. And the large eddy simulation and direct numerical simulation model represent the trend of the future turbulent models.

Third, grid generation is more difficult. How to get a suitable computational grid to make the calculation accurate and quick becomes a practical problem. Many institutes have gone on numerical simulation for a variety of airfoils commonly used pre-processing software GAMBIT for geometric modelling and the structural C-type grid for computing grid. The mesh lines always extend in the distance of 10 times of the chord length in the wake of the trailing edge in order to stabilize the computations. The points near the airfoil are clustered since this is where the flow is modified the most, while the mesh resolution which is approach the far field boundaries can become progressively coarser since the flow gradients approach zero. Close to the surface, the mesh resolution near the leading and trailing edges must be the most since these are critical areas with the steepest gradients. The application of wall functions to modelling the near-wall region may significantly reduce both the processing and storage requirements of a numerical mode, while producing an acceptable degree of accuracy. The suitable meshes with adequate position for the first near-wall node are needed. So we need check the non-dimensional wall parameter y+ which means the distance from the first layer of viscous wall to the

airfoil surface in order to confirm the grid is suitable (Spezial, 1992). The y+ is defined as:

$$y^+ = \frac{\rho y_p \sqrt{\frac{\tau_w}{\rho w}}}{\mu}$$

(2.1)

In "Eq. (1)", y_p is the distance from the first computational node to the wall and the subscript w denotes wall properties. A.Firooz and M.Gadami (2006) conducted a grid independence analysis of NACA4412 using seven meshes of varying cell number. The results showed that different mesh density would get different results of airfoil aerodynamic performance. N.EI Gharbi and R.Absi (2009) present a comparative study between different near wall treatments.

Finally, more researches are still concentrated in the airfoil static stall performance simulation. Stall typically occurs at large angles of attack depending on the airfoil design. The boundary layer separates at the tip rather than further down the airfoil causing a wake to flow over the upper surface drastically reducing lift and increasing drag forces (Burton, 2011). This condition is considered dangerous in aviation and is generally avoided. However, for wind turbines, it can be utilized to limit the maximum power output to prevent generator overload and excessive forces in the blades during extreme wind speeds and could also occur unintentionally during gusts. It is therefore preferable that the onset of the stall condition is not instantaneous for wind turbine airfoils as this would create excessive dynamic forces and vibrations. However, due to the lack of effective turbulence models, the simulation of separation flow of airfoils is still not very accurate. When Manish and Chakrabartty (2007) studied the symmetric airfoil NACA0012 under the condition that the wind speed was 0.14 Mach number, the chord length was 1 and the Reynolds number was 2.2×10^6, simulation results showed that the difference of the experimental values with the calculated value was small before the airfoil stalled. After stalling, deviation became larger and the calculated stall angle was higher 2-3.25 degree than the experimental value. Ronald and Sally (2001) studied the aerodynamic performance of NACA0015 using the 2D unstructured grid and the Reynolds number was 1.2×10^6. The results illustrated that airfoil stall angle of attack was higher 4 degree than the experimental value. This also indicates that the stall

forecast based on a two-dimensional grid numerical simulation is not accurate. Some researchers get more accurate results by building the three-dimensional grid model. However, on the predicting overall airfoil aerodynamic performance, simulation based on a two-dimensional grid is realistic. Following the numerical simulation is in order to understand the flow trends, rather than the specific values. In addition, the two-dimensional grid is much smaller than the three-dimensional grid in the mesh size and the computing time. Therefore, from the economic considerations, the above deviation is acceptable. (Myose, 2006)

2.1.3   Principle of airfoil aerodynamic performance

In addition to the general analysis of the airfoil aerodynamic characteristics and flow details, another important thing is to study combined with the characteristics of the actual operation. On the one hand, with the increasing of the scale of the wind turbine wheel blade section, the operation range of the Reynolds numbers expands (10^5 -10^7). The impact of different Reynolds number to the airfoil aerodynamic characteristics becomes one of the research focuses. On the other hand, due to the wind turbine working in the field under the low-altitude environment, the surface is easy to contaminate. The effect of different surface roughness to the airfoil aerodynamic characteristics becomes another research focus. Third, the natural wind turbulence and possible upstream wind turbine wake flow will make the large change of the airfoil blade section turbulence intensity, so it is significant to study the different degrees of turbulence airfoil aerodynamic characteristics. Fourth, wind machines often run at off-design conditions. Therefore, the airfoil characteristics within the full angle of attack from 0 degree to 360 degree should be concerned. Fifth, under the running state, the dynamic response such as leaves waving and shimmy, as well as the natural wind shear, turbulence, gusts, etc. will cause the pitching motion and vertical fibrillation of the cross-section airfoil. Therefore, airfoil dynamic stall becomes a research focus. The last one, based on the important position of the transition phenomenon in the aerodynamic performance of airfoil boundary layer flow calculation, more and more airfoil analysis and design takes the impact of the transition into account. Corresponding to the above research, the following will introduce the principle of airfoil aerodynamic performance, research

methods, and its progress, and focuses on the research status quo of the boundary layer transition effects on the aerodynamic performance of wind turbine.

Reynolds number

Reynolds number will change the flow state of the airfoil boundary layer and affect the flow separation, thus changing the aerodynamic characteristics of the airfoil. In wind tunnel experiments, the effect of Reynolds number to airfoil aerodynamic characteristics generally achieve by changing wind speed, that is, by changing Mach number. In the wind tunnel of variable density or temperature, the change of airfoil Reynolds number is usually achieved by changing the working fluid viscosity, which can maintain the same Mach number. The literature (Miley, 1982) pointed from the experimental results of variable Mach number for different airfoil statistics that with the Reynolds number increases, the trend of the airfoil aerodynamic characteristics generally like follows that (C_l / C_d) max will increase, C_{lmax} will increase and C_{dmax} will decrease. The wind tunnel experimental results in the same Mach number show that the aerodynamic performance coefficient C_{lmax} of the different airfoil changes with the Reynolds numbers (Eastman, 1932; Freudenreieh, 2004). With the Reynolds number increasing, C_l of camber airfoils decreases, and C_l of symmetrical airfoil increases while Cd decreases. When the airfoils have the same thickness, the one in the greater curvature change will have a greater aerodynamic performance change along with the Reynolds number (Eastman, 1932). Under the two Reynolds numbers mode, the calculated results from XFOIL illustrated the inconsistency trend of aerodynamic characteristics of the same airfoil. Taking into account the impact of the Reynolds number to the state flow of the boundary layer and the effect of airfoil performance occurs mainly near stall area where the flow separate largely. When using CFD methods, two-equation turbulence model k-w wilcox (Freudenreieh, 2004) and k-w SST are used frequently and the boundary layer transition are taken into account in order to improve the calculation accuracy. Nevertheless, due to the transition model, the calculated results of literature (Freudenreieh, 2004) and experiment are still different. What's more, the airfoil aerodynamic performance change with Reynolds number is also related to surface roughness (Freudenreieh, 2004; Yan, 2011) and free stream turbulence intensity. Summary, there is no mature

theory to follow about the law of the impact of the Reynolds number to airfoil aerodynamic performance which needs to be determined through wind tunnel experiments.

Roughness

The effects of soiling have not been considered by aircraft airfoils as they generally fly at altitudes where insects and other particulates are negligible. Turbines operate for long periods at ground level where insect, dust, grease and rain erosion particulate build up is problematic. The surface roughness, especially the leading edge roughness, makes the transition of boundary layer in advance and after transition, the boundary layer thickness increases, the camber of the airfoil reduces, frictional resistance increases and the stall phenomenon occurs in advance, causing the airfoil aerodynamic performance deteriorate and the sharp decline of the wind turbine output power. Provision is therefore made for the reduced sensitivity to fouling of wind turbine specific airfoil designs (Rooij, 2003).

Corten and Veldkamp confirmed that the accumulation of insect debris lead a wind farm power loss nearly 25% in Canada (Corten, 2002). Khalfanah & Koltub pointed out that a 300kw stall wind machine installation in a dusty place in Egypt has dropped 50% of the total power after 9 months when clean up the leading edge (Antoniou, 1992). The surface roughness not only affects the power output of the wind turbine, but also affects the control of the wind turbine and may cause serious damage. Therefore, designing and using roughness insensitive airfoil and regularly de-icing, anti-corrosion, cleaning and repairing the blade are necessary.

Turbulence intensity

The wind tunnel experiments and numerical analysis of most airfoil are under the lower turbulence intensity the conditions (<1%), however, the wind turbines always run in the high turbulence intensity and the fluctuations are large, because the sea breeze and land breeze turbulence intensity range is 5% to 25% (Antoniou, 1992; Noda, 1999), making the turbulence integral length scale is 0.001 to 500m (Kaimal, 1994). When the integral length scales smaller than the length of airfoil chord, flow can still consider constant. While when the integral length scales greater than the

length of airfoil chord, you must consider the time change of the inflow which called unsteady flow (Sieot, 2006). However, the study of the impact of turbulence intensity to airfoil is mainly in the field of aeroacoustics (Mish, 2001), relatively few about the airfoil aerodynamic performance and more scarce for the wind turbine blade. Earlier studies can be found in Stack's literature (193l). With the increasing of the turbulence intensity, different airfoils have different trends of aerodynamic performance. For example, the aerodynamic performance of NACA0006 decreases with the increase of turbulence intensity (Reynolds numbers are 1.8×10^5 and 1.8×10^6), but the article does not given measurements of turbulence intensity and length scales. Literature (Ouahiba, 2006) uses a rare numerical analysis method to study turbulence intensity of the wind turbine airfoil aerodynamic performance. The results of CFD preliminary analysis of S809 airfoil show that with the increase of turbulence intensity (turbulence intensity are 0.04% and1%, the Reynolds number is 2.0x10), the airfoil suction peak increases and the performance is improved. In short, the wind turbine airfoil aerodynamic performance is strongly influenced by changes of the turbulence intensity.

Full angle of attack

The angle of attack is the angle of the oncoming flow relative to the chord line, and all figures for aerodynamic performance are quoted relative to this angle. In general, the airfoils typically work within the angle of attack of the range of -5 ° ~ 30 °, therefore, the studies of the aerodynamic performance mainly concentrate on this range.

Due to the flow around airfoil causing large-scale vortices and then shedding under the high angle of attack conditions, it increases the difficulty of the wind tunnel measurements and CFD simulation. Therefore, the literatures can rarely see the results from experimental data and CFD simulation in the full angle of attack. Loftin (1954) conducted wind tunnel experiment of full angle of attack for NACA0012. Timmer and Rooij (2001) did the wind tunnel experiment of full angle of attack for DU airfoils with thick of 18% to 30.

NACA airfoil series (Knight, 1929), Du airfoil series (Timmer, 2001), S809 (Hand, 2001) and S822 (Gross, 2010), combined with the aerodynamic design of the wind turbine, are usually used a semi-empirical formula based on the conventional angle of attack range airfoil performance (Moriarty, 2005). The literature (Montgomerie, 2004) gives the detail content and various amendments of the formula. And Moriarty (2005) assumed the flow around the high angle of attack airfoil as the flow around flat. Basing on the airfoil aerodynamic performance of stalling angle and 90° angle of attack to draw empirical formula, and then extrapolated to the aerodynamic characteristics of the angle of attack out of the experimental range.

To adopt CFD method, literature (Li, 2012) on the aerodynamic calculation of the angle of attack of wind turbine airfoil showed that through the establishment of a reasonable numerical model, RANS method can be used to predicted the angle of attack of the airfoil aerodynamic performance and proposed amendment to the semi-empirical formula.

Dynamic stall

Varying natural wind conditions result in altered directions and magnitude of velocities near turbine blades. These inhomogeneous velocity profiles cause unsteady operating conditions for wind turbine rotors such as unsteady angle of attack changes. A combination of stall phenomena, inherently unsteady, and various types of unsteady angle of attack (a) motion create dynamic stall (DS) phenomena. DS results in the development of a dynamic stall vortex and delay of stall, meaning a higher DS angle compared to a static stall angle. Because of these two significant features of DS, the dynamic lift coefficient exceeds the static lift coefficient. DS influences the loading of turbine blades that use stall regulation to control maximum loads. Thus, analysis based on static stall conditions may not be valid. Experimental methods, semi-empirical strategies such as Beddoes–Leishman (BL) models, and numerical models have been applied to predict the aerodynamic loads and flow conditions of wind turbines during DS phenomena.

The study of airfoil dynamic stall phenomenon began in 1960s for the helicopter rotor. McCroskey (1981) comprehensive described the physical phenomena,

mechanism of occurrence, influencing factors and research methods of airfoil dynamic stall. Literature (He, 2006) summarized the research methods and progress of various wind turbine airfoil dynamic stall, including experimental methods (wind field tests, wind tunnel experiments), numerical analysis (boundary layer theory, discrete vortex method, partition solution, CFD method, etc.) and engineering for wind turbine performance and load calculation model (such as Beddoes-Leishman model, ONERA model, etc.). Studies have shown that the geometric shape of the airfoil, surface roughness, reduced frequency, swing volatility and Mach and Reynolds constitute the main factors affecting the dynamic stall. CFD methods played an important role in the dynamic stall and engineering model. The early dynamic stall CFD can be shown from Ehristense & Sorensen (1994). In recent years, with the deepening study of the airfoil dynamic stall, some flow details are concerned. Literature (Qian, 2008) confirmed that the CFD method can simulate the trailing edge vortex shedding caused by high-frequency oscillation and the influencing factors of the oscillation. Literature (Xie, 2009) studied the transition, flow separation and vortex shedding flow details of airfoil dynamic stall using LES and LES- RANS coupling method. The dynamic stall research under the plunging oscillation caused by the blades brandished is earlier seen in the direction of the flapping wing. Among them, KnoHer-Betz effect is the first theory to explain the reason of lift causing. Compared with the dynamic stall study caused by pitching oscillation, vertical fibrillation study is relatively less. The experimental results show that the dynamic stall characteristics under plunging oscillation are strongly influenced by the reduced frequency and average angle of attack. (Soltani, 2009)

An airfoil that has received much attention in investigating DS phenomena is the S809 airfoil. Ramsay et al. (1995) tested a two dimensional (2D) S809 airfoil under stationary and dynamic conditions. In the dynamic case, the airfoil underwent pitch oscillations at different mean angles of attack and oscillating amplitude for Re > $0.75*10^6$ where Reynolds number is defined as Re= $\rho UC/ \mu$ where ρ and μ are the air density and dynamic viscosity, U is the free stream velocity and C is the airfoil chord length. The effects of airfoil roughness were also considered in their study. Somers (1997), at the Delft low speed, low-turbulence wind tunnel, measured aerodynamic coefficients for different Reynolds numbers. The results of these reported

measurements have been used as two references for developing models, conducting new experimental techniques, and advancing computational fluid dynamic (CFD) codes. The Beddoes–Leishman (BL) model, a very popular semi-empirical DS model, has been used for modelling dynamic stall phenomena for HAWT although the BL model was originally developed for helicopters. So far, this model has been developed and used for predicting the unsteady aerodynamic characteristics of S809 airfoils by researchers such as Sheng et al. (2007,2009), Gupta and Leishman (2006), Gonzalez and Munduate (2007) and Johansen (1999). According to Sheng et al. (2007), no DS model has been considered universal yet.

Boundary layer transition

In 1989, Drela simplified EN method and developed the famous airfoil analysis and design software XFOIL which was widely used in wind turbine airfoil analysis and design. In recent years, the EN method combined with CFD is used to predict the airfoil transition (Bordeur, 2001). It is worth noting that the literature (Freudenreieh, 2004) found that when use the EN method, some airfoils are difficult to achieve the high-precision simulation of the transition location and the aerodynamic performance at the same time. Also, different Reynolds numbers need to choose different N values. The uncertainty causes further inconvenience to promote this method. Since 1984, NREL used this approach to develop S801 to S828 wind turbine dedicated airfoils. Using Michel model (Miehel, 1984) to predict the transition location, literature (Zhang, 2009) compiled calculation procedures of inviscid flow coupled with boundary layer equations based on panel theory. Literature (Bertagnolio, 2001) calculated and analyzed a large number of wind turbine airfoils based on CFD technology and chen-Thyson (1971) model with intermittency factor correction. In 1997, wolfe & ochs (1997) pointed out that the commercial CFD software should increase the predictive ability of the transition. The study used a low Reynolds number model and based on CFD technology and k -W SST turbulence model. Literature (Qian, 2006) confirmed that this kind of turbulence model predicted the transition location earlier, so a new distribution pattern of intermittent function was proposed and applied to airfoil analysis. Above all, transition of the contribution to the calculation accuracy of airfoil aerodynamic performance has been widely

appreciated and also, transition prediction method was applied gradually. Literature consistently showed that considering the flow transition is significantly improved the accuracy of lift and resistance prediction of airfoils. Compared with the turbulence model, the lift coefficient increases, the drag coefficient decreases, suction peak and surface pressure value increases. Most of the literature can detailed compare the calculation results with experimental measurements, including the aerodynamic performance, the distribution of pressure and frictional resistance coefficient, the transition position and the separation point on the upper and lower wing surface.

2.1.4   Unsteady condition of airfoil

Wind turbines often run in the natural atmosphere with random changes. With the wind turbine becoming large, flexible and complex load changes with flexible structure interaction, wind turbine blade deformation and structural vibration is inevitable, and may make the blade vibration too big, or the vibration instability resulting in fatigue failure (Hansena, 2006). Security and stability analysis of wind turbine blades, as well as large-size blade design must be built on the foundation of the research of blade aeroelastic characteristics. Therefore, the aeroelastic problem of wind turbine blade has aroused great concern of researchers.

From the beginning of the last century, people began to research structure aeroelastic process. Aerodynamics pioneers such as Theodorsen got the first batch of theoretical formulas for developing the basis of the theory based on the unsteady aerodynamic study of the two-dimensional vibration plate. Theodorsen (1935) presented the lift and pitching moment for this type of airfoil under simple harmonic motion. Part of this general solution is the Theodorsen function, which is probably the best-known analytical expression that relates the effect of the shed wake on airfoil lift in the frequency domain. This expression has still been in use in the field of aviation dynamics (Theodorsen, 1935). Garrick (1938) showed that the indicial response and Theodorsen function were related through a Fourier transform. R.T. Jones (1939) developed a two-state approximation to lift theory (Jones, 1938) which could be used in either the time domain (as an approximation to Wagner's indicial response), in the frequency domain (as an approximation to the Theodorsen function), in the differential equation domain (for time marching), or in the Laplace domain (for

general airfoil motion) (Jones, 1939). Sears (1940) applied this operational form to some interesting problems of practical interest. W.P. Jones (1945) was the first to formulate an exact Laplace domain version of the Theodorsen function. However, at that time there was concern as to whether or not this function was truly valid for negative real arguments of s (Edwards et al., 1989).

Later, renewed interest in two-dimensional aerodynamics centered around finite-state approximations to the Wagner, Theodorsen, and Laplace solutions. Hassig (1971) used rational functions in the Laplace domain to approximate the exact solutions. Vepa (1976) introduced the method of Pade´ approximants to give a finite-state representation of lift force in the frequency domain, as did Dowell (1980). Edwards et al. (1978, 1979) attacked both the incompressible and compressible airfoil behavior in two dimensions. They established the mathematical rigor of the Laplace domain generalization of the Theodorsen function, D(s), and applied it numerically to problems of aeroelasticity. It is interesting to note here that there is also a two-dimensional model of unsteady aerodynamics for rotary wings in which the returning wake is treated by layers of vorticity below the airfoil in a two-dimensional plane. Loewy (1957) used this concept to develop an analog to the Theodorsen function for rotary wings. Dinyavari and Friedmann (1984) rotary-wing researchers, in trying to accommodate the need for general motion theories in rotorcraft, have used the Wagner function in a convolution integral (Beddoes, 1983), thus ignoring the returning wake.

During the end of the last century and the beginning of this century, due to the rise of computational fluid dynamics (CFD), more and more scholars began to use the numerical method to study the aerodynamic performance of structure. The more well-known methods are Larsen's discrete vortex method (Larsen, 1998) and Sun's sub-block iteration (block iterative) method (2008).

Naca0012 is a classic airplane airfoil model. LeMaitre et al and so on (2003) have used numerical method to simulate models under different Reynolds numbers conditions, as well as analyze aerodynamic performance under the conditions of the 0 degree of angle of attack, and achieved some progress. First, calculated the aerodynamic coefficients on the different angle of attack and compared with the

theoretical value. Then calculated the aerodynamic performance under the small amplitude conditions and compared with the Theodorsen tablet theoretical values. Finally, by calculating the aerodynamic performance under different amplitude conditions, the validity of the theoretical value was explored.

From the discussion, a problem occurred. Theodorsen flat panel flutter theory uses the small amplitude assumption, and on this assumption, the theory has also been proven to be very effective. But if leaving from this assumption which means gradually increasing the amplitude, whether Theodorsen theory can also be effective, is worth exploring. Comparison with variety of aerodynamic performance of NACA0012 under the forced vibration amplitude can be found that with the vibration forced amplitude increasing which means moving away from the assumptions of Theodorsen theory, various aerodynamic performances will eventually deviate from the theoretical value under the small amplitude conditions. Taking advantage of CFD method for calculating aerodynamic performance on variety of amplitudes of NACA0012, traditional flat panel theory really should be based on the small amplitude assumptions, and to some extent, the application scope of the traditional flat panel theory can be found.

2.2   Review of Aerodynamic Methods for Onshore Wind Turbine

The prediction of aerodynamic loads is fundamental to the design and simulation of wind turbine systems. A number of codes have been developed to model wind turbine behaviour. As there are not many FOWT experiments, majority of these codes are used by the wind industry to validate wind turbine designs. Currently three major approaches analysing aerodynamic performance of wind turbine are blade element momentum theory (BEMT) (Matha, 2011), vortex lattice method (VLM) (Minu, 2014) and computational fluid dynamics (CFD) (Anand, 2014).

2.2.1   Wind tunnel experimental measurements

To confirm the accuracy of the simulation results, wind tunnel experiments are necessary. In early 90's, many scientists detected three-dimensional stall vortex system and unsteady phenomena of finite wings. Freymuth (1988) visualized the unsteady, three-dimensional vortex structures elicited by various three-dimensional

lifting surfaces driven through diverse motion histories. Due to vortex pinning and straining near the tip of a rapidly pitching wing, Robinson and Wissler (1988) documented the lift enhancement and prolongation using surface pressure measurements. Also using surface pressure measurements, Lorber *et al.* (1992) characterized dynamic stall at elevated Reynolds numbers over a broad parameter range, using a wing oscillating in pitch. More detailed surface pressure data was employed to characterize the vortex dynamics in the root region of a rapidly pitching wing by Schreck et al. (1991). Unified comprehension of the vortex dynamics governing the root, mid-span and tip regions was provided by Schreck and Helin (1994), by combining flow visualization with surface pressure topologies. In addition to vortex pinning near the wing tip and root, these experiments revealed radical vortex deformation near the wing mid-span associated with dramatic spatial and temporal lift fluctuations. Subsequently, Piziali (1994) confirmed the existence of these structures and interactions for higher-aspect-ratio geometries.

Two other experiments were carried out in wind tunnels and arrived at different conclusions. Using two-dimensional airfoil performance as a baseline, Barnsley and Wellicome (1992) stated that the combination of rotational and three-dimensional effects appeared to suppress the loss of leading edge suction across the entire span, compared to two-dimensional behaviour. Alternatively, Ronsten (1992) used non-rotating blade data as a baseline and noted that rotation generated significant differences in lift behaviour only at the pressure measurement station farthest inboard on the blade.

However, these experiments are very expensive. It is not easy to get many experimental results in detail. Several articles present the computational predictions of NREL Phase VI rotor, a stall-regulated two bladed wind turbine with full-span pitch control and a power rating of 20 kW. The blade uses specially designed S809 airfoil for which experimental aerodynamic performance parameters are available.

National Renewable Energy Laboratory (NREL) conducted Unsteady Aerodynamics Experiment (UAE) (Lee, 2001), which provides comprehensive high-quality data for a modified Grumman 20KW two bladed turbine, tested in the NASA Ames 80ft*120ft wind tunnel. The most important results are in the Phase VI of the

experiments (Schreck, 2002). Experimental measurements included blade pressures and resulting integrated air loads, shaft torque, sectional inflow conditions, blade root strain, tip acceleration and wake visualization. Both upwind and downwind configurations with rigid and teetering blades were run for speeds from 5 m/s to 25 m/s.

In particular, wind turbine blades can experience large changes in angle of attack associated with sudden large gusts, changes in wind direction, atmospheric boundary layer effects or interaction with the unsteady wake shed from the tower support on downwind, horizontal axis wind turbines. These influences are described in detail in several reports by the National Renewable Energy Laboratory (NREL) based on the NREL Unsteady Aerodynamics Experiments, such as Robinson et al.(1999). Therefore, yawed and unsteady pitch configurations are also available. Selected NREL Phase VI experimental cases (Hand, 2001) are shown as table 2.1.

Table 2.1 Different yaw experiment tests of NREL Phase Vi wind turbine

TEST	WIND SPEED	YAW ANGLE
Upwind baseline case	7m/s (pre-stall), 10m/s (onset of stall), 15m/s (post stall)	-30,0,30,60 degrees
Wake flow visualization	5,7,10,15m/s	0,-10,-30,-60 degrees
Sweep wind speed case	5 to 25 m/s 25 to 5 m/s	0 degrees

2.2.2   Potential flow methods

Being computationally cheap and highly efficient, Blade Element Momentum method (BEM) is the most common used method for engineering design in industry. This theory is an extension of actuator disk theory, first proposed by the pioneering propeller work of Rankine and Froude in the late 19th century. The BEM theory,

generally attributed to Betz and Glauert (1935), actually originates from two different theories: blade element theory and momentum theory (see Leishman 2000).

BEM is a very engineering model based on simple momentum and strip theory. Analysis codes used to verify the stability and the ability of a FOWT structure to withstand experienced loads (e.g. Bladed, FAST or HAWC2) all base aerodynamic calculations on the BEM method. The classical BEM method determines induced velocities at the rotor plane by assuming equilibrium between applied aerodynamic loads and the induced flow field. The mentioned aerodynamic effects are trying to be realized by engineering correction models, since BEM methods cannot model a turbulent region behind the rotor, dynamic stall condition and yawed inflow conditions. Therefore, several models were developed based on BEM and their performance was improved by introducing new models as accounting for dynamic stall, dynamic wake, and tip losses (Snel and Schepers, 1993; Leishman and Beddoes, 1989; Shen et al., 2005). Predictions of yaw loads are also based on blade element theory, modified to account for the varying flow direction over the disc of a rotor operating in yaw, but assuming averaged inflow due to the wake. Zhong et al. (1991) and Ackerman (1991) have shown that improvements to blade element theory can be obtained by further modifications, which attempt to account for wake direction. In order to predict the induced velocity field more accurately, a number of approaches with some degree of wake modelling were required. Such as, Gould and Fiddes (1991) using a prescribed wake, BareiB and Wagner (1993), Rosen et al. (1990) and Simones et al. (1991) using free wakes and Voutsinas et al. (1994) using a large number of vortex particles to discretise the wake field are computationally considerably more expensive but still quite possible to carry out on a work station. Madsen et al.12 (2003) investigated the influence of yaw on a local inflow angle at specified blade sections by using an incompressible structured mesh Navier–Stokes flow solver and a blade element/momentum model at a wind speed of 7 m/sec for a yaw angle of 45°. The results showed that the classical inflow model used in the blade element/momentum method should be tuned better to capture the effect of rotor downwash flow more accurately.

However, this traditional BEM theory with common corrections cannot accurately predict aerodynamic flow effects, as Sebastian and Lackner (Sebastian & Lackner, 2011; Sebastian & Lackner, 2010) have shown. In other words, BEM theory does have its limitations.

BEM models are provided that good airfoil data are available for lift and drag coefficients as a function of angle of attack. However, such data may not always be available. Moreover, these models are dependent on empirical corrections to 2D airfoil results to account for 3D effects, such as tip loss, rotational flow and dynamic stall (Robin, 2006) limiting their use, especially for off-design conditions. Finally, many of the primary features of the airflow in and around wind turbine rotor blades such as the rotation of the turbine wake and the expanding wake downwind of the turbine are described by the results of the BEM theory. The real airflow is much more complicated to be accurately captured by BEM theory results. In spite of the limitations listed above, BEM theory has been used widely as a reliable model for calculating the induced velocity and elemental forces on wind turbine blades, and it has been retained as a useful model in AeroDyn. Therefore, the accuracy of the simulation results getting from these models is still doubtful, especially using in the offshore floating wind turbine in which the large platform motions will cause the complicated aerodynamic phenomenon.

To obtain more physical details and still retain high computational efficiency 3D inviscid aerodynamic models were introduced, including lifting line (Whale et al. 1999), panel methods (Hess, 1975), vortex lattice methods (Landahl and Stark, 1968), and Boundary Integral Equation (BIEM) (Preuss et al. 1980) methods. Duque et al.[11](2003) used a lifting-line method based on two-dimensional airfoil performance data to calculate the aerodynamic loading on the rotor blades when they operate at yaw angles of 10°, 30° and 60° for a wind speed of 10 m/sec. The results showed that the lifting-line method requires using proper stall delay and dynamic stall models to improve the prediction accuracy. VLM is a viable method as it can represent the non-uniform induced effects associated with the vertical wake trailing from the turbine. Pesmajoglou (2000) used free vortex lattice model in an unsteady condition of wind turbine. This technique is used to analyse three situations: steady

yaw, sinusoidally oscillating yaw and a random time history of yaw generated by an incident turbulent wind. Garrel (2003) set up a model ECN's AWSM applying the lifting line free vortex wake method. Though airfoil coefficients are not needed in these methods, issues arise because potential flow methods cannot handle viscous effects and separation.

2.2.3   CFD methods

Three-dimensional flow over rotating blades can be significantly different than the flow over a wing, and there can also be dramatic differences between 2-D and 3-D simulations. Rotating blades can have significant spanwise (or radial) flow. Also, of course, the blade speed varies linearly from root to tip. For these reasons, time-accurate three-dimensional and compressible rotating blade simulations are essential.

CFD solves Euler of Reynolds-Averaged Navier-stokes (RANS) equations, provides more physically realistic simulation. There are some turbulence models. The Baldwin-Lomax zero equation model (Baldwin and Lomax, 1978) and the two-equation k-e model (Launder and Spalding, 1974) are popular regardless of their problems in reproducing the stall characteristics of airfoils and rotor blades (Haase, 1997). The k-w/k-e SST model (Menter, 1994) is widely used for wind turbine simulations (Sorensen et al., 2002) for its capability in simulating attached and lightly separated airfoil flows. For massive separated flows, it is better to use the more advanced and costly Detached Eddy Simulation (DES) approach that combines large eddy simulation (LES) in the separated regions and RANS inside boundary layers. This gives DES the ability to better resolve flow separation and the stall of an airfoil (Johansen et al., 2002). Though the cost of these approaches is significantly higher than any of the previously mentioned simpler methods, advances in computer technology are making possible to handle large, dynamic problems with parallel platforms.

Several authors have performed CFD computations of wind turbines with a variety of methods. The generalized actuator disc method combines the BEM method and the Navier-Stokes equations, representing the blade geometries by surface forces that act upon the incoming flow. This method has been applied to study turbines (Mikkelsen,

2003), turbine wakes (Sorensen et al., 1998; Ivanell et al., 2007) and wind farms (Sorensen et al., 2007). The method was improved by the more sophisticated actuator line (Sorensen and Shen, 2002) and actuator surface (Shen et al. 2007, 2009) approaches. On the other hand, there have been several CFD studies in literature performing 3D rotor flow simulations. Benjanirat (2003) evaluated turbulence models for the prediction of wind turbine aerodynamics. The RANS solver was also used for the prediction of aerodynamic loads on NREL Phases II and III by Gupta (2007). Duque et al (1999) compared the accuracy of BEM, vortex lattice method and Reynolds averaged Navier–Stokes (RANS) simulations. The performance of the same rotor was also predicted by Sørensen and Michelsen (2000), and the results show a reasonable agreement with the experiment. Therefore, CFD has been used to improve the aerodynamic design of wind turbines including tip shapes, winglets and hub modelling where it captures flow physics better at which BEM models are no longer applicable. An extensive grid parameter study was conducted in order to rule out any effect of the computational grid settings on the CFD results by Christian Kress (2013). As the development of the CFD technology, there are more different CFD codes and turbulence models to be used in the wind turbine area. Duque et al. (2003) performed computations of the NREL Phase VI turbine with the NASA compressible RANS flow solver Overflow-D, based on a finite differences approach and overset grid (Buning et al., 1991). The authors compared the results of Overflow-D and the lifting line code CAMRAD II wih the experiments, and extensively discussed the aerodynamic performance of the wind turbine. Postsdam and Mavriplis (2009) used the unstructured and multi-grid RANS code NSU3D to predict the aerodynamics of an isolated wind turbine rotor, and the results were computed with both experiments and predictions with the code Overflow. Moreover, researchers at Risø computed the isolated rotor with and without wind tunnel walls using a multi-block, structured mesh, incompressible solver EllipSys3D with a RANS turbulence model (Sørensen, 2009) and a detached eddy simulation. Performance was generally well captured although stall initiation at 10 m/s wind speed was missed. In addition, Computational studies on HAWT using RANS with different turbulence models were conducted by Xu (2001) and Benjanirat (2007). Wind turbines are often operated in a complicated wind phenomenon. Therefore,

Madsen (2003) and Tongchitpakdee[14] (2005) analysed numerical simulation of the aerodynamics of horizontal axis wind turbines under yawed flow conditions with different CFD codes. Sezer-Uzol and Long[13] (2006) computed NREL Phase VI turbine at different wind speeds and yaw angles using the finite volume flow solver PUMA2 with rotating unstructured tetrahedral grids, showing good agreement with experiments, but the inviscid nature of the code resulted in limited ability to predict situations where massive flow separation occurs. Yuwei li (2011) computed the effect of the wind speed (5, 10, 15 and 25 m/s) at a fixed blade pitch angle of 3 with constant rotational speed using unsteady Reynolds-Averaged Navier-Stokes (RANS) and Detached Eddy Simulation (DES) turbulence models, both showing little difference in the averaged forces and moments. The effect of angle of attack is evaluated by dynamically changing the pitch from -15 to 40 at constant wind speed of 15m/s. When wind turbines in pitch motion during standstill, numerical investigations are performed to illustrate the possibilities of state of the art CFD methods for this problem by Sørensen (2012). Time-step, grid resolution and the effect of different types of modelling are investigated, ranging from fully turbulent Reynolds-averaged Navier-Stokes (RANS), transitional RANS, to transitional delayed detached-eddy simulation computations. Dong Ok Yu (2013) did similar research as Sørensen in 2013, which was accounted for by using a correlation-based transition turbulence model. A comparative study about the prediction capabilities of a Navier–Stokes method and a vorticity transport method was made for a few yawed flow conditions by Kim et al. (2010). The study also examined the effect of the instrumentation boom and the enclosure mounted upstream of the rotor. As mentioned previously, even though several studies were previously conducted to predict the aerodynamics of the wind turbine rotor at yaw, the detailed unsteady flow features and the blade loading behaviours for a wide range of operating conditions are still not fully understood and are subject to further investigations. Madsen (2012) considered the complex flow phenomena and rotor aerodynamics in a sheared inflow condition. The uncertainty in computing the aerodynamic forces for these common inflow cases is a limitation for the further optimization and design of MW turbines. One area of influence is the impact on development of new individual blade pitch control algorithms to alleviate fatigue loads, e.g., in wind farm operation that

requires accurate computation of the aerodynamic loads. Another area of uncertainty from sheared inflow is the power curve measurements where it is unclear if periods with strong shear in inflow should be let out because of possible changed power coefficient for the turbine. Although the research work comprises all the three different types of sheared flow mentioned above, it is mainly the sheared atmospheric inflow that is considered in the present study. An aerodynamic thrust and power have been computed along with the azimuth angle variation of the blade for an extreme coherent gust (ECG), an extreme operation gust (EOG) condition, based on a predefined function. Thanh-Toan Tran (2013) built accurate aerodynamic analysis method for the calculation of various design loads using advanced computational fluid dynamics (CFD) in ECG and EOG conditions with recurrence periods of 50 years. For the wind turbine considered here, the power control mechanism is based on the stall regulation principle, which implies the development of large flow separations on the suction side of the blade that induce complex 3D unsteady effects. To compare the 2D airfoils and 3D blades simulations, the successes and failures of the computations are highlighted and explained by various researchers. Sorensen et al. (2002) studied 3D aerodynamic effects as a function of wind speeds using the multi-block, finite volume, incompressible RANS flow agreement with experimental measurements evidenced the advantages of CFD approaches for wind turbine simulations. To compare with the 2D airfoils results, the capability of CFD in predicting complex 3D wind turbine aerodynamics is demonstrated in this paper with NREL Phase VI data campaign as a case study (Mukesh, 2013). Hartwanger (2008) analyse the blade sections in 2D and the results used to construct and validate a 3D CFD model of the turbine. The 3D results were used to develop estimates for actuator disk induction factors. In order to determine the airfoil characteristics from 3D rotor blade, several approaches were detected by researches. Johansen (2004) describes a method for extracting aerofoil characteristics from 3D computational fluid dynamics (CFD) rotor computations. Based on the knowledge of the detailed flow in the rotor plane, the average sectional axial induction is determined for each wind speed. In recent years, Guntur and Sorensen (2012) summarised four of the popular techniques and analyse the reliability of these simpler methods of estimating the 3D effective AOA compared some of the more

rigorous CFD based methods. The details of which are given in the following sections.

Though many researches of detecting aerodynamic performance of wind turbine have been done since 2000, we need also notice that most studies consider the rotor-only geometry, excluding the tower and nacelle; in most cases only one blade was included in the simulation. Hsu et al. (2013) used a finite element based an Arbitrary-Lagrange-Eulerian (ALE) method CFD code to simulate the NREL Phase VI wind turbine in a wide range of wind velocities with rotor-only configuration, and the full wind turbine through sliding interface method. The interest in the study of blade tip geometric modifications or use of winglets has been increased in the last few years. Imamura H et al. have conducted numerical analysis of the horizontal axis wind turbine with winglets in 1998. Raymond Chow and C.P.van Dam (2011) applied a simple, continuous full-chord fence at the maximum chord location of the NREL 5MW rotor blade. The fence increased energy capture by nearly 1% at a wind speed of 8 m/s and slightly increased blade loading over the length of the span. Martin Martin O. L. Hansen (2004) computed using computational fluid dynamics for a standard tip and a swept tip. The difference in the near-tip flow for the two tips for various tip speed ratios is examined and 3D airfoil data are extracted. Therefore, various tip loss corrections based on the Prandtl tip loss function are analysed. Comparisons with measurements and theoretical analyses show that existing tip loss correction models are inconsistent and fail to predict correctly the physical behaviour in the proximity of the tip. A new tip loss correction model is proposed that remedies the inconsistency by Wen Zhong Shen (2005). Comparisons between numerical and experimental data show that the new model results in much better predictions of the loading in the tip region. And then, Johansen and Sørensen (2006) have conducted a parametric analysis to test the effect of different winglets on the power production of a commercial wind turbine. In 2009, Chattot JJ (2009) detected effects of blade tip modifications on wind turbine performance using vortex model. There is an increased interest in the study of blade tip geometric modifications to improve the aerodynamic performance of turbine rotors and possibly making them less sensitive to wind gusts by using their structural response to variable loadings. Blade structure-fluid dynamic response is very important for the wind turbine design. Bazilevs et al.

(2011) studied the rotor of the NREL 5MW baseline wind turbine using both a finite element approach and a NURB-based (Non-Uniform Rational B-splines) approach for the geometry, which has the potential for coupled aerodynamic/structural analysis. Monier (2013) investigated winglet design and optimization using CFD. The main objective is to maximize the torque and hence increase the power by an addition of an optimized winglet. CFD has some limitations as well. The main limitation of the CFD methods is that they require much more computational time compared with the other methods. Another limitation is that the turbulence models cannot accurately capture the strong vortices at high wind speeds.

2.3   Review of Aerodynamic Method for Floating Offshore Wind Turbine

2.3.1   Small-scale experiment

In these last years, wind tunnel-based aerodynamic experiments on model FOWTs has been undertaken very limited. As the limitation of expense and equipment, there are only scale model floating offshore wind turbine experiments. Robertson et al. (2013) from the University of Maine conducted deepCwind scaled floating offshore wind system test. Sant et al. have conducted power and hot-wire near wake measurements on a 46 cm diameter rotor installed on a model TLP platform in a small wind tunnel/wave tank facility (Farrugia, 2014; Sant, 2014). The experimental studies of thrust and power amplitude variations under increasing rotor loading have led to interesting observations which opened up new hypotheses by Sant et al. (2015). The influence of rotor pitching in an FOWT model was recently studied by Rockel et al. (2014) using Particle Image Velocimetry (PIV) measurements in a wind tunnel. Bayati (2013) conducted tunnel experiments on a 1/25 scale wind turbine model installed on a 2 DOF3 rig to reproduce surge and pitch motion of a floating platform. Bayati et al. (2014) are now developing a more complex wind tunnel test rig with six DOFs capable of reproducing a wider range of motions experienced by wind turbines in real operating conditions.

The Marin Stock Wind Turbine (MSWT) is designed to have a similar non-dimensional thrust response as the NREL 5MW wind turbine such that different

floating foundation concepts can be evaluated in the Wind/Wave Basin at MARIN (Martin, 2012). 1=50th scaled-down tests were chosen. Froude-scaling laws were used to model winds and waves and the coupled behaviour was studied. Large Reynolds effects caused a poor turbine performance (C_T and C_P) which led to the new MSWT geometry, which was designed to match model and full-scale CT and CP (Martin, 2012; Ridder, 2014). Model-scale tests in which the MSWT was used showed great improvement in both C_T and C_P over the full range of TSR. Steven Martin (2015) concluded two main rotor scaling methodologies for small scale testing of floating wind turbine systems. The first, termed direct airfoil replacement, redesigns the profile of the blade using a multipoint airfoil optimization algorithm, which couples a genetic algorithm (GA) and XFOIL, such that the local non-dimensional lift force is similar to the full scale. The second, the geometrically free rotor design (GFRD) methodology, which utilizes the Python based multi-objective GA DEAP and blade-element momentum (BEM) code CCBlade, results in a more simplistic but less accurate design.

2.3.2 Aero-Servo-Elastic Simulation tool

In recent years, a variety of wind turbine aero-servo-elastic simulation tools have been expanded to include the additional loading and responses representative of fixed-bottom offshore support structures (Cheng, 2002; Eecen, 2003; Kühn, 2001; Lindenburg, 2005; Passon, 2005; Veldkamp, 2005). To enable offshore floating wind turbine design, the following are required: accurate modelling of the coupled wind turbine structural dynamics, aerodynamics, platform hydrodynamics, a mooring system and control algorithms. A number of studies have assessed the preliminary design of offshore floating wind turbines. For the hydrodynamic-loading calculations, many codes use Morison's equation. The time-domain dynamics models employed by Fulton, Malcolm, and Moroz (2006), and Withee (2004) used Morison's equation to compute the hydrodynamic loading on the TLPs. It ignores the potential effects of free-surface memory and atypical added-mass-induced couplings between modes of motion in the radiation problem (Cummins, 1962; Ogilvie, 1964) and takes advantage of G. I. Taylor's long-wavelength approximation (Cummins,1962; Ogilvie, 1964; Sclavounos, 2005) to simplify the diffraction

problem. These negligence and approximations inherent in Morison's representation limit its applicability for analysing many of the proposed support platform concepts for offshore floating wind turbines. Report (Jonkman, 2010) and (Jonkman and Musial, 2010) document the specifications of the floating system, which are needed by the OC3 participants for building aero-hydro-servo-elastic models. Matha (2009) presented results of the analysis using the fully coupled time-domain aero-hydro-servo-elastic design code FAST with AeroDyn and HydroDyn. The report provides a description of the development process of a TLP model, which is a modified version of a Massachusetts Institute of Technology design derived from a parametric linear frequency-domain optimization process. And then, by describing aerodynamic and hydrodynamic effects due to rotor and platform motions and usage of non-slender support structures, Matha and Schlipf (2011) detected the current major modelling challenges for floating offshore wind turbine design tools. Though Zambrano, MacCready, Kiceniuk, Roddier, and Cermelli (2005, 2007) employed a more sophisticated hydrodynamics model in the time-domain dynamics program, their aerodynamics and structural-dynamics models were unsophisticated, consisting only of a single horizontal drag force for the aerodynamics model and the six rigid-body modes of motion of the support platform for the full-system structural-dynamics model. Also, the concept analysed by Nielsen, Hanson, and Skaare (2006, 2007) and Larsen and Hanson (2007) had such a large draft (120 m) that it would be difficult to construct and be deployable only at sites with very deep water.

On the other hand, many frequency-domain studies have been conducted recently. Lee (2005) used linear frequency-domain hydrodynamics techniques to analyse a TLP design and a taut-leg spar-buoy design for a 1.5-MW wind turbine. Wayman, Sclavounos, Butterfield, Musial, and Jonkman (2006) also used a similar process to analyse multiple TLP designs and a shallow-drafted barge design for a 5-MW wind turbine. Bulder et al. (2002) used linear frequency-domain hydrodynamics techniques to find the response amplitude operators (RAOs) and amplitude standard deviations of the six rigid-body modes of motion for the support platform of a tri-floater design for a 5-MW wind turbine. Through frequency-domain analysis, Vijfhuizen (2006) designed a barge for a 5-MW wind turbine, which was also a platform for an oscillating water column (OWC) wave-energy device.

One limitation of frequency-domain linear analyses is that they cannot capture the nonlinear dynamic characteristics and transient events that are important considerations in wind turbine analysis. Several other offshore floating wind turbine studies have addressed this limitation. Using what they termed a "state-domain" technique, Henderson and Patel (2003) used RAOs to prescribe the motions of a 700-kW wind turbine to determine the effect that platform motions have on turbine fatigue loads. They showed that platform motions have little effect on power capture and rotor loads; instead, these were dominated by the aerodynamics of the rotor. They also showed, though, that platform motions have a substantial effect on the nacelle and tower loads, which are dominated by inertia. As a result, the tower would have to be strengthened if the platform motions could not be reduced. The same conclusions were drawn independently by Fulton, Malcolm, and Moroz (2006) and by Withee (2004). These researchers used different time-domain aero-servo-elastic wind turbine simulators that had been adapted to include the effects of platform motion and hydrodynamic loading of TLP designs for a 5-MW and 1.5-MW wind turbine, respectively. In a more recent analyses, Nielsen, Hanson, and Skaare (2006, 2007) and Larsen and Hanson (2007) drew similar conclusions. These researchers used a combined aero-servo-elastic, hydrodynamic, and mooring program to design a deep-drafted spar buoy (called "Hywind") to support a 5-MW wind turbine and develop its corresponding control system. This study, in particular, was important because the computer program simulations were verified by the response of a scaled-down model in a wave tank experiment. Finally, Zambrano, MacCready, Kiceniuk, Roddier, and Cermelli (2006, 2007) demonstrated the technical (but not economic) feasibility of smaller floating wind turbines. They used a time-domain model to determine the support platform motions and mooring tensions for a semisubmersible platform that supports three wind turbines of either 90 kW or 225 kW each and a TLP that supports a single 1-kW turbine.

The prediction of aerodynamic loads is fundamental to the design and simulation of wind turbine systems. A number of codes have been developed to model wind turbine behaviour. As there are not many FOWT experiments, majority of these codes are used by the wind industry to validate wind turbine designs. These involved the use of high fidelity codes based blade element momentum methods, vortex lattice

methods and free-wake vortex methods. Analysis codes used to verify the stability and the ability of a FOWT structure to withstand experienced loads (e.g. Bladed, FAST or HAWC2) all base aerodynamic calculations on the BEM method. Jonkman (2009) described the specifications of the NREL offshore 5-MW baseline wind turbine—including the aerodynamic, structural, and control-system properties—and the rationale behind its development. And then, Jonkman (2010) presented the development of a simulation tool for modelling the coupled dynamic response of offshore floating wind turbines, the verification of the simulation tool through model-to-model comparisons, and the application of the simulation tool to an integrated loads analysis for one of the promising system concepts. Otherwise, paper (Jonkman, 2008) presented the influence of conventional wind turbine blade-pitch control actions on the pitch damping of a wind turbine supported by an offshore floating barge with catenary moorings. However, as the results showed, BEM simulation cannot predict a turbulent wake state. Other simulation methods are discussed as well. Minu Jeon showed the characteristics of aerodynamic load predictions in platform pitching motion using the vortex lattice method (VLM) (Jeon, 2014). These results show that a turbulent wake state (TWS), which is undesirable condition and cannot predicted in BEMT simulation, arises when a floating wind turbine is operated at a low-speed inflow condition. In addition, the rotor experiences a TWS when the floating platform undergoes upward pitching motion. A generalized dynamic wake model, which is mainly used as a dynamic inflow model during wind turbine simulations, is not suitable in highly loaded rotor conditions such as recirculating flows, as it assumes that the mean induced velocity is small relative to the mean inflow velocity (Suzuki, 2000). Free vortex models (FVM) may improve the simulation of complex aerodynamic operating conditions. References (Garrel, 2003; Gupta, 2006; Micallef, 2010) described the development and application of wind turbine aerodynamics simulation module. Sebastion (2012) & Lackner (2011) provide some insight on wake dynamics using a free-wake vortex code. The FVM code Wake Induced Dynamics Simulator (WInDS) was developed at the University of Massachusetts at Amherst to predict the aerodynamic loading and wake evolution of an FOWT to a higher degree of accuracy than is possible via momentum balance methods (Sebastian, 2012). The results from these tests show that WInDS is able to

accurately predict the aerodynamically-derived loads and wake structures generated by various fixed and rotary-wing cases, and may therefore be applied to more complex cases, like FOWT s, with a degree of confidence. Thomas Sebastian (2010) selected different first-order aerodynamic analysis tools to predict loads and performance values of a floating horizontal axis wind turbine Results indicate that current methods for predicting the aerodynamic loads acting on an offshore floating wind turbine are lacking, though free vortex methods may provide a framework that accurately captures the physics of the flow field. Tonio Sant (2015) applied numerical simulation tools (FAST and WInDS) to investigate the time varying rotor thrust and shaft power characteristics of floating offshore wind turbines under different rotor yaw angles and regular sea wave conditions.

Mooring and anchor design can appreciably affect the dynamic response of offshore wind platforms that are subject to environmental loads. Improved modelling fidelity can be achieved through the use of finite element mooring theory. This can be accomplished by the new FASTlink coupling module, which couples FAST with OrcaFlex, a commercial simulation tool used for modelling mooring line dynamics. Reference (8) can be considered as a third-party assessment of the coupling which investigates the accuracy and stability of the FAST/OrcaFlex coupling operation.

2.3.3   CFD methods

CFD, which solves Euler of Navier-stokes equations, provides more physically realistic simulation. The current investigations employ an advanced transitional modelling technology coupled with the Spalart-Allmaras turbulence model and an efficient sliding interface method to address both physical and numerical modelling challenges faced in the wind turbine CFD simulations. Therefore, CFD method is an appropriate choice to simulate flow separation and wake interaction, though it incurs a significant computational cost. CFD helps to study the finer details of certain scenarios which are not possible with the software like FAST. Matha (2012) presented the identification and analysis of the aerodynamic inflow conditions on a representative catenary moored FOWT and discusses differences and design implications with respect to the bottom-mounted and onshore wind turbines. The results show the influence of wave induced motions on inflow conditions, e.g. a

decrease in mean and increase in variance of inflow velocity probability density functions. These influences and interdependencies are described and evaluated.

At the SWE a continuing study (Matha, 2011) comparing BEM and CFD for a generic multi-megawatt rotor with prescribed FOWT pitch motion is currently conducted with a full three-dimensional CFD model of the rotor in the RANS code FLOWer (a RANS/LES CFD solver for structured meshes, developed by the German Aeronautical and Aerospace Centre DLR). The results of the NREL study indicate that the current state-of-the-art in wind turbine analysis relies too much on subjective, loosely-defined parameters and too little on an accurate understanding of the physical phenomena that drive wind turbine aerodynamics. This problem is further exacerbated when attempting to analyse floating horizontal axis wind turbines (HAWTs). Then Thanhtoan Tran (2014) also illustrated the unsteady aerodynamic effects of a floating offshore wind turbine experiencing the prescribed pitching motion of a supporting floating platform as a sine function. The major objective of the present work is to show the different predictions among traditional blade element momentum, general dynamic wake and advanced computational fluid dynamics approach for a floating offshore wind turbine (FOWT). The pitching motion intermediately causes a transient flow condition which is one of the potential operating and the simulation problems for a floating wind turbine. In particular, the pitching and yawing motion may cause more power in a floating offshore HAWT system because of the above issues. Reference (Anand, 2014) focusses on verifying the values of induction factors using Computational Fluid Dynamics (CFD) simulations for floating offshore wind turbines at a selected sea state. The study includes steady state calculations as well as transient calculations for pitching motions of the turbine due to waves. When Hywind spar buoy wind turbine in an extreme pitching motion, a comparison of the rotor loads occurring during this selected motion using three different aerodynamic methodologies, blade-element/momentum theory, a lifting line free vortex wake method and CFD were conducted by Matha (2013). The results show distinct variations in extreme load predictions during the motions. The same methodology is adopted in the surge condition. Various surge conditions are investigated and wake plots are also shown. Vaal (2014) investigated the effect of the back and forth surge motion of a floating

wind turbine on the integrated loads and induced velocity. Because of the surge motion, the wind turbine rotor experiences an apparent wind effect and, in addition, will be moving into and out of its own wake. Results for different dynamic inflow models are compared with an actuator disc model in FLUENT, where wake dynamics are inherently accounted for as part of the flow solution. One of the major conclusions of their work is that the effects of the variation of induced velocities with time seem to have little effect on integrated loads and hence current dynamic wake models in BEM are suitable for global load analysis. This is also consistent with the work of Farrugia et al. (2014). Micallef (2015) performed using an actuator disc Navier Stokes model, a Blade Element Momentum model and a Generalized Dynamic Wake model on the NREL 5 MW reference rotor in order to confirm or reject these observations on a full-scale surging rotor. A research gap in the literature has been identified in relation to the rotor performance under different tip speed ratios in surge. Bekiropoulus et al. (2011) performed a RANS analysis using the FLOWer solver. Wake results are shown in this work but the relationship between rotor loading and wake geometry is not investigated. Sean Quallen (2014) predicted less overall platform motion. Predicted power is shown to rely heavily on system pitching and surging motions. The system simulation shows that the crowfoot model eliminates the need for a geometric line approximation. Wu (2015) developed a computational fluid dynamics (CFD) model for simulations of rotor under floating platform induced motion in OpenFOAM. Six degree of freedom (6DOF) solid body motion solver was extended to couple with multiple motions, especially for the motion of rotor coupled with the surge-heave-pitch motion of floating platform. But the combined effects are not studied in greater detail for various floating systems. The dynamic models developed previously were not good enough in predicting various behaviours due to its limited capabilities.

2.3.4   Scaling effects

As experiments described above, nowadays only scale wind tunnel experiments have been conducted to study aerodynamic performance of FOWT. The flow around an airfoil at the scale of a wave basin brings new distinct challenges than at full scale which will cause scaling effects caused by Froude-scaling to both wind and waves

during model tests. The capacity of standard engineering tools for the design of wind turbines to capture this complexity may be questioned. Gueydon (2015) applied a common solution that consists of optimizing the load coefficients of the rotor to reproduce the measured rotor loads. Several approaches (XFOIL + FAST, RANS + FAST, Optimization with XFOIL and FAST, Optimization with FAST only) are compared. In addition, Make (2015, 2014) did some researches to get correct aerodynamic characteristics at model-scale conditions as well. First a 3D CFD study was performed in which the behaviour of the flow over the commonly studied NREL 5MW baseline turbine and the MSWT geometries was performed. Both model and full-scale conditions were studied for a fixed non-moving platform and rotor-only turbine. It was found that scaling effects are indeed significant and a highly three-dimensional and additionally separated flow was observed. Based on these findings two methods were proposed to expand the applicability of BEMT-based tools to off-design and model scale conditions. First, instead of using commonly used 2D XFOIL data, 2D CFD RANS data was used. The use of purely 2D data from 2D CFD RANS computations did however not result in the desired improvements when compared to XFOIL-based results. The second proposed method is based on the use of 2D airfoil data obtained by post-processing of 3D flow data coming from 3D CFD computations. This new approach was shown to be successful and can therefore be extremely useful for future model-scale FOWT testing campaigns to do preliminary performance predictions. A comparative study of these tools against model-scale experiments showed that standard BEMT based tools using 2D airfoil data coming from XFOIL, are not suitable for model-scale performance predictions due to the large scaling (Ridder, 2014). Therefore instead of using XFOIL, data coming from 2D RANS computations was used. Although the RANS based results were useful in analysing 2D scaling effects its use in conjunction with BEMT did not result in improved performance predictions due to the highly 3D character of the flow which is not considered within the conventional BEMT (Fernandes, 2014).

Variants of optimizations are applied to a semisubmersible floating wind turbine at scale 1/50th, the DeepCwind semisubmersible platform. The effects of the differences between these 3 methods on the motions of the floater in waves and wind are analysed. Multiple approaches to obtain these coefficients have been proposed

and often these coefficients are simply tuned to better fit the measured thrust and power delivered by the rotor.

This work seeks to first numerically confirm the experimental observations made on very small scale rotors but in this case, on a full scale 5 MW rotor. If confirmed, these observations must be intrinsically linked to the wake behaviour. The methodology used permits to understand the underlying wake physics which enables this behaviour to occur. This enables rotor designers to have a better understanding of the additional complexity which must be considered when surge motion is present.

2.4   Conclusions

There are various methods analysing aerodynamic performance of wind turbine blade. For the 2D aifoil, early studies rely on wind tunnel experiments and theoretical analysis. However, in recent years, CFD methods play an increasingly important role to analyse the detail flow field characteristics. Reynolds number, roughness, turbulence intensity, angle of attack, dynamic stall and boundary layer transition are significant parameters to affect the aerodynamic performance of airfoil.

For the 3D wind turbine, as there are not many FOWT experiments, two major approaches are applied to analyse aerodynamic performance: potential flow method and computational fluid dynamics method (CFD). Blade element momentum method (BEM) is the most common used method for engineering design in industry. However, this method cannot model a turbulent region behind the rotor, dynamic stall condition and yawed inflow conditions. Therefore, several models were developed to improve the aerodynamic performance. This tradition BEM theory with common corrections still has its limitations, especially in complicated simulation condition. Several CFD studies in literature perform 3D rotor flow simulations. It estimates aerodynamic performance better and can describe the flow field. However, most studies focused on the rotor-only geometry.

Floating offshore wind turbine are combined aerodynamic, hydrodynamic and mooring system dynamic effects. Rotational and transitional motions primarily cause oblique flow conditions. In last years, several wind tunnel based aerodynamic experiments on model FOWTs has been undertaken. Aero-servo-elastic simulation

tools like Bladed, FAST or HAWC2 based on BEM method are used to verify the stability and the ability of a FOWT structure. Several CFD studies are conducted in different motions. The major objective of the work is to show the different predictions among traditional BEM, GDW and CFD approach for a FOWT.

3. COMPUTATIONAL FLUID DYNAMICS METHOD

3.1 Overview

Computational fluid dynamics is, in part, the art of replacing the governing partial differential equations of fluid flow with numbers, and advancing these numbers in space and/or time to obtain a final numerical description of the complete flow field of interest. This is not an all-inclusive definition of CFD; there are some problems which allow the immediate solution of the flow field without advancing in time or space. In any event, all such problems involve the manipulation of, and the solution for, numbers. The end product of CFD is indeed a collection of numbers, in contrast to a closed-form analytical solution. However, in the long run the objective of most engineering analyses, closed form or otherwise, is a quantitative description of the problem, i.e. numbers (Anderson, 1976). Of course, the instrument which has allowed the practical growth of CFD is the high-speed digital computer. CFD solutions generally require the repetitive manipulation of thousands, or even millions, of numbers—a task that is humanly impossible without the aid of a computer. Therefore, advances in CFD, and its application to problems of more and more detail and sophisticated, are intimately related to advances in computer hardware, particularly in regard to storage and execution speed. This is why the strongest force driving the development of new supercomputers is coming from the CFD community (Graves, 1982).

3.2 Governing Equations

The cornerstone of computational fluid dynamics is the fundamental governing equations of fluid dynamics—the continuity, momentum and energy equations. These equations speak physics. They are the mathematical statements of three fundamental physical principles upon which all of fluid dynamics is based: (1) mass is conserved; (2) F = ma (Newton's second law); (3) energy is conserved. These fundamental principles can be expressed in terms of mathematical equations, which in their most general form are usually partial differential equations.

Mass conservation equations which known as the continuity equation:

$$\frac{\partial \rho}{\partial t}+\frac{\partial}{\partial x_i}(\rho u_i)=S_m$$

(3.1)

This equation is a normal form of mass conservation equations which is suitable for compressible and uncompressible flow. ρ means the flow density. S_m is a continuous quality which is added from two dispersed items.

Continuity equation in the Cartesian coordinate system can be described as:

$$\frac{\partial \rho}{\partial t}+\frac{\partial}{\partial x}(\rho u)+\frac{\partial}{\partial y}(\rho v)+\frac{\partial}{\partial z}(\rho w)=S_m$$

(3.2)

In the i direction of inertial coordinate system, the momentum conservation equation is:

$$\frac{\partial}{\partial t}(\rho u_i)+\frac{\partial}{\partial x_j}(\rho u_i u_j)=-\frac{\partial p}{\partial x_i}+\frac{\partial \tau_{ij}}{\partial x_j}+\rho g_i+F_i$$

(3.3)

Where P means static pressure, g_i and F_i defines gravity volume force and external volume force in the i direction, respectively.

Stress tensor can be defined as:

$$\tau_{ij}=\left[\mu\left(\frac{\partial u_i}{\partial x_j}+\frac{\partial u_j}{\partial x_i}\right)\right]-\frac{2}{3}\mu\frac{\partial u_l}{\partial x_l}\delta_{ij}$$

(3.4)

3.3   Turbulence Model for RANS Equations

Reynolds average is a method which divided the instantaneous variables of Navier-Stokes equation into two parts: time average value and turbulent fluctuation value. The velocity can be defined as:

$$u_i=\bar{u}_i+u_i'$$

(3.5)

Where $\bar{u}_i$ is the time average velocity and u_i' is the turbulent fluctuation velocity.

Similarly, $\emptyset=\bar{\emptyset}+\emptyset'$

(3.6)

where $\emptyset$ denotes pressure, energy and so on.

Then substitute the equations above into the instantaneous continuity equation and momentum equation and get the average results. Therefore, we can get the continuity equation and momentum equation under the Cartesian coordinates.

$$\frac{\partial \rho}{\partial t} + \frac{\partial}{\partial x_i}(\rho \overline{u_i}) = 0 \tag{3.7}$$

$$\rho \frac{Du_i}{Dt} = -\frac{\partial \rho}{\partial x_i} + \frac{\partial}{\partial x_j}\left[\mu\left(\frac{\partial \overline{u_i}}{\partial x_j} + \frac{\partial \overline{u_j}}{\partial x_i} - \frac{2}{3}\delta_{ij}\frac{\partial \overline{u_i}}{\partial x_l}\right)\right] + \frac{\partial}{\partial x_j}(-\rho \overline{u_i' u_j'}) \tag{3.8}$$

The two equations above are both Reynolds Average Navier-Stokes (RANS) equations. They have the same form with instantaneous Navier-Stokes equation. The difference between these two methods is that the velocity and other solving variables are changed into the time-average variable. The extra expression $-\rho \overline{u_i' u_j'}$ indicates the Reynolds stress which describes the effect of turbulence. If we want to solve this equation, the expression $-\rho \overline{u_i' u_j'}$ must be simulated to enclose this equation. Boussinesq assumption is a normal method to simulate $-\rho \overline{u_i' u_j'}$ which supposes that Reynolds stress and average velocity gradient are directly proportional, shown as following equation:

$$-\rho \overline{u_i' u_j'} = \mu_t \left(\frac{\partial u_i}{\partial x_j} + \frac{\partial u_j}{\partial x_i}\right) - \frac{2}{3}\delta_{ij}(\rho k + \mu_t \frac{\partial u_i}{\partial x_j}) \tag{3.9}$$

Turbulence models are required to modify the RANS equations to simulate the turbulent flow. There are three categories of turbulence models.

First is the turbulent transport coefficient model which was proposed by Boussinesq in 1877 for solving the 2D flow problem. The second-order correlation amount of speed pulsation is defined as the product of the average velocity gradient and turbulent viscosity coefficient.

$$-\rho \overline{u_1' u_2'} = \mu_t \frac{\partial u_1}{\partial x_2} \tag{3.10}$$

Then extended it to three-dimensional and described this using Cartesian tensor:

$$-\rho \overline{u_i' u_j'} = \mu_t \left(\frac{\partial u_i}{\partial x_j} + \frac{\partial u_j}{\partial x_i}\right) - \frac{2}{3}\rho k \delta_{ij} \tag{3.11}$$

The objective of the model is calculating the turbulent viscosity coefficient μ_t. According to the numbers of differential equations which were needed in the modelling establishment, it can be divided into zero-equation models, one-equation models and two-equation models.

Boussinesq assumption (Wikipedia) is applied in the Spalart-Allmaras one-equation model and k-e two-equation model. The advantage of Boussinesq assumption is that it can reduce the computation time when calculate the turbulent viscosity coefficient. Otherwise, it considers that the turbulent viscosity coefficient μ_t is an isotropic scalar. This term is not strictly true especially for some complex flow. So this assumption has the limitation.

Another method is to calculate every component of turbulent stress in the transport equation. It needs to solve an extra scalar equation such as the turbulent dissipation rate equation which means that extra 4 transport equations and 7 transport equations should be solved for 2D and 3D turbulent flow problems respectively. Obviously, it requires more time and more internal memory of computer.

Third one is large-eddy simulation. The first two methods mentioned above were statistical average of all vortex which were on the foundation of statistical structure of turbulence. However, large-eddy simulation was divided the turbulence into large-scale and small-scale turbulence. By solving the 3D modified Navier-Stokes equation, the motion characteristics of large-scale turbulence was founded. On the other hand, small-scale turbulence motion still applied the above-mentioned model.

In the realistic situation, suitable models must be based on the characteristics of specific issues. The general principle of choice may meet the features such as high precision, simple application, saving calculation time and generalization. Therefore, the first one is commonly used in CFD simulations. The following contents described several concrete turbulent models which will be applied in the CFD calculations of this thesis.

3.3.1 One equation Spalart-Allmaras model

The Spalart–Allmaras model is a one-equation model that solves a modelled transport equation for the kinematic eddy turbulent viscosity. The Spalart-Allmaras model was designed specifically for aerospace applications involving wall-bounded flows and has been shown to give good results for boundary layers subjected to adverse pressure gradients. It is also gaining popularity in turbo-machinery applications.

In its original form, the Spalart-Allmaras model is effectively a low-Reynolds number model, requiring the viscosity-affected region of the boundary layer to be properly resolved ($y^+ \approx 1$ meshes). In the CFD software, the Spalart-Allmaras model has been extended with a y^+ insensitive wall treatment (Enhanced Wall Treatment), which allows the application of the model independent of the near wall y^+ resolution.

The formulation blends automatically from a viscous sub-layer formulation to a logarithmic formulation based on y^+. On intermediate grids, ($1< y^+ <30$), the formulation maintains its integrity and provides consistent wall shear stress and heat transfer coefficients. While the y^+ sensitivity is removed, it still should be ensured that the boundary layer is resolved with a minimum resolution of 10-15 cells.

The Spalart-Allmaras model was developed for aerodynamic flows. It is not calibrated for general industrial flows, and does produce relatively larger errors for some free shear flows, especially plane and round jet flows. In addition, it cannot be relied on to predict the decay of homogeneous, isotropic turbulence.

3.3.2 Two equations $k−\varepsilon$ model

Standard $k−\varepsilon$ model

The Standard $k−\varepsilon$ mode is a well-established model capable of resolving through the boundary layer. It is required to solve turbulent kinetic energy equations and dissipation rate equations. Turbulent kinetic energy transport equations are derived by exact equations. However, dissipative equation is using physical inference and mathematical simulation original equations. This model assumes that the flow is

totally turbulent and the effect of molecular viscosity can be ignored. Therefore, standard k- ε model is only suitable for totally turbulent flow model.

Re-Normalisation Group (RNG) $k-\varepsilon$ model

Re-Normalisation Group (RNG) $k-\varepsilon$ model is an instant Navier-Stokes equation which is derived by RNG mathematical method. The turbulent kinetic energy and dissipation rate equation are similar to the standard $k-\varepsilon$ model.

Realizable $k-\varepsilon$ Model

The second model is Realizable $k-\varepsilon$, an improvement over the standard $k-\varepsilon$ model. It is a relatively recent development and differs from the standard $k-\varepsilon$ model in two ways. The realizable $k-\varepsilon$ model contains a new formulation for the turbulent viscosity and a new transport equation for the dissipation rate, ε, that is derived from an exact equation for the transport of the mean-square vorticity fluctuation. The term "realizable" means that the model satisfies certain mathematical constraints on the Reynolds stresses, consistent with the physics of turbulent flows. Neither the standard $k-\varepsilon$ model nor the RNG $k-\varepsilon$ model is realizable. It introduces a Variable C_{μ} instead of constant. An immediate benefit of the realizable $k-\varepsilon$ model is that it provides improved predictions for the spreading rate of both planar and round jets. It also exhibits superior performance for flows involving rotation, boundary layers under strong adverse pressure gradients, separation, and recirculation. In virtually every measure of comparison, Realizable k demonstrates a superior ability to capture the mean flow of the complex structures.

These three $k-\varepsilon$ models are similar. They all have the k and ε transport models. The difference are: 1. the method of turbulent viscosity calculation is different. 2. The turbulent Prandtl number which used to control turbulent diffusion is different. 3. The relationship of produce item is different.

3.3.3 Shear stress transport (SST) $k-\omega$ model

The SST $k-\omega$ turbulence model (Menter 1993) is a two-equation eddy-viscosity model which has become very popular. The shear stress transport (SST) formulation combines the best of two worlds. The use of a $k-\omega$ formulation in the

inner parts of the boundary layer makes the model directly usable all the way down to the wall through the viscous sublayer, hence the SST $k-\omega$ model can be used as a Low-Re turbulence model without any extra damping functions. The SST formulation also switches to a $-\varepsilon$ behaviour in the free-stream and thereby avoids the common $k-\omega$ problem that the model is too sensitive to the inlet free-stream turbulence properties. Authors who use the SST $k-\omega$ model often merit it for its good behaviour in adverse pressure gradients and separating flow. The SST $k-\omega$ model does produce a bit too large turbulence levels in regions with large normal strain, like stagnation regions and regions with strong acceleration. This tendency is much less pronounced than with a normal $k-\varepsilon$ model though.

3.4   Near-wall Function

The wall will have an obvious effect on turbulent flow. When it is very close to the wall, viscous damping will reduce the tangential velocity fluctuation and the wall will also prevent the normal velocity fluctuation. When the place is a little far away from the wall, due to the increase of the average velocity gradient, turbulence energy generated and increased immediately which made the turbulent flow strengthen. Therefore, the processing of the near wall will have an obvious effect on the simulation result because wall is the main resource of vortices and turbulence.

The use of a RANS turbulence model implies a constraint on the grid in the vicinity of a wall. Either the turbulent boundary layer is completely computed or the turbulent boundary layer is modelled. According to the results of experimental studies, the near wall zone can be divided into three layers as shown in figure 3.1. The innermost layer is called viscous sub-layer and the flow is almost laminar. Molecular viscosity plays a decisive role for momentum, heat and mass transport. The outer region is fully turbulent. Between these two is the blending region. Molecular viscosity and turbulence both make a considerable function in this region. Figure 3.2 shows the different layers in the near-wall region. Here y^+ and u^+ are given by $y\mu_\tau/v$ and u/μ_τ respectively, where $\mu_\tau = \sqrt{\tau_w/\rho}$
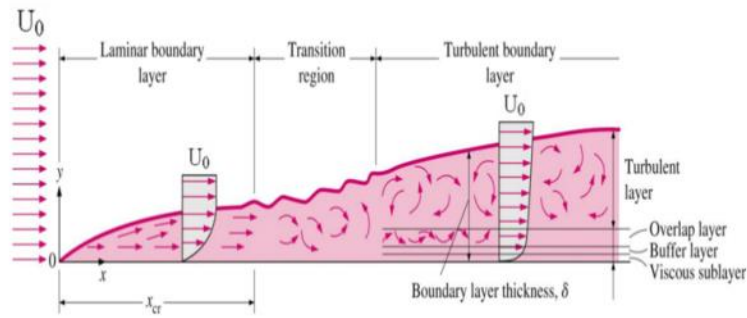
Figure 3.1 Boundary layer (Yunus, 2006)
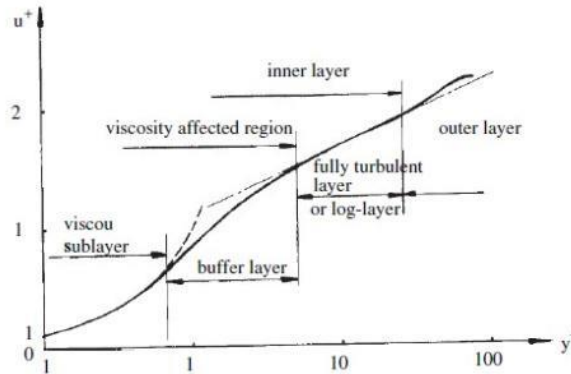
Figure 3.2 Different layers in the near-wall region (Fluent 14.0 user's guide)

3.4.1 Wall function and near wall model

There are two ways to process near wall conditions. One is applying semi-empirical formula called wall function to correlate the viscous stress at the wall with flow data in the fully turbulent region (log-layer). As laminar sub-layer and buffer layer are not resolved, this approach can avoid modifying the models and simulate the effect of wall on the turbulence directly. For most high Reynolds flow problems, wall function method can save calculation resource and have a certain accuracy. Therefore, it is commonly used in the industry and called 'high-Reynolds' turbulence modelling. In addition, when we study the low Reynolds problems, wall function method is not suitable as it cannot satisfy the assumption conditions. So it needs a suitable model which could have been solved to the wall. 'low-Reynolds' turbulence modelling is to modify the turbulent model through resolve the inner layer. The turbulence models have to be modified with near-wall models in order to account for the presence of the wall, since near the wall the flow is almost laminar. Damping functions have to be introduced in the turbulence equations to damp the turbulence adequately near the

wall. Figure 3.3 shows different grids to be used for both approaches. The first approach results in lower cost computations and is often used for industrial applications, but is only valid for flows where the assumptions for the use of wall functions are valid. If not, the second approach can be used if the near-wall models are appropriate for the type of flow being considered.
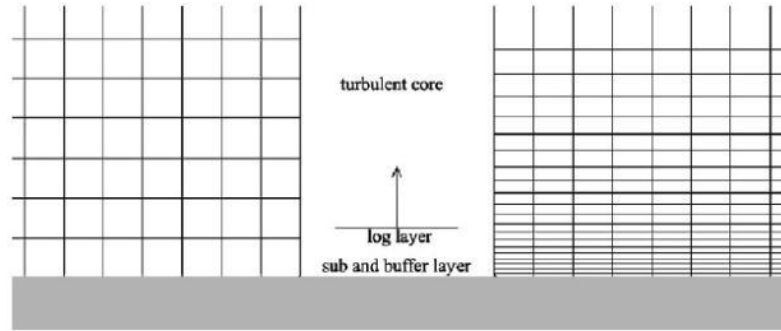
Figure 3.3 Left: grid for high-Reynolds turbulence modelling. Right: grid for low-Reynolds (Fluent 14.0 user's guide)

Standard wall function

According to the average velocity wall law, $U^* = \frac{1}{k}\ln(Ey^*)$, Where $U^* \equiv \frac{U_p C_\mu^{1/4} k_p^{1/2}}{\tau_w/\rho}$, $y^* \equiv \frac{\rho y_p C_\mu^{1/4} k_p^{1/2}}{\mu}$. What's more, k=0.42 which denotes Von Karman constant. E=9.81 which is an experimental constant. U_p, k_p and y_p denote the average velocity, turbulent energy and distance from the wall at point P, respectively. μ denotes the dynamic viscosity coefficient.

Normally, when $y^* > 30\sim60$, the average velocity meets the logarithmic distribution. When y^* is out of this region, $U^* = y^*$.

Non-equilibrium wall function

In the Non-equilibrium wall function method, the velocity distribution is more sensitive to the pressure gradient.

$$\frac{\tilde{U} C_\mu^{1/4} k^{1/2}}{\tau_w/\rho} = \frac{1}{k}\ln(E\frac{\rho C_\mu^{1/4} k^{1/2} y}{\mu}) \tag{3.31}$$

Where, $\tilde{U} = U - \frac{1}{2}\frac{dp}{dx}[\frac{y_v}{\rho k^* k^{\frac{1}{2}}}\ln\left(\frac{y}{y_v}\right) + \frac{y-y_v}{\rho k^* k^{\frac{1}{2}}} + \frac{y_v^2}{\mu}]$

y_v denotes the physical viscous sub-layer thickness which can be calculated as:

$$y_v \equiv \frac{\mu y_v^*}{C_\mu^{1/4} k_p^{1/2}} \tag{3.32}$$

Where, $y_v^* = 11.225$

Non-equilibrium wall function is applying a double layer concept when calculate the turbulence kinetic energy from the near-wall control body. In addition, it need solve turbulence kinetic energy k. Assume the control volume adjacent to the wall is constituted by a viscous sub-layer and fully turbulent. The following equations showed the turbulent amount as:

$$\tau_t = \begin{cases} 0 & y < y_v \\ \tau_w & y > y_v \end{cases} \qquad k = \begin{cases} (\frac{y}{y_v})^2 k_p & y < y_v \\ k_p & y > y_v \end{cases} \qquad \varepsilon = \begin{cases} \dfrac{2vk}{y^2} & y < y_v \\ \dfrac{k^{\frac{3}{2}}}{C_l y} & y > y_v \end{cases} \tag{3.33}$$

Where $C_l = kC_\mu^{-3/4}$, y_v is a dimensional thickness of the viscous sub-layer, $y_v \equiv \frac{\mu y_v^*}{\rho C_\mu^{1/4} k_p^{1/2}}$

Using the equations above, we can calculate the average turbulent kinetic energy and its dissipation rate of the control volume which close to the wall. Therefore, this method abandoned the partial equilibrium assumption in the standard wall function.

Comparison between these two functions

Standard wall function will have a good result for the high-Reynolds flow problems. Non-equilibrium wall function is extended the wall function to the pressure gradient and non-equilibrium flow process. However, if the flow deviated from the ideal conditions, the wall function is not suitable. Table 3.1 showed the detail positive and negative of these two wall functions.

Table 3.1 Comparison of different wall functions

	Positive	Negative
Standard wall function	More application, small calculation, more accuracy	Only suitable for the high-Reynolds flow
Non-equilibrium wall function	Considering the pressure gradient, can calculate the separation, reattachment and hitting problems	For the low-Reynolds flow problems. But, it is not suitable for the strong pressure gradient, strong volume force and strong 3-D problems

3.4.2   Near-wall treatment on the grid requirements in the turbulent calculation

Solving the turbulent problem is relied on the mesh as turbulence and average flow has a strong Interaction. For the near-wall grid, different near-wall treatments have different grid requirements. The distance from the first layer grid to the wall must be in the logarithmic zone. Usually, the calculation distance is *y+* or *y**.

$$y^+ \equiv \rho u_\tau y / \mu \qquad\qquad (3.34)$$

If the grid is in the logarithmic zone, y^+ is similar to the $y*$ which is >30~60. Different numbers of y^+ is corresponding to the different near-wall layers.

$$\begin{cases} y^+ < 5 & laminar\ sublayer \\ 5 < y^+ < 30 & buffer\ region \\ y^+ > 30 & turbulent\ region \end{cases} \qquad\qquad (3.35)$$

With the introduction of blending functions between the low-Reynolds approach and the high-Reynolds approach, the right choice for the distance from the wall for the first cell becomes more obsolete. We must refrain the first layer is in the buffer region. So the y^+ is better less than 5 or more than 30.

3.5   Discretization Methods

Discretization methods Analytical solutions of partial differential equations involve closed-form expressions which give the variation of the dependent variables continuously throughout the domain. In contrast, numerical solutions can give answers at only discrete points in the domain, called grid points. For example,

consider Figure 3.3, which shows a section of a discrete grid in the xy-plane. For convenience, let us assume that the spacing of the grid points in the x-direction is uniform, and given by Δx, and that the spacing of the points in the y-direction is also uniform, and given by Δy, as shown in Figure 3.3. In general, Δx and Δy are different. Indeed, it is not absolutely necessary that Δx or Δy be uniform; we could deal with totally unequal spacing in both directions, where Δx is a different value between each successive pairs of grid points, and similarly for Δy. However, the vast majority of CFD applications involve numerical solutions on a grid which involves uniform spacing in each direction, because this greatly simplifies the programming of the solution, saves storage space and usually results in greater accuracy. This uniform spacing does not have to occur in the physical xy space; as is frequently done in CFD, the numerical calculations are carried out in a transformed computational space which has uniform spacing in the transformed independent variables, but which corresponds to non-uniform spacing in the physical plane. In this chapter we will assume uniform spacing in each coordinate direction, but not necessarily equal spacing for both directions, i.e. we will assume Δx and Δy to be constants, but that Δx does not have to equal Δy.
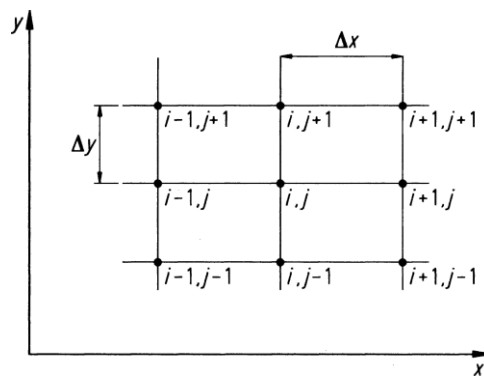
Figure 3.4 Discrete grid points (Anderson, 2009)

The method of finite-differences is widely used in CFD, and therefore most of this chapter will be devoted to matters concerning finite differences. The philosophy of finite difference methods is to replace the partial derivatives appearing in the governing equations of fluid dynamics with algebraic difference quotients, yielding a system of algebraic equations which can be solved for the flow-field variables at the specific, discrete grid points in the flow (as shown in Figure 3.4). Let us now proceed

to derive some of the more common algebraic difference quotients used to discretize the partial differential equations.

Finite difference representations of derivatives are based on Taylor's series expansions. For example, if $u_{i,j}$ denotes the x-component of velocity at point (i, j), then the velocity $u_{i+1,j}$ at point (i+1, j) can be expressed in terms of a Taylor's series expanded about point (i, j), as follows:

$$u_{i+1,j} = u_{i,j} + \left(\frac{\partial u}{\partial x}\right)_{i,j} \Delta x + \left(\frac{\partial^2 u}{\partial x^2}\right)_{i,j} \frac{(\Delta x)^2}{2} + \left(\frac{\partial^3 u}{\partial x^3}\right)_{i,j} \frac{(\Delta x)^3}{6} \dots \tag{3.36}$$

Equation (3.36) is mathematically an exact expression for $u_{i+1,j}$ if:

(a) The number of terms is infinite and the series converges,

(b) And/or $\Delta x \to 0$.

For numerical computations, it is impractical to carry an infinite number of terms in Eq. (3.36). Therefore, Eq. (3.36) is truncated. For example, if terms of magnitude $(\Delta x)^3$ and higher order are neglected, Eq. (3.36) reduces to

$$u_{i+1,j} \approx u_{i,j} + \left(\frac{\partial u}{\partial x}\right)_{i,j} \Delta x + \left(\frac{\partial^2 u}{\partial x^2}\right)_{i,j} \frac{(\Delta x)^2}{2} \tag{3.37}$$

We say that Eq. (3.37) is of second-order accuracy, because terms of order $(\Delta x)^3$ and higher have been neglected. If terms of order $(\Delta x)^2$ and higher are neglected, we obtain from Eq. (3.36),

$$u_{i+1,j} \approx u_{i,j} + \left(\frac{\partial u}{\partial x}\right)_{i,j} \Delta x \tag{3.38}$$

where Eq. (3.38) is of first-order accuracy. In Eqs. (3.37) and (3.38), the neglected higher-order terms represent the truncation error in the finite series representation. For example, the truncation error for Eq. (3.37) is

$$\sum_{n=3}^{\infty} \left(\frac{\partial^n u}{\partial x^n}\right)_{i,j} \frac{(\Delta x)^n}{n!} \tag{3.39}$$

and the truncation error for Eq. (3.38) is

$$\sum_{n=2}^{\infty} \left(\frac{\partial^n u}{\partial x^n}\right)_{i,j} \frac{(\Delta x)^n}{n!} \tag{3.40}$$

This paper used second-order upwind discretization scheme in the CFD calculation. When second-order accuracy is desired, quantities at cell faces are computed using a multidimensional linear reconstruction approach. In this approach, higher-order accuracy is achieved at cell faces through a Taylor series expansion of the cell-cantered solution about the cell centroid. Overall, second-order upwind discretization scheme is more accurate and stable.

3.6   Description of CFD Solver STAR CCM+

STAR-CCM+ provides the world's most comprehensive engineering physics simulation inside a single integrated package. Much more than just a CFD solver, STAR-CCM+ is an entire engineering process for solving problems involving flow (of fluids or solids), heat transfer, and stress. It provides a suite of integrated components that combine to produce a powerful package that can address a wide variety of modelling needs. (STAR CCM+ users' guide)

STAR-CCM+ is based on object-oriented programming technology. It is designed to handle large models quickly and efficiently using a unique client–server architecture that seamlessly meshes and simultaneously solves and post-processes over multiple computing resources without requiring additional effort from the user. STAR-CCM+ recently became the first commercial CFD package to mesh and solve a problem with over one billion cells. The object-oriented nature of the code can be seen in the user interface. An object tree is provided for each live simulation, containing object representations of all the data associated with the simulation. The objects presented on the simulation tree reside on the server, which can run as either a serial or a parallel process. A client interface connects to a server, and displays the simulation objects available on that server.

The most general view of the STAR-CCM+ workflow is depicted in the illustration below (Figure 3.5). Elements on the illustration can be clicked to jump to further documentation for that step.
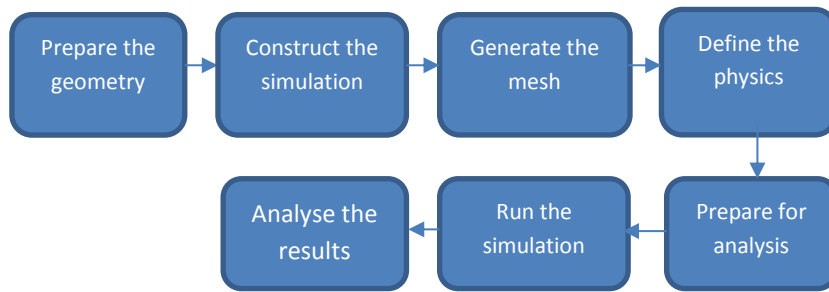
Figure 3.5 General sequence of operations in a Star CCM+ analysis

3.7 Uncertainty Analysis in CFD Verification and Validation (ITTC rules)

Discussion and methodology for estimating errors and uncertainties in computational fluid dynamics (CFD) simulations have reached a certain level of maturity with recognition of importance through editorial policies (Freitas, 12), increased attention and recent progress on common terminology (AIAA, 13), advocacy and detailed methodology (Roache, 14), and numerous case studies (Meta, 15). Progress has been accelerated in response to the urgent need for achieving consensus on concepts, definitions, and useful methodology and procedures, as CFD is applied to increasingly complex geometry and physics and integrated into the engineering design process. Such consensus is required to realize the goals of simulation-based design and other uses of CFD such as simulating flows for which experiments are difficult (e.g., full-scale Reynolds numbers, hypersonic flows, off-design conditions). In spite of the progress and urgency, the various viewpoints have not converged and current approaches fall short of providing practical methodology and procedures for estimating errors and uncertainties in CFD simulations.

The present work provides a pragmatic approach for estimating errors and uncertainties in CFD simulations. Previous work on verification (Stern et al., 16) is extended and put on a more rigorous foundation and combined with subsequent work on validation (Coleman and Stern, 17) thereby providing a comprehensive framework for overall procedures and methodology. The philosophy is strongly influenced by experimental fluid dynamics (EFD) uncertainty analysis (Coleman and Steele, 18), which has been standardized. Hopefully, CFD verification and validation procedures and methodology can reach a similar level of maturity and user variability can reach similar low levels, as for EFD. The work is part of a larger

program (Rood, 19) for developing and implementing a strategy for verification and validation of Reynolds averaged Navier-Stokes (RANS) ship hydrodynamics CFD codes. The program includes complementary CFD and EFD towing-tank investigations and considers errors and uncertainties in both the simulations and the data in assessing the success of the verification and validation efforts. The work also benefited from collaboration with the 21st and 22nd International Towing Tank Resistance Committees (ITTC 1996, 1999). The procedures proposed in this paper were adopted on an interim basis by the 22nd ITTC and also were recommended and used at the recent Gothenburg 2000 Workshop on CFD in Ship Hydrodynamics (Larsson et al., 2000).

The focus is on verification and validation methodology and procedures for CFD simulations with an already developed CFD code applied without requiring availability of the source code for specified objectives, geometry, conditions, and available benchmark information. The methodology and procedures were developed considering RANS CFD codes, but should be applicable to a fairly broad range of codes such as boundary-element methods and certain aspects of large-eddy and direct numerical simulations. The present work differs in many respects from recent literature. The presentation is relatively succinct with intention for use for practical applications (i.e., industrial CFD) for which numerical errors and uncertainties cannot be considered negligible or overlooked.

The definitions of errors and uncertainties and verification and validation that are used in any approach need to be clearly stated. The present and Roache (1998) definitions for errors and uncertainties are consistent with those used for EFD. The AIAA (1998) definitions are from an information theory perspective and differ from those used in EFD, but are not contradictory to the present definitions. The present concepts and definitions for verification and validation are closely tied to the present definitions of errors and uncertainties and equations derived for simulation errors and uncertainties thereby providing the overall mathematical framework. The Roache (1998) and AIAA (1998) definitions are broader, but not contradictory to the present definitions. The present approach includes both the situations (1) of estimating errors and the uncertainty of those estimates and (2) of estimating uncertainties only.

Richardson extrapolation (RE) is used for verification, which is not new; however, the present generalizations for J input parameters and concept of correction factors based on analytical benchmarks, which provides a quantitative metric to determine proximity of the solutions to the asymptotic range, accounts for the effects of higher-order terms, and are used for defining and estimating errors and uncertainties constitute a new approach. The use of quantitative estimates for errors and the use of uncertainties for those estimates also constitute a new approach in verification and validation.

The purpose of the uncertainty analysis is to provide methodology and procedures for estimating the uncertainty in a simulation result.

3.7.1   Verification and validation methodology

The definitions of errors and uncertainties directly follow those used in experimental uncertainty analysis. The simulation error δ_S is defined as the difference between a simulation result S and the truth T and is composed of additive modelling δ_{SM} and numerical δ_{SN} errors (i.e., $\delta_S = S\text{-}T = \delta_{SM} + \delta_{SN}$).For certain conditions, both the sign and magnitude of the numerical error can be estimated as where is an estimate of the sign and magnitude of δ_{SN} and ε_{SN} is the error in that estimate. The simulation value is corrected to provide a numerical benchmark S_C, which is defined

$$S_C = S - \delta_{SN}^*$$
(3.41)

Verification is defined as a process for assessing simulation numerical uncertainty U_{SN} and, when conditions permit, estimating the sign and magnitude δ_{SN}^* of the simulation numerical error itself and the uncertainty in that error estimate U_{ScN}. For the uncorrected simulation approach, numerical error is decomposed into contributions from iteration number δ_I, grid size δ_G, time step δ_T, and other parameters δ_P, which gives the following expression for simulation numerical uncertainty

$$U_{SN}^2 = U_I^2 + U_G^2 + U_T^2 + U_P^2$$
(3.42)

For the corrected simulation approach, the solution is corrected to produce a numerical benchmark S_C and the estimated simulation numerical error δ_{SN}^* and corrected uncertainty U_{S_CN} are given by

$$\delta_{SN}^* = \delta_I^* + \delta_G^* + \delta_T^* + \delta_P^* \tag{3.43}$$

$$U_{S_CN}^2 = U_{I_C}^2 + U_{G_C}^2 + U_{T_C}^2 + U_{P_C}^2 \tag{3.44}$$

Validation is defined as a process for assessing simulation modelling uncertainty U_{SM} by using benchmark experimental data and, when conditions permit, estimating the sign and magnitude of the modelling error δ_{SM} itself. The comparison error E is given by the difference in the data D and simulation S values

$$E = D - S = \delta_D - (\delta_{SM} + \delta_{SN}) \tag{3.45}$$

Modelling errors δ_{SM} can be decomposed into modelling assumptions and use of previous data. To determine if validation has been achieved, E is compared to the validation uncertainty U_V given by

$$U_V^2 = U_D^2 + U_{SN}^2 \tag{3.46}$$

If $|E| < U_V$, the combination of all the errors in D and S is smaller than U_V and validation is achieved at the U_V level. If $U_V \ll |E|$, the sign and magnitude of $E \approx \delta_{SM}$ can be used to make modelling improvements. For the corrected simulation, equations equivalent to Eqs. (3.45) and (3.46) are

$$E = D - S_C = \delta_D - (\delta_{SM} + \varepsilon_{SN}) \tag{3.47}$$

$$U_{V_C}^2 = U_{E_C}^2 - U_{SM}^2 = U_D^2 + U_{S_CN}^2 \tag{3.48}$$

3.7.2   Verification procedures

A verification study was undertaken to assess the simulation numerical uncertainty U_{SN} and numerical errors δ_{SN} which given as last section. U_I, U_G and U_T are the uncertainties arising from the iterative, grid-spacing convergence, and time-step convergence errors, respectively.

Convergence Studies

Iterative and parameter convergence studies are conducted using multiple solutions (at least 3) with systematic parameter refinement by varying the i_{th} input parameter Δx_i while holding all other parameters constant. The present work assumes input parameters can be expressed such that the finest resolution corresponds to the limit of infinitely small parameter values. Many common input parameters are of this form, e.g., grid spacing, time step, and artificial dissipation. Additionally, a uniform parameter refinement ratio

$$r_i = \frac{\Delta x_{i,2}}{\Delta x_{i,1}} = \frac{\Delta x_{i,3}}{\Delta x_{i,2}} = \frac{\Delta x_{i,m}}{\Delta x_{i,m-1}} \qquad (3.49)$$

between solutions is assumed for presentation purposes, but not required. Iterative errors must be accurately estimated or negligible in comparison to errors due to input parameters before accurate convergence studies can be conducted.

Careful consideration should be given to selection of uniform parameter refinement ratio. The most appropriate values for industrial CFD are not yet fully established. Small values (i.e., very close to one) are undesirable since solution changes will be small and sensitivity to input parameter may be difficult to identify compared to iterative errors. Large values alleviate this problem; however, they also may be undesirable since the finest step size may be prohibitively small (i.e., require many steps) if the coarsest step size is designed for sufficient resolution such that similar physics are re-solved for all m solutions. Also, similarly as for small values, solution changes for the finest step size may be difficult to identify compared to iterative errors since iterative convergence is more difficult for small step size. Another issue is that for parameter refinement ratio other than $r_i = 2$, interpolation to a common location is required to compute solution changes, which introduces interpolation errors. Roache (1998) discusses methods for evaluating interpolation errors. However, for industrial CFD, $r_i = 2$ may often be too large. A good alternative may be $r_i = \sqrt{2}$, as it provides fairly large parameter refinement ratio and at least enables prolongation of the coarse-parameter solution as an initial guess for the fine-parameter solution.

Convergence studies require a minimum of *m=3* solutions to evaluate convergence with respect to input parameter. Note that *m=2* is inadequate, as it only indicates

sensitivity and not convergence, and that *m>3* may be required. Changes between medium-fine $\varepsilon_{i,21} = \hat{S}_{i,2} - \hat{S}_{i,1}$ and coarse-medium $\varepsilon_{i,21} = \hat{S}_{i,3} - \hat{S}_{i,2}$ solutions are used to define the convergence ratio

$$R_i = \varepsilon_{i,21}/\varepsilon_{i,32} \tag{3.50}$$

and to determine convergence condition where $\hat{S}_{i,1}, \hat{S}_{i,2}, \hat{S}_{i,3}$ correspond to solutions with fine, medium, and coarse input parameter, respectively, corrected for iterative errors. Three convergence conditions are possible:

(*i*) Monotonic convergence: $0 < R_i < 1$

(*ii*) Oscillatory convergence: $R_i < 0$ $\hspace{3cm}$ (3.51)

(*iii*) Divergence: $R_i > 1$

For condition (*i*), generalized Richardson extrapolation (RE) is used to estimate U_i or δ_i^* and U_{i_c}. For condition (*ii*), uncertainties are estimated simply by attempting to bound the error based on oscillation maximums and minimums S_L, i.e., $U_i = \frac{1}{2}(S_U - S_L)$. For oscillatory convergence (*ii*), the solutions exhibit oscillations, which may be erroneously identified as condition (*i*) or (*iii*). This is apparent if one considers evaluating convergence condition from three points on a sinusoidal curve (Coleman et al., 2001). Depending on where the three points fall on the curve, the condition could be incorrectly diagnosed as either monotonic convergence or divergence. Bounding the error based on oscillation maximum and mini-mum for condition (*ii*) requires more than *m=3* solutions. For condition (*iii*), errors and uncertainties cannot be estimated.

Generalized Richardson Extrapolation

For convergence condition (*i*), generalized RE is used to estimate the error due to selection of the *i^{th}* input parameter and order-of-accuracy P_i. The error is expanded in a power series expansion with integer powers of Δx_i as a finite sum. The accuracy of the estimates depends on how many terms are retained in the expansion, the magnitude (importance) of the higher-order terms, and the validity of the assumptions made in RE theory.

With three solutions, only the leading term can be estimated, which provides one-term estimates for error and order of accuracy

$$\delta_{RE_{i,1}}^{*(1)} = \frac{\varepsilon_{i,21}}{r_i^{p_i}-1} \tag{3.52}$$

$$p_i = \frac{\ln(\frac{\varepsilon_{i,32}}{\varepsilon_{i,21}})}{\ln r_i} \tag{3.53}$$

With five solutions, two terms can be estimated, which provides two-term estimates for error and orders of accuracy

$$\delta_{RE_{i,1}}^{*(2)} = \frac{r_i^{q_i}\varepsilon_{i,21}-\varepsilon_{i,32}}{(r_i^{q_i}-r_i^{p_i})(r_i^{p_i}-1)} - \frac{r_i^{p_i}\varepsilon_{i,21}-\varepsilon_{i,32}}{(r_i^{q_i}-r_i^{p_i})(r_i^{q_i}-1)} \tag{3.54}$$

$$p_i = \frac{\ln[(a_i+\sqrt{b_i})/[2(\varepsilon_{i,21}\varepsilon_{i,43}-\varepsilon_{i,32}^2)]]}{\ln(r_i)}$$

$$q_i = \frac{\ln[(a_i-\sqrt{b_i})/[2(\varepsilon_{i,21}\varepsilon_{i,43}-\varepsilon_{i,32}^2)]]}{\ln(r_i)} \tag{3.55}$$

Solutions for analytical benchmarks show that the range of applicability for Eqs. (3.54) and (3.55) is more restrictive than that for Eqs. (3.52) and (3.53) since all five solutions must be both monotonically convergent and sufficiently close to the asymptotic range to evaluate p_i and q_i in Eq. (3.55). In general, *m=2n+1* solutions are required to estimate the first *n* terms of the error expansion.

Estimating Errors and Uncertainties with Correction Factor

The concept of correction factors is based on verification studies for 1D wave equation, 2D Laplace equation, and Blasius boundary layer analytical benchmarks for which it is shown that a multiplicative correction factor is useful as a quantitative metric to determine proximity of the solutions to the asymptotic range, to account for the effects of higher-order terms, and for estimating errors and uncertain-ties. The error is defined as

$$\delta_{i,1}^* = C_i \delta_{RE_{i,1}}^* = C_i \left(\frac{\varepsilon_{i,21}}{r_i^{p_i}-1} \right) \tag{3.56}$$

where two expressions for the correction factor C_i were developed. The first is based on solution of Eq. (3.56) for C_i with $\delta^*_{RE_{i,1}}$ based on Eq. (3.52) but p_i replacing with the improved estimate $p_{i_{est}}$

$$C_i = \frac{r_i^{p_i-1}}{r_i^{p_{iest}-1}} \tag{3.57}$$

$p_{i_{est}}$ is an estimate for the limiting order of accuracy of the first term as spacing size goes to zero and the asymptotic range is reached so that $C_i \rightarrow 1$. Similarly, the second is based on a two-term estimate of the power series which is used to estimate $\delta^*_{RE_{i,1}}$ where p_i and q_i are replaced with $p_{i_{est}}$ and $q_{i_{est}}$

$$C_i = \frac{(\frac{\varepsilon_{i,32}}{\varepsilon_{i,21}}-r_i^{q_{iest}})(r_i^{p_i}-1)}{(r_i^{p_{iest}}-r_i^{q_{iest}})(r_i^{p_{iest}}-1)} + \frac{(\frac{\varepsilon_{i,32}}{\varepsilon_{i,21}}-r_i^{p_{iest}})(r_i^{p_i}-1)}{(r_i^{p_{iest}}-r_i^{q_{iest}})(r_i^{q_{iest}}-1)} \tag{3.58}$$

Eq. (3.57) roughly accounts for the effects of higher-order terms by replacing p_i with $p_{i_{est}}$ thereby improving the single-term estimate, while Eq. (3.58) more rigorously accounts for higher-order terms since it is derived from a two-term estimate. Both expressions for C_i only require three solutions to estimate errors using Eq. (3.56). Solutions for analytical benchmarks show that correction of error estimates with both expressions for C_i yields improved error estimates.

Expressions for uncertainties are developed from error estimates in Eq. (3.56). When solutions are far from the asymptotic range, C_i is sufficiently less than or greater than 1 and only the magnitude of the error is estimated through the uncertainty U_i. Eq. (3.56) is used to estimate U_i by bounding the error $\delta^*_{i,1}$ by the sum of the absolute value of the corrected estimate from RE and the absolute value of the amount of the correction

$$U_i = (|C_i| + |1 - C_i|)|\delta^*_{RE_{i,1}}| \tag{3.59}$$

It is shown by Wilson and Stern (2002) that Eq. (3.59) is not conservative enough for C_i <1, which motivates development of an improved estimate

$$U_i = (2|1 - C_i| + 1)|\delta^*_{RE_{i,1}}| \tag{3.60}$$

When solutions are close to the asymptotic range, C_i is close to 1 so that is estimated using Eq. (3.56) and is estimated by

$$U_{i_c} = |1 - C_i| |\delta^*_{RE_{i,1}}| \tag{3.61}$$

Eq. (3.61) has the correct form for both $C_i < 1$ and $C_i > 1$. It should be recognized that using the corrected simulation approach requires in addition to C_i close to 1 that one have confidence in Eq. (3.56). There are many reasons for lack of confidence, especially for complex three-dimensional flows.

As pointed out by Roache (2003) Eqs. (3.60) and (3.61) have the short-coming that as $C_k \rightarrow 1$ the method reverts to Richardson Extrapolation, which produces only ~50% uncertainty estimate. Based on this criticism a further revision of the uncertainty estimates have been presented by Wilson et al. (2004). The final uncertainty estimates for the uncorrected and corrected approaches respectively are given as

$$U_i = \begin{cases} (9.6(1 - C_i)^2 + 1.1)|\delta^*_{RE_{i,1}}|, & |1 - C_i| < 0.125 \\ (2|1 - C_i| + 1)|\delta^*_{RE_{i,1}}|, & |1 - C_i| \geq 0.125 \end{cases} \tag{3.62}$$

$$U_{iC} = \begin{cases} (2.4(1 - C_i)^2 + 0.1)|\delta^*_{RE_{i,1}}|, & |1 - C_i| < 0.25 \\ (|1 - C_i|)|\delta^*_{RE_{i,1}}|, & |1 - C_i| \geq 0.25 \end{cases} \tag{3.63}$$

These uncertainty estimates merge smoothly with the previous uncertainty estimates and provide 10% factor of safety in the limit $C_i = 1$.

Estimating uncertainties with GCI

In the GCI approach (Roache, 1994) the uncertainty U_i (3.62) is defined using the error estimate from RE multiplied by a factor of safety F_S to band simulation error

$$U_i = F_S |\delta^*_{RE_{i1}}| \tag{3.64}$$

where $\delta^*_{RE_{i1}}$ is based on a single-term estimate as given by (3.52) with either assumed or estimated (observed) order of accuracy. If the order of accuracy is assumed (e.g. based on theoretical values), only two solutions are required for evaluation of (3.52).

In Reference (Ecaf, 2000), the GCI approach was extended for situations where the solution is corrected with an error estimate from RE as

$$U_i = (F_S - 1)\left|\delta^*_{RE_{i1}}\right| \tag{3.65}$$

An alternative expression for the uncertainty in the corrected solution has also been proposed in Reference (Roache, 1998), which is based on a standard three-grid error estimate, i.e. (3.52), but with the change between fine and medium solutions $\varepsilon_{i_{21}} = S_2 - S_1$ replaced by the change between the numerical benchmark and fine solution $\varepsilon_{i_{1C}} = S_1 - S_C$ which can be written in the following alternative form:

$$U_{i_C} = \left(\frac{1}{r_i^{p_i-1)}}\right)\left|\delta^*_{RE_{i1}}\right| \tag{3.66}$$

3.7.3   Validation procedures

First, consider the approach in which the simulation numerical error is taken to be stochastic and thus the uncertainty U_{SN} is estimated. From a general perspective, if we con-sider the three variables U_V, $|E|$, and U_{reqd} there are six combinations (assuming none of the three variables are equal):

1) $|E| < U_V < U_{reqd}$

2) $|E| < U_{reqd} < U_V$

3) $U_{reqd} < |E| < U_V$ 　　　　　　　　　　　　　　　　　　　　　(3.67)

4) $U_V < |E| < U_{reqd}$

5) $U_V < U_{reqd} < |E|$

6) $U_{reqd} < U_V < |E|$

In cases 1, 2 and 3, $|E| < U_V$; validation is achieved at the U_V level; and the comparison error is below the noise level, so attempting to estimate δ_{SMA} is not feasible from an uncertainty standpoint. In case 1, validation has been achieved at a level below U_{reqd}, so validation is successful from a programmatic standpoint.

In cases 4, 5 and 6, $U_V < |E|$, so the comparison error is above the noise level and using the sign and magnitude of E to estimate δ_{SMA} is feasible from an uncertainty standpoint. If $U_V \ll |E|$, then E corresponds to δ_{SMA} and the error from the modelling assumptions can be determined unambiguously. In case 4, validation is successful at the $|E|$ level from a programmatic standpoint.

Now consider the approach in which the simulation numerical error is taken to be deterministic and thus δ_{SN}^* and the uncertainty U_{V_C} are estimated. A similar set of comparisons can be constructed using $|E_C|$, U_{V_C}, and U_{reqd} . Since E_C can be larger or smaller than E, but U_{V_C} should always be less than U_V, the results for a given corrected case are not necessarily analogous to those for the corresponding uncorrected case. That is, a variable can be validated in the corrected but not in the uncorrected case, or vice versa. For cases 4, 5, and 6 in which $U_{V_C} < |E_C|$, one can argue that E_C is a better indicator of δ_{SMA} than is E , assuming that one's confidence in using the estimate δ_{SN}^* is not misplaced.

3.7.4   Conclusion of uncertainty analysis in CFD

Therefore, as described above, the overall CFD validation procedures can be conveniently divided into 3 steps and shown below.

Preparation, which involves selection of the CFD code and specification of objectives, geometry, conditions, and available benchmark information. The objectives might be prediction of certain variables at certain levels of validation.

Verification, which is defined as a process for assessing simulation numerical uncertainty U_{SN} and, when conditions permit, estimating the sign and magnitude of the simulation numerical error δ_{SN}^* itself and the uncertainty in its error referred to as the corrected simulation numerical uncertainty U_{SCN}. Iterative and input parameter convergence studies are conducted using multiple solutions with systematic parameter, as described in Section 3.7.2.

Validation, which is defined as a process for assessing simulation modelling uncertainty U_{SM} by using benchmark experimental data and, when conditions permit, estimating the sign and magnitude of the simulation modelling error δ_{SN} itself. The

comparison error E (difference between data D and simulation S values) and validation uncertainty U_V (combination of uncertainties in data and portion of simulation uncertainties that can be estimated) are used, as described in Section 3.7.3.

3.8   Conclusion

This chapter gives a short description of CFD theory, different turbulence models, wall functions, CFD commercial software STAR CCM+ and uncertainty analysis in CFD verification.

First, CFD is the fundamental governing equations of fluid dynamic. The governing equations must satisfy three physical principles: (1) mass is conserved; (2) F = ma (Newton's second law); (3) energy is conserved. It consists of continuity, momentum and energy equations.

Then, to solve the governing equations, Reynolds average is a common method. When substitute the average value and pulsation value into the instantaneous continuity equation and momentum equation, we can get thee average results which means Reynolds Average Navier-Stokes (RANS) equations. Turbulence models are required to modify the RANS equations to simulate the turbulent flow. Three turbulence models, namely, one equation Spalart-Allmaras model, two equations $k-\varepsilon$ model and Shear Stress Transport (SST) $k-\omega$ model, are described in this chapter.

When using the CFD solutions, the near-wall will have an obvious effect on the turbulent flow. The near wall zone can be divided into three layers. The innermost layer is called viscous sub-layer. The outer region is fully turbulent. Wall function can be used to calculate the near-wall layer in some conditions.

To make sure the accuracy of the CFD results, the uncertainty analysis for estimating errors and uncertainties is significant. ITTC made the methodologies of verifications and validation from 1999 and the newest one is in 2008. The overall procedures can be divided into 3 steps: preparation, verification and validation.

4. NUMERICAL ANALYSIS OF OSCILLATING AIRFOIL AERODYNAMICS

4.1 Overview

Wind turbines often run in the complex natural atmosphere. So, varying natural wind conditions will make directions change and velocities increase dramatically over the turbine blades. These inhomogeneous velocity profiles cause unsteady operating conditions for wind turbine rotors such as unsteady angle of attack changes. A combination of stall phenomena, inherently unsteady, and various types of unsteady angle of attack (α) motion create dynamic stall (DS) phenomena. DS will lead a dynamic stall vortex and delay of stall which will produce a higher DS angle compared to a static stall angle. Because of these two significant features of DS, the dynamic lift coefficient exceeds the static lift coefficient. DS influences the loads of turbine blades which use stall regulation to control maximum loads. Since DS phenomena cannot be prevented, studying the unsteady aerodynamics is crucial to understanding the effect and assists in modifying common wind turbine designs.

Experimental methods, semi-empirical strategies such as Beddoes–Leishman (BL) model, and numerical models have been applied to predict the aerodynamic loads and flow conditions of wind turbines during DS phenomena. Ramsay (1995) tested a two dimensional (2D) S809 airfoil under stationary and dynamic conditions. Somers (1997), at the Delft low speed and low-turbulence wind tunnel, measured aerodynamic coefficients for different Reynolds numbers. The Beddoes–Leishman (BL) model, a very popular semi-empirical DS model, has been used for modelling dynamic stall phenomena for HAWT although the BL model was originally developed for helicopters. So far, this model has been developed and used for predicting the unsteady aerodynamic characteristics of S809 airfoils by researchers such as Sheng et al. (2009), Gupta and Leishman (2006), Gonzalez and Munduate (2007). However, wind tunnel tests are time-consuming and expensive. So, with the development of computer technology and turbulence model, studying aerodynamic performance of wind airfoils with the method of computational fluid dynamics (CFD) has become an important way and trend. CFD numerical simulation is able to

describe complex geometric boundaries and flow structures. However, two problems need to be addressed when testing aerodynamic performance of wind turbine airfoil using the CFD numerical simulation are computing speed and accuracy. The rapid development of computer technology has weakened the simulation of two-dimensional airfoil problem, but the calculation accuracy has still been a very prominent problem. The accuracy of the CFD simulation is not only related to the software itself, but also to the turbulence model factors associated with the users. It requires users to build the experience about how to use the software in order to play a better role of CFD numerical simulation.

In recent years, with the deepening study of airfoil dynamic stall, some flow details are concerned. Literature (Qian, 2008) confirmed that the CFD method can simulate trailing edge vortex shedding caused by high-frequency oscillation and influent factors of oscillation. Literature (Spezial, 1992) studied the transition, flow separation and vortex shedding flow details of airfoil dynamic stall using Large Eddy Simulation (LES) and LES- RANS coupling method. The dynamic stall research under the plunging oscillation caused by the blades brandished is earlier seen in the direction of the flapping wing.

This article presents aerodynamic performance of S809 and S814 airfoil using a commercial CFD commercial package, ANSYS FLUENT 14. As STAR CCM+ software is not suitable for calculating 2D models, FLUENT 14 was chosen. Static Results are compared with the experimental data. S-A turbulence model and k-ε RNG turbulence model are compared to choose. A time step refinement study is also performed at dt =0.01, 0.005, 0.0025. Moreover, to present the aerodynamic analysis of S809 airfoil during pitch, plunge and pitch-plunge combined motion, this study analyses the effects of various reduced frequencies (k), mean angles of attack (α) and angle of attack amplitudes (h) on the lift and drag coefficient for an oscillating airfoil at a Reynolds number (Re) of 1×10^6. The calculating results have a better agreement with the experimental data. From the results, the unsteady state has an obvious hysteresis phenomenon. The whole learning process will be divided into two steps.

The first step is detecting the aerodynamic characteristic of 2D wind turbine airfoil on steady condition using the CFD method.

Second, the 2D wind turbine airfoil will be calculated and analysed on the unsteady condition using the CFD method and theoretical method. Calculating the pitching oscillation may be the first step and then calculating other oscillating motions such as plunge or combined motion. The theoretical method mainly uses the Leshiman-Beddoes semi-empirical model.

The aim of this research is to assess the prediction capabilities of airfoil aerodynamic performance and set up the experience of airfoil aerodynamic design in order to provide fast and effective detection means of numerical simulation performance.

4.2   Aerodynamic Characteristics of Steady Airfoil

The Reynolds Numbers of the large-scale wind turbine blade is always small, especially in the connecting zone of blade and hub. Therefore in order to meet the requirements of structure and strength, the thickness should increase uniformly along the length of the blade which means the tip should use the thin airfoil while the root should use the thick airfoil.

Generally, the profile in the 75% span (r/R=0.75) is the centre area to generate power. So, it should have the higher lift-to- drag ratio to get the biggest power coefficient. In addition, the relative thickness should be sufficient to keep the stiffness and weight of the structure. When near the root (r/R=0.3) and the tip (r/R=0.95) of the blade, the aerodynamic performance of the airfoil is not only good, but also changing constantly. Considering from the structure and stiffness, the thickness of the airfoil in the root of the blade should be big which guarantees higher maximum lift coefficient (Cl_{max}), while the airfoil in the tip is opposite which needs small thickness.

Over the past decade, commonly used airfoil families for horizontal axis wind turbines (HAWTs) have included the NACA 44XX, NACA 23XXX, NACA 63XXX, and NASA LS (Ramsay, 1995) series airfoils. All these airfoils suffer noticeable performance degradation from roughness effects resulting from leading-edge contamination. By using the NREL airfoils, which are specifically designed for HAWTs, the annual energy production loss due to airfoil roughness effects can be cut in half relative to previously used aircraft airfoils.

The NREL airfoil families have been designed using the Eppler code to accommodate the unique operating requirements of stall-regulated, variable-pitch, and variable-rpm wind turbines. Many of the existing NREL airfoil families address the needs of stall-regulated wind turbines. Nine airfoil families consisting of 25 airfoils have been designed for various size rotors since 1984. The appropriate blade length and generator size for each airfoil family along with the corresponding airfoils comprising each family from blade root to tip are shown in Table 4.1. The airfoil designations starting with the S801 and ending with the S828 represent the numerical order in which the airfoils were designed between 1984 and 1995. Seven of the airfoil families are designated "thick" which indicates that the outer-blade airfoils are 16% to 21% thick. Greater thickness helps provide greater blade flap stiffness for tower clearance, lower blade weight important for large machines, and helps accommodate aerodynamic over-speed control devices for stall-regulated machines. The two airfoil families labelled "thin" (11% to 15%) are more suited to downwind rotors of small to medium blade length. For most all blades, very thick airfoils are desired for the blade-root to accommodate structural and dynamic considerations. The blade-root airfoil thickness falls in the range of 18% to 24%. Thicknesses greater than 26% were found to result in undesirable performance characteristics. (Tangler, 1995).

Table 4.1 NREL Airfoil Family

Blade Length (meters)	Generator (kW)	Thickness Category	Airfoil Family (root--------------------------------tip)			
1-5	2-20	Thick		S823		S822
5-10	20-150	Thin		S804	S801	S803
5-10	20-150	Thin	S808	S807	S805	S806
5-10	20-150	Thick		S821	S819	S820
10-15	150-400	Thick	S815	S814	S809	S810
10-15	150-400	Thick	S815	S814	S812	S813
10-15	150-400	Thick	S815	S814	S825	S826
15-25	400-1000	Thick		S818	S816	S817
15-25	400-1000	Thick		S818	S827	S828

The ordinary wind turbine is always about 150-400kw. So according to the reference from the National Renewable Energy Laboratory, S809 are chosen to analyse the aerodynamic performance. The main object of this chapter is to clarify the influence from different grid density and turbulence models to the airfoil aerodynamic performance due to computing three kinds of grid (12150, 16470 and 48100 grid nodes) and two kinds of turbulence models (S-A and Standard K-e with standard wall function). And the computational data obtained with FLUENT using the 2D incompressible Reynolds Averaged Navier-Stokes (RANS) equations will be compared to the measurements performed at the low-turbulence wind tunnel at Delft University of Technology, The Netherland.

4.2.1   Model

The S809 airfoil is a 21% thick wind turbine airfoil that has been designed at National Renewable Energy Laboratory (NREL), Colorado, USA, by Somers. See Figure 4.1 (Franck, 2001). The three primary design criteria were restrained maximum lift, insensitive to surface roughness, and low profile drag. When start computing, the changing of the angle of attack (from 0° to 20°) can be through the method, changing the flow direction.

Based on the performance tests of this airfoil in the low-turbulence wind tunnel at Delft University of Technology, The Netherland, the results have been published in the literature (Somers, 1997). Compared to the results with the CFD numerical simulation of this airfoil, we can analyse the differences in calibration of the numerical simulation accuracy.
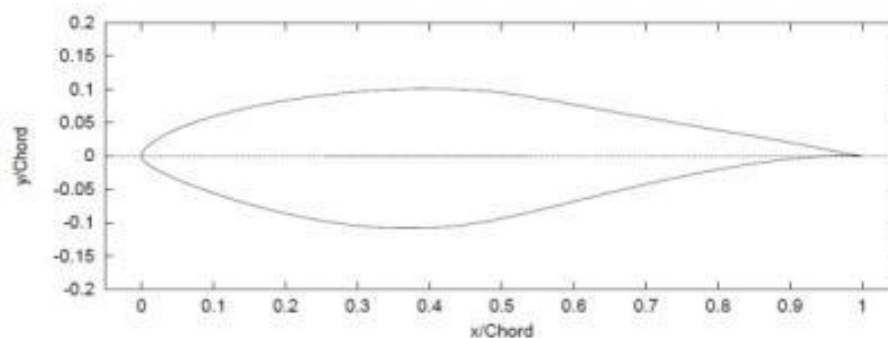
Figure 4.1 S809 Airfoil (Franck, 2001)

4.2.2 Method

Interactive viscous-flow method

For two-dimensional external steady incompressible flows, the boundary-layer equations can be written with eddy viscosity v_t and with b denoting $1+v_t/v$:

$$\frac{\partial u}{\partial x} + \frac{\partial v}{\partial y} = 0 \tag{4.1}$$

$$u\frac{\partial u}{\partial x} + v\frac{\partial v}{\partial y} = u_e\frac{du_e}{dx} + v\frac{\partial}{\partial y}\left(b + \frac{\partial u}{\partial y}\right) \tag{4.2}$$

Where u_e is the external velocity. The boundary conditions for flow over an airfoil in the absence of mass transfer are:

$$u = v = 0, \text{ at } y = 0 \tag{4.3}$$

$$u \to u_e(x), \text{ as } y \to \infty \tag{4.4}$$

The boundary conditions for the wake require the specification of a dividing line, $y = 0$, to separate the upper and lower parts of the inviscid flow. The normal pressure gradient across the shear layer is neglected and the boundary conditions become

$$u \to u_e(x), \text{ as } y \to \infty \tag{4.5}$$

$$v = 0, \text{ at } y = 0 \tag{4.6}$$

$$u \to u_e(x), \text{ as } y \to -\infty \tag{4.7}$$

See the method description in detail in Reference (Clarck, et al., 1986).

Numerical simulation

The numerical simulation of 2D airfoil was using the commercial CFD software, FLUENT. The governing equations for the turbulent incompressible flow encountered in this research are the steady-state Reynolds Averaged Navier-Stokes (RANS) equations. The turbulent viscosity is computed through two different turbulence models: one equation Spalart-Allamams turbulence model and two equations Standard k-e turbulence model. The second order upwind method is used for the convection term.

The airfoil numerical simulation parameters were determined by the Reynolds number (1.0×10^6).

$$Re = \frac{\rho u C}{\mu} \qquad\qquad\qquad (4.8)$$

In "Eq. (4.1)", ρ is the air density which equal to 1.225kg/m^3 and μ means the dynamic viscosity coefficient equal to 1.7894×10^{-5} (define the temperature is 15 ^{o}C) What's more, C is the airfoil chord and u is the airflow relative velocity.

And the far field boundaries were considered as the pressure-out and the surface of the airfoil was the no slip wall.

Wall treatment

The grid quality will affect the calculation results. The application of wall functions to modelling the near-wall region may significantly reduce both the processing and storage requirements of a numerical mode, while producing an acceptable degree of accuracy. The suitable meshes with adequate position for the first near-wall node are needed. So we need check the non-dimensional wall parameter y$^+$ which means the distance from the first layer of viscous wall to the airfoil surface in order to confirm the grid is suitable. According to Eq. 3.34, y^+ is defined as $y^+ \equiv \rho u_\tau y / \mu$.

Computational domain and mesh generation

C-meshes were used for the computation with the Gambit software. The computational domain extended 16C (16 times of the chord length) upstream of the leading edge of the airfoil and 20C downstream of the trailing edge where C is the length of the chord (see Figure 4.2 and Figure 4.3).

Velocity inlet boundary condition was applied upstream with speed of 14.6m/s and outflow boundary condition was applied downstream.

As it can be seen, the mesh lines were extended in the distance of 20 times of the chord length in the wake of the trailing edge in order to stabilize the computations. The points near the airfoil were clustered since this is where the flow is modified the most, while the mesh resolution which is approach the far field boundaries can become progressively coarser since the flow gradients approach zero, see Figure 4.4.

Close to the surface, the mesh resolution near the leading and trailing edges must be the highest since these are critical areas with the steepest gradients. Here, I set the boundary AF-FE-ED as velocity inlet and AB-BC-CD as outflow. Wall condition is applied in the airfoil.
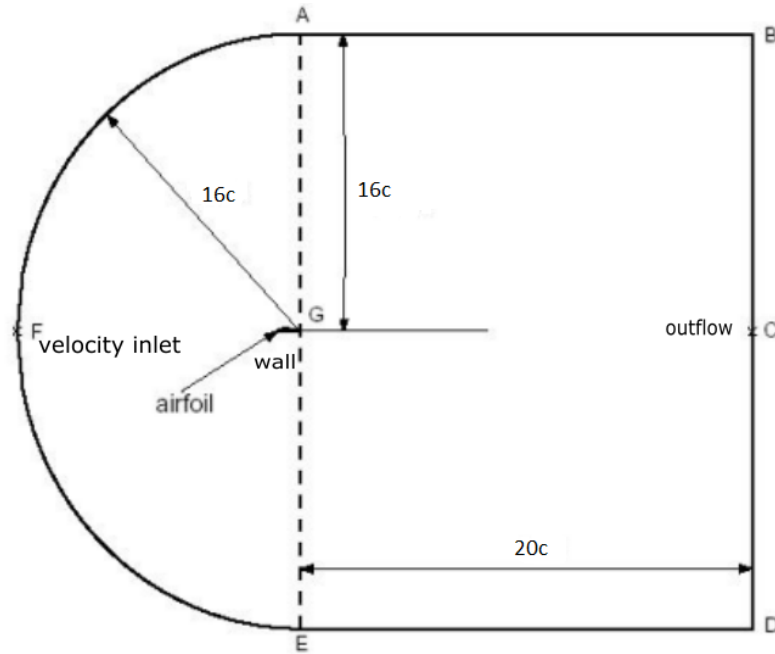
Figure 4.2 Computational domain
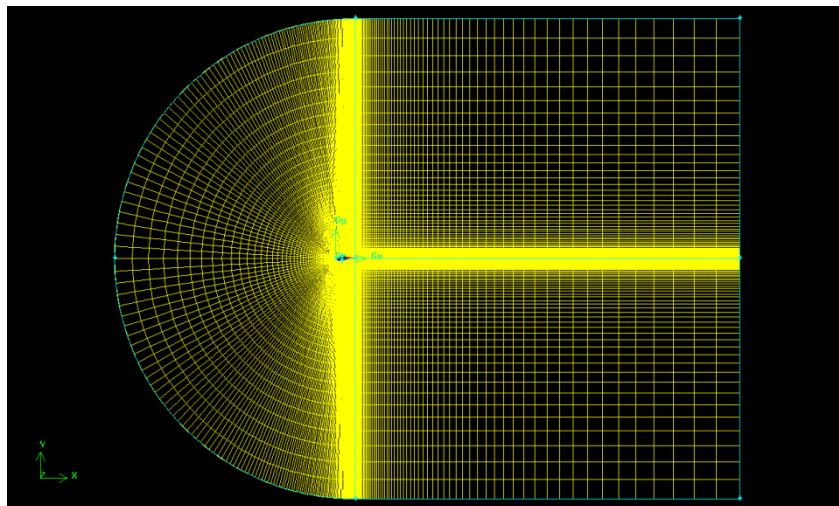
Figure 4.3 C-mesh for S809
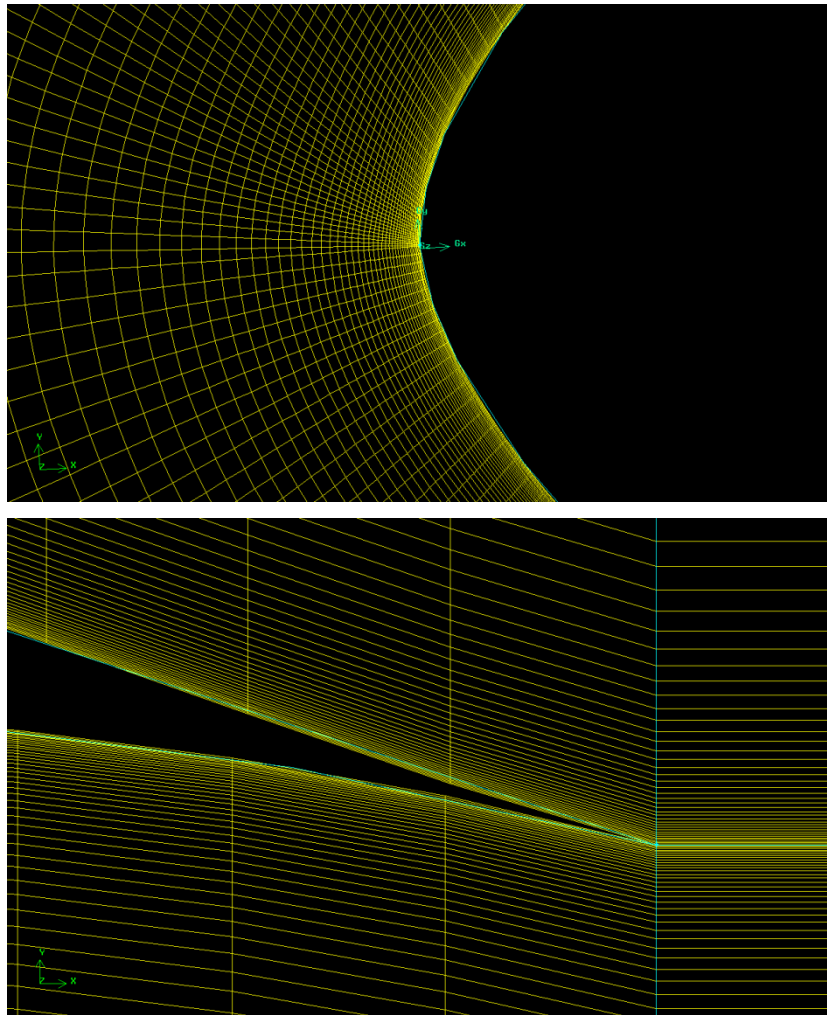
Figure 4.4 Mesh around S809 at leading and edging

4.2.3   Uncertainty analysis

A grid independence analysis was conducted using two meshes of varying cell number. The extent domain of upwind may result in difference of the results. Therefore, I detected two different distances from the inlet to the airfoil, 16c and 20c, respectively. Each mesh was processed using the same turbulence model(S-A turbulence model), at a free-stream velocity of 14.6m/s (Re=1×10^6). Table 4.2 shows the node and y$^+$ characteristics of each mesh.

Figure 4.5 shows drag and lift coefficient with S-A model at different angle of attack. And it should be noted that the lift coefficient is defined as $C_l = \frac{F_L}{\frac{1}{2}\rho U_\infty^2 C}$ where F_L is

the lift force. The drag coefficient is similarly defined as $C_d = \frac{F_D}{\frac{1}{2}\rho U_\infty^2 C}$ where F_D is the drag force.

Table 4.2 Three different grids

Grid	Nodes	y^+
Mesh 1	16c 52000	0.8-2
Mesh 2	16c 60000	0.8-2
Mesh 3	Upwind 20c	0.8-2
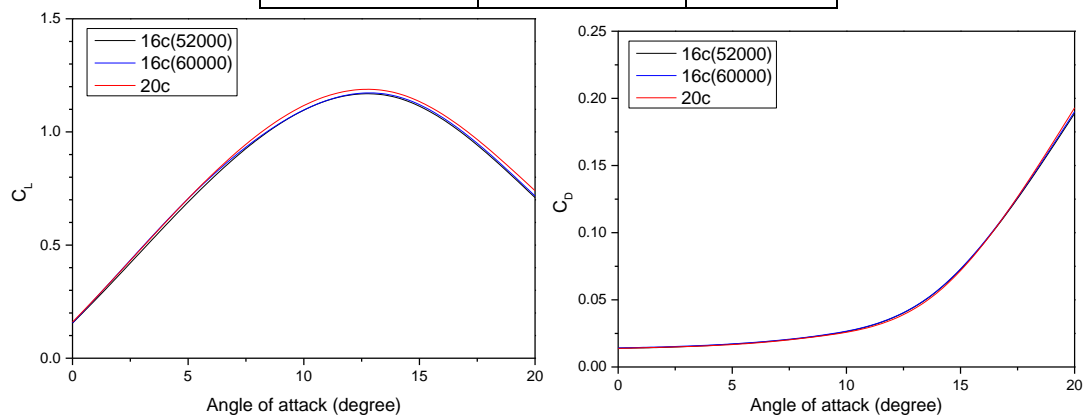
Figure 4.5 Comparison of Cl and Cd at different mesh grid

It can be seen from the figures that there is no difference with three results. Therefore, the grid is dependent. Mesh 1 was chosen for the following calculation.

4.2.4 Computational results and discussion of S809

Different turbulence models will get different results of airfoil performance. This report chose several turbulence models: Spalart-Allmaras turbulence model, Standard, RNG and Reliable k-e turbulence model with standard wall function, Standard and SST k-w turbulence model with low-Reynolds correction. The models were both solving Reynolds Average Navier-Stokes equations. The Spalart-Allmaras model was a one-equation model, while the k-e and k-w turbulence models were two-equation models.

Results were presented as lift and drag coefficient as function of angle of attack (see Figure 4.6-4.9). Pressure coefficient curves at 0, 5, 9, 14 degree respectively were shown from Figure 4.11 to 4.12. The experimental results and verification results were chosen from reference (Wolfe, 1989).
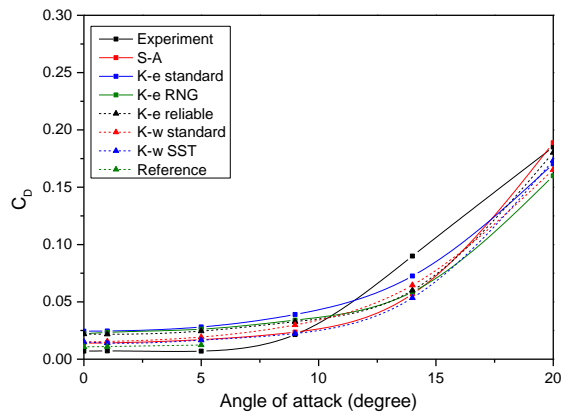
Figure 4.6 Drag Coefficient Curve (Fully turbulent model)
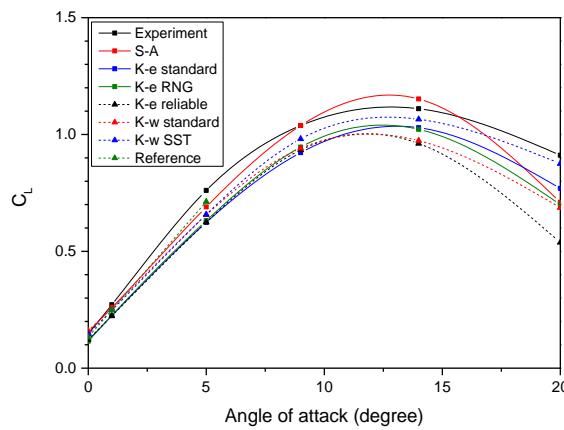
Figure 4.7 Lift Coefficient Curve (Fully turbulent model)
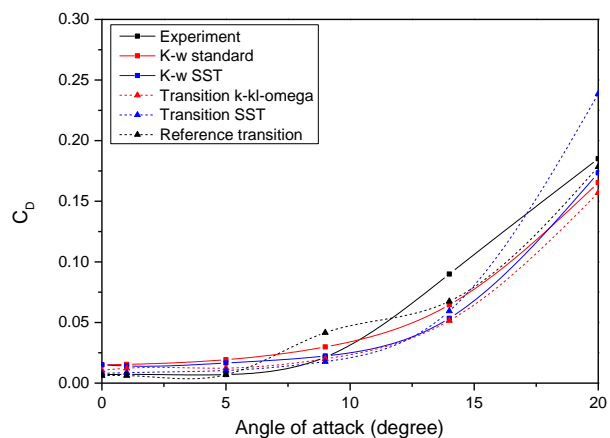
Figure 4.8 Drag Coefficient Curve (Transition model)
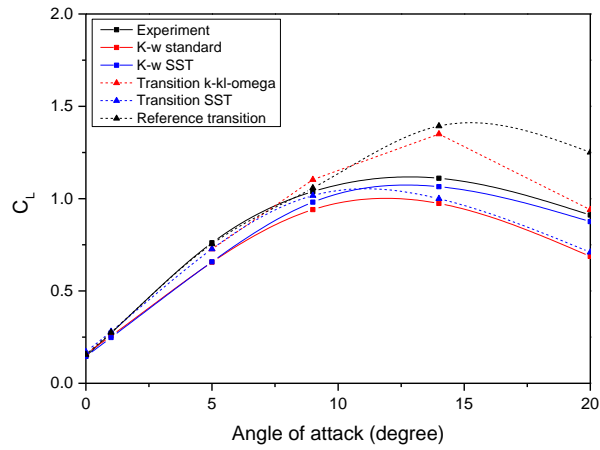
Figure 4.9 Drag Coefficient Curve (Transition model)
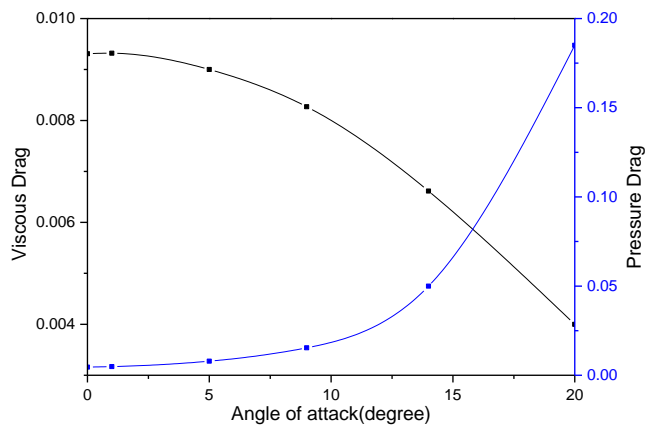
Figure 4.10 Drag Distribution (Spalart-Allmaras turbulence model)
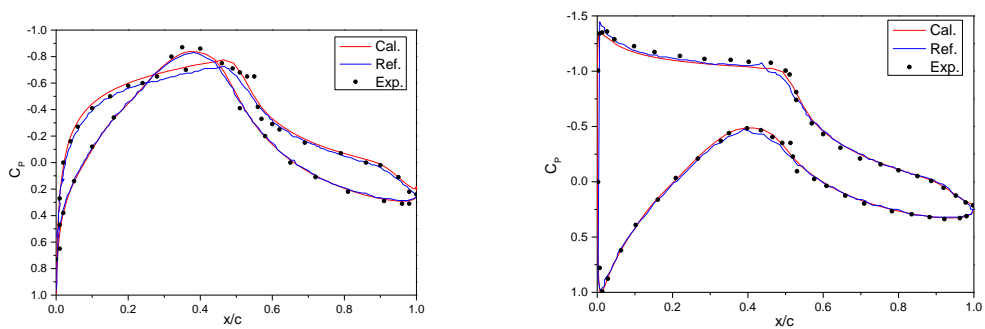
Figure 4.11 Pressure Distribution for $\alpha=0^{o}$ (left) and 5° (right) (Transition model)
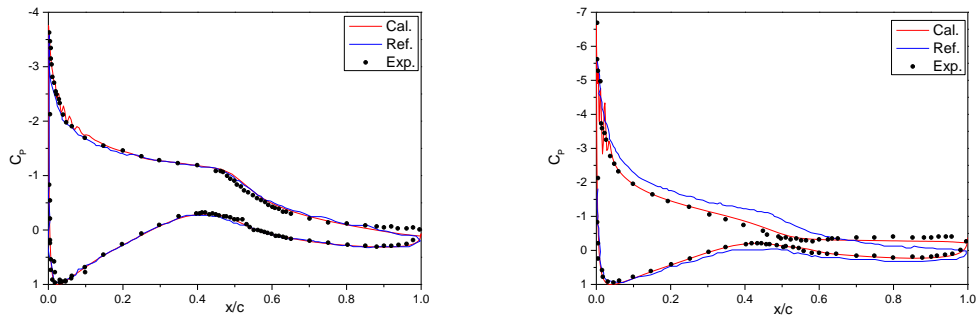
Figure 4.12 Pressure Distribution for $\alpha=9^{o}$ (left) and 14° (right) (Transition model)

Table 4.3 Comparisons between calculated and experimental aerodynamic coefficients, Fully turbulent calculations

α	C_L					C_D				
	REF.	CAL.	EXP.	ERRO1 (Ref. Vs Exp.)	ERRO2 (Cal. Vs Exp.)	REF.	CAL.	EXP.	ERRO1 (Ref. Vs Exp.)	ERRO2 (Cal. Vs Exp.)
0	0.132	0.155	0.147	-10	5	0.011	0.011	0.007	54	60
1	0.249	0.259	0.272	-8	-5	0.011	0.012	0.007	53	68
5	0.712	0.690	0.761	-6	-9	0.012	0.013	0.007	77	84

Table 4.4 Comparisons between calculated and experimental aerodynamic coefficients, Transition turbulent calculations

α	C_L					C_D				
	REF.	CAL.	EXP.	ERRO1 (Ref. Vs Exp.)	ERRO2 (Cal. Vs Exp.)	REF.	CAL.	EXP.	ERRO1 (Ref. Vs Exp.)	ERRO2 (Cal. Vs Exp.)
0	0.159	0.171	0.147	6	16	0.0062	0.0080	0.0070	-11	14
1	0.276	0.280	0.272	1	3	0.0062	0.0086	0.0072	-14	19
5	0.754	0.727	0.761	-1	-4	0.0069	0.0088	0.0070	1	25
9	1.058	1.017	1.039	2	-2	0.0416	0.0178	0.0214	95	-17
14	1.393	1.000	1.110	25	-10	0.0675	0.0600	0.0900	-25	-33
20	1.251	0.710	0.911	37	-22	0.1784	0.1734	0.1851	-4	-6

It can be shown from the Figures 4.6 and 4.7 that the trend of the lift and drag coefficient curves is similar compared calculation results with experimental results. Spalart-Allmaras and k-w turbulence models have better results, because Spalart-Allmaras turbulence model is designed for calculating aerodynamic performance of wind turbine blade. Moreover, the simulation drag coefficient shows a larger difference with experimental data, especially when the angle of attack is smaller than 9°. Therefore, other CFD results (Wolfe, 1989) are chosen to make a validation. Seen from the Table 4.3, the two CFD results are similar, while have a large difference with experimental results. The predicted drag coefficients are between 50% and 80% higher than the experiment results. This overprediction of drag was expected since

the actual airfoil has laminar flow over the forward half, not fully turbulent. Therefore, transition model mixed laminar and turbulent is applied to get a better result. Software Fluent has two transition models: Transition k-kl-omega model and Transition SST model. The results compared with fully turbulent calculation is shown as Figure 4.8 and 4.9. There is a better agreement with the experimental results at the small angle of attack seen Table 4.4.

The Figure 4.6 shows the change of lift coefficient with angel of attack. The stall angle of attack, which means the airfoil reached the maximum lift coefficient, was around 12 degree. When the angle of attack was smaller than the stall angle, the lift coefficient increased with the angle ascending. And after the maximum value, the lift decreased dramatically.

According to the knowledge of aerodynamic, the main reason of forming the lift was the pressure difference from the suction surface to the pressure surface. The larger the area contained within the upper and lower surfaces, the greater the lift was. Therefore, we can analyse the lift coefficient curve associated with the pressure coefficient curve shown from the Figure 4.11 to Figure 4.12.

When the angle was between 0 and 4 degree, flow attached to the surface of the airfoil. So, at this time, the pressure was almost the same at the both upper and down sides of the airfoil which made the lift small.

When the angle reached 5 degree, the pressure difference of the airfoil surface began to rise. Therefore, the separation phenomenon appeared near the trailing edge of the airfoil. So, the lift increased gradually.

When the angle was 9 degree, the separation of the leading edge was very obvious and the trailing vortex was appeared. The lift coefficient closed to the maximum because of the big pressure difference of the airfoil. Also, due to the trailing vortex beginning to move towards the leading edge, the flow separated from the surface of the airfoil which leads the pressure remained level on the trailing edge.

When the angle got to 14 degree, the boundary layer of the whole suction surface of the airfoil was separated. Besides, the separated trailing vortex attached to the

boundary again at the trailing edge of the airfoil which was called the second vortex. Therefore, the lift coefficient declined.

The drag coefficient almost stayed stable when the angle of attack smaller than 10 degree while after 10 degree, the drag coefficient curve mounted sharply. The reason to explain the phenomenon more specifically should be linked to the Figure 4.10. It can be seen from the Figure 4.10 that resistance was consisted of pressure drag and viscous drag. When the angle was smaller than 10 degree, the pressure drag coefficient and viscous drag coefficient curves stayed stable both. Due to the small pressure difference, the viscous drag was the major component of the total resistance. So, the drag did not show a large change. However, after 10 degree, the pressure drag coefficient curve climbed considerably while the viscous drag coefficient curve descended because the pressure difference began to decline. Therefore, due to the pressure drag playing the main role, the drag coefficient curve showed an increasing.

All over, transition model calculation gets a better result which is more close to the real condition. Moreover, Spalart-Allmaras and k-w turbulence model are better than k-e model due to the more accurate values. When the angle was larger than 10 degree, the separation phenomenon appeared near the trailing edge of the airfoil which made the computational results had a deviation.

4.3   Aerodynamic Characteristics of Oscillating Airfoil

Due to the complex unsteady condition, the fluctuations on the angle of attack (AOA) and wind velocity over the blades promote changes on forces and moments with respect to the steady state. Sometimes, natural wind has a strong wind shear with altered direction and velocity magnitude that causes dynamic stall (DS) phenomena in horizontal axis wind turbines (HAWT) which may result in dynamic blade loading, variable performance and failing stall regulation parameters. Since DS phenomena cannot be prevented, studying the unsteady aerodynamics is crucial to understanding the effect and assists in modifying common wind turbine designs. Experimental methods, semi-empirical strategies such as Beddoes–Leishman (BL) models, and numerical models have been applied to predict the aerodynamic loads and flow conditions of wind turbines during DS phenomena. Ramsay et al. (1995) tested a two

dimensional (2D) S809 airfoil under stationary and dynamic conditions. Somers, at the Delft low speed, low-turbulence wind tunnel, measured aerodynamic coefficients for different Reynolds numbers. The Leishman-Beddoes (LB) model, a very popular semi-empirical DS model, has been used for modelling dynamic stall phenomena for HAWT although the BL model was originally developed for helicopters.

Compared to restricted experimental methods based on test speed ranges, measuring equipment, and accuracy and size of the model, well-established CFD methods are progressing to investigate complex aerodynamic problems attributed to unsteady, transient and dynamic flow. Due to developments in commercial computational software it is feasible to compute unsteady airfoil flows.

4.3.1 Computational method

This study is organized to give an overview of the numerical simulation using a commercial CFD package, ANSYS Fluent 12.1, as an accurate, time efficient and economic way of simulating an oscillating freestream over a stationary S809 airfoil. Results for dynamic stall are compared with prior experimental pitch oscillating S809 airfoil studies.

The oscillation system is $\alpha = \alpha_{mean} + \alpha_{amp} \sin(2\pi f t)$ where α_{mean} is the mean angle of the wind with relative velocity and α_{amp} is the pitch oscillation amplitude. For this simulation, the airfoil is aligned with the horizontal axis. The sinusoidal oscillating of an airfoil has a reduced frequency k, $k = \frac{2\pi f C}{2 U_\infty}$ where f is the oscillation frequency. (Kobra, 2012)

According to these equations above, different α_{mean}, α_{amp} and k will affect the results. Therefore, these three factors will be analysed and compared respectively.

Dynamic mesh method

Here, in order to simulate the sinusoidal oscillation, the calculation applied dynamic mesh technology. In the calculation model, the pitching motion was realised by controlling the angle velocity w, $w = \frac{d\alpha}{dt} = 2\pi f \alpha_{amp} \cos(2\pi f t)$.

In the Fluent, there are three functions to realise the update of the mesh. The first method is regarding the grid as spring and the deformation is controlled by the elongation and shortening. The second one is applying the additional layer technology which is suitable for the structure mesh. The third method is remeshing the grid when the deformation of the grid is over the given data of skew factor and maximum and minimum scale of mesh. A code was added as a user-defined function to the commercial CFD code, Fluent. The code alters the direction of the airfoil at each time step based on the sinusoidal equation to simulate a proper α for the boundary conditions.

Grid generation

Using a C grid layout, both structure mesh and triangle mesh have been used to not only make the calculation accuracy but also efficient. The mesh contained 35564 as shown in Figures 4.13-4.15. Around the airfoil 80 nodes were distributed with high resolution on the leading and trailing edge. In the wake of the airfoil 70 nodes and 110 nodes are placed in a horizontal and in vertical lines, respectively. The boundary of the computational domain was located approximately 20C form the airfoil. Velocity inlet boundary condition was applied upstream with speed of 14.6m/s ($Re=10^6$) and outflow boundary condition was applied downstream.
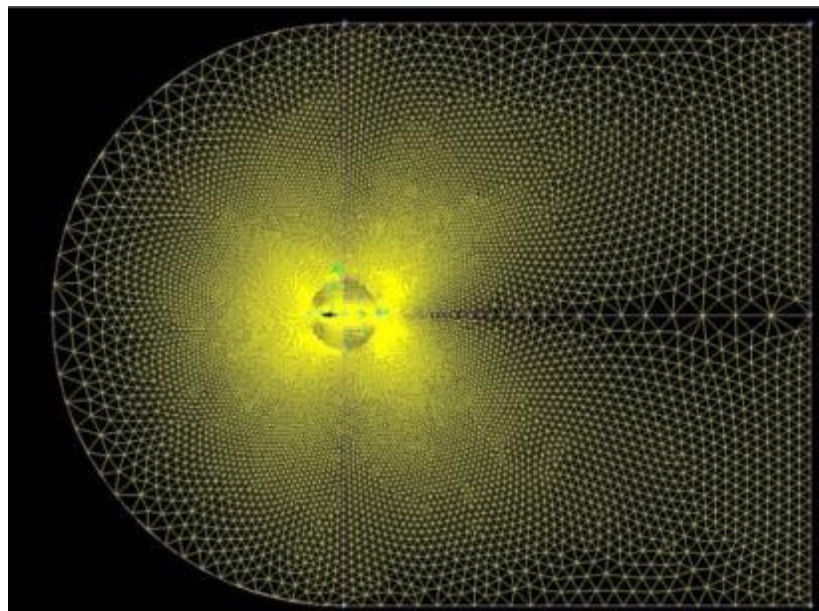
Figure 4.13 C-mesh
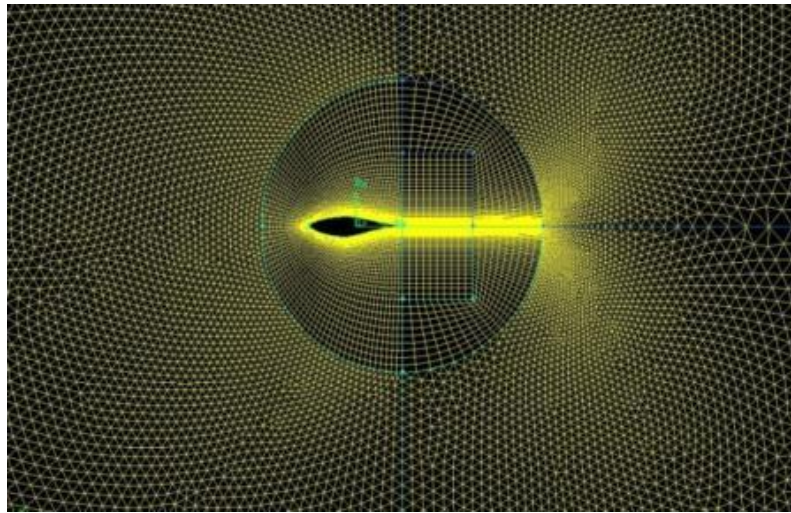
Figure 4.14 Mesh of the motion region
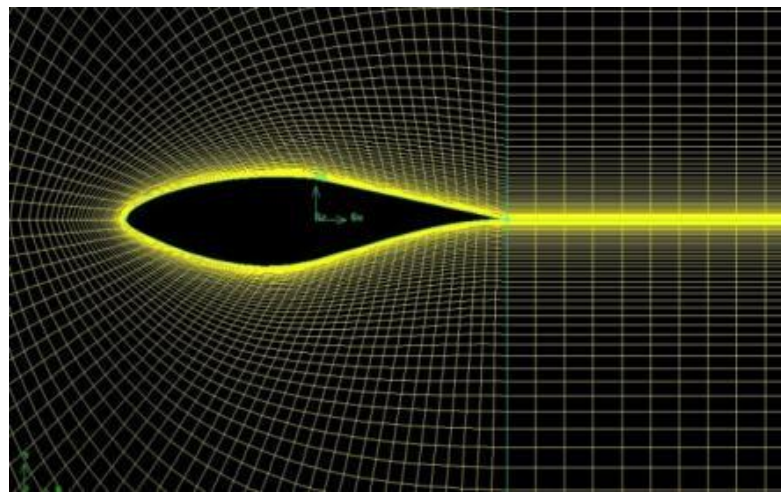
Figure 4.15 Mesh around airfoil

Viscous model

According to the conclusions in section 2, turbulence modes will influent the calculation results. So, S-A turbulence model and k-e RNG turbulence model were chosen to compare.

the S-A model yields less separation compared with the experiment. The *k-e* and the *k-w* models predict attached flow. The SST *k-w* model predicts the separation and profile shape fairly well.

Simulation setup

The 2D domain geometry simulation used the segregated solver and implicit and absolute velocity formulation to set up the numerical simulation in Fluent. The Simple algorithm was chosen for coupling the momentum pressure equations. For spatial discretization, a second-order upwind differencing scheme was applied. Since the time step size is a crucial parameter for unsteady cases and is a function of amplitude, frequency and the far field velocity, a number of time-step refinements have been employed to ensure the temporal accuracy of the results and to get the details of the flow. The time step is proportional to the characteristic time of the airfoil ($\frac{\tau C}{U_\infty}$).

4.3.2   Pitch motion

Numerical approach for turbulence modelling and time step

The unsteady cases were obtained for $\alpha_{mean} = 14^o$ and $\alpha_{amp} = 5.5^o$. For the numerical simulation, realizable S-A model and k-e RNG model with Low-Re corrections were applied. The predicted results were compared with the experimental data reported by Ramsay et al (1995) on an oscillating S809 aerofoil for the same Reynolds number (Re=10^6) and reduced frequency (k=0.026). The aerodynamic coefficients simulated for dynamic stall conditions with reduced frequency, k, of 0.026 at Re $= 10^6$ are presented in Figure 4.16 and 4.17. In addition, the time step should be analysed which is a significant parameter for unsteady case. The unsteady case was obtained for $\alpha_{mean} = 8^o$ and $\alpha_{amp} = 5.5^o$. The turbulence model was k-e RNG model and the k and Re were 0.026 and 10^6, respectively. The selected time steps should be small enough to make the results independent of the time step size. As the time step decreases, signs of unsteadiness will appear especially for separated flows. On the other hand, the selected time steps are large enough to damp out the unsteadiness. The aerodynamic coefficients are presented in Figure 4.18 and 4.19.
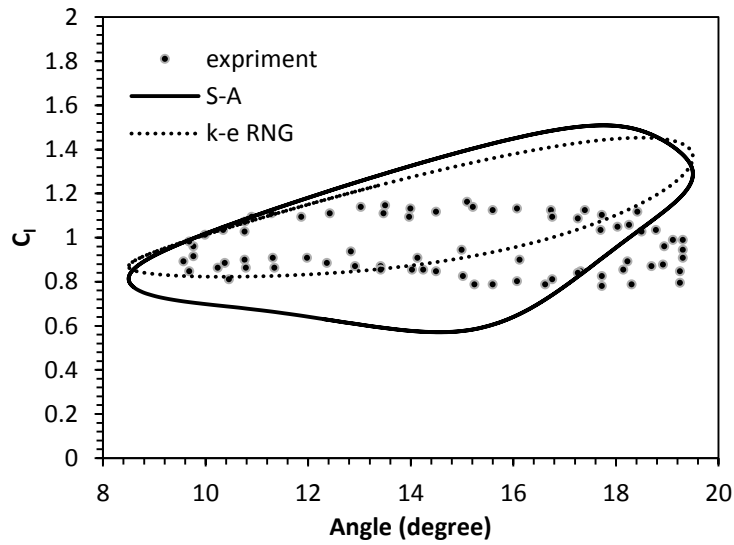
Figure 4.16 Lift coefficient for dynamic stall when k=0.026, $\alpha_{mean} = 14^{o}$, $\alpha_{amp} = 5.5^{o}$
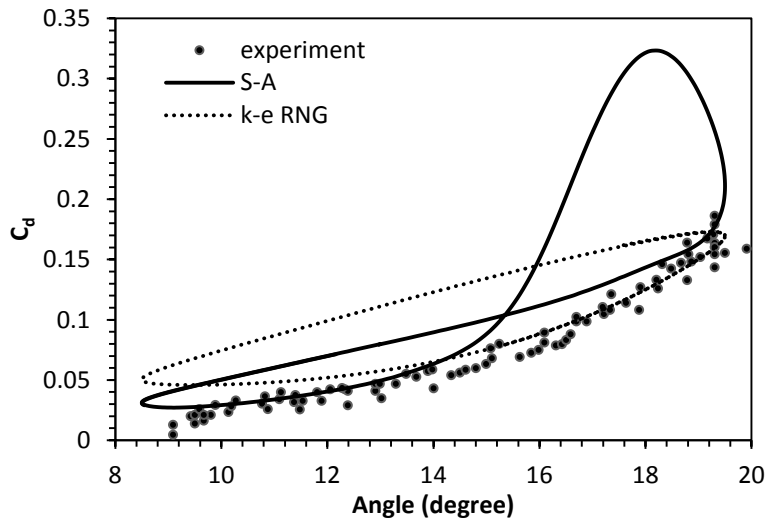
Figure 4.17 Drag coefficient for dynamic stall when k=0.026, $\alpha_{mean} = 14^{o}$, $\alpha_{amp} = 5.5^{o}$
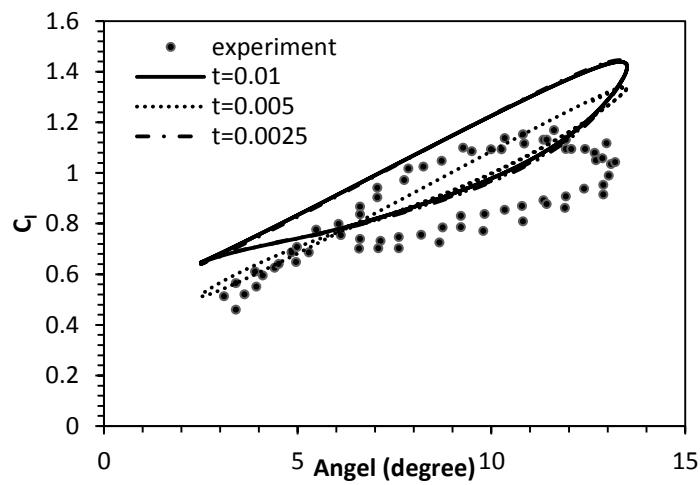
Figure 4.18 Lift coefficient for unsteady case when k=0.026, $\alpha_{mean} = 8^{o}$, $\alpha_{amp} = 5.5^{o}$
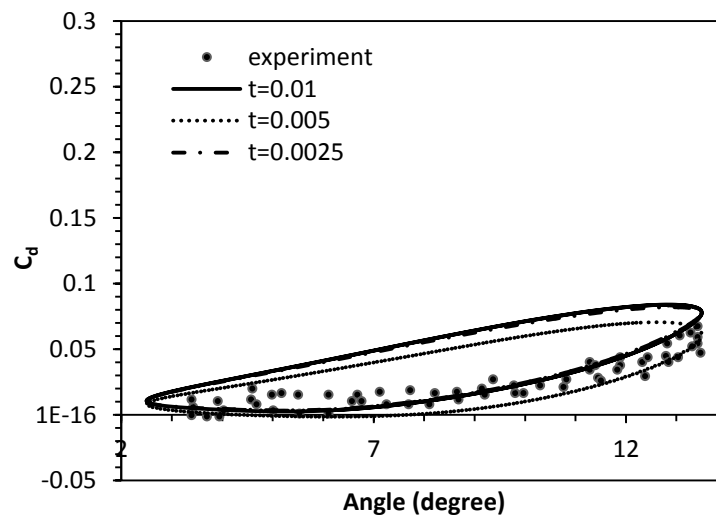
Figure 4.19 Drag coefficient for unsteady case when k=0.026, $\alpha_{mean} = 8^o$, $\alpha_{amp} = 5.5^o$

It can be seen from the figures that the calculation results and experimental results describe a similar phenomenon. For the k-e RNG model, at upstroke, the maximum lift occurred at 16°. The unsteady condition results in a higher maximum lift coefficient compared to the steady condition. This increased lift coefficient phenomenon is almost the same for both numerical and experimental results. The k-e RNG model can demonstrate substantially better results for lift and drag coefficients when Re is low. Figure 4.18 and 4.19 show that when the time step is 0.005, the results of both drag and lift coefficient are closer to the experimental data. And the results are independent of the time step size.

For the numerical results at upstroke, the drag curve is over predicted, but at downstroke, there is an agreement between the predicted drag coefficient and the experimental one. All lift curves are liner up to about $\alpha=12^o$ where the greatest lift discrepancies occur. At angles of attack around 14°, adverse pressure gradients cause reversed and separated flow. At small angles of attack, although the numerical results over predict and under predict the results for downstroke and upstroke respectively, resulting in wider loops, the overall trend of the numerical results is the same as that of the experimental results. The maximum pre-stall lift coefficient for this case is near 1.5 and occurs when the airfoil is traveling with the angle of attack increasing. In contrast, when the model is traveling through decreasing angles of attack the stall recovery is delayed and a hysteresis behaviour is exhibited in the lift

coefficient that can be seen throughout all of the unsteady data. To obtain some measure of this hysteresis behaviour, the lift coefficient on the "return" portion of the curve, at the angle of attack where maximum lift coefficient occurs, can be used. For the case discussed here, decreasing lift coefficient is 1.25, a 16.7% decrease of the unsteady maximum value (1.5). In comparison, the steady state maximum lift coefficient is 1.4.

Having the knowledge of the vorticity field, of the upstroke and downstroke is helpful in investigating the complexity of the boundary layer and vortex shedding during dynamic flow. At high α during stall, the main discrepancy between the numerical and experimental results comes from the specified characteristic, the vortex shedding from both the leading and trailing edges. The high lift coefficient during dynamic stall is a result of the clockwise leading edge vortices, called dynamic stall vortices. The interaction of the dynamic stall vortex and the trailing edge vortex, rotating in opposite directions, causes small 2D and 3D eddies, resulting in a complex flow field. Increasing α moves the location of the boundary layer separation toward the leading edge, and vortices are separated from the upper and lower sides alternatively. Equal angles at upstroke and downstroke demonstrate different flow conditions.

Therefore, the conclusion from the analysis above is that the k-e RNG turbulence model with t=0.005 is better to choose to calculate the unsteady case. The cases below all used this model.

Reduced frequency effects

Although the S809 is designed for high Reynolds numbers and is very thick for operating at low Reynolds numbers with a relatively enlarged drag coefficient, this study is seeking to investigate the effects of the high reduced frequency on such a thick airfoil. Three unsteady cases with different reduced frequencies are considered and compared.

Figure 4.20 and 4.21 present the effects of the reduced frequency on the aerodynamic coefficient. As the reduced frequency increases, the vortices separate from the trailing edge and are located at a streamwise level with almost zero transverse

distance between alternative sign vortices. The difference between upstroke and downstroke values increases, resulting in wider loops and the overall shape of the loops has changed. Comparing the aerodynamic coefficients of high reduced frequency to those of low reduced frequency, at high α, the maximum drag coefficient is more than double and the maximum lift coefficient a bit greater, and at low α, thrust is generated. For the higher reduced frequencies (k = 0·05 and 0·077) the hysteresis in the air loads is larger than at the lowest reduced frequency, as would be expected.
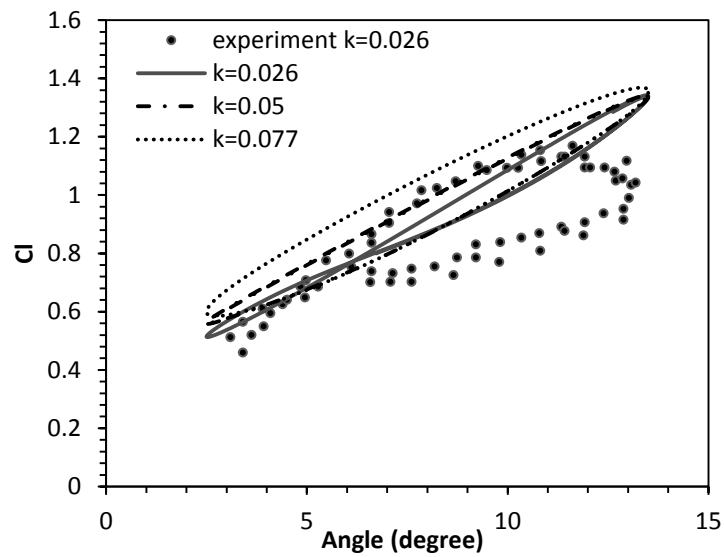
Figure 4.20 Lift coefficient at different reduced frequencies when α_{mean} = 8°, α_{amp} = 5.5^o
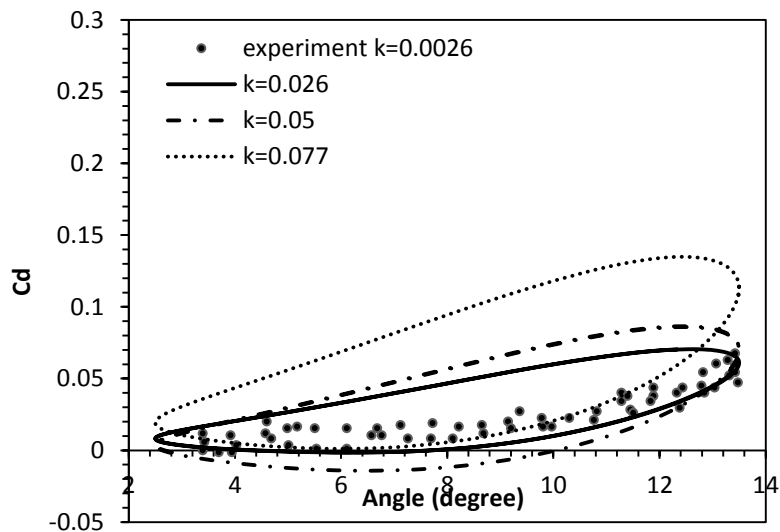
Figure 4.21 Drag coefficient at different reduced frequencies when α_{mean} = 8°, α_{amp} = 5.5^o

Aerodynamic characteristics at different α_{mean}

The variation of predicted lift coefficient *Cl* is shown in 4.24 for reduced frequency k = 0.026, Re=10^6, angle of attack amplitude α_{amp} = 5·5° and three values of α_{mean}8°, 14°and 20°. The variation of Cd is shown in Figure 4.25.
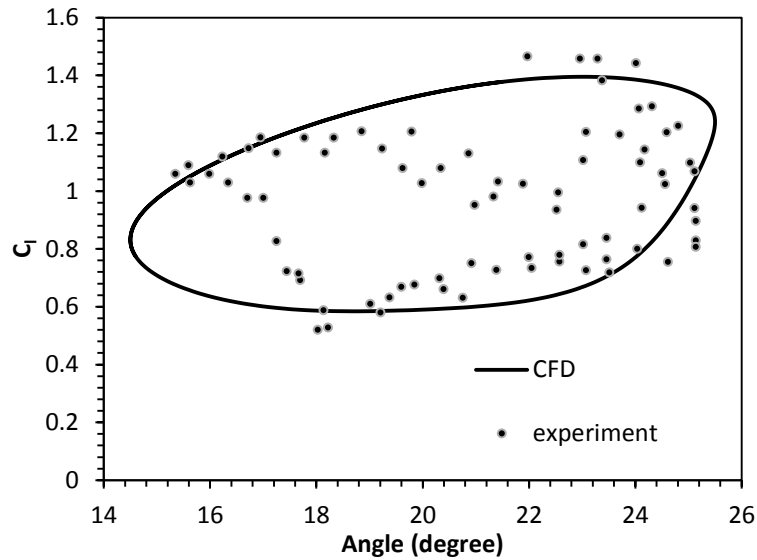
Figure 4.22 Lift coefficient curve when k=0.026, α_{mean} = 20°, α_{amp} = 5.5°
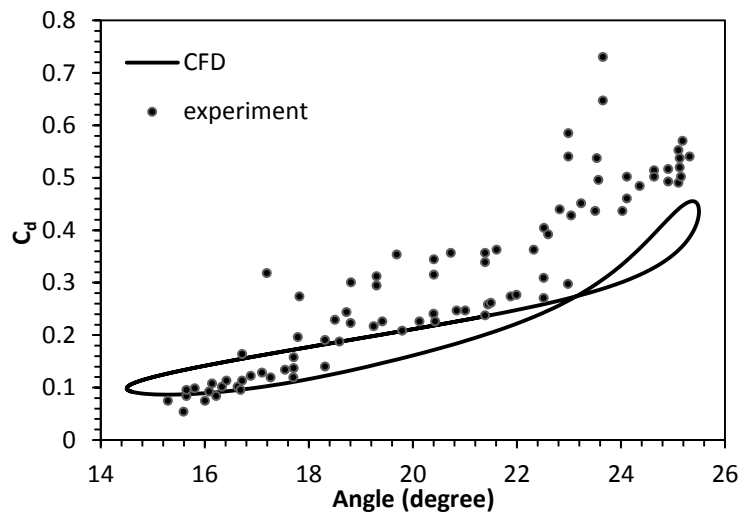
Figure 4.23 Drag coefficient curve when k=0.026, α_{mean} = 20°, α_{amp} = 5.5°
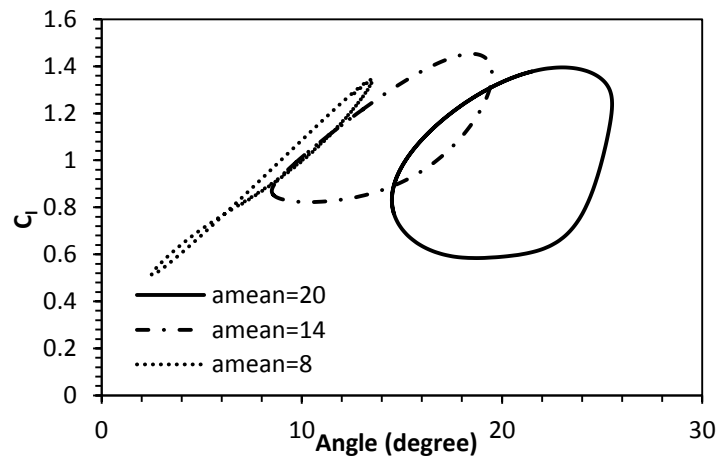
Figure 4.24 Lift coefficient curve compared with different α_{mean} when k=0.026
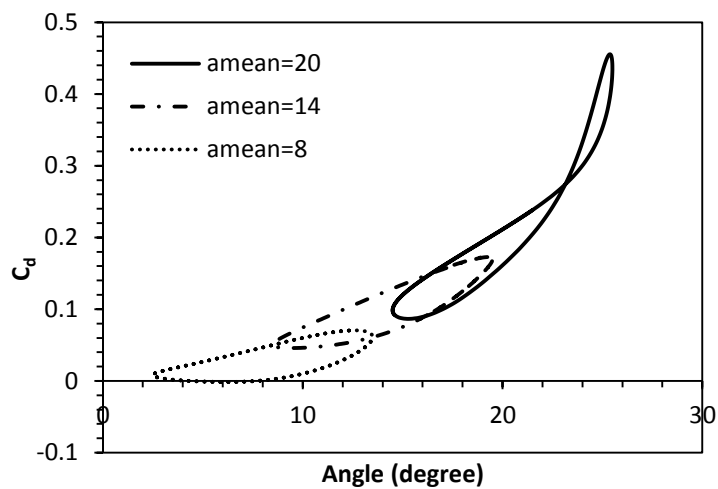
Figure 4.25 Drag coefficient curve compared with different α_{mean} when k=0.026

The agreement between predictions and measurements was found to be good for low mean angles of attack. However, for the higher values of α_{mean}, some transient overshoots and undershoots were seen in the *Cl* measurements that were not predicted by the model. The angle of attack in the experiments also showed deviations from the prescribed nominal angle of attack history.

For mean angles of attack of 8° and 14° the hysteresis loop is predicted well by the model. Stall is delayed to a slightly higher angle of attack than in the static case. The flow reattachment process is delayed to a lower angle of attack than in the static case. For the highest mean angle of attack $\alpha_{mean} = 20°$, the experimental data show some deviations over the cycles, but the air loads are predicted well by the model on average. Again the agreement between the model and the experiment is reasonably good for $\alpha_{mean} = 8°$ and 14°, but *Cd* is under-predicted for $\alpha_{mean} = 20°$. However, it

should be noted that the measurements of Cd were obtained by integrating the pressure data across the thickness of the aerofoil, which is known to be very sensitive to the number of chordwise pressure points.

4.3.3 Plunge motion

From the static experiment, the static stall angle is 13.4 degree of the airfoil when the wind velocity is about 20m/s. Therefore, the dynamic plunge should be calculated before and after the stall angle of attack, respectively. The plunge oscillation can be described as $h(t) = -h_0 \cos(2\pi ft)$. And the effective angle of attack can be defined as $\alpha_E = \alpha - \tan^{-1}(\dot{h}(t)/U_\infty)$. Figure 4.26 shows the disciplines of effective angle of attack when angle of attack is 0 degree, amplitude is 0.02m and frequency is 3.5Hz. It can be illustrated from the figure that when the airfoil plunges up, the values of effective angle are negative. While when the airfoil plunges down, the values are positive.

The calculation value of the plunge motion comparing with the experimental one is shown in Figure 4.27. The calculating Mach number is 0.059, frequency is 2.5Hz, angle of attack is 13.4 degree and amplitude is 0.02m. From the all, the change trend is basically same, but the corresponding time has some difference. The calculation peak of the normal force is smaller and the maximum value appears delayed. And at the half of the back, the lasting time of declining is shorter. The reason of generating the difference is that the consideration of the plunge effect is not very comprehensive.
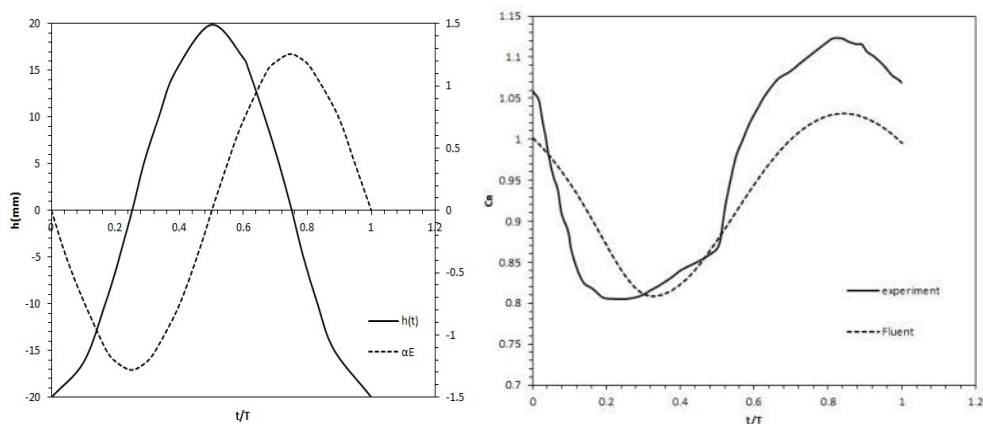
Figure 4.26 Disciplines of effective angle of attack (left)

Figure 4.27 Normal force of plunging motion (right)

The effect of frequency

Figure 4.28 describes the normal force coefficient curves of different frequencies. The Mach number is 0.059, amplitude is 0.02 and mean angle of attack is 13.4 degree. It can be seen from the figure that at the beginning, the normal force decreased for a long time, and then it began to increase with a slower velocity. This variation of the normal force is related to the plunge oscillation of the airfoil. Overall, before ¼ cycle and after ¾ cycle, the normal force increased with the increase of the frequency. However, on the contrary, between ¼ cycle and ¾ cycle, the normal force decreased with the increase of the frequency. Moreover, the increase of the frequency can speed up the variation of the normal force which made the unsteady characteristics of the airfoil more obvious.

The effect of amplitude

Figure 4.29 describes the normal force coefficient curves of different amplitude. The frequency is 3.5Hz, the Mach number is 0.059 and the mean angle of degree is 13 degree. From the picture, the effects on normal force mainly concentrate on the time that before ½ cycle and after ¾ cycle. With the increase of the amplitude, the change of the normal force has a wider range. That is to say, the amplitude contributes a great deal to the normal force. Moreover, the increase of the amplitude accelerates the variation of the normal force coefficient, but it does not affect the time of the inflection point.

The effect of Mach number

Figure 4.30 describes the normal force coefficient curves of different Mach numbers. The frequency is 3.5Hz, amplitude is 0.02m and mean angle of attack is 13 degree. As is shown, the changing range and velocity of the normal force reduce with the increase of the Mach number. And the time related to the inflection point of the normal force is in advance. When the Mach number is small, Mach number changes a little while normal force has an obvious variation. However, in the large Mach number, the variation of the normal force is not very clear. Overall, before ¼ cycle and after ¾ cycle, normal force decreases with the increase of Mach number. However, on the contrary, between ¼ cycle and ¾ cycle, normal force increases with

the increase of the Mach number. Mach number is a significant parameter which affects the plunge oscillation. And the small Mach number has a bigger effect than the large one.
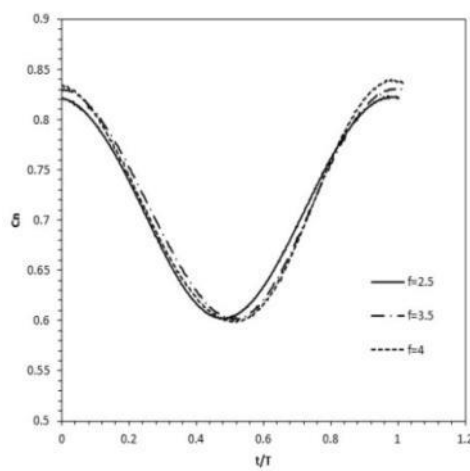
Figure 4.28 Normal force of plunging motion at different frequencies (left)
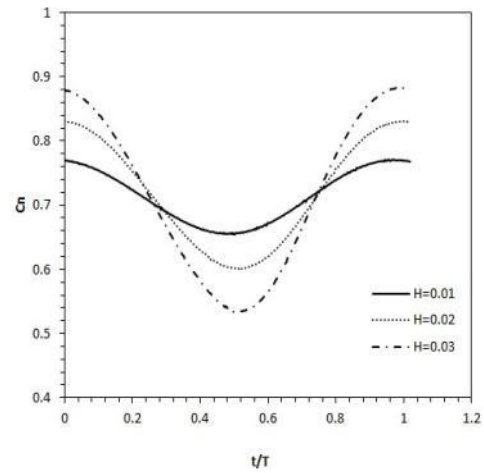
Figure 4.29 Normal force of plunging motion at different amplitudes (right)
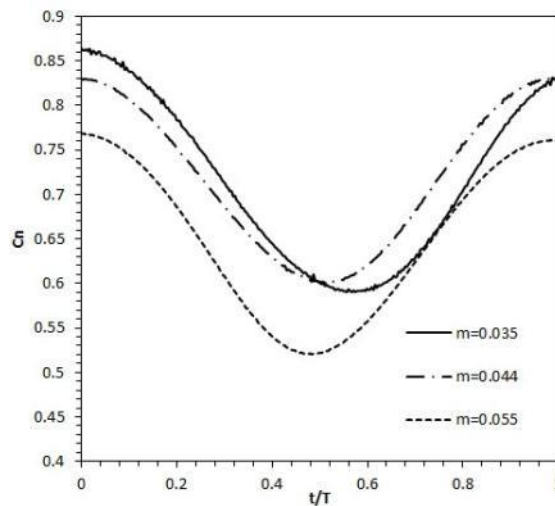
Figure 4.30 Normal force of plunging motion at different Mach numbers

4.3.4 Pitch-surge combined motion

Variation of normal force coefficient is discussed after coupled motion. The pitch motion can be described as

$$\alpha(t) = \alpha_{mean} + \alpha_{amp} \sin(2\pi f_{pitch} t) \tag{4.9}$$

The plunge motion can be described as

$$h(t) = -h_0\sin(2\pi f_{plunge}t + \varphi) \qquad\qquad (4.10)$$

Figure 4.31 and Figure 4.32 show the comparison of normal and thrust force coefficient of two motions (pitch motion and pitch-plunge coupled motion). The calculation pitch and plunge frequencies are both 0.61, Mach number is 0.059, and amplitude is 0.02m.

Seen from the figures, both pitch and pitch-plunge cases behave quite similarly. However, due to plunge motion offsetting a part of pitch motion, aerodynamic performance changes a little. Adding plunge motion makes normal force smaller compared with pure pitch motion and in contrast, thrust force becomes larger.
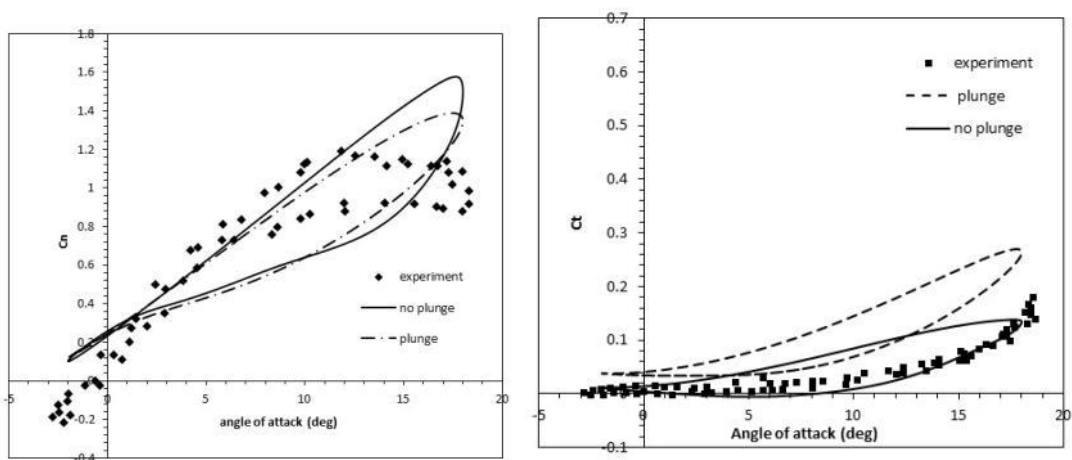
Figure 4.31 Normal force coefficient of two motions (pitch motion and coupled motion) (left)

Figure 4.32 Tangent force coefficient of two motions (pitch motion and coupled motion) (right)

4.4   Conclusion

The report used CFD method and fluent software to do numerical simulations of S814 airfoil model, and got aerodynamic coefficients (CL, Cd and CP). Compared with the experimental results, two conclusions had been got as below.

1) The selection of grid density had a great influence for the aerodynamic performance of the wind turbine airfoil. As a 2D airfoil, the model which have 48100 grid nodes and the value of Y plus is smaller than 2 will have a better calculating result.

2) Different turbulence models will get different results of airfoil performance. Due to the results above, we can see that the S-A turbulence model was a better choice than the Standard k-e turbulence model when the grid was out of consideration.

It can be seen from all the analysis and results above, the CFD method using fluent software is suitable for calculating aerodynamic characteristics of wind turbine airfoils. The S-A turbulence model was better among all the turbulence models and $y^+ \approx 1$ got a better result.

Moreover, this chapter presents unsteady aerodynamic predictions of S809 airfoil using CFD method. Pure pitch, pure plunge and pitch-plunge at different reduced frequencies, mean angles of attack, frequencies, amplitudes and Mach numbers are compared between experiment and computation. The simulations are made using 2D unsteady RANS computations. According to the results, k-ε RNG turbulence model and time step dt =0.05 are better to use to calculate the unsteady cases. The calculation results have a better agreement with the experimental data. However, at upstroke, drag curve is over predicted a bit. From the results, the unsteady state has an obvious hysteresis phenomenon. The difference between steady state behaviour and unsteady hysteresis behaviour is a main reason that unsteady testing should be required for airfoils used in wind turbine applications. So the maximum lift coefficient is smaller than that at steady state. At higher α_{mean}, the results show a bigger difference compared with the experiment. The highest lift coefficient cannot be predicted accurately. It is caused by the density of the mesh and inaccuracy by the CFD method itself. So, mesh with smaller scale will be tested in the next step.

 In the pitch motion, with the increasing of reduced frequency and mean angle of attack, the difference between upstroke and downstroke values increase. In the plunge motion, the calculation peak of the normal force is smaller and the time to get the maximum is delayed. The reason of generating the difference is that the consideration of plunge effect is not very comprehensive. The phenomenon of pitch-plunge motion is similar as the pitch motion. However, plunge motion offsets a part of pitch motion which makes the normal force smaller and thrust larger.

5.   THE PHYSICS OF WIND TURBINE

5.1   Overview

As wind energy becomes the most promising renewable energy source, the study of floating offshore wind turbine (FOWT) which combined aerodynamic, hydrodynamic and mooring-system dynamic effects gets more attention gradually. Wind turbine aerodynamics is exceptionally complex, and it becomes more complex for a FOWT than for an onshore or fixed offshore system. In particular, while a fixed wind turbine has simple flow state, the FOWT experiences complex flow states when the floating platform is in motion (Leishman, 2002). FOWT includes three translation components (heavy in the vertical, sway in the lateral and surge in the axial) and three rotational components (yaw about the vertical axis, pitch about the transverse and roll about the longitudinal) as shown in Figure 5.1 (Jonkman, 2007). In addition to significant pitch motions, large lower-frequency translational surge motions are predicted as well. These rotational and translational motions primarily cause oblique flow conditions on a rotor turbine, rotor-wake interactions and influence the unsteady aerodynamics of the rotor. Unsteady aerodynamic effects can be mainly divided into two parts, unsteady profile aerodynamics and dynamic inflow effects. Additionally, modern large blades are of increased flexibility allowing for larger tip deflections. The platform motions make the rotor blades rapid drop in wind speed which leads tip speed ratios increasing. As the rotor blade begins to pitch back, it interacts with its own wake which develops turbulence region. These include the normal working state (NWS), the turbulent wake state (TWS), the vortex ring state (VBS) and the windmill braking state (WBS). Figure 5.2 shows how various flow states occur when the floating platform undergoes pitching motion (Minu, 2014).
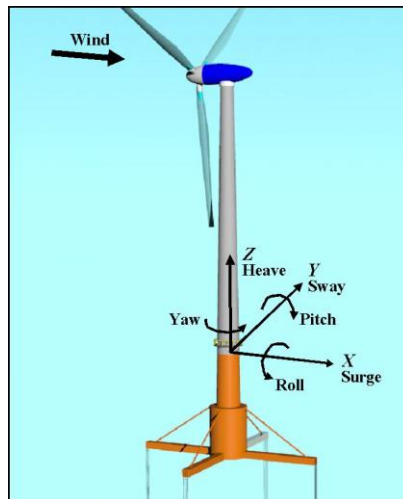
Figure 5.1 Degrees of freedom for a FOWT platform and its effects on the surrounding (Thanhtoan, 2014)
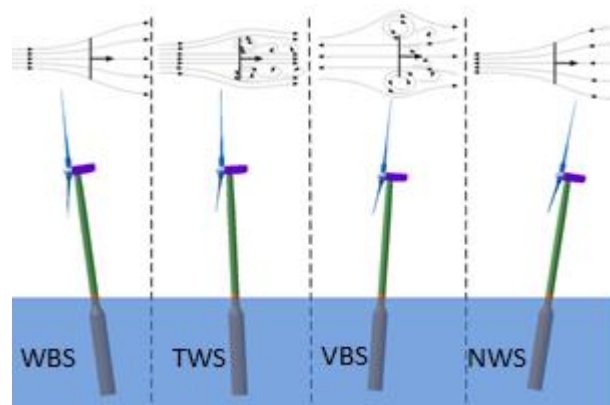
Figure 5.2 Platform pitching motion flow-field (Thanhtoan, 2014)

This has led to research into floating wind turbines, see for example Musial et al (2004). Several prototype concepts have been deployed. For example Hywind, a spar design floating wind turbine. With the increasing of single power and tower height, the largest power of offshore wind turbine has reached 5 MW. In this study, Phase IV of the IEA Annex XXIII offshore Code Comparison Collaboration (Jonkman, 2010), which considered the spar buoy concept, was chosen to show the critical effects of unsteady aerodynamic loads because of platform motion. Moreover, to compare the aerodynamic performance between different platform conditions, the Tension leg platform designed by Massachusetts Institute of Technology (MIT) was chosen.

The major objective of this chapter is to get general information of NREL floating offshore wind turbines. Moreover, there is a simple definition of parameters and load cases. A dimensionless metric, reduced frequency k is often used to characteristic the

degree of unsteadiness of an aerodynamic system. And the axial and the tangential induction factors are two most important factors that a BEM code calculates iteratively. Finally, short descriptions of FAST software theory and settings are described.

5.2 General Information of NREL 5MW Wind Turbine

5.2.1 NREL 5-MW wind turbine on the OC3-Hywind spar

Phase IV of the IEA Annex XXIII Offshore Code Comparison Collaboration (OC3) involves the modelling of an offshore floating wind turbine. As in previous phases of the OC3 project, Phase IV uses the turbine specifications of the National Renewable Energy Laboratory (NREL) offshore 5-MW baseline wind turbine (Jonkman, 2009), which is a representative utility-scale, multi-megawatt turbine that has also been adopted as the reference model for the integrated European UpWind research program.[1] In Phase IV, the rotor-nacelle assembly of this 5-MW turbine—including the aerodynamic and structural properties—remains the same, but the support structure (tower and substructure) and control system properties have been changed.

Numerous floating platform concepts are possible for offshore wind turbines, including spar-buoys, tension leg platforms (TLPs), barges, and hybrid concepts thereof. At the request of the OC3 participants, the spar-buoy concept called "Hywind," developed by Statoil of Norway, (Nielsen, 2006; Skaare, 2007) and Larsen and Hanson (2007). This concept was chosen for the modelling activities of Phase IV, such as design, suitability to modelling, and propinquity to commercialization. Finn Gunnar Nielsen and Tor David Hanson of Statoil were contacted and graciously supplied detailed platform and mooring system data. The data provided was for the conceptual version of the Hywind platform developed to support a 5-MW wind turbine, as analysed by Nielsen, Hanson, and Skaare (Nielsen, 2006; Skaare, 2007) and Larsen and Hanson (2007). At the request of Statoil, the originally supplied data has been condensed and sanitized by Jason Jonkman of NREL so that it is suitable for public dissemination. Aspects of the original data were also adapted slightly by Jason Jonkman so that the platform design is appropriate for supporting the NREL 5-MW baseline turbine, which has properties that are slightly

different than the turbine properties used by Statoil in their development of the system. The new system is referred to as the "OC3-Hywind" system in this report, to distinguish it from Statoil's original Hywind concept.

The NREL 5-MW baseline wind turbine is a representative utility-scale multi-megawatt turbine suitable for floating offshore applications and all the data of the turbine are in the public domain. This wind turbine is a conventional three-bladed upwind variable-speed blade-pitch-to-feather-controlled turbine. Basic physical properties of the NREL 5MW and floating system of OC3 are given in Appendix A.

As described above, there are six rigid-body platform DOFs including translational surge, sway, and heave motions and rotational roll, pitch, and yaw motions. Positive surge is defined along the positive X-axis, sway is along the Y-axis, and heave is along the Z-axis. Positive roll is defined about the positive X-axis, pitch is about the Y-axis, and yaw is about the Z-axis.

5.2.2   NREL 5-MW wind turbine on a floating offshore tension leg platform

As a basis for the development of the FAST TLP model, a TLP design from Tracy's study "Parametric Design of Floating Wind Turbines" (Tracy, 2007) (conducted at the MIT Mechanical Engineering Department) was selected. Tracy's thesis contains a parametric optimization study conducted for several different floating-platform concepts for NREL's 5-MW baseline wind turbine. The study resulted in a number of designs that show Pareto fronts for mean-square acceleration of the turbine versus multiple cost drivers, including platform displacement and total mooring-line tension. The technical data of TLP platform can be seen in Appendix B.

5.3   Parameters Defining Class

5.3.1   Reduced frequency analysis

For a floating offshore wind turbine, the platform motion (surge, sway, heave, roll, pitch, and yaw) may cause an aerodynamic unsteadiness. A dimensionless metric, reduced frequency k is often used to characteristic the degree of unsteadiness of an aerodynamic system. The reduced frequency is defined as the equation 5.1 where ω, C and V mean oscillation frequency, airfoil chord and velocity, respectively.

$$k = \frac{\omega c}{2V} \qquad (5.1)$$

According to Theodorsen's theory (Theodorsen, 1935), the ranges of k can be divided into steady, quasi-steady, unsteady and highly unsteady regions as oscillating airfoils. The degree of flow unsteadiness as determined by reduced frequency is shown in table 5.1.

Table 5.1 Degree of flow unsteadiness, as determined by reduced frequency

Range	Flow Type
k=0	Steady
0<k≤0.05	Quasi-steady
0.05<k≤0.2	Unsteady
k≥0.2	Highly unsteady

The local overall velocity of wind turbine blade section is defined as equation 5.2. It is a resultant velocity of wind velocity component U_∞ and rotor speed Ω.

$$V = \sqrt{U_\infty^2 + (r\Omega)^2} \qquad (5.2)$$

Equation 5.2 may be substituted into equation 5.1 where c is the local blade chord and is a function of r.

$$k = \frac{\omega c(r)}{2\sqrt{U_\infty^2 + (r\Omega)^2}} \qquad (5.3)$$

Sebastian illustrates the cut-in, rated and cut-out reduced frequency curves for the NREL 5-MW wind turbine, see figure 5.3. With the use of the NREL 5-MW turbine at rated operating conditions as an example, an oscillation of 0.1 Hz would yield unsteady loading for the inboard quarter span of the blade, whereas an oscillation of 0.04 Hz would be expected to be aerodynamically quasi-steady throughout the span.
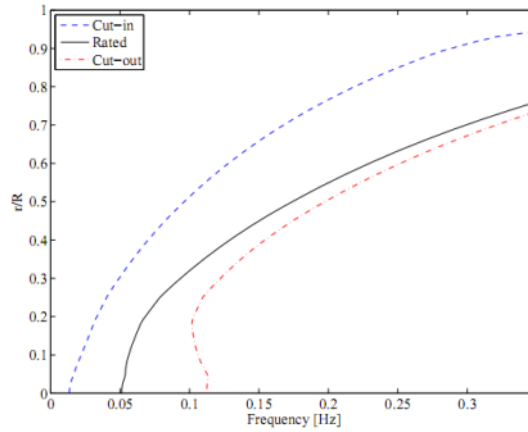
Figure 5.3 Reduced frequency curves for the NREL 5-MW turbine

5.3.2   Load cases

5.3.2.1 Steady wind

Table 5.2 showed the uniform wind speed, rotor speed, pitch angle and tip speed ratio for calculating the aerodynamics of the 5MW NREL wind turbine. The four different wind speeds that are explored in these measurements have been chosen because they describe different performance characteristics of the turbine.

The tip speed ratio, λ, is defined as the ratio between the blade tip speed and the wind velocity.

$$\lambda = \frac{Bladetipspeed}{Windspeed} = \frac{\Omega R}{U_\infty} \tag{5.4}$$

Omega, Ω, is the angular velocity of the rotor, R is the rotor radius and U_∞ is the freestream velocity.

Stall can often occur when the tip speed ratio, λ, is low. This is due to the high angle of attack, α, each blade element experience at low λ. Surface friction will slow the flow next to the airfoil surface due to the viscosity of the air. These results in a separation of the boundary layer on the upper surface of the airfoil and a wake forms above the blade which reduce lift and increase drag. Stalling starts at the root of the blade where is high. This effect is sometimes used to limit the wind turbine power in high winds, and a well designed stalling system has a nearly constant output even though the wind speed changes.

When the tip speed ratio is high, the inner part of the wind turbine blade can experience negative angle of attack. This will result in the blade working as a propeller and transferring power to the wind instead of extracting it. This can give a higher velocity in parts of the wake compared to the freestream velocity.

Table 5.2 Basic condition parameters for the baseline NREL 5MW rotor

U_∞ (m/s)	Speed (RPM)	Pitch(^{o})	TSR
8	9.16	0	7.55
11	12.1	0	7.13
15	12.1	10.45	5.39
20	12.1	17.47	3.99

5.3.2.2 External conditions

Various critical design load cases (DLC) must be considered and analysed based on wind turbine design guidelines such as IEC-61400-1 and GL Guidelines 2010 etc. (Germanischer, 2010) during the practical design process of a wind turbine. In this study, some critical DLC conditions for practical numerical demonstration are selected according to GL Guidelines 2010. Selected DLCs for numerical simulations are normal wind profile (NWP) and extreme operating gust (EOG) conditions.

The external conditions described in the present section shall be considered as a minimum for the design of a wind turbine. Each type of external condition may be subdivided into a normal and an extreme external condition. The normal external conditions generally concern long-term structural loading and operating conditions, while the extreme external conditions represent the rare but potentially critical external design conditions. The design load cases consist of a combination of these external conditions with the wind turbine operational modes. The normal and extreme conditions which are to be considered in design according to wind turbine classes are prescribed in the following sections.

The external conditions to be considered in design are dependent on the intended site or site type for a wind turbine installation. Wind turbine classes are defined in terms of wind speed and turbulence parameters. In addition, the external conditions are also defined together with the wind turbine class. The intention of the classes is to cover most applications. The values of wind speed and turbulence parameters are intended

to represent the characteristic values of many different sites and do not give a precise representation of any specific site. The goal is to achieve wind turbine classification with clearly varying degrees of robustness governed by the wind speed and turbulence parameters. Table 5.3 specifies the basic parameters which define the wind turbine classes.

A plant designed for the wind turbine class with a reference wind speed V_{ref} is so designed that it can withstand the environmental conditions in which the 10-min mean of the extreme wind speed with a recurrence period of 50 years at hub height is equal to or less than V_{ref}.

Table 5.3 Basic parameters for wind turbine classes

Wind turbine class	I	II	III	S
− Vref[m/s]	50	42.5	37.5	Values to be specified by the manufacturer
− Vave[m/s]	10	8.5	7.5	
− A $I15$ (-)	0.18	0.18	0.18	
− a (-)	2	2	2	
− B $I15$ (-)	0.16	0.16	0.16	
− a (-)	3	3	3	

A = category for higher turbulence intensity values

B = category for lower turbulence intensity values

I15 = characteristic value of the turbulence intensity at 15 m/s

a = slope parameter for turbulence characteristics

Therefore, a wind turbine shall be designed to withstand safely the wind conditions defined by the selected wind turbine class. The design values of the wind conditions shall be clearly specified in the design documentation. The wind regime for load and safety considerations is divided into the normal wind conditions, which will occur frequently during normal operation of a wind turbine, and the extreme wind conditions, which are defined as having a 1-year or 50-year recurrence period. In all load cases, the influence of an inclination of the mean flow with respect to the horizontal plane of up to 8° shall be considered. The flow inclination (upflow) angle may be assumed to be invariant with height.

Normal wind conditions

Wind speed distribution

The wind speed distribution at the site is significant for the wind turbine design, because it determines the frequency of occurrence of the individual load components. In the following, the Weibull distribution (equation 5.5) and the Rayleigh distribution (equation 5.6) are given. For design in the standard wind turbine classes, the Rayleigh distribution (equation 5.6) shall be taken for the load calculations. (Germanicher Lloyd wind energy, 2010)

$$P_W(V_{hub}) = 1 - exp[-\left(-\frac{V_{hub}}{c}\right)^k] \tag{5.5}$$

$$P_R(V_{hub}) = 1 - exp[-\pi\left(-\frac{V_{hub}}{2V_{ave}}\right)^2] \tag{5.6}$$

$$With\ V_{ave} = \begin{Bmatrix} \frac{c\sqrt{\pi}}{2}, if\ k = 2 \\ c\Gamma\left(1+\frac{1}{k}\right) \end{Bmatrix} \tag{5.7}$$

Where $P_W(V_{hub})$ denotes Weibull probability distribution: cumulative probability function, i.e. the probability that $V < V_{hub}$. $P_R(V_{hub})$ is Rayleigh probability function: cumulative probability function, i.e. the probability that $V < V_{hub}$. V_{hub} denotes 10-min mean of the wind speed at hub height [m/s]. V_{ave} annual average wind speed at hub height [m/s]. c is scale parameter of the Weibull function [m/s]. k denotes shape parameter of the Weibull function. For design in the standard wind turbine class, the value $k = 2$ shall be taken. Γ denots gamma function.

The distribution functions indicate the cumulative probability that the wind speed is less than V_{hub}. From this, it obtains that $(P\{V_1\} - P\{V_2\})$ specifies the proportion of the time in which the wind speed varies within the limits V_1 and V_2. On derivation of the distribution functions, the corresponding probability density functions are obtained.

Normal wind profile model (NWP)

According to GL Guidelines 2010, the normal wind profile (NWP) model defines the average wind speed as a function of height z above the ground. The assumed wind profile is used to define the average vertical wind shear across the rotor swept area.

The normal wind speed profile is calculated by the following power law:

$$V(z) = V_{hub}\left(\frac{z}{z_{hub}}\right)^{\sigma} \tag{5.8}$$

where $V(z)$ means the wind speed at the height z, z_{hub} means the hub height above ground, σ means the power law exponent which is normally assumed as 0.2, and V_{hub} means the freestream wind velocity at the hub height. For the NREL 5-MW baseline model considered herein, z_{hub} is 90 m.

Extreme wind conditions

The extreme wind conditions are used to determine the extreme wind loads action on wind turbines. These conditions include peak wind speeds due to storms and rapid changes in wind speed and direction. These extreme conditions include the potential effects of wind turbulence, with the exception of the extreme wind speed model (EWM), so that only the deterministic effects need to be considered in the design calculations. The extreme coherent gust (ECG) represents the transient coherent gust characteristics of natural wind speed. The coherent gust magnitude V_{cg} for design for the standard wind turbine classes is assumed as 15 m/s. The wind speed for the extreme coherent gust (ECG) condition is defined by the following equations:

$$V(z,t) = \begin{cases} V(z) & \text{for } t < 0 \\ V(z) + 0.5V_{cg}\left(1 - \cos\left(\frac{\pi t}{T}\right)\right) & \text{for } 0 \leq t \leq T \\ V(z) + V_{cg} & \text{for } t > T \end{cases} \tag{5.9}$$

Here, T = 10 sec is the rise time and *V(z)* is the normal wind profile (NWP).

Furthermore, the extreme operating gust (EOG) represents the transient gust characteristics of natural wind speed. The gust magnitude V_{gustN} at hub height for a recurrence period of N years shall be calculated for the standard wind turbine classes by the following relationship:

$$V_{gustN} = \beta \sigma_1 B \tag{5.10}$$

where V_{gustN} means the maximum value of the wind speed for the extreme operating gust, with an expected recurrence period of N years, σ_1 means standard deviation of the longitudinal wind velocity component at hub height, and B is size reduction factor. Related equations for σ_1 and B can be found in Guideline for the certification of wind turbine (Germanischer Lloyd, 2010).

The wind speed for the extreme operating gust (EOG) condition for a recurrence period of N years is defined by the following equations.

$$V(z,t) = \begin{cases} V(z) - 0.37 V_{gustN} \sin\left(\frac{3\pi t}{T}\right)\left(1 - \cos\left(\frac{2\pi t}{T}\right)\right) & \text{for } 0 \le t \le T \\ V(z) & \text{for } t < 0 \text{ and } t > T \end{cases} \tag{5.11}$$

Here, the recurrence period, N is considered as 50 years, the extreme gust blowing time, T is considered as 14.0 sec. Also, the present wind turbine model is considered as Class I with turbulence category A in order to analyse the most severe extreme gust condition.

5.4   FAST Software Introduction

A number of design tools available to the offshore wind industry have the capability to model floating offshore wind turbines in a coupled time-domain dynamic analysis. This section presents the methods employed by those design tools and includes four categories: structural dynamics, aerodynamics, hydrodynamics and mooring lines.

FAST with AeroDyn and HydroDyn by NREL is a publicly available simulation tool for horizontal-axis wind turbines that was developed by the National Renewable Energy Laboratory (NREL), largely by Jonkman. The FAST code was developed for the dynamic analysis of conventional fixed-bottom wind turbines, but has been extended with additional modules to enable coupled dynamic analysis of floating wind turbines.

ADAMS by MSC ADAMS (Automatic Dynamic Analysis of Mechanical Systems) is a commercially available general-purpose MBS (multibody system) code developed by MSC Software Corporation. The code is not wind turbine-specific and also is used by the automotive, aerospace, and robotics industries. ADAMS models of wind turbines can be generated using the FAST tool's FAST-to-ADAMS pre-processor functionality.

Bladed by GL Garrad Hassan GH Bladed is an integrated software tool for calculating wind turbine performance and dynamic response. It originally was developed by GL Garrad Hassan for modelling onshore fixed-bottom wind turbines. It has been extended, however, to include hydrodynamic loading for modelling

offshore wind turbines. In the last year, the core structural dynamics of the code has been re-written to incorporate MBS.

SIMPACK by SIMPACK AG SIMPACK is a commercially available general purpose code developed by SIMPACK AG. The code is used by the automotive, railway, aerospace, and robotics industries. A version of SIMPACK—SIMPACK Wind—offers extensions to the original code that allow integrated wind turbine simulation. The SIMPACK code has been used to model a floating wind turbine in Matha et al (2011).

This paper chose the FAST code to simulate the floating wind turbine. FAST (Fatigue, Aerodynamics, Structures, and Turbulence) Code is an open, comprehensive, aero-elastic and time based numerical simulation tool capable of modelling the dynamics and performance of a wind turbine system from wind data and the physical properties of two- and three-bladed horizontal-axis wind turbines (HAWTs) developed by the National Renewable Energy Laboratory (Jonkman, 2004). In this research work, FAST is used for modelling land-based and offshore wind turbines which includes coupling of hydrodynamics, aerodynamics, structural mechanics, control system etc. Among its many abilities, FAST can incorporate user defined controllers to adjust the nacelle heading and rotor blade pitch with changing wind speed and direction.

Aerodynamic loads are computed by the AeroDyn subroutines, as described by Laino and Moriarty (Laino & Hansen, 2002; Moriarty & Hansen, 2005). AeroDyn uses two modes for calculating the effect of wind turbine wakes: the blade element momentum (BEM) theory and the generalized dynamic-wake (GDW) theory (Burton, 2001). BEM theory is one of the most commonly used aerodynamic analysis methods for many wind turbine designers. To solve tip and hub losses, effects of high tip speed ratios, dynamic stall, and non-axisymmetric flow, factor corrections are required to modify the BEM theory, including the Beddoes-Leishman dynamic stall model at wind speeds below 8m/s. GDW theory is a more recent model useful for modelling skewed and unsteady wake dynamics for higher wind speed according to the Pitt and Peters method of dynamic inflow derivatives and is based on a

potential flow solution to Laplace's equation. The induced velocities in the rotor plane are described by a system of first-order differential equations.

HydroDyn module solves the hydrodynamic forces on the floating platform (Jonkman, 2007). This module is used in conjunction with the WAMIT pre-processor to resolve the radiation, diffraction and hydrostatic restoring force coefficients. In parallel, Morison's equation gives the fluid resistance caused by viscous effects. Mooring system loads are also calculated by utilizing a quasi-static mooring line representation. Figure 5.4 shows the simulation progress by FAST (Jonkman, 2014).
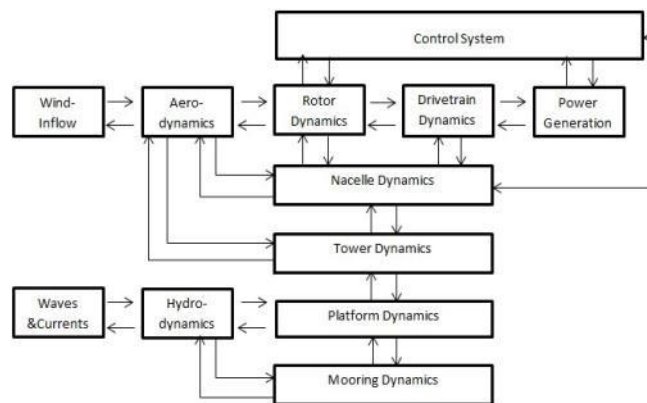
Figure 5.4 Interfacing modules to achieve fully coupled aero-hydro-servo-elastic simulation

5.5 Blade Element Momentum (BEM) Theory

Blade element momentum theory is the most common method using in the wind turbine industry to analyse aerodynamic performance of rotors. It combined momentum theory and blade element theory together which will be described concretely in the following sessions.

5.5.1 Momentum theory

Momentum theory is a classic aerodynamic theory of wind turbine. The function of wind turbines is converting the kinetic energy of the wind into mechanical energy. Therefore, momentum theory is to answer how much kinetic energy can be absorbed by wind turbine. The following part is divided into two conditions to apply momentum theory, considering or not considering vortex rotation.

Not consider rotation *of wake vortex*

First, assume a simple ideal condition:

1) The wind turbine can be simplified into a flat disc without yaw angle, roll angle and cone angle, see Figure 5.5.

2) Blades rotate without friction resistance.

3) Turbine flow model can be simplified into a unit flow pipe.

4) Air static pressure before the wind turbines is equal to that after the wind turbines, namely $P_1=P_2$.

5) The thrust on the blades is uniform

6) Do not consider vortex rotation after the turbine blade.
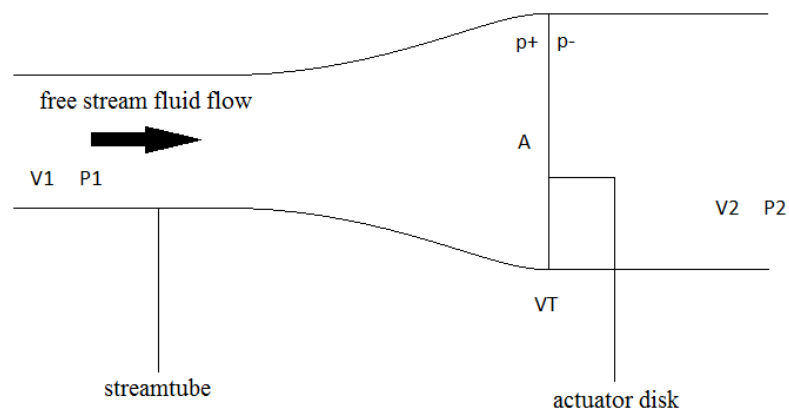
Figure 5.5 Flow condition in the streamtube

When using one dimensional momentum equation into the wind pipe, the axial force of wind turbine can be defined as:

$$T = \dot{m}(V_1 - V_2) \tag{5.12}$$

Where $\dot{m}$ is the air flow through the turbine:

$$\dot{m} = \rho A V_T \tag{5.13}$$

Then replace $\dot{m}$ of Equation (5.13) into Equation (5.12), so

$$T = \rho A V_T(V_1 - V_2) \tag{5.14}$$

However, the axial force can have a different presentation:

$$T = A(p^+ - p^-) \tag{5.15}$$

As Bernoulli's equation means:

$$\frac{\rho V_1^2}{2} + p_1 = \frac{\rho V_T^2}{2} + p^+ \tag{5.16}$$

$$\frac{\rho V_2^2}{2} + p_2 = \frac{\rho V_T^2}{2} + p^- \tag{5.17}$$

According to the assumption, $P_1 = P_2$, when Equation (5.16) minus Equation (5.17):

$$p^+ - p^- = \rho(V_1^2 - V_2^2)/2 \tag{5.18}$$

By Equation (5.14), Equation (5.15) and Equation (5.18):

$$V_T = (V_1 + V_2)/2 \tag{5.19}$$

The equation indicates that the wind speed through the wind turbines is an average speed of wind speed before the wind turbines and wake velocity after the wind turbines. Set the axial induction factors $a_1 = u_a/V_1$, u_a is the axial induced velocity at the blade. So

$$V_T = V_1(1 - a_1) \tag{5.20}$$

$$V_2 = V_1(1 - 2a_1) \tag{5.21}$$

Substitute Equation (5.20) and Equation (5.21) into Equation (5.14):

$$T = 4a_1(1 - a_1).\rho A V_1^2/2 \tag{5.22}$$

$$C_T = \frac{T}{\left(\frac{\rho A V_1^2}{2}\right)} = 4a_1(1 - a_1) \tag{5.23}$$

So the axial induction factors a_1 can be written as:

$$a_1 = 1 - (V_1 + V_2)/2U_1 \tag{5.24}$$

This equation indicates that if wind turbines absorb all the wind energy (when $V_2 = 0$), a_1 reaches the maximum value 0.5. However, in reality, a_1 is always smaller than 0.5.

Based on energy equation, the absorbed energy (shaft power P) is equal to the difference of kinetic energy between front and back of the wind turbine rotor.

$$P = \frac{\dot{m}(V_1^2 - V_2^2)}{2} = \rho A V_T (V_1^2 - V_2^2)/2 \tag{5.25}$$

When $\frac{dP}{da_1} = 0$, P will get the limit value:

$$\frac{dP}{da_1} = 2\rho A V_1^3 (1 - 4a_1 + 3a_1^2) = 0 \tag{5.26}$$

To solve Equation (5.26), $a_1 = 3$ and $a_1 = 1/3$ are the two solutions. As $a_1 < 0.5$, a_1 has only one solution, 1/3. So,

$$\frac{d^2 P}{da_1^2} = 2\rho A V_1^3 (6a_1 - 4) \tag{5.27}$$

Where $a_1 = 1/3$, $\frac{d^2 P}{da_1^2} < 0$, P reaches the limitation. Due to the continuity of P, the limit value is the maximum:

$$P_{max} = \frac{16}{27} \left(\frac{1}{2}\rho A V_1^3\right) \tag{5.28}$$

Correspondingly, the maximum power coefficient is:

$$C_{P_{max}} = \frac{P_{max}}{\frac{1}{2}\rho A V_1^3} = 16/27 \approx 0.593 \tag{5.29}$$

This value is called Betz limit which shows that in the ideal condition, wind turbine can absorb 59.3% wind energy.

Consider rotation of wake vortex

Actually, the wake vortex is rotating. If compared to angular velocity of rotor airflow and rotor angular velocity is a small amount, 1D momentum equation still can be used and hypothesise $P_1=P_2$. There is an assumption that wind turbine plate is

constituted with many small circles which are symmetric with rotor axis (inner radius r, outer radius $r+dr$).

$$dT = d\dot{m}(V_1 - V_2) \tag{5.30}$$

When,

$$d\dot{m} = \rho V_T dA = \rho V_T 2\pi r dr \tag{5.31}$$

If Equation (5.14) is still available, then

$$V_1 - V_2 = 2a_1 V_1 \tag{5.32}$$

Substitute Equation (5.31) (5.32) and (5.20) into Equation (5.30):

$$dT = 4\pi r \rho V_1^2 a_1 (1 - a_1) dr \tag{5.33}$$

The axial force on the whole rotor:

$$T = \int dT = 4\pi \rho V_1^2 \int_0^R a_1 (1 - a_1) r dr \tag{5.34}$$

Due to momentum equation, the torque acting on the circle is:

$$dM = d\dot{m}(u_t r) \tag{5.35}$$

Where $u_t = \omega \cdot r$, ω means circumferential induced velocity at the radius r. setting the angular induction factor $a_2 = \omega/2\Omega$, Ω means the rotating angular velocity. Substitute $u_t = 2a_2 \Omega r$, Equation (5.20) and (5.31) into Equation (5.35):

$$dM = 4\pi r^3 \rho V_1 a_2 (1 - a_1)\Omega dr \tag{5.36}$$

Therefore, the wind turbine shaft power is:

$$P = \int dP = \int \Omega dM = 4\pi \rho \Omega^2 V_1 \int_0^R a_2 (1 - a_1) r^3 dr \tag{5.37}$$

Setting the tip speed ratio $\lambda = \Omega R/V_1$, $A = \pi R^2$, so

$$P = \rho A V_1^3 \cdot \frac{4\lambda^2}{R^4} \cdot \int_0^R a_2 (1 - a_1) r^3 dr \tag{5.38}$$

Therefore, rotor power coefficient is:

$$C_P = \frac{8\lambda^2}{R^4} \cdot \int_0^R a_2(1 - a_1)r^3 dr \tag{5.39}$$

5.5.2 Blade element theory

The basic theory of Blade element theory is to divide rotor blade into many small sections along the spanwise which called blade element. There are no disturbances of flow between every section. Blade element can be defined as 2D airfoil. The force and moment can be obtained by integral along the spanwise of rotor blade.

According to momentum theory (considering wake vortex rotation), axial velocity $V_a = V_1(1 - a_1)$and tangential velocity $V_T = \Omega r(1 + a_2)$. The actual airflow speed pass through wind turbines is $\vec{W} = \vec{V_a} + \vec{V_t}$. For every blade element, α is angle of attack, φ is inflow angle and θ is twist angle shown in Figure 5.6.

$$\varphi = arctg[\frac{V_1(1-a_1)}{\Omega r(1+a_2)}] \tag{5.40}$$

$$\alpha = \varphi - \theta \tag{5.41}$$

When the value of α is confirmed, lift coefficient C_l and drag coefficient C_d can be gotten by looking up experimental results. As

$$dF_n = dY cos\varphi + dX sin\varphi \tag{5.42}$$

$$dF_t = dY sin\varphi - dX cos\varphi \tag{5.43}$$

Normal force coefficient C_n and tangential force coefficient C_t are

$$C_n = C_l cos\varphi + C_d sin\varphi \tag{5.44}$$

$$C_t = C_l sin\varphi - C_d cos\varphi \tag{5.45}$$

Axial force on every blade element is

$$dT = cdr \cdot \rho W^2/2 \cdot C_n \tag{5.46}$$

Where c is the chord. Therefore, the total axial force on the blade is

$$dT = N_b cdr \cdot \rho W^2/2 \cdot C_n \tag{5.47}$$

Where N_b is the number of blades. Similarly, momentum infinitesimal is

$$dM = N_b crdr \cdot \rho W^2/2 \cdot C_t \tag{5.48}$$
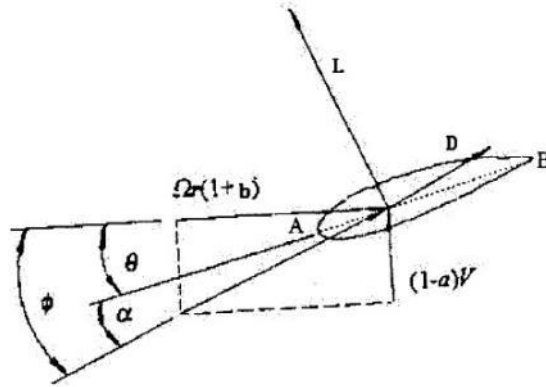
Figure 5.6 Momentum theory (Moriaty, 2005)

5.5.3   Blade element momentum theory

In order to calculate the aerodynamic characteristics of wind turbine, we need to get the axial induction factor a_1 and angular induction factor a_2 first. From the momentum theory that

$$dT = 4\pi r \rho V_1^2 a_1 (1 - a_1) \tag{5.49}$$

$$dM = 4\pi r^3 \rho V_1 a_2 (1 - a_1) \Omega dr \tag{5.50}$$

In addition, from the blade element theory, that

$$dT = N_b cdr \cdot \rho W^2/2 \cdot C_n \tag{5.51}$$

$$dM = N_b crdr \cdot \rho W^2/2 \cdot C_t \tag{5.52}$$

Combined Equation (5.49) and (5.51),

$$4\pi r \rho V_1^2 a_1 (1 - a_1) dr = N_b cdr \cdot \rho W^2/2 \cdot C_n \tag{5.53}$$

So $a_1(1 - a_1) = \sigma/4 \cdot W^2/V_1^2 \cdot C_n$ \hfill (5.54)

Where $\sigma = N_b c/2\pi r$

As $sin\varphi = (1 - a_1)V_1/W$, $\frac{W^2}{V_1^2} = (1 - a_1)^2/sin^2\varphi$, substitute into Equation (5.54)

$$\frac{a_1}{(1-a_1)} = \sigma C_n/4sin^2\varphi \tag{5.55}$$

Similarly, Combined Equation (5.50) and (5.52),

$$4\pi r^3 \rho V_1 a_2(1-a_1)\Omega dr = N_b crdr \cdot \rho W^2/2 \cdot C_t \tag{5.56}$$

So $a_2(1-a_1) = \sigma/4 \cdot W/V_1 \cdot C_t \cdot W/\Omega r$ \qquad (5.57)

As $sin\varphi = (1-a_1)V_1/W$, $cos\varphi = (1+a_2)\Omega r/W$, $\frac{W}{V_1} = (1-a_1)/sin\varphi$,

$\frac{W}{\Omega r} = (1+a_2)/cos\varphi$, substitute into Equation (5.57)

$$\frac{a_2}{(1-a_2)} = \sigma C_t/4sin\varphi co \tag{5.58}$$

The algorithm of axial induction factor a_1 and angular induction factors a_2 for an iterative solution is as follows:

1) Assume the initial value of a_1 and a_2

2) Calculate inflow angle φ, $\varphi = arctg[\frac{V_1(1-a_1)}{\Omega r(1+a_2)}]$

3) Calculate angle of attack α, $\alpha = \varphi - \theta$

4) Calculate lift coefficient C_l and drag coefficient C_d

5) Calculate normal force coefficient C_n and tangential force coefficient C_t

6) Calculate a_1 and a_2 again

5.5.4   Tip and hub loss correction and modified BEM theory

Tip and hub loss correction

When the flow past around the rotor blade section, pressure difference is occurred between upper and lower section. It will induce a decrease of circulation in tip and hub which will make the reduction of torque. So a modification for tip and hub loss is necessary. AeroDyn uses a theory originally developed by Prandtl (Glauert, 1935).

$$F = F_t \cdot F_r \tag{5.59}$$

$$F_t = 2/\pi \cdot \arccos(e^{-f_t}) \tag{5.60}$$

$$f_t = N_b/2 \cdot (R - r)/R\cos\varphi \tag{5.61}$$

$$F_r = 2/\pi \cdot \arccos(e^{-f_r}) \tag{5.62}$$

$$f_r = N_b/2 \cdot (r - r_n)/r_n \sin\varphi \tag{5.63}$$

Where F is the tip and hub loss correction, F_t is the tip loss correction and F_r is the hub loss correction. r_n is the hub radius.

This correction factor is used to modify the momentum part of the blade element momentum equations, replacing Equation (5.51) and (5.52) with the following:

$$dT = 4\pi r\rho V_1^2 a_1(1 - a_1)F dr \tag{5.64}$$

$$dM = 4\pi r^3 \rho V_1 a_2(1 - a_1)\Omega F dr \tag{5.65}$$

Glauert Correction

Another limitation of the BEM theory is that when the induction factor is greater than about 0.4, the basic theory becomes invalid. This occurs with turbines operating at high tip speed ratios (e.g. constant speed turbine at low wind speeds), as the rotor enters what is known as the turbulent wake state (a > 0.5). According to momentum theory, this operating state results when some of the flow in the far wake starts to propagate upstream, which is a violation of the basic assumptions of BEM theory. Physically, this flow reversal cannot occur, and what actually happens is more flow entrains from outside the wake and the turbulence increases. The flow behind the rotor slows down, but the thrust on the rotor disk continues to increase. To compensate for this effect, Glauert (1926) developed a correction to the rotor thrust coefficient based on experimental measurements of helicopter rotors with large induced velocities. While this model was originally developed as a correction to the thrust coefficient of an entire rotor, it has also been used to correct the local coefficient of the individual blade elements when used with BEM theory. Because of this, it is important to understand the Glauert correction's relationship to the tip-loss model. When the losses near the tip are high, the induced velocities are large; therefore, the possibility of a turbulent wake near the tips increases. Thus, for each

element the total induced velocity calculation must use a combination of the tip-loss and Glauert corrections. Buhl (2004) derived a modification to the Glauert empirical relation that included the tip-loss correction as follows:

$$C_T = \frac{8}{9} + \left(4F - \frac{40}{9}\right)a + (\frac{50}{9} - 4F)a^2 \tag{5.66}$$

or solving for the induction factor,

$$a = \frac{18F - 20 - 3\sqrt{C_T(50 - 36F) + 12F(3F - 4)}}{36F - 50} \tag{5.67}$$

This empirical relationship is different from those in the models of other authors (Manwell, 2002; Burton, 2001). But, this relationship is necessary to eliminate a numerical instability when using the Glauert correction to calculate the elemental thrust in conjunction with the tip-loss correction model.

Skewed Wake Correction

Another disadvantage of blade element momentum theory is that it was originally designed for axisymmetric flow. Often, however, wind turbines operate at yaw angles relative to the incoming wind, which produces a skewed wake behind the rotor. The BEM model needs to be corrected to account for this skewed wake effect. The formulation used in AeroDyn is based on an equation originally developed by Glauert (1926) who was primarily interested in the autogyro. The basic formula of the skewed wake correction he derived is

$$a_{skew} = a[1 + K\frac{r}{R}cos\psi] \tag{5.68}$$

where the constant K is a function of the skew angle.

Many skewed wake correction models are derived from this formulation. The one implemented in AeroDyn is based on a method developed by Pitt and Peters (1981) (see also Snel and Schepers, 1995). Assuming steady inflow conditions, the skewed wake formulation is

$$a_{skew} = a[1 + \frac{15\pi}{32}\frac{r}{R} \ tan\frac{\chi}{2}cos\psi] \tag{5.69}$$

where ψ is defined as the azimuth angle that is zero at the most downwind position of the rotor plane, after accounting for both tilt and yaw (see Figure 5.7). This position has the greatest amount of induced velocity, whereas the most upwind position (*cosψ = -1*) has the least induced velocity.
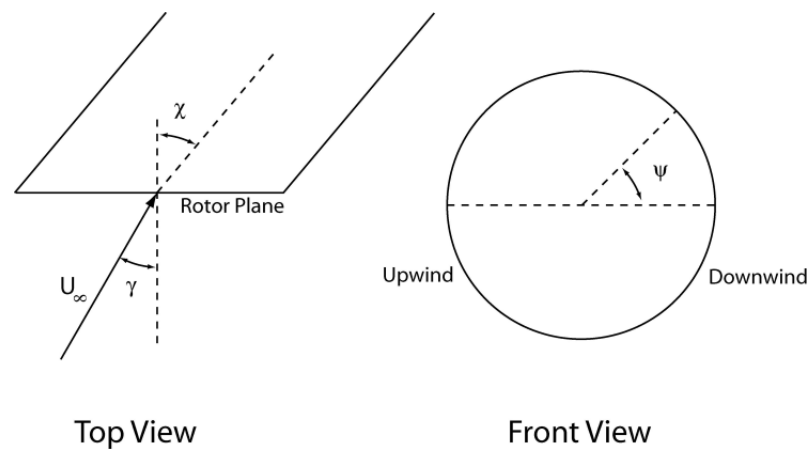

Figure 5.7 Coordinates used in skewed wake correction (Moriarty, 2005)

5.5.5   Final Iteration Procedure for Blade Element Momentum Theory

Now that all of the equations for BEM theory have been established, AeroDyn identifies the iteration procedure to calculate the induced velocities, angles of attack, and thrust coefficients for each blade element along the span of a blade. To begin the calculation, the axial induction factor is first estimated. See the specific procedure in AeroDyn Theory Manual (Moriarty, 2015).

5.6   Generalized Dynamic Wake (GDW) Theory

The GDW method is based on a potential flow solution to Laplace's equation. Kinner (1937) used this solution to develop the equations for the pressure distributions in the rotor plane, which consist of an infinite series of Legendre functions in the radial direction and trigonometric functions in the azimuthal direction. In his derivation, Kinner started from the Euler equations (inviscid and incompressible flow), assumed that the induced velocities were small in comparison to the mean wind speed and regarded the rotor as an infinite number of slender blades, to keep the solidity low.

The main advantages of the generalized dynamic wake method over blade element momentum theory include inherent modelling of the dynamic wake effect, tip losses,

and skewed wake aerodynamics. The dynamic wake effect is the time lag in the induced velocities created by vorticity being shed from the blades and being convected downstream. Notice that the BEM theory has no time lag, but the GDW does. However, the time constant is shorter than that exhibited by the data in the figure. The small oscillations in the BEM prediction are due to structural vibrations and not the aerodynamic model itself. We estimate that similar amplitude structural oscillations also appear in the GDW model.

5.6.1   Basic Derivation

The basic governing equations of the generalized dynamic wake are derived from the Euler equations. Assuming that the induced velocities are small perturbations relative to the freestream inflow, conservation of momentum simplifies to

$$\frac{\partial u_i}{\partial t} + U_{\infty j} \frac{\partial u_i}{\partial x_j} = -\frac{1}{\rho} \frac{\partial p}{\partial x_i} \tag{5.70}$$

and conservation of mass resulting in

$$\frac{\partial u_i}{\partial x_i} = 0 \tag{5.71}$$

finally leading to Laplace's equation for the pressure distribution:

$$\nabla^2 p = 0 \tag{5.72}$$

It is convenient to non-dimensionalize these equations with the rotor tip speed, which is a widely used convention in rotorcraft aerodynamics, and also the hub-height wind speed, which is common in wind turbine aerodynamics. This results in the following non-dimensional quantities:

Time: $\hat{t} = \Omega t$ (5.73)

Displacements: $\hat{x}_i = x_i/R$ (5.74)

Velocities: $\hat{u}_i = u_i/\Omega R$ and $\hat{U}_\infty = U_\infty/\Omega R$ (5.75)

Pressure: $\phi = \dfrac{P}{\rho \cdot (\Omega R)^2}$ (5.76)

The two primary equations for the generalized dynamic wake are then made dimensionless. Laplace's equation is also true for the dimensionless pressure:

$$\nabla^2 \phi = 0 \qquad (5.77)$$

and the momentum equation becomes

$$\frac{\partial \widehat{u}_i}{\partial \widehat{t}} + \widehat{U}_{\infty j} \frac{\partial \widehat{u}_i}{\partial \widehat{x}_j} = -\frac{\partial \phi}{\partial \widehat{x}_i} \qquad (5.78)$$

The boundary conditions for these differential equations are given by the aerodynamic loading on the rotor blades and the requirement that the pressure return to ambient pressure far from the rotor. Also, the pressure discontinuity across the rotor plane must apply a force equal to the rotor thrust.

Using linear superposition, the pressure field can be divided into two components: one modelling the spatial variation of the pressure distribution, ϕ^V, and one modelling the unsteadiness, ϕ^A, where:

$$\phi = \phi^V + \phi^A \qquad (5.79)$$

By dividing the pressure field into two components, it can be divided into two separate equation sets as follows:

$$\frac{\partial \widehat{u}_i}{\partial \widehat{t}} = -\frac{\partial \phi^A}{\partial \widehat{x}_i} \qquad (5.80)$$

And $\widehat{U}_{\infty j} \dfrac{\partial \widehat{u}_i}{\partial \widehat{x}_j} = -\dfrac{\partial \phi^V}{\partial \widehat{x}_i} \qquad (5.81)$

5.6.2 Method of solution for Generalized Dynamic Wake Calculations

Kinner developed the pressure distribution that satisfies Laplace's equation (Equation 5.77) and that gives pressure discontinuity across a circular disk (the rotor). This solution was originally developed for the problem of a circular wing, but with different boundary conditions, also applies to a yawed actuator disk. Specific equations to describe this method can be found in AeroDyn Theory Manual (Moriarty, 2015).

5.7 Fast Settings and Load Cases

In this paper, all simulations start off with a stationary rotor located at the origin, operating in a constant wind, constant rotor speed and blade pitch settings to derive the prescribed motions possible to be run. The oscillation frequencies for each of the individual platform degrees-of-freedom (surge, sway, heave, roll, pitch, and yaw) were computed with wind and wave loading in 320m of water via FAST by applying an initial perturbation to each of the DOFs. This motion is caused by the regular wave occurring during that timeframe coinciding with a wind velocity. All computations were performed at the sea level atmosphere temperature of 15°C and pressure of 1.013×10^{5} Pa. Table 5.4 summarizes the environmental conditions for FAST simulations (Jonkman, 2010), below-rated (U_{∞} = 8m/s, Ω = 9.16rpm) and rated (U_{∞} = 11.4m/s, Ω = 12.1rpm) wind and operating conditions were chosen in all computations. The rated condition causes maximum wind thrust loading. To understand the flow unsteadiness from a blade element level, a severe condition was chose as the wave height was 5m and periodic was 8s which confirmed the oscillating in this frequency f=1/T=0.125Hz.

Table 5.4 Wind and sea state definitions for FAST simulations

	$U_{\infty(}$ m/s	Ω	H_s (m)	T_p (s)
Below-rated	8	9.16	1.83	12.72
Severe sea condition	8	9.16	5	8
Rated	11.4	12.10	2.54	13.35
Above-rated	18.0	12.10	4.09	15.33

The FAST simulations were conducted with the following settings:

• Choosing the regular wave. Each simulation lasted 800.

• Wind was defined as constant, unidirectional and without shear.

• Using equilibrium BEM dynamic model.

• Six platform DOFs were switched on.

• Blade pitch and generator torque controllers were switched on.

Figure 5.8, Figure 5.9 and Figure 5.10 illustrate the resulting FAST-simulated platform kinematics at three different conditions of Phase IV wind turbine with spar

platform, respectively. Similarly, Figure 5.11, Figure 5.12 and Figure 5.13 show the platform motions of Tension leg platform.

As the figures show, the amplitudes of the sway, heave, roll and yaw are very small for spar-buoy platform. The relatively planar motion of the turbine is due to the constant and unidirectional freestream wind and aligned wave direction. Surge and pitch DOFs appear to be the largest amplitude modes which will influence the aerodynamic performance a lot. These two motions have been approximated by two appended sine functions. The CFD simulations were set-up for FAST platform motion results. The results were averaged to get the mean thrust, torque and hence the induction factors which will be compared with CFD simulations in the following chapters. The details of the case output values used to set-up the CFD simulation are given in Table 5.5 and Table 5.6 for spar platform and TLP platform, respectively. The platform motion of TLP is significantly smaller than that of spar platform.
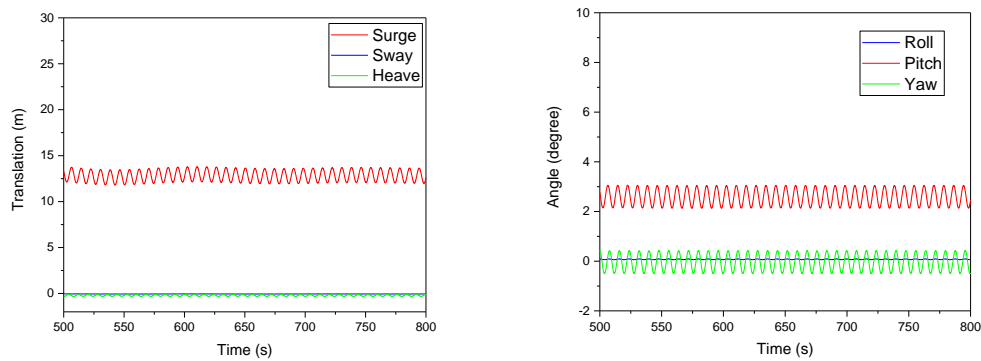

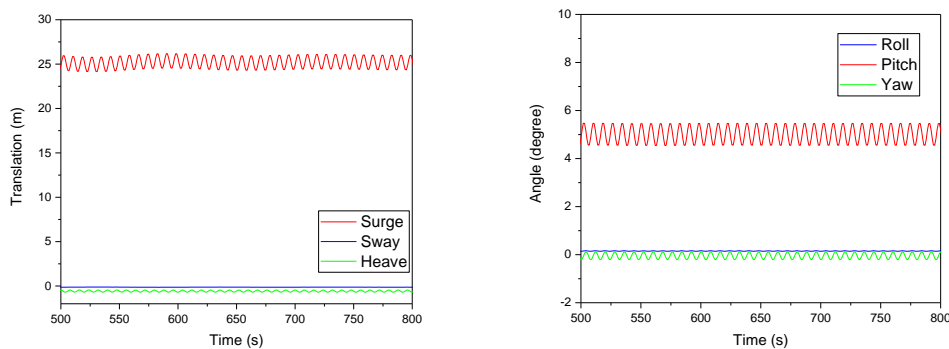Figure 5.8 Below-rated condition of Spar platform

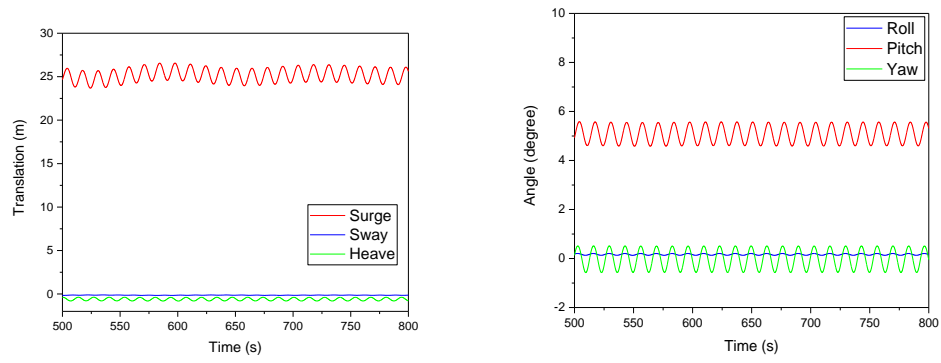Figure 5.9 Severe sea condition at below-rated of Spar platform

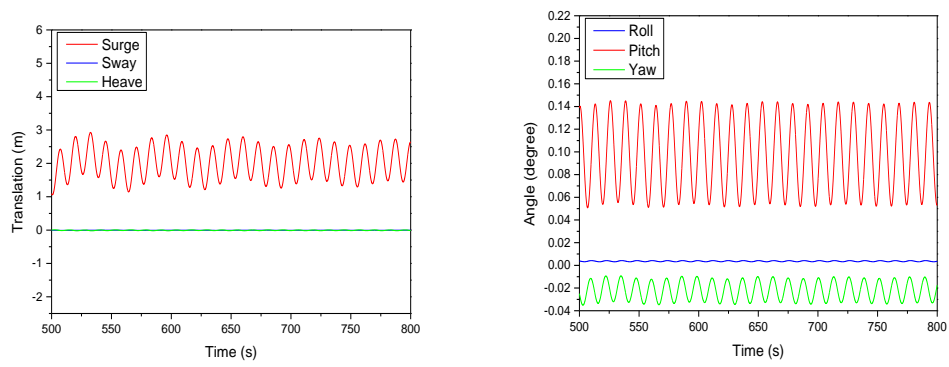Figure 5.10 Rated condition of Spar platform

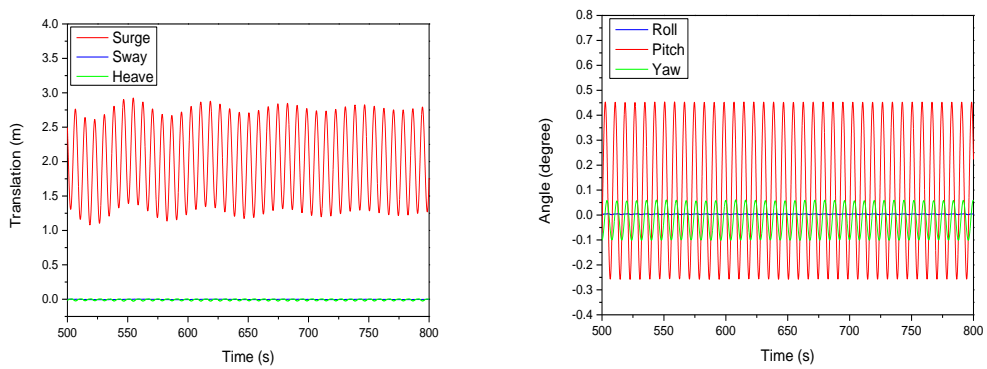Figure 5.11 Below-rated condition of TLP platform

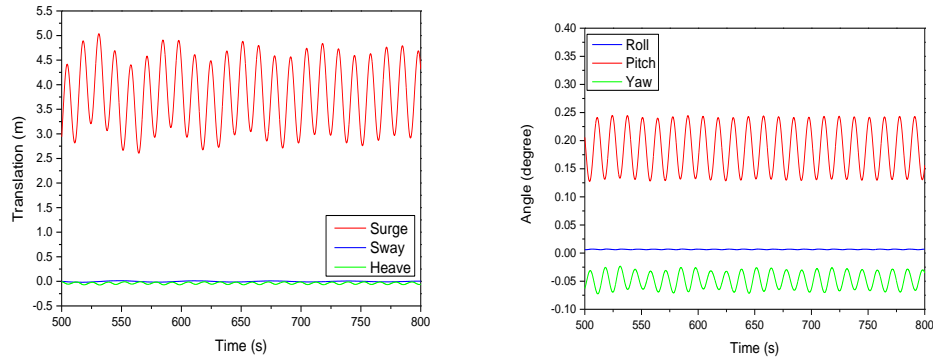Figure 5.12 Severe sea condition at below-rated of TLP platform

Figure 5.13 Rated condition of TLP platform

Table 5.5 Output from FAST of Spar platform

Condition	Platform Pitching Amplitude (deg)	Platform Mean Pitch Angle (deg)	Platform Surge Amplitude (m)
Below-rated	0.336	2.5	0.7
Severe sea condition	0.36	5	0.65
Rated	0.49	5	1.14

Table 5.6 Output from FAST of TLP platform

Condition	Platform Pitching Amplitude (deg)	Platform Mean Pitch Angle (deg)	Platform Surge Amplitude (m)
Below-rated	0.0445	0.098	0.656
Severe sea condition	0.3535	0.0978	0.737
Rated	0.055	0.186	0.85

5.8 Compare the Bending Moment at the Tower Base and Blade Root

In this session, the design loads for a floating spar foundation is studied by analysing the bending moment at the blade and tower base for various values of water depth, wave height and wind speed. Figure 5.14 shows the results as follows. As the figure shows, for each water depth, the bending moment at the tower and blade are almost same. However, the change in the wave height and wind speed will affect the bending moments of blade roots and tower base. The blade and tower bending moment increase with the wind speed and wave height increasing.
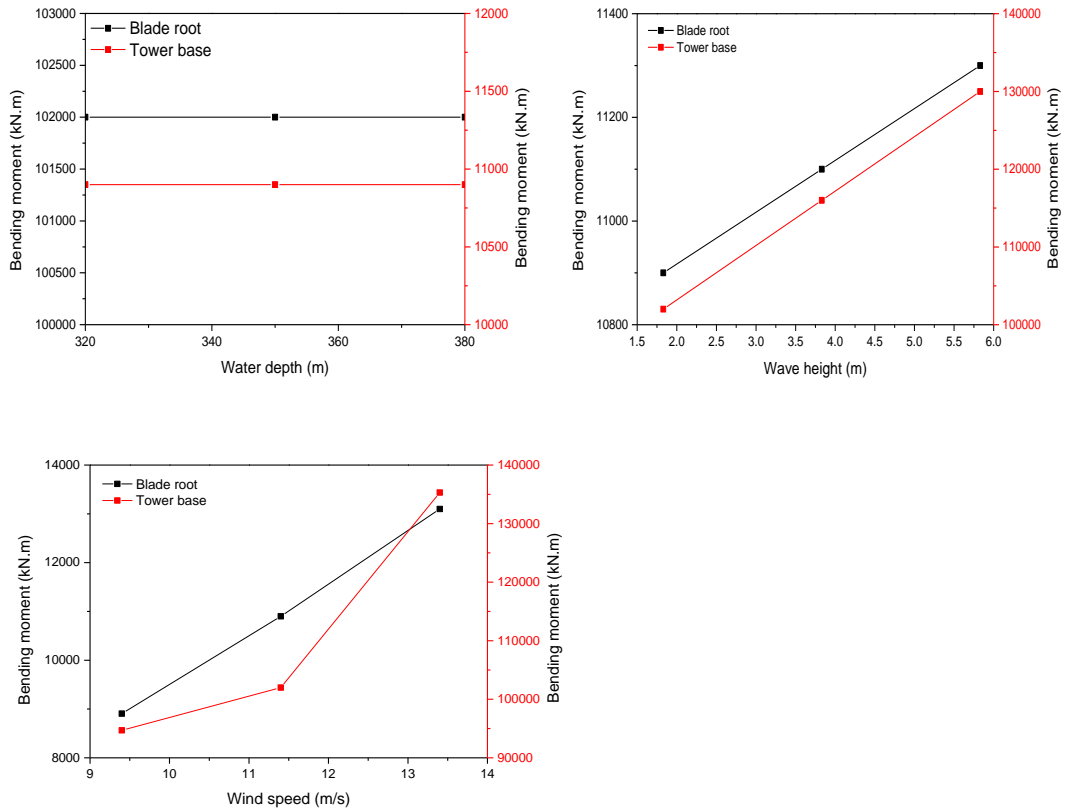
Figure 5.14 Compare the bending moment at the tower base and blade root

5.9 Conclusion

FOWT includes six DOFs motion, namely, heavy, sway, surge, yaw, pitch and roll. These translation and rotational motions will have a big influence on the unsteady aerodynamic performance of the rotor. The turbulence phenomenon can be described as normal working state (NWS), turbulent wake state (TWS), vortex ring state (VBS), and windmill braking state (WBS). Jonkman from NREL developed an open code simulation tool called FAST which is capable of modelling the dynamics and performance of a wind turbine. Aerodynamic loads are computed by the AeroDyn subroutines which was consist of two modes: Blade Element Momentum (BEM) and Generalize Dynamic Wake (GDW). BEM theory is to calculate how much kinetic energy can be absorbed by wind turbine. And then divide rotor blade into many small sections to calculate the force and moment. GDW method is to solve Laplace's equation applying a potential flow solution. For applying it into the FOWT, HydroDyn module was added. This module is used in connection with the WAMIT.

NREL gives the detail design of 5MW FOWT using spar platforms and tension leg platforms (TLP). Three different wind and sea conditions (below-rated, rated and severe condition) were chosen. Seen from the results, surge and pitch DOFs appear to be the largest amplitude modes. Others are very small, even close to zero. Moreover, the platform motion of TLP is significantly smaller than that of spar platform. Comparing the bending moment at the tower base and blade root, the change in the wave height and wind speed will affect the bending moments of blade roots and tower base.

This chapter got the platform motions and aerodynamic performance of two types FOWT by FAST which will be used as the input values in the CFD simulation.

6. DETECT AERODYNAMIC PERFORMANCE OF NREL PHASE VI WIND TURBINE

In order to prove the accuracy of the CFD method, the NREL Phase VI wind turbine was chosen to compare with the experimental results. The NREL Phase VI Unsteady Aerodynamic Experiment (Simms, 2001; Hand, 2001) provides an excellent validation test case for 3D CFD Rotor analyses. The commercial software Star CCM+ was chosen to conduct simulations.

6.1   Geometry and Mesh

The Phase VI test campaign performed in the NASA Ames National Full- Scale Aerodynamic Complex (NFAC) was completed in the year 2000. The 2-bladed, 10.058m diameter, stall regulated turbine has a power rating of 20kW. The technical data for NREL Phase VI wind turbine can be shown in Appendix C. Figure 6.1 describes the blade model in STAR CCM+.
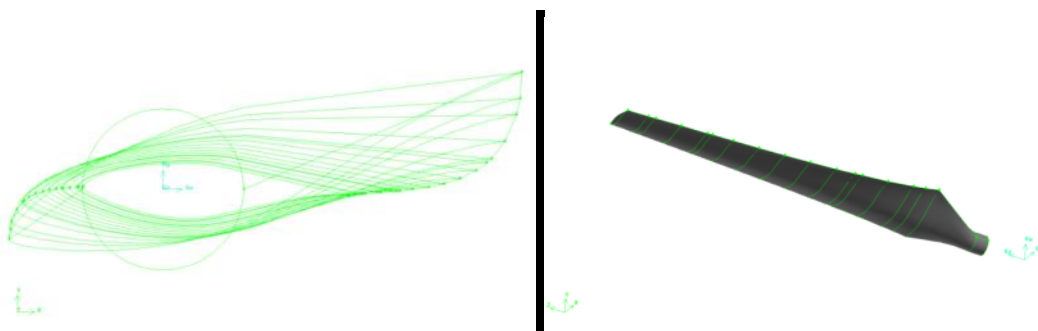

Figure 6.1 Blade Geometry

Chapter 4 described 2D computations on the S809 airfoil in order to define the most suitable models to be used, especially the turbulence model. The turbulence model has a significant effect on numerical solution as the stall-regulated wind turbine has large separation areas. Benjanirat (2003) presented some examples of the influence of turbulence modelling. According to the 2D results in Chapter 4, S-A and k-w turbulence model can get better results compared with k-e turbulence model. As S-A model is a one-equation model, k-w turbulence model is chosen to solve complex 3D problem. K-w SST turbulence model is good for adverse pressure gradients and separating flow. Therefore, this paper use k-w SST turbulence model to simulate.

The trailing edge of S809 blade airfoil is very sharp and results in poor structure mesh near the trailing edge. So the very sharp trailing edge was rounded through a radius of 0.001 m. Such modification should not have a considerable effect on the numerical results since even experimentally it is not possible to generate a blade with a very sharp training edge. The mesh was generated using the Star CCM+ mesh generator. The total unstructured grid was 20 million and there were about 18 million grids around the blades. The detailed mesh around the blade can be seen in Figure 6.3. The thickness of the first cell to the wall was kept at $2*10^{-5}$ m so that the y^{+} value can be kept around 1. Such y^{+} is suitable for the low Reynolds number k–w SST turbulence model. The computational domain is a cylinder with a diameter 5 times of the blade length (5D), upwind length is 5.5D and downwind length is 15D. The inlet and outlet are defined as velocity inlet and pressure outlet, respectively (see Figure 6.2).
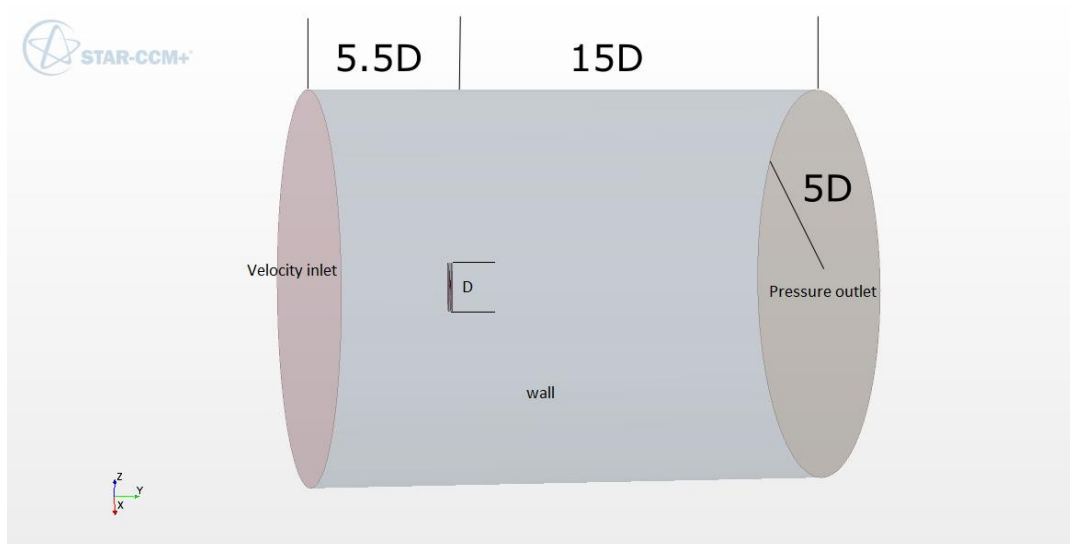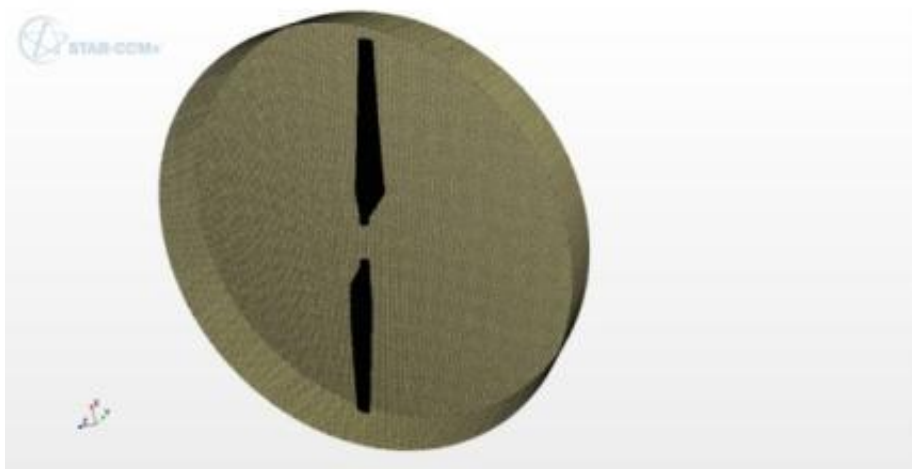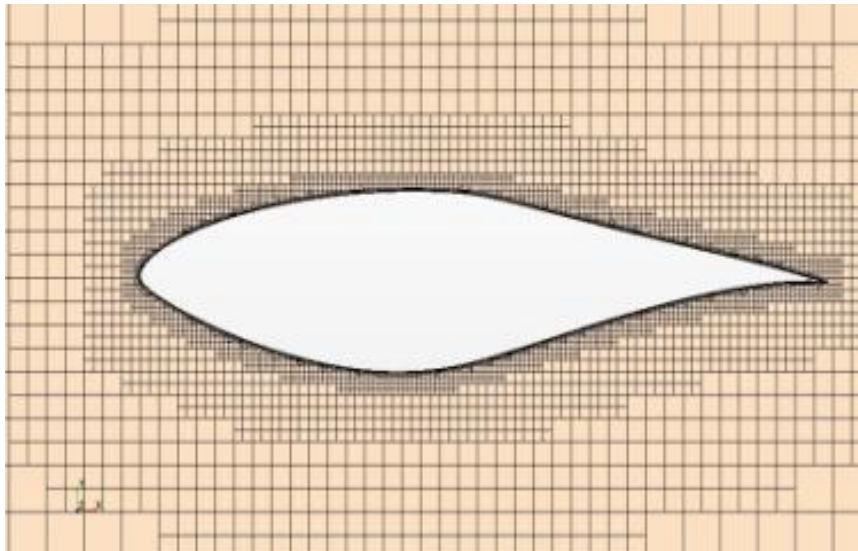

Figure 6.2 Boundary conditions

Figure 6.3 Blade surface mesh

6.2   Simulation Conditions

Computations are conducted of 5 wind speed (5, 7, 10, 13 and 15 m/s) at a fixed blade pitch angle of 3 with constant rotational speed 72 RPM using unsteady Reynolds-Averaged Navier-Stokes (RANS) turbulence models (show as table 6.3). It used two CFD models: one blade symmetry model and two blades whole model. There are two methods describing the wind turbine rotation, Reference Frame Method (REM) and Rigid Body Motion Method. Four different flow cases with different wind speeds and wind yaw angles are investigated: 7m/s with 30° yaw, 7m/s with 60° yaw, 10m/s with 30° yaw and 10m/s with 60° yaw.

Table 6.1 Operating conditions

Wind speed (m/s)	Rotor speed (RPM)	Density (kg/m^3)	Pitch angle (degree)
5	71.69	1.243	2.988
7	71.87	1.246	2.988
10	72.10	1.246	2.988
13	72.09	1.227	2.979
15	72.06	1.224	2.981

6.3   Results and Discussion

6.3.1   Compare Reference Frame Model (RFM) with Rigid Body Motion

RFM neglecting the unsteady inflow, which is a fair choice considering that the experimental data set is arrived statistically from a large number of repeated measurements. However, rigid body motion method described the unsteady phenomena more like a real wind turbine condition. Figure 6.3 shows the results of the power and thrust versus wind speed using these two methods compared with experiment. Mechanical power P is calculated by monitoring the moment M about the flow axis and multiplying with the angular velocity Ω: $P=M\Omega$.

As the figure shows, for wind speeds between 7 and 10m/s, steady computations are performed more close to the experimental results (Hand, 2001) while the results are not as good at high wind speeds. Nevertheless, the overall trend of the curve is correctly predicted. This lack of accuracy in computations for higher speeds can be analysed as the computed flow field is unsteady for wind speeds beyond 10 m/s. This

unsteadiness is not forced by the rotor motions, as if the yaw angle or wind speed fluctuations were not equal to zero, but is only due to aerodynamic phenomena. The large separations are the cause of this unsteadiness. Therefore, time-accurate computations are performed for higher wind speeds. Overall, rigid body motion results compare well with experimental results at all wind velocities. The largest difference of power is shown at 10m/s, where an over-prediction around 18% is observed. However, the thrust had a bigger difference which can reach over 20% at 13m/s.
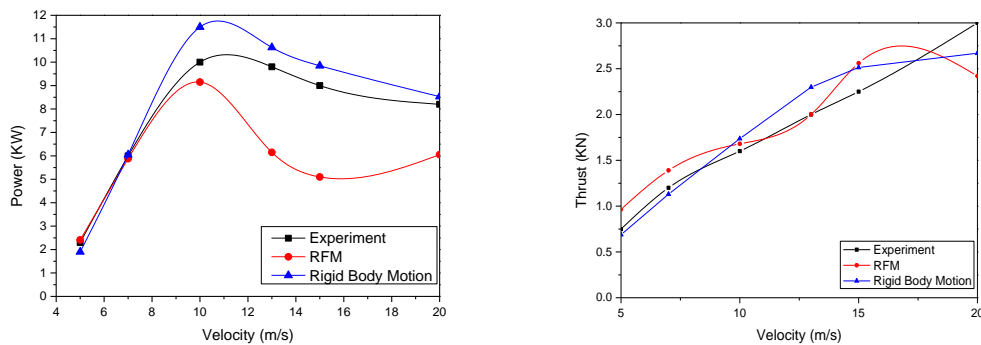

Figure 6.4 Power and thrust curves compared with RFM and Rigid body motion

6.3.2   Compared with symmetry method

When yaw cases were not considered, a single blade by imposing the periodic condition to account for the other blade can be applied. Figure 6.4 and 6.5 described the boundary conditions in detail. One-blade model will save nodes and CPU time as shown in Table 6.4. According to Figure 6.6, power and thrust CFD results both have a good agreement with experiment. Compared the power results with these two boundary conditions, there is no obvious difference. However, the thrust results showed a big discrepancy especially at higher wind speed, where can reach over 30% at 10m/s. Whole boundary condition showed a better results.
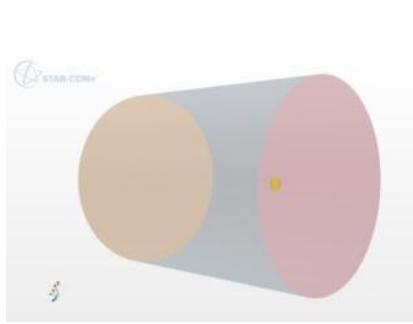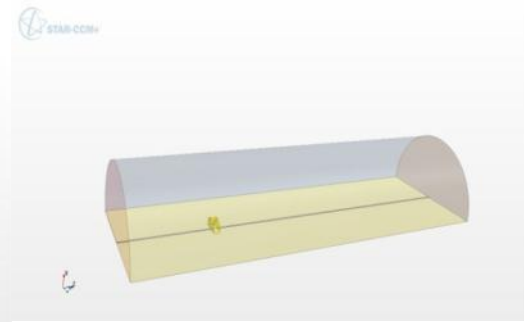
Figure 6.5 whole boundary condition   Figure 6.6 symmetry boundary condition

Table 6.2 Simulation procedures compare

	Nodes	CPU Time (32 cores)
ONE-Blade Model	2722248	8 hours
TWO-Blade Model	6055541	20 hours
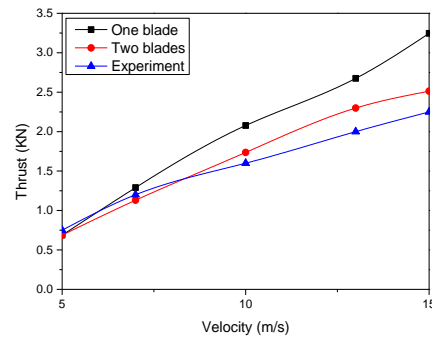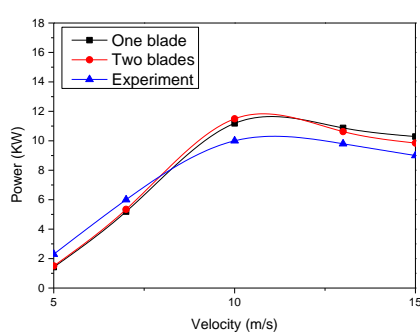
Figure 6.7 Power and thrust curves compared with two boundary conditions

6.3.3   Comparison of span wise sectional details

The experiment pressure measurements are available at five span-wise sections 30%, 46.7%, 63.3%, 80% and 95% r/R. Therefore, the CFD simulation chose these 5 span-wise sections to have a comparison.

Figure 6.11-6.14 show the chord-wise pressure coefficient distributions at different span-wise sections of the blade at 5m/s, 7m/s, 10m/s and 13m/s. The pressure coefficient is calculated using: $Cp = (P - P_\infty)/(\frac{1}{2}\rho_\infty[U_\infty^2 + (\Omega r)^2]$. As RANS turbulence models cannot solve separated flow accurately. Therefore, some deviations between CFD simulation and experimental results are observed.

At 5m/s and 7m/s wind speed, the flow is mostly attached and is in good agreement with the measured pressure distribution except up to 30% span, where flow is separated.

At 10 m/s wind speed, as flow separation close to mid-span and resulting localized transient stall effects making the peak suction pressure practically difficult to capture in the experiments, a discrepancy in pressure near the leading edge of suction surface (Peak suction pressure) is observed at 46.7 % span.

At 13 m/s, there is a discrepancy between the computed and experimental pressure coefficient distributions in the suction surface of the inboard span of 30%. This is due to the large separation and strong vortices, which occurred at this speed and especially in this section. So it becomes difficult for the turbulence model to capture the separation.
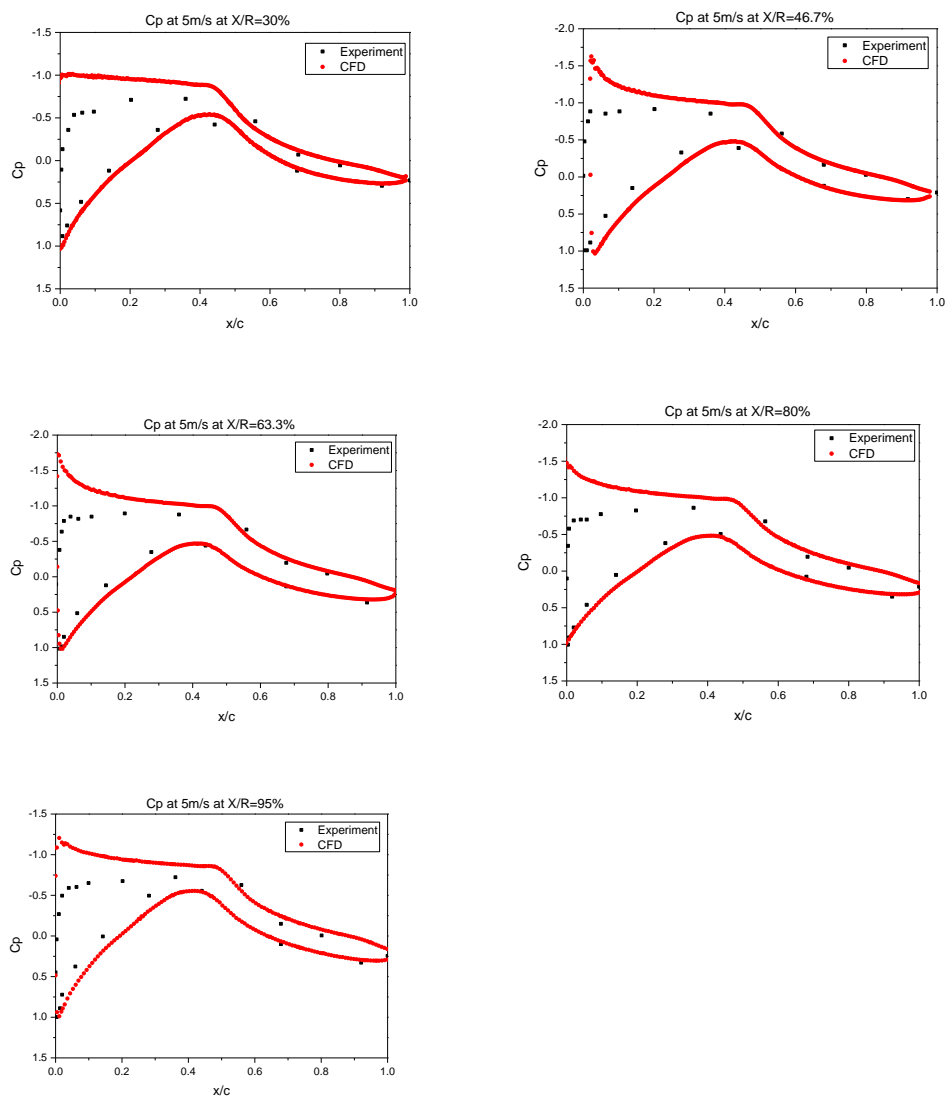

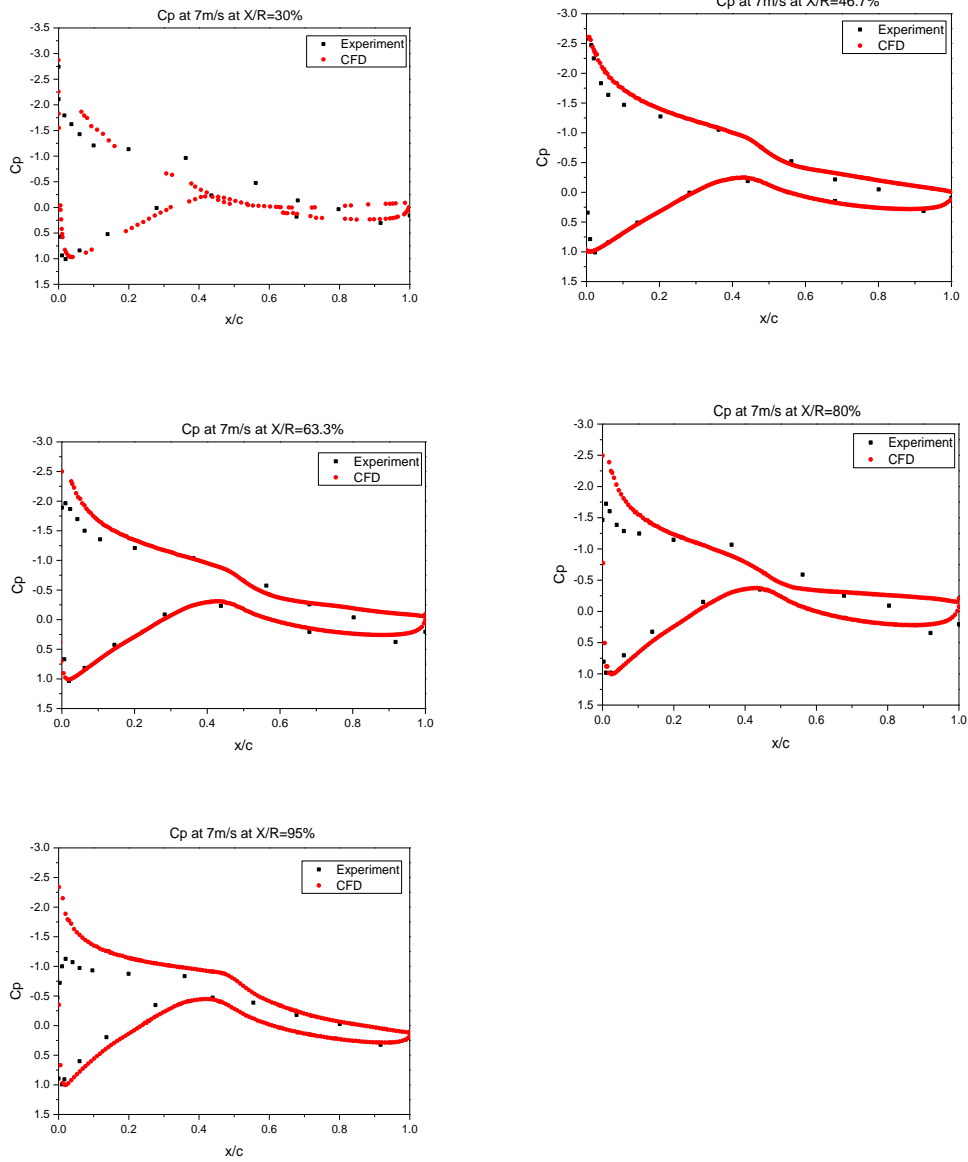Figure 6.8 Comparison of CFD and measured pressure distribution at 5m/s wind speed

Figure 6.9 Comparison of CFD and measured pressure distribution at 7m/s wind speed
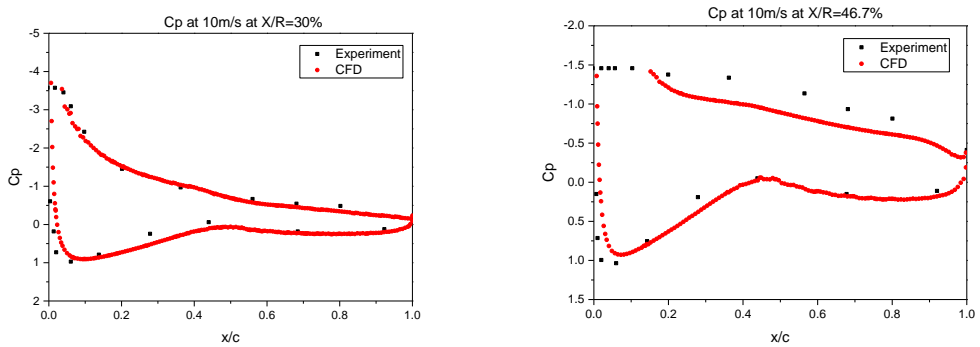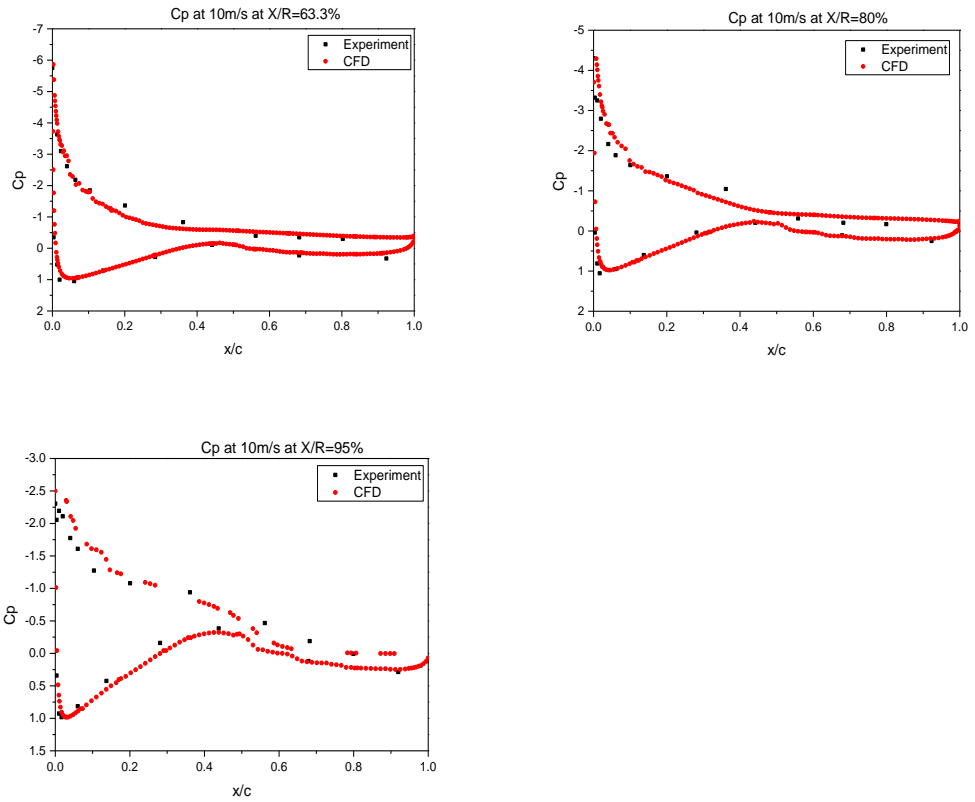
Figure 6.10 Comparison of CFD and measured pressure distribution at 10m/s wind speed
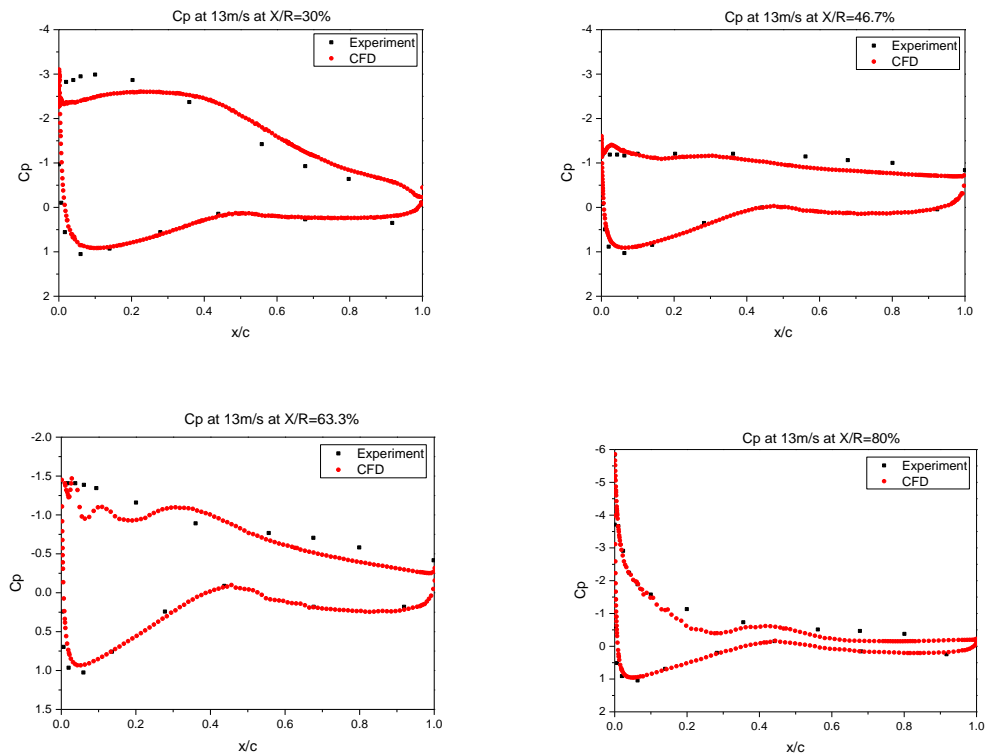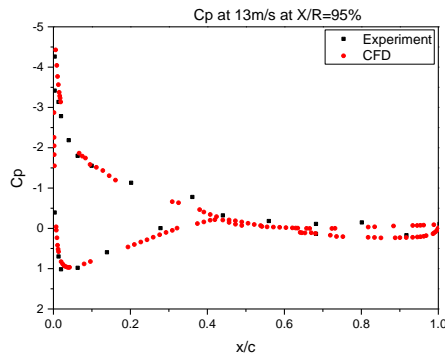
Figure 6.11 Comparison of CFD and measured pressure distribution at 13m/s wind speed

6.3.4 Comparison with other CFD predictions

Figure 6.15 showed a comparison with different CFD predictions. CFX and GRI (Acusolve) results are from the reference (Mukesh, 2013). Note that the Risoe (Ellipsys 3D) predictions are for fully turbulent flow conditions (Sorensen, 2002; Johansen, 2002).
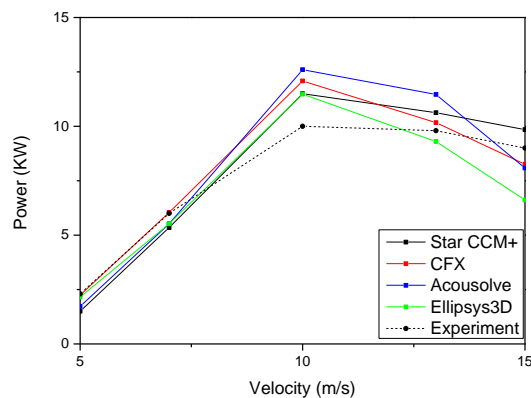
Figure 6.12 Power curve with different CFD methods

6.3.5 Compared with different fixed yaw angles (skewed flow)

In the present study, the calculations were made for the wind speeds of 7 and 10 m/s at the yaw angles of 30° and 60° to describe the skewed flow phenomena. Figure 6.16 showed the solid modelling of the NREL phase VI rotor configuration and definitions of coordinate system, rotor azimuthal position and yawed wind velocity direction. The blade at 12 o'clock position (azimuth angle = 0 deg) is designated as Blade 2, and the Blade 1 is at 6 o'clock position. Wind speed in the positive y-direction with different yaw angles has been considered for the test computations as

seen in Figure 6.17. The results are compared with available experimental data which as shown in Table 6.4 for the validation of the present method. To study the dynamic nature of the rotor behaviours at yaw, the detailed flow physics are also analysed. Schreck and Robinson (2000) analysed the blade surface pressure and local inflow data from the NREL unsteady aerodynamics experiment to characterize the dynamic stall vortex generated on the blade during yawed operations. The wind speed and turbine yaw angle will change the vortical flow field. Leishman presented the challenges in modelling the unsteady aerodynamics of wind turbines, and the significance and modelling of dynamic stall for the wind turbines.

Comparison of the power at different yaw angles has been shown in figure 6.18. When the yaw angle increased, the aerodynamic loadings are significant reduced as expected. Because of the wind component, aligned tangent to the rotor disk plane, the local angle of attack at the blade sections changes periodically, resulting in low magnitudes at the advancing blade and high magnitudes at the retreating blade.

Table 6.3 NREL Phase Vi experiment cases (Hand, 2001)

TEST	WIND SPEED	YAW ANGLE
Upwind baseline case	7m/s (pre-stall), 10m/s (onset of stall), 15m/s (post stall)	-30,0,30,60 degrees
Wake flow visualization	5,7,10,15m/s	0,-10,-30,-60 degrees
Sweep wind speed case	5 to 25 m/s 25 to 5 m/s	0 degrees
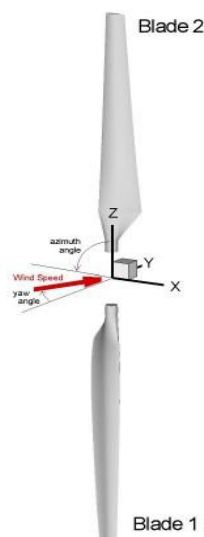
Figure 6.13 Two blade wind turbine rotor (Nilay, 2006)
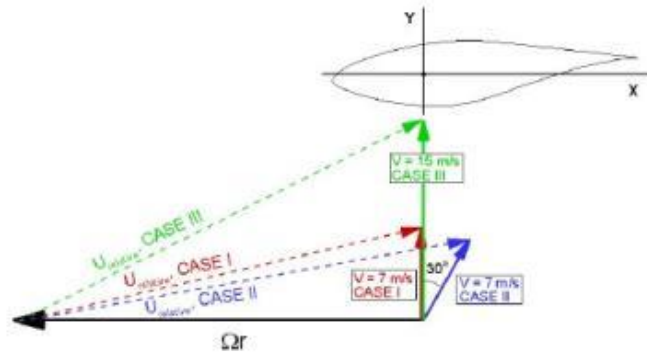
Figure 6.14 Velocity vectors for the wind (Nilay, 2006)
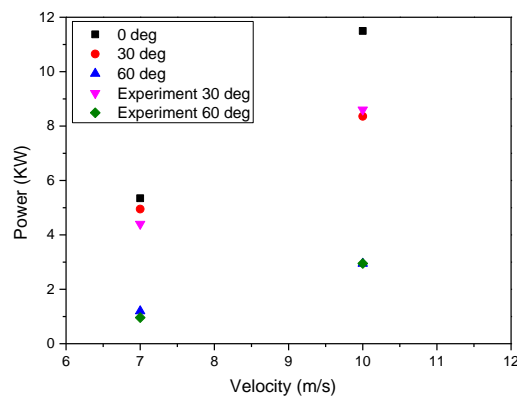
Figure 6.15 Power compared with different yaw angles

Figure 6.19 and 6.20 predicted chord-wise distributions of the surface pressure coefficient at 30° and 60° yaw angles at a wind speed of 7 m/sec. The results compared with the experiment at five radial locations along the blade. In the case of 30° yaw angle, the present results are in good agreement with the measurement at all radial locations, except the root of the blade which had a big difference. When the yaw angle of the rotor is increased to 60°, the pressure distributions are noticeably changed, resulting in a significant reduction of the leading-edge suction peak and also of the blade loading, as estimated from the pressure difference between the blade's upper and lower surfaces. Figure 6.21 showed this phenomenon clearly by comparing with different yaw angles. This is because the angle of attack at the blade sections is decreased because of the reduction in the wind velocity component perpendicular to the rotor disk plane. The highest differences between the averaged

Cp distributions and experiments are observed for the 60° yaw case. This occurs due to the cyclic unsteady variation of blade surface pressure as the blade rotates.

To understand the unsteady aerodynamic loading behaviour better, Figure 6.22 showed the pressure streamlines around the blade at different yaw angles. It is shown that the streamline are fairly smooth and well-behaved over the blade, indicating that the flow is mostly attached to the blade surface. The tangential wind velocity component is aligned parallel to the blade chord, and thus, the local inflow angles of the attack at the rotor blade sections are directly influenced. It is observed that the flow transition on the blade suction surface occurs near the mid-chord, along most of the span, for all azimuthal positions. This is because the inflow condition at the blade sections does not change much along the span, as indicated by the streamline traces and the pressure distributions.

Next, the simulations were turn to an increased wind speed of 10 m/sec for the yaw angles of 30° and 60°. The flow stalls at the inboard portion, accompanying leading-edge flow separation and rotating vortical flow structure. Figure 6.23 and 6.24 compared the chordwise distributions of the pressure coefficient with the measurement. It is shown that the present results agree well with the measurement even at this increased wind speed, although the pressure at the suction side of the innermost blade section is slightly over-predicted near the leading edge. Similar to the 7 m/sec wind speed case, the increment of yaw angle leads to a significant reduction of the leading-edge suction pressure peak at all radial locations. In Figure 6.25, the flow characteristics around the blade was shown a deviation at different yaw angles. At 0° yaw angle, the flow separates from the leading edge. However, when the yaw angle increased, the flow remains mostly attached.
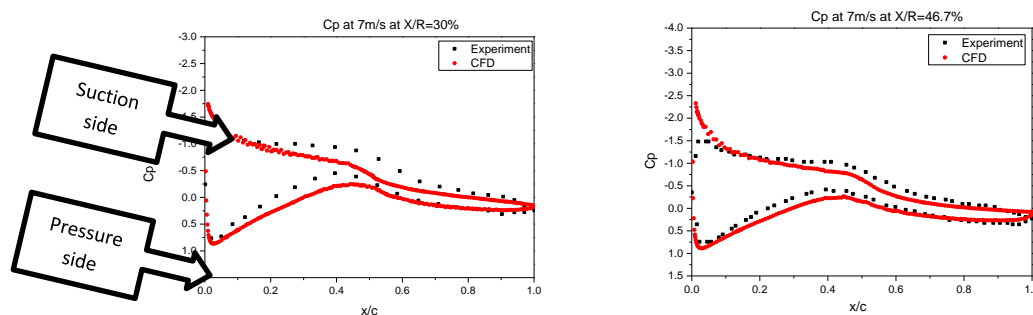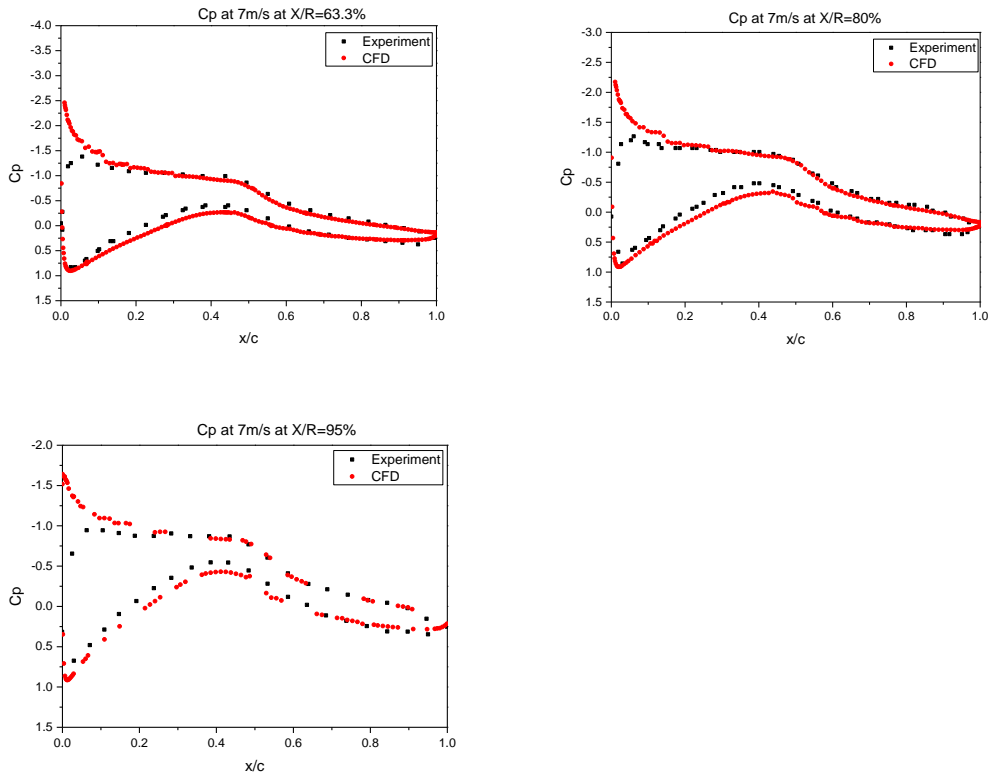
Figure 6.16 Pressure coefficients at different spanwise sections at 7m/s at 30° yaw angle
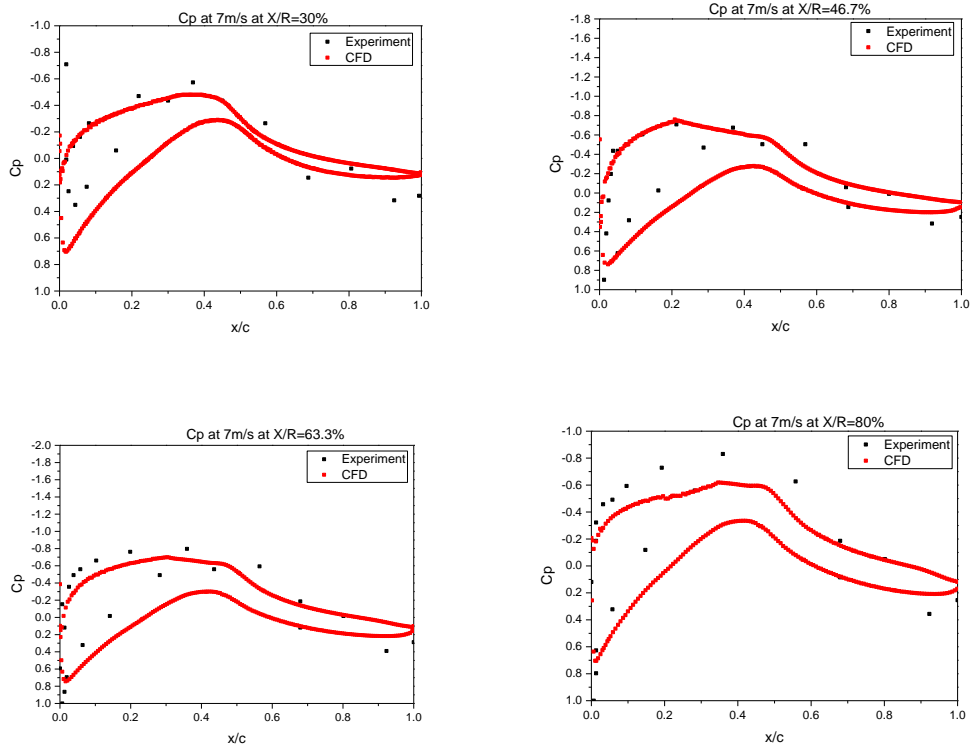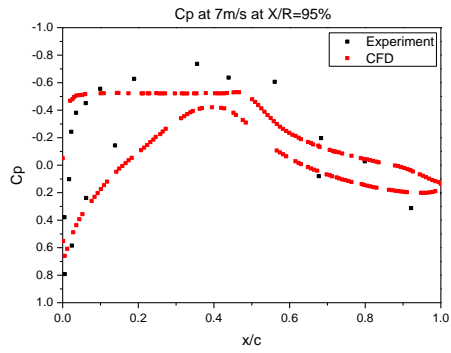
Figure 6.17 Pressure coefficients at different spanwise sections at 7m/s at 60° yaw angle
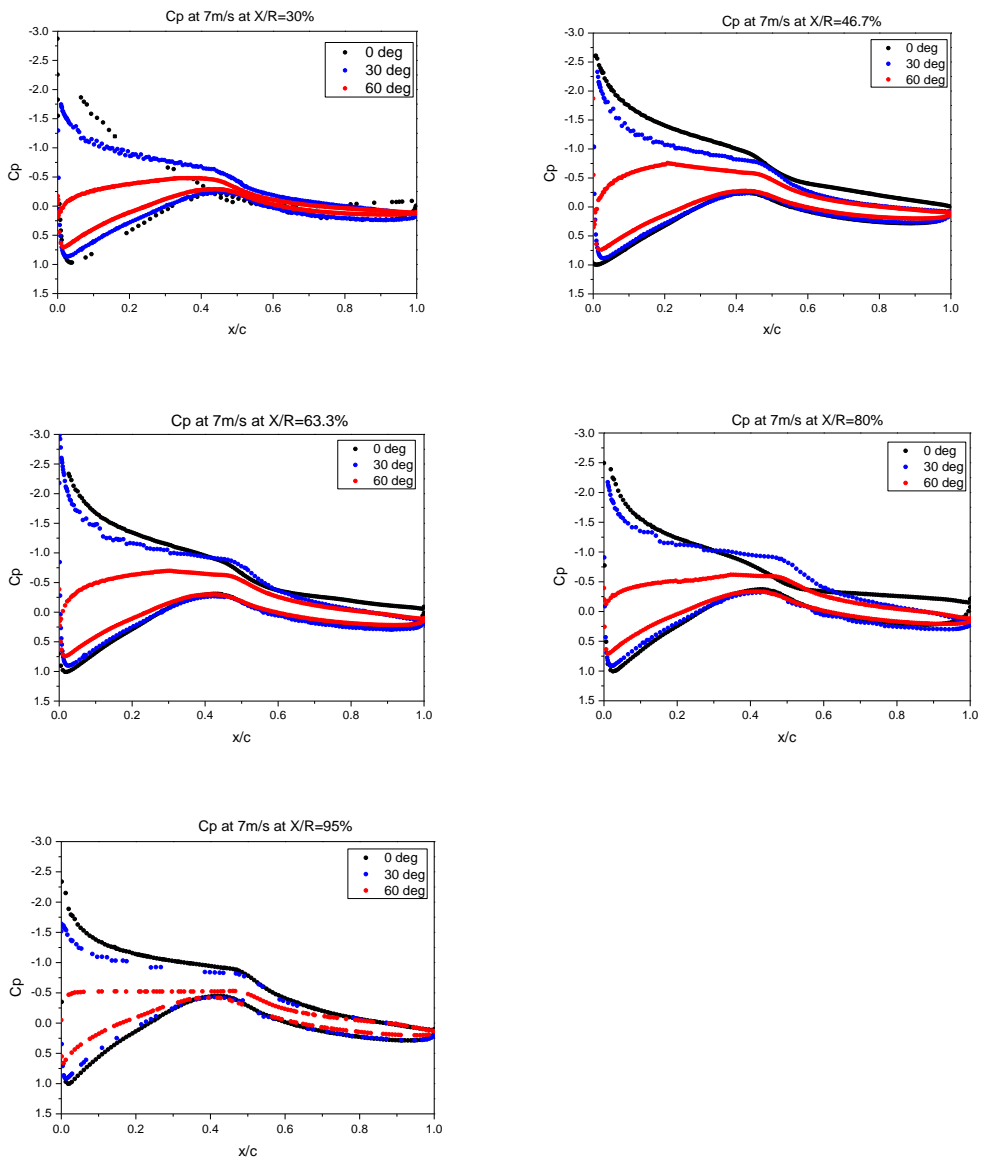
Figure 6.18 Pressure coefficients at different spanwise sections at 7m/s
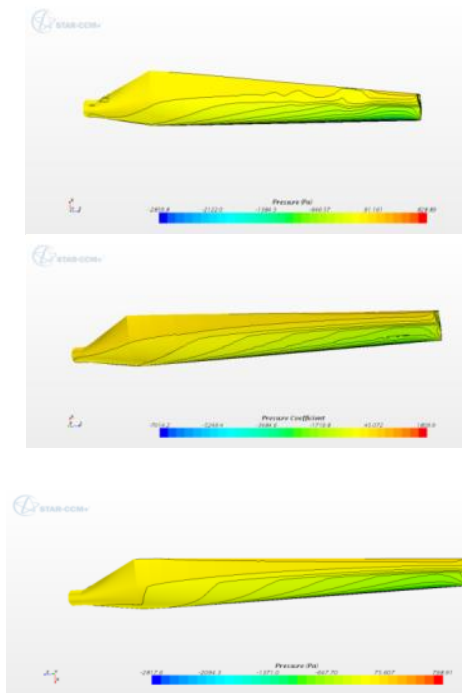
Figure 6.19 Pressure streamlines at 7m/s at 0°, 30°, 60° yaw angle
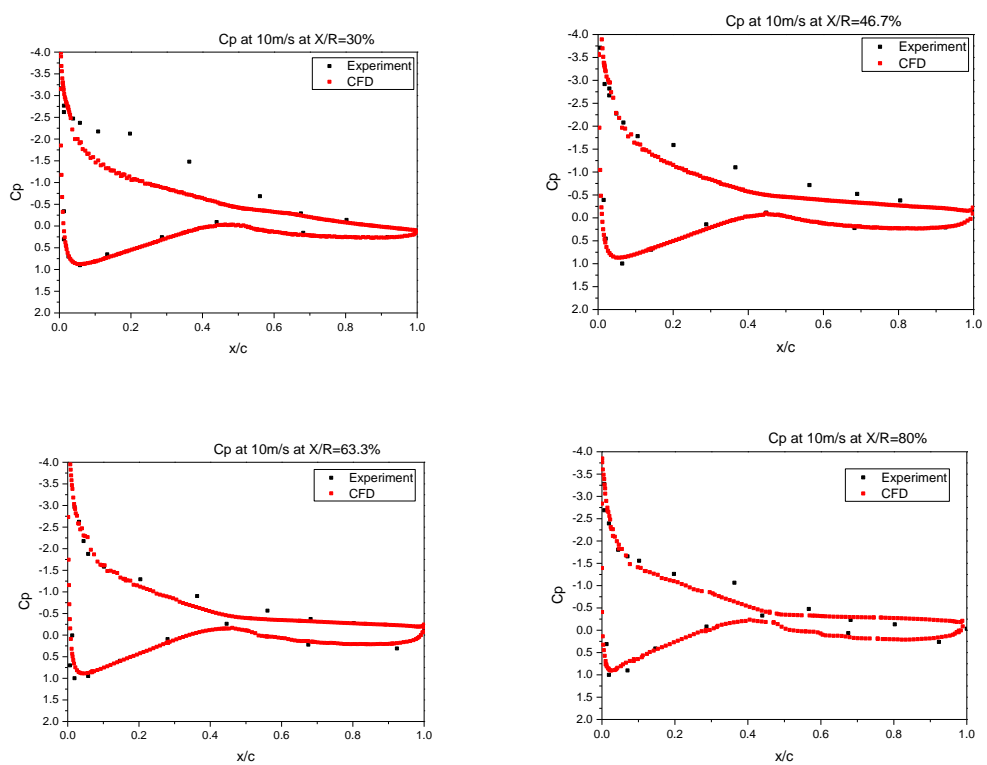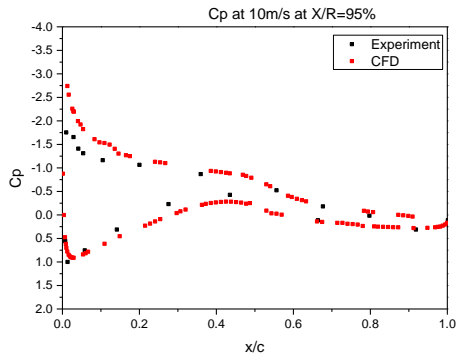
Figure 6.20 Pressure coefficients at different spanwise sections at 10m/s at 30° yaw angle
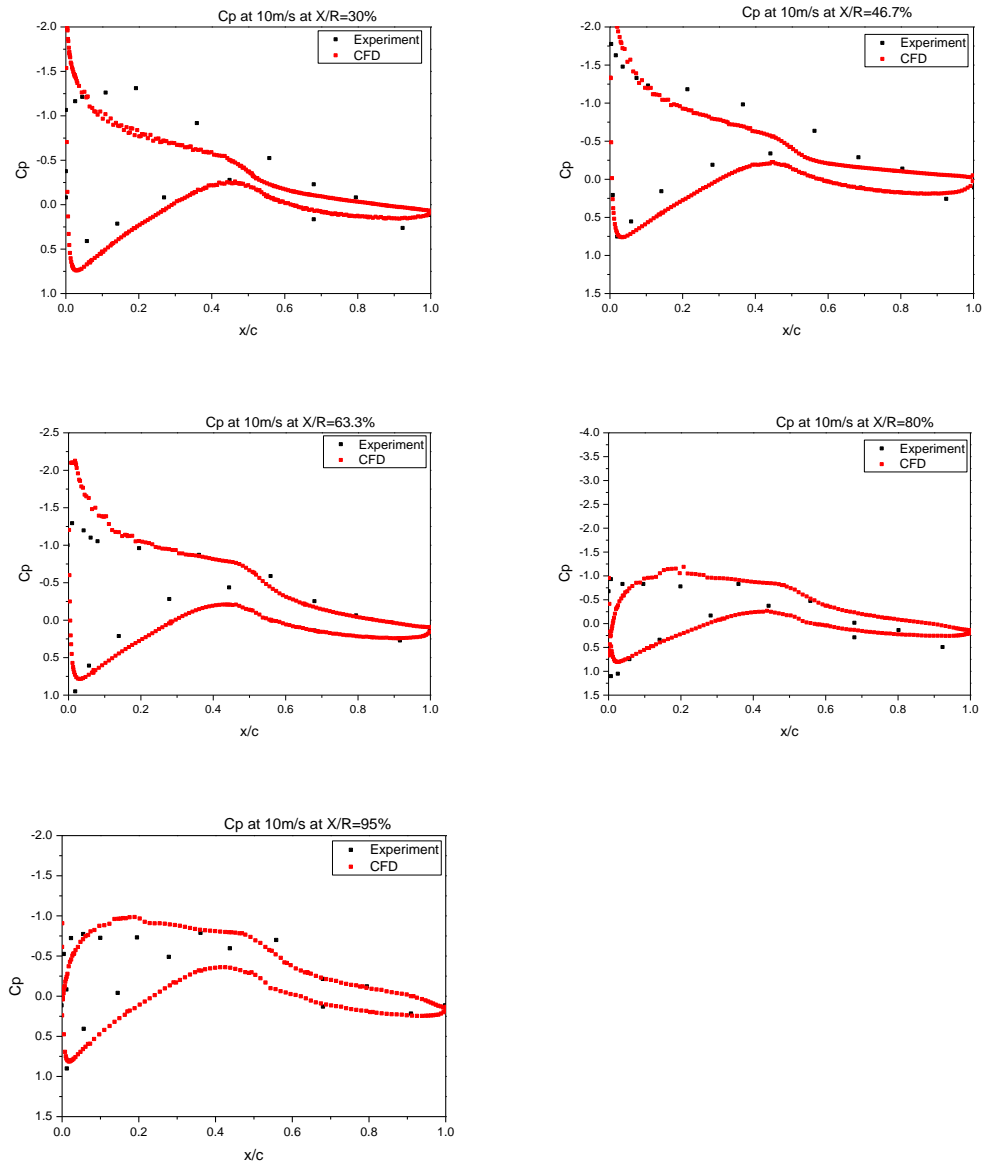
Figure 6.21 Pressure coefficients at different spanwise sections at 10m/s at 60° yaw angle
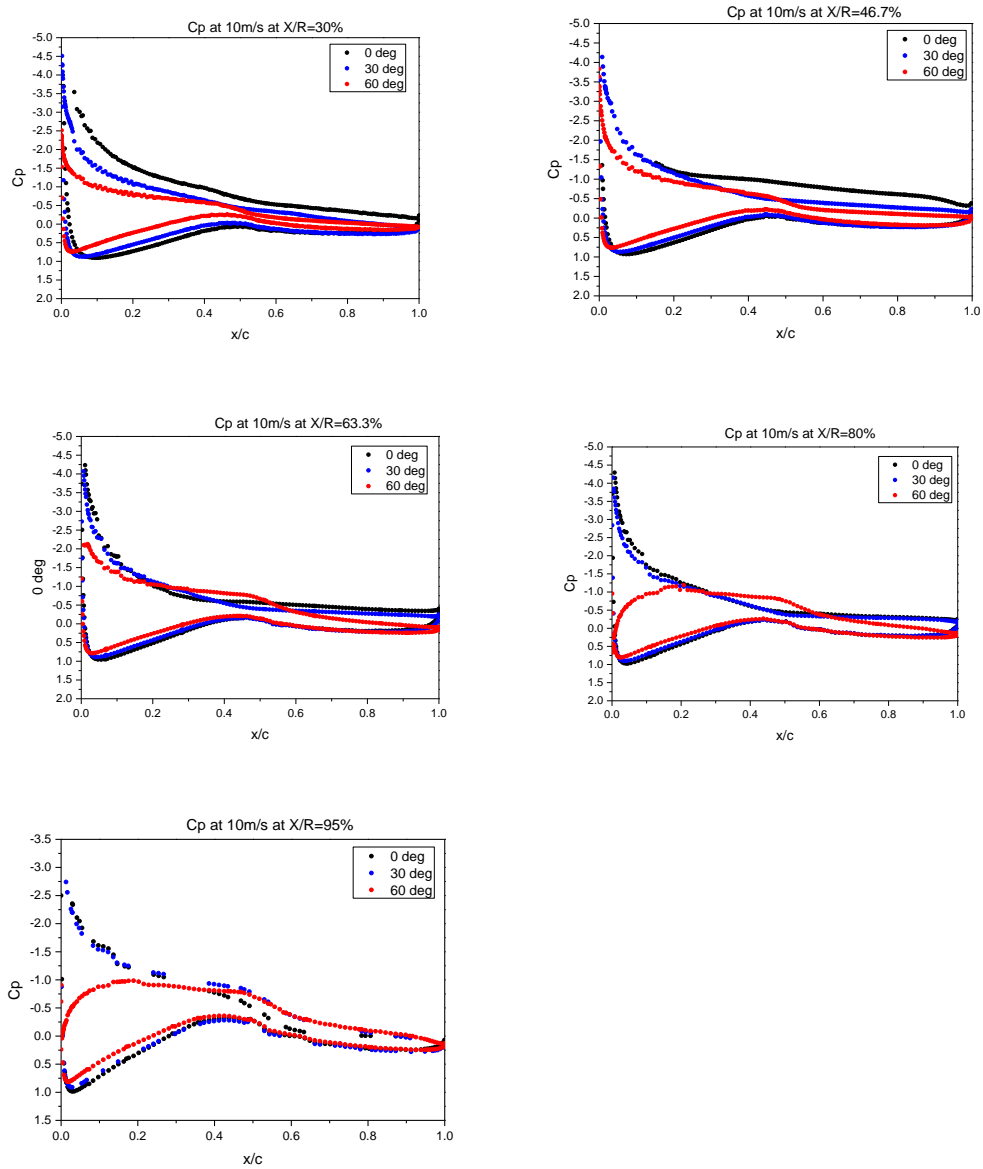
Figure 6.22 Pressure coefficients at different spanwise sections at 10m/s
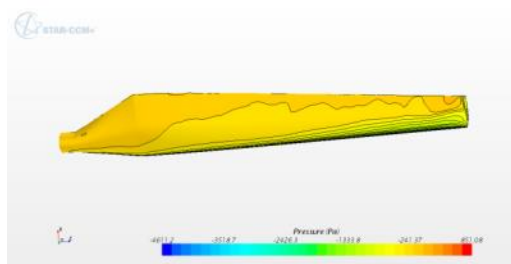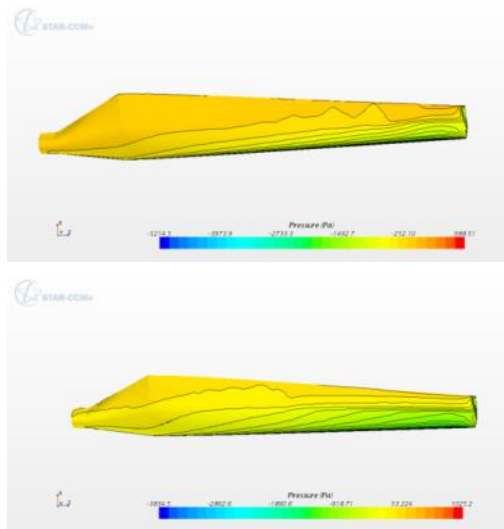
Figure 6.23 Pressure streamlines at 10m/s at 0°, 30°, 60° yaw angle

6.4   Conclusion

This chapter calculated the aerodynamic performance of NREL phase Vi in order to confirm the accuracy of CFD method. Computations carried out with five different wind speeds (5, 7, 10, 13 and 15 m/s) at a fixed blade pitch angle of 3 with constant rotational speed 72 RPM. Reference Frame Method (RFM) and Rigid Body Motion Method were applied to describe the wind turbine rotation in the STAR CCM+. At small wind speeds, steady computations are performed more close to the experimental results. However, the results are not as good as at high wind speeds. Overall, rigid body motion results compare well at all wind speeds.

Two CFD models are applied: one blade symmetry model and two blades whole model. There is no obvious difference of power compared with these two models. However, the thrust results showed a big difference especially at high wind speeds. In general, whole boundary condition showed better results. Therefore, rigid body motion method and whole boundary condition are better simulation models.

Different fixed yaw angles are simulated to describe the skewed flow phenomena. Detailed flow physics are analysed. Chord wise distributions of the surface pressure coefficient compared with different yaw angles. When the angle increased, the pressure distributions are changed.

Overall, CFD method can predict aerodynamic performance of wind turbine accurately.

7. AERODYNAMIC PERFORMANCE OF NREL 5MW WIND TURBINE USING CFD METHOD

This simulation was used commercial software STAR CCM+. It was developed by CD-Adapco, Inc. The three dimensional, unsteady Reynolds-averaged Navier-Stokes equations with k-ω SST turbulence model were executed in the STAR CCM+ software package. This commercial code that was based on a finite volume approach allows researchers to perform fluid dynamic formulations, solutions algorithms, meshing schemes and post-processing.

7.1 Numerical Modelling

The following section will provide details of the numerical simulation approaches used in this study and will discuss the numerical methods applied to the current CFD model.

7.1.1 Physics modelling

The RANS method uses a time-average formulation of the Navier-Stokes Equations to model turbulent flows in CFD. The occurring nonlinear Reynolds stress term requires the introduction of turbulence models (for example, two equation models such as k-ω) to close the RANS equations. The turbulence model selected in this study was k-w SST.

In the fluid domain, STAR-CCM+ offers a comprehensive range of efficient solvers for flow regimes. The segregated solver is ideally suited for incompressible and weakly compressible flows, but also performs well into the supersonic regime. The coupled algorithm yields robust and accurate solutions in compressible flow, particularly in the presence of shocks, and is the solver of choice for high-Rayleigh number natural convection. Coupled explicit is particularly suited for high speed, short timescale, transient compressible flows. (STAR CCM+ user's guide) Coupled flow needs more resources like memory and computational time as it solves coupled equations for pressure and velocities. Therefore, segregated flow is a good choice for most cases, as well as for this case.

All current simulations employed a semi-implicit method to solve the pressure-linked equation (SIMPLE). A finite-volume based unstructured parallelized coupled algebraic multi-grid solver with a second order advection scheme. In unsteady simulation, a first-order central difference scheme was used for temporal discretization. To obtain the aerodynamic power and thrust of unsteady simulations of the wind turbine blade and function was adopted to extract the aerodynamic blade root load during the simulation of the pitch and surge motions of a wind turbine. A simple user field function was also created to define the simple pitch and surge of an offshore wind turbine platform. Rigid body motion was applied to define the real motion of a wind turbine blade under each specific motion using unsteady time-accurate simulations. The superposing motions technique was applied to define the sine function of complex motions of a platform.

7.1.2 Transition model

The transition model from laminar to turbulent flow is modelled using Langtry and Menter correlation based Gamma-Theta transition model.

Wiki Gamma-Re (y-Re) transition model is a two equation model used in Computational Fluid Dynamics (CFD) to modify turbulent transport equations to simulate laminar, laminar-to-turbulent and turbulence states in a fluid flow. The Gamma-Re model does not intend to model the physics of the problem but attempts to fit a wide range of experiments and transition methods into its formulation. The transition model calculated an intermittency factor that creates (or extinguishes) turbulence by slowly introducing turbulent production at the laminar-to-turbulent transition location.

Until recent, steady state solutions have been the standard solution in HAWT rotor CFD computations, but lately, the need for estimating rotor performance and especially rotor loads during operation in wind shear or in yaw has pushed. Transient computations with a full resolution of the boundary layer on the blades are very time consuming, however, and their use as real life design tools will probably remain limited for a while yet.

The transition model in some references (Niel, 2012; Lanzafame, 2013; Laursen, 2007) showed that it under-predicts lift forces for an airfoil section for angles of attack that are near the stall region due to early separation. So, I am interested in that if it is able to predict stall accurately for multi-element airfoils with any of the models in STAR CCM+.

7.1.3 Computational domain and boundary conditions

In this research work, the blade geometry was generated in gambit. The hub was not included in the geometry. As described above, the 5MW NREL wind turbine rotor blade has a radius of 63 meters and is composed of eight aerodynamic shapes including six airfoils and 2 cylinders with 13.3 degrees twist angle, as shown in Figure 7.1
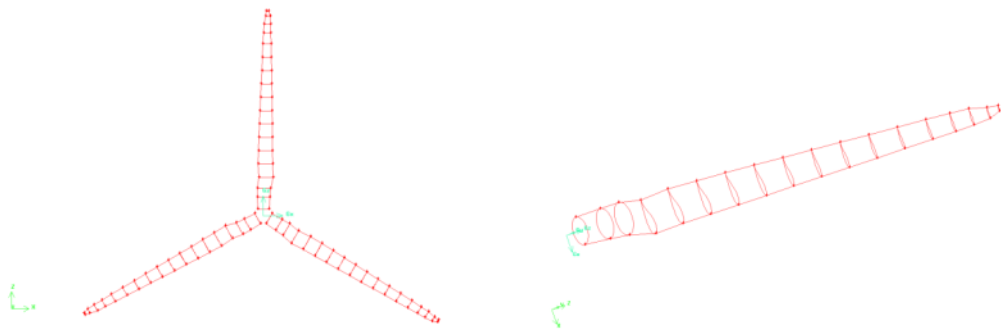
Figure 7.1 Wind turbine blade shape with sketch view

To model a 6-DOF prescribed motion, the CFD model contained a rotating region in the immediate vicinity of the blades, and a fixed region far away from the blades. The two regions interacted through a sliding boundary and the dynamic mesh capability in STAR CCM+. This was to ensure that the mesh in the rotor domain had almost no relative nodal displacement, as the mesh on the blade had first node on the order of microns to yield a $y^+=1$, where y^+ was a non-dimensional wall distance for wall bounded flow. The hexahedral computation domain was applied with dimension of 1291×630(Length × Diameter), and extends 5.5 and 15 times the rotor radius in the negative (upstream) and positive (downstream) x-direction, respectively, see as figure 7.2.
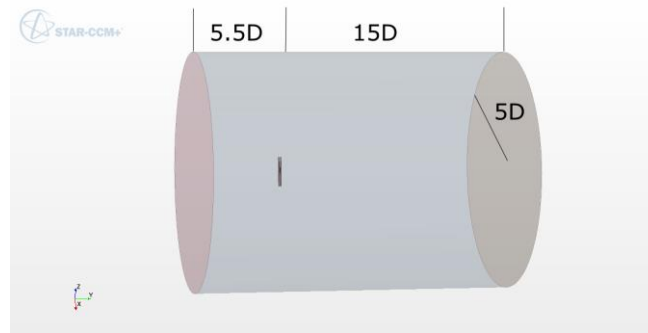
Figure 7.2 Calculation domain

7.1.4 Mesh generation

The mesh methods of all regions were prism layer, surface remesher, and trimmer. For blade surface, a refine grid was generated at the leading edge with a maximum and minimum grid size. C-grid type mesh was created in the blade domains. Figure 7.3 shows computational meshes for the upwind three-bladed turbines, which illustrate the grid density around the rotor and steady regions. The blade surface mesh resolution near the tip region is shown in Figure 7.4.
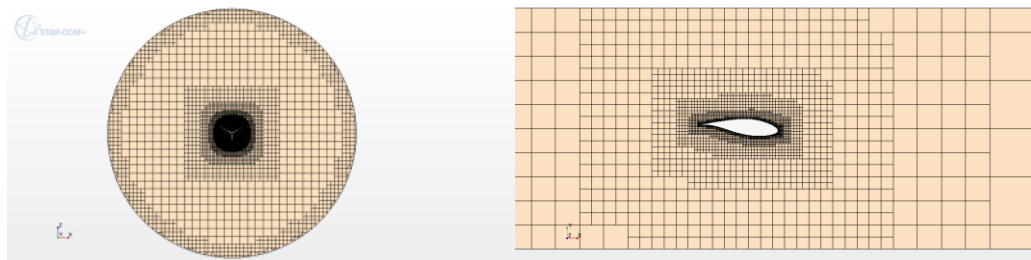
Figure 7.3 Volume mesh

Figure 7.4 Blade surface grids in the tip region

7.2   Post- processing Formulations

7.2.1   Wind turbine physics

Forces and moments

The available energy in the wind for a given cross section normal to the wind direction is $P = \frac{1}{2}\rho U_\infty^2 A$.

The lift force on a wind turbine blade is defined to be perpendicular to the incoming wind, U_{rel} in figure 7.5. This force is a consequence of the pressure difference on the upper and lower side of the airfoil.

$$dF_L = \frac{1}{2}\rho C_l(\alpha)cU_{rel}^2 dr \tag{7.9}$$

The drag force is defined to be parallel to the incoming flow U_{rel}. The cause of this force is both viscous friction at the surface and unequal pressure on the airfoil surfaces facing away from and towards the incoming flow.

$$dF_D = \frac{1}{2}\rho C_d(\alpha)cU_{rel}^2 dr \tag{7.10}$$
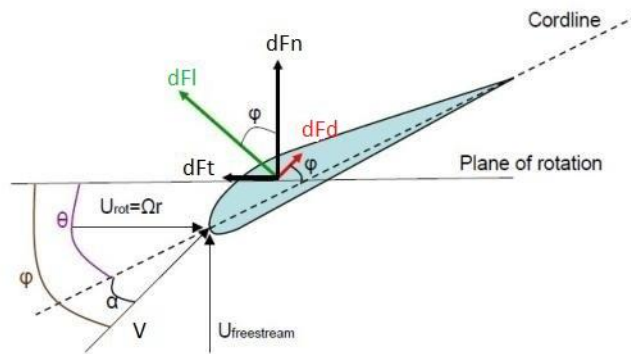
Figure 7.5 Forces on the blade geometry of a horizontal axis wind turbine (Kari, 2011)

The lift and drag coefficients, C_l and C_d, are dependent on the angle of attack and are known for a given blade profile. Torque and thrust forces a wind turbine experience are dependent on the lift and drag forces. A simplified explanation of these components is that the lift force contributes to increasing the power production while the drag force has the opposite effect.

Power and thrust coefficient

The blades on a wind turbine are rotating due to the incoming wind. This creates a torque on the horizontal axis which is converted to electrical energy by the use of a generator. It is impossible to extract all the available power from the wind. Limitations in the physics behind the turbine as well as mechanical losses contribute to lowering the efficiency. A parameter that explains how well a wind turbine can extract power from the wind is the power coefficient, C_P. This is defined as the ratio between produced and available power.

$$C_P = \frac{Rotor\ power}{Power\ in\ the\ wind} = \frac{P}{\frac{1}{2}\rho U_\infty^3 A} \tag{7.11}$$

Modern wind turbines have a power coefficient of around 50%. This is close to the maximum C_P that a wind turbine can achieve: $C_{Pmax} = 16/27 = 59.26\%$. This is known as the Betz limit.

In addition to the torque created by the wind, there is also a force in the streamwise direction induced by the pressure drop over the rotor. This causes fatigue loads on the turbine, and therefore the construction must be built so it can withstand these forces. The thrust coefficient is defined as the relation between the thrust force on the turbine and the dynamic force in the wind.

$$C_T = \frac{Thrust\ force}{Dynamic\ force} = \frac{T}{\frac{1}{2}\rho U_\infty^2 A} \tag{7.12}$$

7.2.2 Yaw angles

A real turbine in operation will not always experience wind perpendicular to the rotor plane. In periods of the production time, the incoming wind will be oblique as shown in figure 7.6.
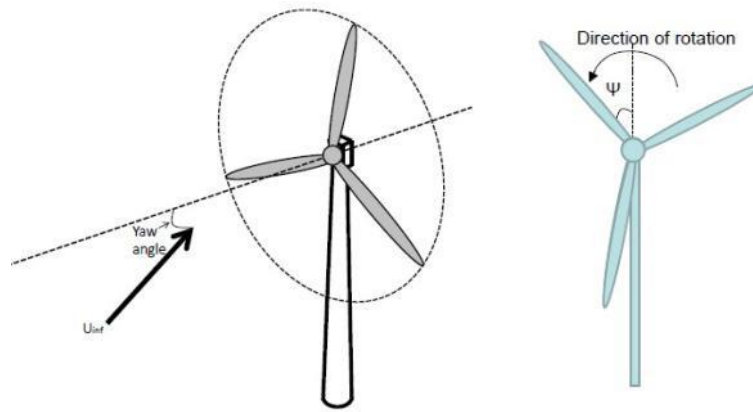
Figure 7.6 Oblique inflow on a wind turbine (Kari, 2011) Figure 7.7 Blade position(Kari, 2011)

Because of the oblique inflow, the wind turbine blades will experience other dynamical loads than those already described. The wind turbine blades will move partially in and out of the wake and the incoming flow. This causes the relative wind velocity every element of the blade experience, U_{rel}, to change with position of the blade, ψ. Definition of the wind turbine blade position is shown in figure 7.7.

When the rotor plane on a turbine is not perpendicular to the wind, the efficiency will decrease. Therefore most modern wind turbines today have a yaw system which rotates the rotor plane in to the wind. If this yaw system is very sensible and constantly rotate the rotor plane perpendicular to the incoming wind, the mechanical components will experience reduced lifetime due to the constant motion. Therefore this is a matter that must be carefully considered and developed. (Erich, 2006)

There are conflicting aims when it comes to the matter of controlling wind turbine yaw motion. Since the efficiency decrease for a wind turbine with the rotor plane oblique to the incoming flow, one should think that the optimum situation in a wind park would be having all the rotor planes perpendicular to the incoming wind direction. This is not necessarily the case. In some situations, the reduced power output from one unit due to deviation from the incoming flow, can give increased power output from a unit downstream of the first. It is therefore reasonable to assume that there can be a combination of yaw angle and maximum power output from a wind farm. (Erich, 2006)This matter will not be discussed further in this thesis, but for more information on this subject see Krogstad and Adaramola (2011).

There are two different forces that are the origin for the natural yaw moment on a wind turbine oblique to the incoming flow. These are the forces F_n and F_t shown in figure 7.5. When the rotor plane is perpendicular to the incoming flow, F_n and F_t will be symmetrical about the vertical and horizontal line that crosses the centre of the rotor plane respectively. When the incoming flow is oblique, this is no longer the case. The turbine will then experience a natural yaw moment that will try to turn the rotor in to or out of the wind. A positive yaw moment tries to rotate the construction in the clockwise direction. The yaw moment for a downstream wind turbine with the rated power of $140kW$ can be in the order of $4000Nm$. (Verelst, 2010)

The force F_t will act on the distance from the tower and to the blade element where it has its origin. This will cause the moment M_{ZI}. The arm will be horizontal and follow the blade in to the centre of the rotor. If the rotor plane is divided in a vertical line through the centre, the side where the total F_t is largest will be determining for the direction of the rotation M_{ZI} causes. See figure 7.8.

The position of the blade, Ψ, will be of importance for the quantity of the moment since the force F_t vary with position, see equation (7.13).

$$M_{z1} = F_t r \sin \psi \tag{7.13}$$
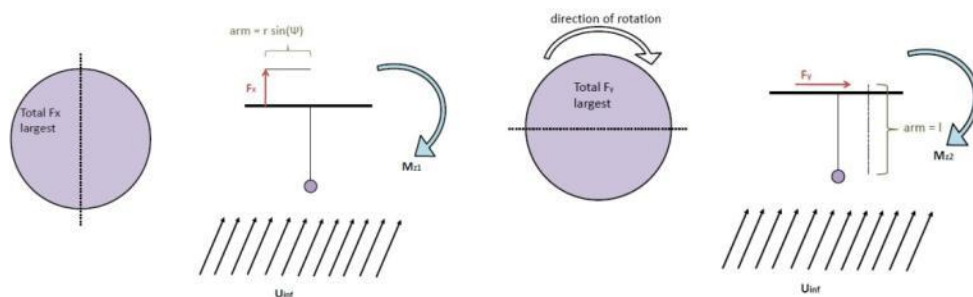
Figure 7.8 The force F_t and the moment caused by this, M_{ZI} (Left) (Kari, 2011)

Figure 7.9 The force F_n and the momentum caused by this, M_{Z2} (Right) (Kari, 2011)

F_n is in its entirety determining for the power production. The horizontal part of this force will also be the origin of a yaw moment about the tower axis, M_{Z2}. The distance from the tower and in to the rotor plane will be the arm in this moment. If the rotor plane is divided with a horizontal line through the centre, the part where the total F_n is largest will be determining for the rotational direction caused by M_{Z2}. See Figure 7.9.

Since the force F_n is no longer symmetrical when the inflow is oblique, M_{Z2} will also be dependent on the blade position.

$$M_{z2} = F_n l \sin \psi \qquad (7.14)$$

7.2.3   Wind turbine wakes

After three diameters downstream of the rotor plane, much of the periodic nature in the flow is lost and the tip vortices diffuse. This is what is known as the near wake area, and is usually described as two to four diameters length from the rotor plane. The near wake is the far wake, where turbulence and velocity profiles are more evenly distributed due to diffusion of turbulence and vorticity generated at the rotor. (Manwell, 2003)

Turbines downwind of other units will experience higher turbulence levels due to producing upwind machines. This increased turbulence results in larger loads and material fatigue which reduce turbine lifetime. The energy capture is also reduced because of the increased turbulence levels for downstream units, but the steady state load is reduced due to the lower mean velocity of the flow. (Erich, 2006)

Wake expansion

A wind turbine extract kinetic energy is from the wind, and therefore reduces the mean velocity of the flow passing through the rotor. Assuming that the mass affected is completely separated from the surrounding air and does not experience any boundary effects, a stream tube can be constructed which illustrate the air passing a wind turbine, see figure 7.10. As the air passes through the rotor, both velocity and static pressure is reduced. Since the air is not compressed and the mass flow rate in the stream tube remains the same, the cross-sectional area of the streamtube must expand due to the lower air velocity. The part of the streamtube in figure 7.10 that continues downstream from the rotor is what is known as the wake. (Tony, 2001)

As the wake extends downstream of the rotor, the centreline velocity deficit decrease, and the width increase. (Ainslie, 1988) The growth rate, dr/dx, can be used to describe how much the wake expands when moving downstream. (Leonardo, 2009) When the thrust coefficient increases, the expansion of the wake increases.

Low velocities will cause a large jump in velocity from U_1 to U_4 in figure 7.10. This will again result in a turbulent-wake state, which is a formation of eddies that brings momentum in to the wake from the outer flow. (Martin, 2008)

The rotor thrust coefficient has a large influence on the extent of the wake due to the significant influence on the loss of impulse behind the rotor. The wake behind the rotor is also dependent on the turbine operating conditions, as for instance the tip speed ratio, blade pitch angle etc.
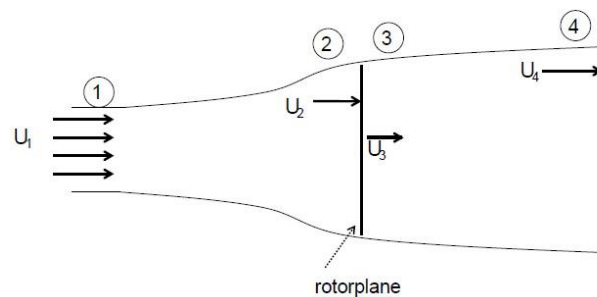
Figure 7.10 Streamtube (Martin, 2008)

Wake rotation

When air is passing the rotor disc it experience a torque. This is the origin for the power production and rotation of the blades. An equal and opposite torque is required due to Newton's third law, and this causes the wake to rotate in the opposite direction to that of the rotor. Due to the wake rotation there will be a tangential velocity component which increase the kinetic energy in the wake. This is compensated for by a drop in the static pressure of the air in addition to the reduction in static pressure when the wind passes through the rotor. (Tony, 2001)

Wake rotation in a streamtube is illustrated in figure 7.11.
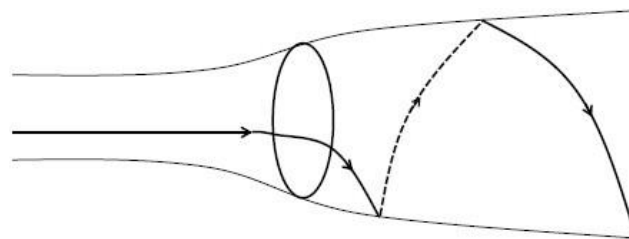
Figure 7.11 Rotation of the wake behind a wind turbine (Martin, 2008)

Wake with yaw angle

The rotor acts like a disc seen from a global perspective, and when the incoming wind is not perpendicular to the rotor plane there will be a discontinuity in the pressure drop across the disc. The pressure drop generates the thrust which again induce a velocity normal to the rotor plane that deflects the wake as shown in figure 7.12. Hence it follows that when the rotor plane is not perpendicular to the incoming wind flow, the wake will be asymmetric. This results in the downwind part of the rotor being closer to the wake centreline, and experience higher induced velocities and forces. (Manwell, 2003)
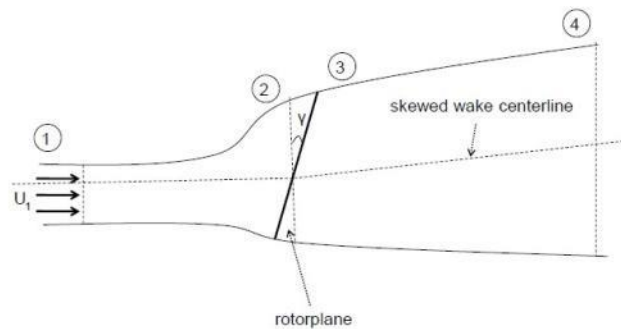
Figure 7.12 Streamtube for oblique inflow (Martin, 2008)

7.2.4   Angle of attack from CFD results

It is well known that the actual incidence of the flow around a wing or blade is difficult to define owing to the wake-induced effects stemming from the vortical flow around the rotating blades. This will affect the local inflow angle. Here we will present a method of determining this local angle of attack α. Using CFD data to obtain the annular average of the axial velocity (and thereby the induction a) at a given radial position in the rotor plane. (Verlst, 2010; Manwell, 2003; Tokuyama, 2009)

The method, which was originally proposed by Hansen et al. (1997) is a way to determine the actual inflow velocity taking into account the decrease in axial flow due to the presence of the rotor. The velocity field within an annulus of a given radial location (see figure 7.13) was obtained and averaged, and this procedure was carried out at different stream wise positions to obtain axial velocities as a function of the stream wise position. Johansen (2004) described this method and made some validations with CFD results in detail.

By sweeping this annular plane from upstream to downstream of the rotor in the axial direction, the aver-aged axial velocity can be plotted as a function of the distance from the rotor plane, and the axial induction factor α can be determined by reading the axial velocity in the rotor plane (Figure 7.14). Once the velocities are known at a set of upstream and downstream positions, its value at the rotor plane can be estimated by interpolation. Once the velocity V is obtained, given the local blade twist angle θ and its rotational speed Ω, the local effective AOA can be calculated as

$$\alpha_E = tan^{-1}\left(\frac{V}{r\Omega}\right) - \theta \qquad (7.15)$$
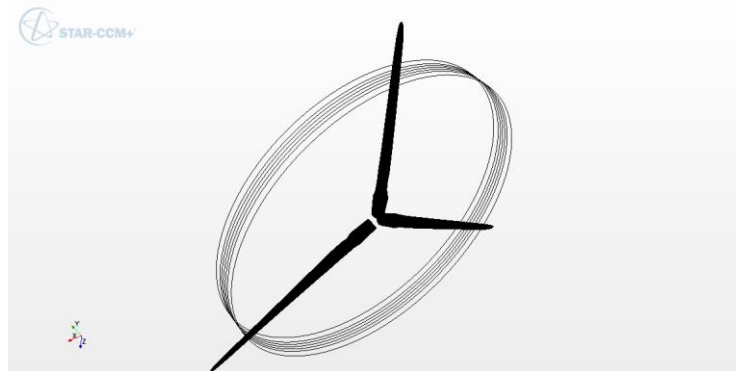
Figure 7.13 Principle of the axial velocity method
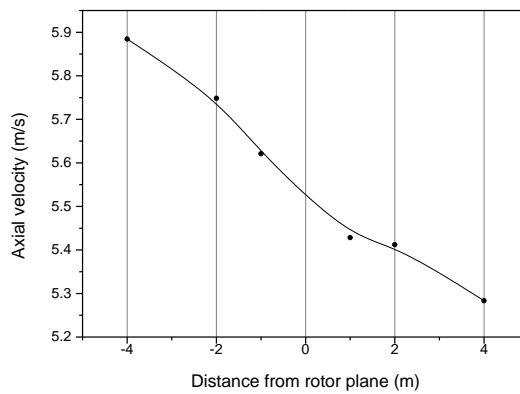
Figure 7.14 Annular average of axial velocity as a function of axial distance from rotor plane, at span wise position r/R=0.8, V=8m/s

7.3   Grid Uncertainty Analysis

By detecting the accuracy of the grid, three different element types were given in Table 7.3 to compare. In the case of wind speed 8m/s and rotation 9.16rpm, Fig.7.15 and Fig.7.16 illustrate the aerodynamic power and thrust results over a range of

elements compared within three approaches, CFD, blade element momentum (BEM) and generalized dynamic wake (GDW). The present CFD results show overall good correlations with those obtained by the FAST code.

Table 7.1 Three different mesh sizes

CFD mesh type	Case 1	Case 2	Case 3
Maximum size	0.03 m	0.024 m	0.015 m
Minimum size	0.09 m	0.072 m	0.045 m
Total number (million)	9.06	17.5	27.8
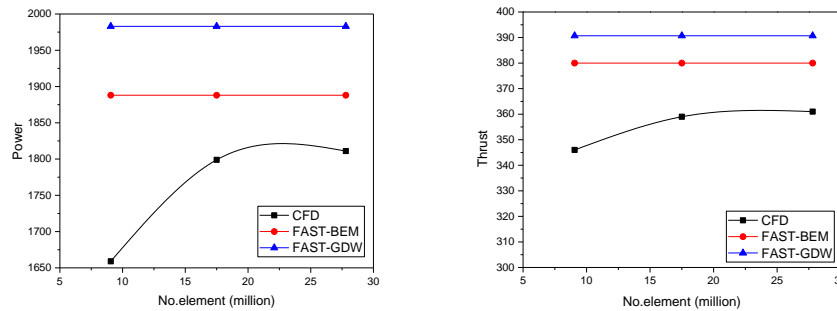
Figure 7.15 Power with different elements   Figure 7.16 Thrust with different elements

As the figures show, there are about 9% and 23% differences in the predicted aerodynamic power and thrust between the present CFD method and BEM, respectively. Nevertheless, the discrepancy between BEM and GDW is small, only 4.6% and 2.3%. It is attributed to several effects will be explained later. The simulation results between case 2 and case 3 are almost the same. However, there is a big difference compared with case 1. Flow unsteadiness for the condition of pitch and surge motion for rotating blades must be higher than that of the previous comparison case. Therefore, case 3 is chosen for the unsteady simulation in order to capture complex wake effect behind the rotating blades.

Then a verification study was undertaken to assess the simulation numerical uncertainty, U_{SN} and numerical errors, δ_{SN}. In the above section 3.8, it had a detailed description of uncertainty analysis in CFD verification and validation methodology and procedures according to ITTC guidelines. Xing and Stern (2010) state that the Richardson extrapolation method (Richardson, 1910) is the basis for existing quantitative numerical error estimates for time-step convergence and grid-spacing. This study generates a so-called grid-triplet study Roache's (1998) grid convergence (GCI) is useful for estimating uncertainties arising from grid-spacing errors. Grid-

spacing convergence studies were carried out following the correlation factor (CF) and GCI methods of Stern et al (2006). The verification parameters of power and thrust for the grid spacing convergence studies are demonstrated in Table 7.5.

For the mesh convergence study, a uniform refinement ratio (r_G) was chosen to be $\sqrt{2}$. Based on the mesh refinement ratio, the final mesh numbers for each mesh configuration are listed in Table 7.4. Moreover, the rated velocity and rotation speed were chosen as 11.4 m/s and 12.1 rpm. As can be seen from the results listed in Table 7.5, reasonably small levels of uncertainty were estimated for power and thrust. Uncertainties U_G (1.817% and 0.874%) were predicted for power, and 0.137% and 0.0171% for thrust, respectively. The difference was so small to ignore. Therefore, we can identify that the mesh method is suitable for this simulation

Table 7.2 The final cell numbers for each mesh configuration as a result of the mesh convergence study

Mesh configuration	Cell number (million)		
	Station region	Rotation region	Total
Fine	0.165	55.737	55.98
Medium	0.165	27.486	27.95
Coarse	0.165	16.795	13.96

Table 7.3 Grid convergence study for Power and Thrust

Parameter	r_G	Solutions			R_G	δ_G^* %S_1	U_G %S_1	U_{Gc} %S_1	GCI	S_c
		S1	S2	S3						
Power (Kw)	$\sqrt{2}$	4719.12	4674.65	4607.11	0.66	-0.94	1.817	0.874	2.27	4719.18
Thrust (KN)	$\sqrt{2}$	666.5	665.7	664.2	0.53	0.12	0.137	0.0171	0.1715	666.50

7.4   Results and Discussion

7.4.1   Detect the hub and tower effects

According to the literature reviews above, most researchers detect the aerodynamic performance using the rotor only wind turbine in CFD simulation. In this paper, three different conditions, rotor only, with hub and whole wind turbine, were compared. The rated condition of NREL 5MW wind turbine was chosen for this study, namely wind speed is 11.4 m/s and rotation is 12.1 rpm. Figure 7.17 and 7.18 show the wind turbine models using in the simulations. As figure 7.19 shows, power and thrust decrease with the order of rotor only, with hub and whole wind turbine. Table 7.6

describes the concrete numbers of power and thrust which can be shown that the results are almost same. In detail, the differences of power are 1.9% and 0.96%, compared between condition 1 and 2, 2 and 3, respectively. In addition, thrust differences are smaller, 0.57% and 0.65%, respectively. The reasons will be described as follows. Consequently, other analysis and simulations below are choosing the rotor-only models for time saving and computation smaller.

Figure 7.17 Wind turbine model with hub   Figure 7.18 Whole wind turbine model
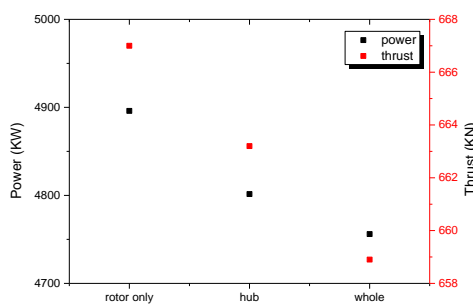
Table 7.4 Power and thrust compared with different conditions			
NO.		Power (kW)	Thrust (kN)
1	Rotor only	4896	667
2	With hub	4802	663.2
3	Whole	4756	658.9

Figure 7.19 Power and thrust compared with different conditions

High speed flow trailing from the blade tips is readily observed by figure 7.20 and 7.21. As shown in figure 7.22 and 7.23, the tip and root vortices from the rotor are clearly visible. The unsteady vortex shedding from the tower is quite coherent as well. To detect whether the tower vortex street will affect the aerodynamic characteristics of the blade, the detailed comparisons at the root and tip (0.7r) of three different conditions were conducted. Figure 7.24 and 7.25 describe the velocity and pressure streamlines at the root of the blade. The existing hub and tower separate the flow over the blade which decreases the velocity a little. Moreover, power and thrust results at the tip are shown in figure 7.26 and 7.27. There is no obvious difference comparing with the three conditions. Inlet and outlet flow is necessary to

detect. The chosen upstream and downstream sections are 4m and a diameter distance from the blade as shown in figure 7.28. Tangential velocity *Vt*, rotation velocity *Vr* and inflow velocity *Vx* at every point around the chosen circle section are described in figure 7.29. The following figures 7.30-7.35 are results of the velocities. There is no obvious difference of velocities compared with these three conditions. At upstream section, maximum of *Vt* is about 5m/s, which means that 3D rotational effect is large. *Vx* reaches the max point about 12.5 m/s at the tip of the blade. Therefore, the tip sensitive is important to detect. At the downstream section, *Vt* and *Vr* are very small which means the rotational effect almost disappeared.
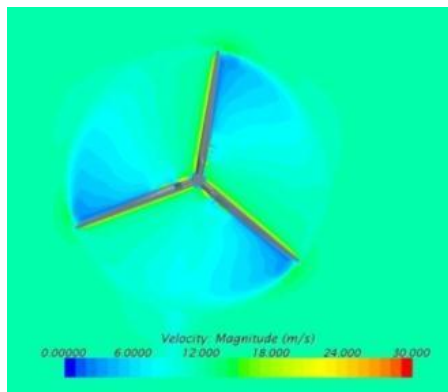
Figure 7.20 Velocity contour of blade
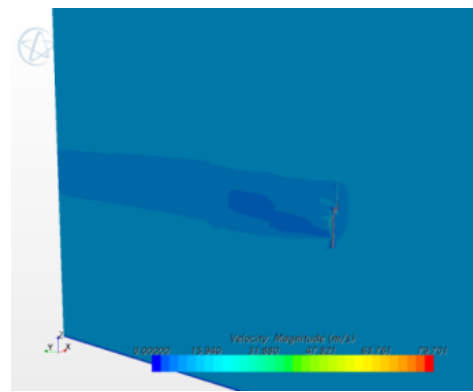
Figure 7.21 Velocity contour of the whole flow
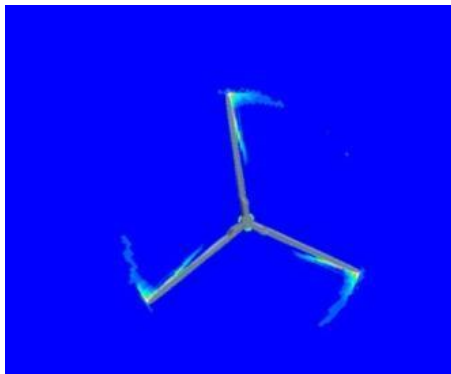
Figure 7.22 Vorticity contour at the rotor plane
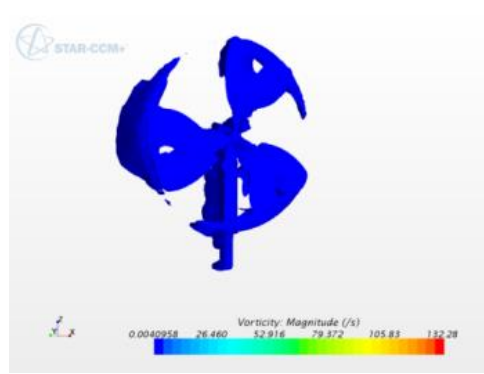
Figure 7.23 Iso-voritcity plot of flow
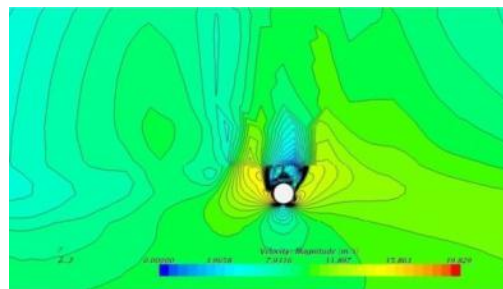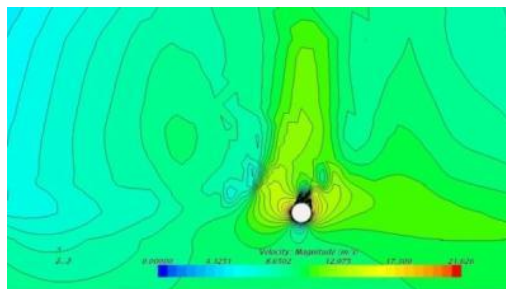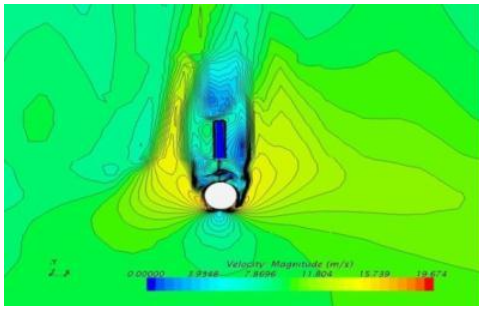
Figure 7.24 Velocity magnitude at the root compared with different conditions (rotor only, with hub and whole)
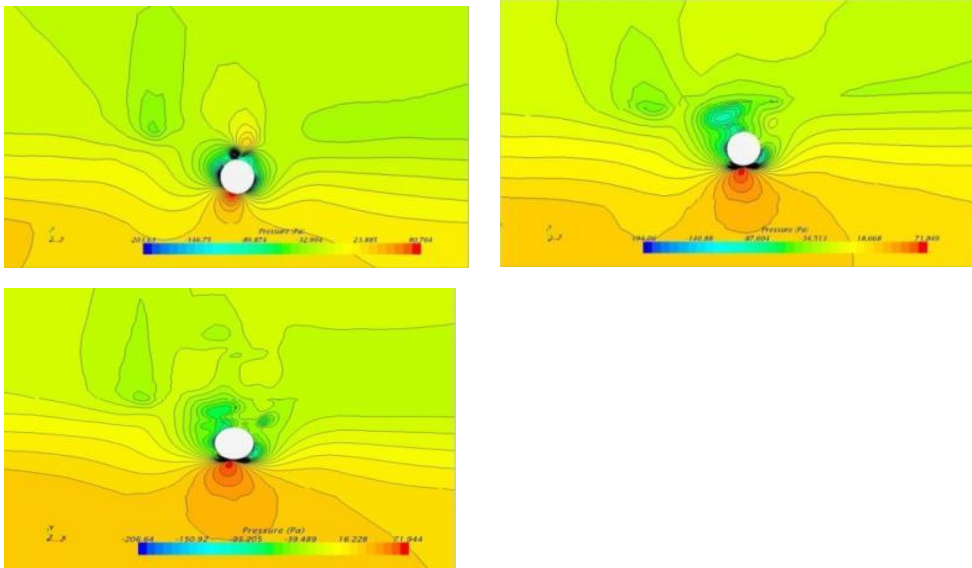
Figure 7.25 Pressure at the root compared with different conditions (rotor only, with hub and whole)
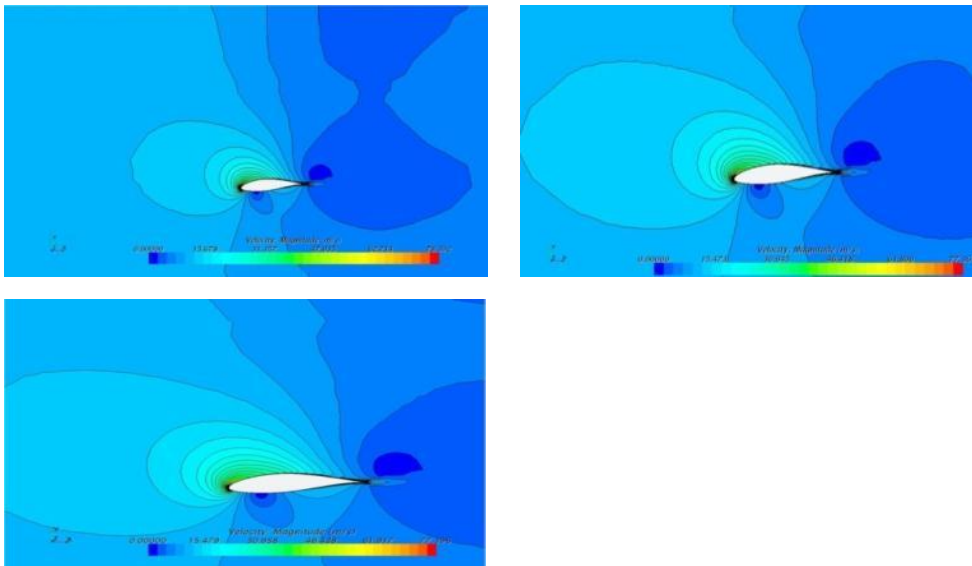
Figure 7.26 Velocity magnitude at the tip (0.7r) compared with different conditions (rotor only, with hub and whole)
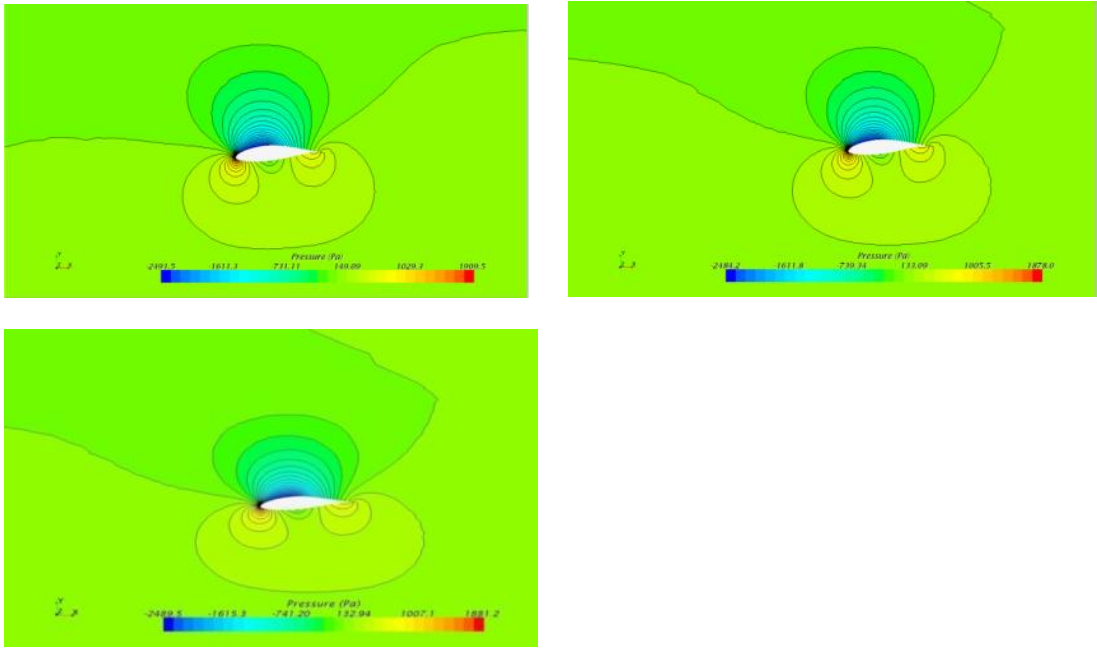
Figure 7.27 Pressure at the tip (0.7r) compared with different conditions (rotor only, with hub and whole)
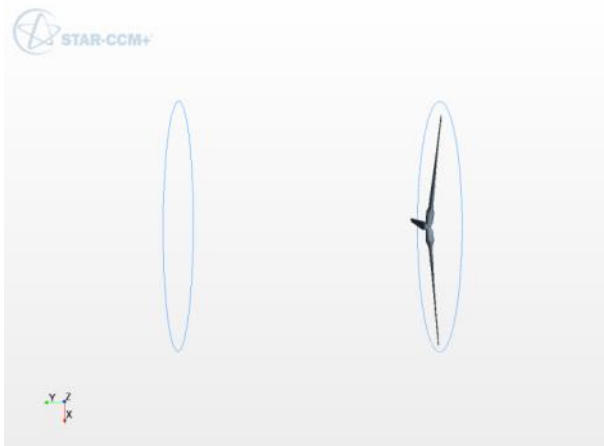
Figure 7.29 Upstream and downstream sections
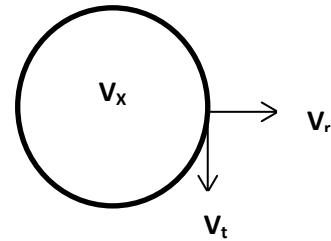
Figure 7.28 Velocity distribution around the circle
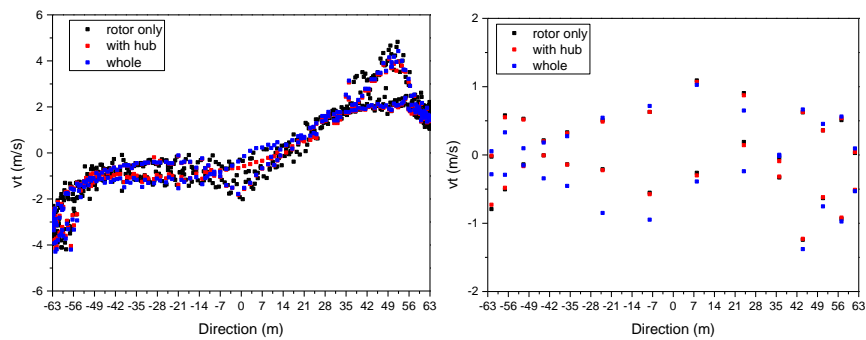
Figure 7.30 v_t compared with different conditions at the upstream (left) and downstream (right) section
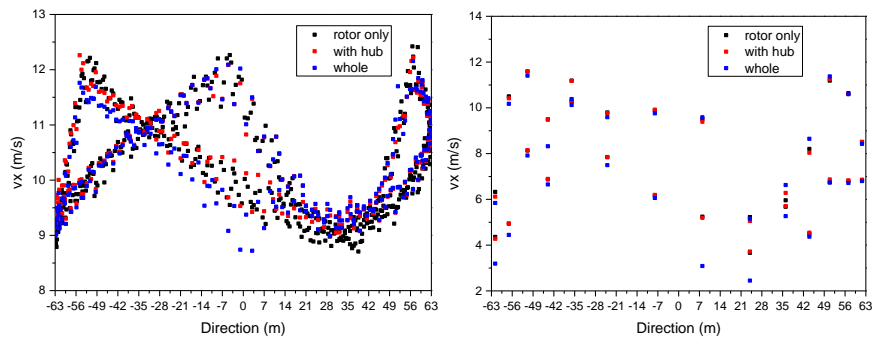
Figure 7.31 v_x compared with different conditions at the upstream (left) and downstream (right) section
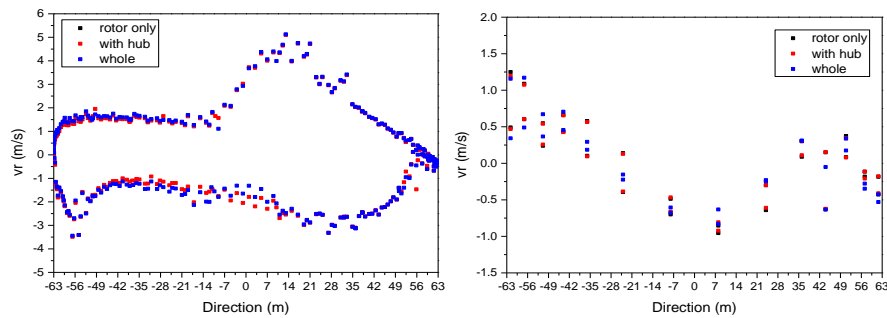
Figure 7.32 v_r compared with different conditions at the upstream section (4m)

7.4.2 Comparison with FAST and other CFD results

According to the analysis above, rotor only wind turbine was chosen to simulate to insure the accuracy and time saving. The power and thrust results versus different wind speed between 7m/s and 20m/s are given in fig.7.36 and fig.7.37. To validate the CFD results from software, STAR CCM+, predictions are compared with other CFD results and FAST data. The overflow2 and ellipsys3d data were from Chow et al. (2012) and Sørensen et al. (2006). It can be observed that the results of different methods match well at low, medium and high wind speeds. My CFD results are most close to overflow2. When wind speeds reach larger than 12m/s, the wind turbine rotor begins to stall. Therefore, the largest power and thrust appears at 12m/s. BEM methods get the largest power and thrust about 5800kW and 800kN, respectively. At high wind speed above the design wind speed, the power keeps stable and the thrust suffers a significant decrease. The root of the blades experience negative angle of attack and provide power and thrust to the flow instead of subtracting it. However, when the wind speed is over the stall velocity, the wind turbine will have a pitch control which can keep the power in a level. Figure 7.38 indicates that wind turbines

have a maximum power coefficient of around 50%. The thrust coefficient reaches a value smaller than 1 even after the tower and nacelle effects have been subtracted, see figure 7.39. For real life wind turbines, the thrust coefficient will be below one. This is due to the local velocity increase at the rotor plane as a consequence of the turbine being in a closure. As there is no experiment data, it is plausible consider that the CFD method can predict the power and thrust accurately at pre-stall, stall and post-stall regions of the wind turbine blade.
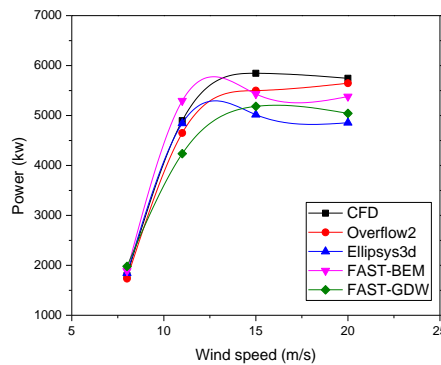
Figure 7.33 Power with different methods
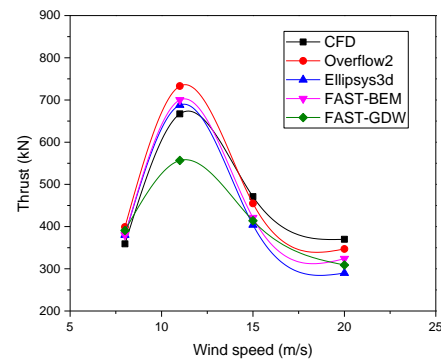
Figure 7.34 Thrust with different methods
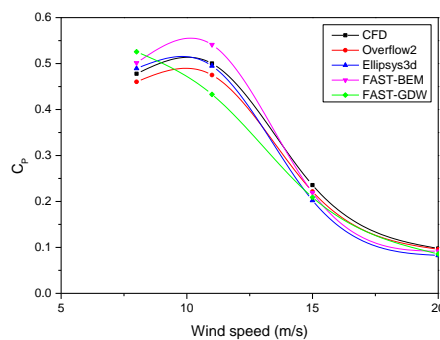
Figure 7.35 C_P with different methods
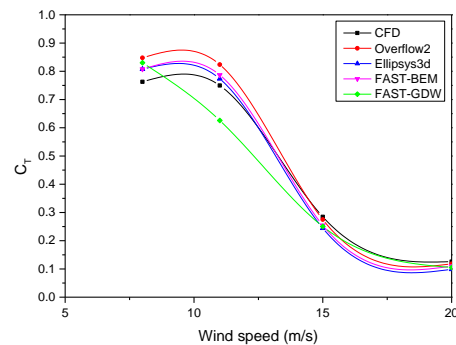
Figure 7.36 C_T with different methods

7.4.3 Span-wise sectional results

To investigate how the aerodynamic torque distribution varies along the blade span, the blade is segmented into 17 span-wises shown in figure 7.40. Figure 7.41 showed the pressure contours at several blade sections. It is clearly showed the large negative pressure at the suction side of the airfoil which creates the desired lift. The patch-wise torque distribution is shown in Figure 7.42. The torque is nearly zero in the cylindrical section of the blade. A favourable aerodynamic torque is created on Patch 4 and its magnitude continues to increase until Patch 12. The torque magnitude decreases rapidly after Patch 12, however, the torque remains favourable all the way

to the last patch. The significant discrepancies appear at blade tip. It can be also clearly visible in Figure 7.43 which showing comparison of the angle of attack within CFD and BEM. The angle of attack is a very significant parameter in potential flow approach.
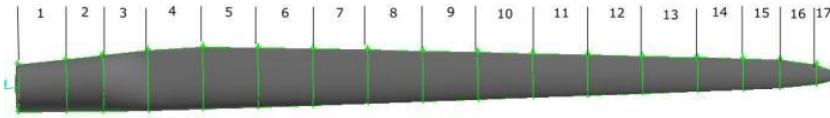
Figure 7.37 Span-wise sections along the blade
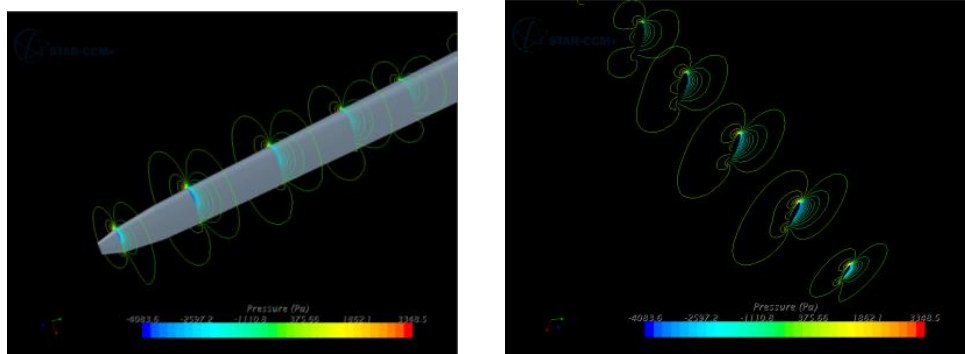
Figure 7.38 Pressure contours at several blade corss-sections
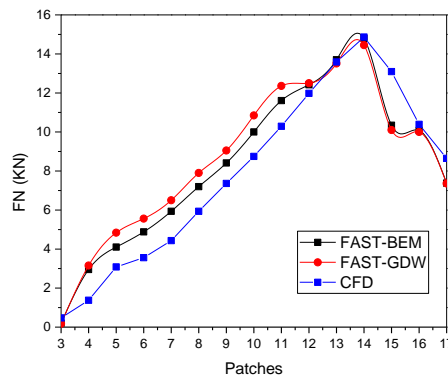
Figure 7.39 Normal force along the radio   Figure 7.40 Angle of attack along the radio
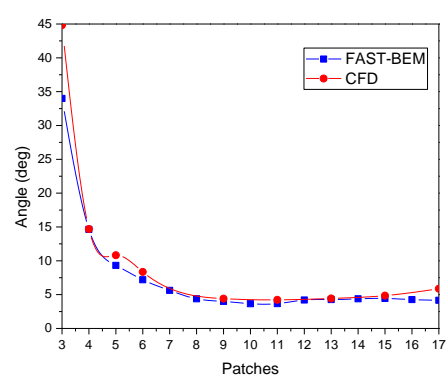
7.4.4   Compared steady condition with dynamic condition

Different operation conditions and distances behind the rotor plane have been measured for the velocity field. The yaw moment, power and thrust curves have also been examined. This has been done for $U_\infty = 8\ m/s$ for the yaw angles $= 0^o$, 30° and 60° using different simulation method CFD, BEM and GDW, respectively. It is clear from the figures 7.44 and 7.45 that when the yaw angle increased, the power and thrust decreased severely. This is due to the reduced rotor plane that is perpendicular to the incoming wind, but also the reduced effective wind speed component that

interacts with the rotor blades. Therefore the wind turbine cannot utilize as much of the kinetic energy in the wind.

Figure 7.45 compares the power and thrust of these three methods, CFD results have a big discrepancy of other two which because when using BEM method there are several factors that may cause inaccuracies in the calculations. Chapter 2 above got the detail reasons. The difference of power and thrust between different yaw angles can be seen in table 7.7. It is clear that the largest difference was appeared at 30 degree which has the largest skew flow. Therefore, BEM may not predict the aerodynamic performance accurately in the oblique flow condition. As shown in table 7.8, the largest discrepancy of power was discovered at 11.4m/s up to 8.17% and 13.5% compared with BEM and GDW, respectively. The difference of thrust increased with the increasing of wind speeds.
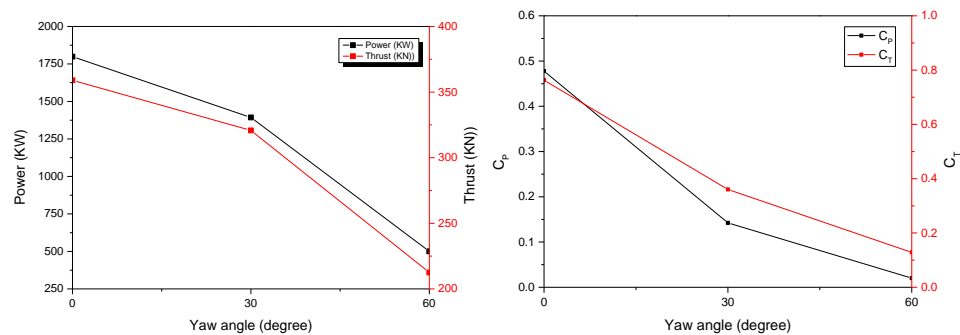
Figure 7.41 Compare power and thrust (CP and CT) with different yaw angles
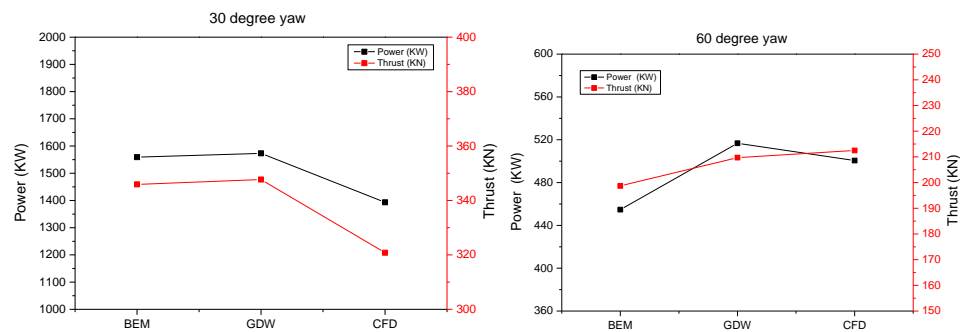
Figure 7.42 Compare power and thrust with different methods

Table 7.5 Difference of power and thrust between different yaw angles for U_∞=8m/s

BEM vs CFD			GDW vs CFD	
Yaw angle (degree)	Power (%)	Thrust (%)	Power (%)	Thrust (%)
0	4.95	5.85	10	8.83
30	11.9	7.8	12.5	8.4
60	9.17	6.5	3.2	1.3

Table 7.6 Difference of power and thrust between different yaw angles for $U_\infty=8$m/s

BEM vs CFD			GDW vs CFD	
Wind speed (m/s)	Power (%)	Thrust (%)	Power (%)	Thrust (%)
8	4.95	5.85	10	8.83
11.4	8.17	4.95	13.5	16.5
15	7.1	10.6	11.34	12.1
20	6.35	13.24	12.22	16.5

Figure 7.46 describes the position number of blades. As the existence of yaw angle, each blade carries a little different aerodynamic loading. Figure 7.48 describes the torque from different sections. When the yaw angle increases, the torque decreases. Compared with BEM, a larger difference showed at 60 degree in figure 7.49, especially after mid-span. So it is important to detect whether the BEM is adapt to simulate the aerodynamic performance in oblique flow.
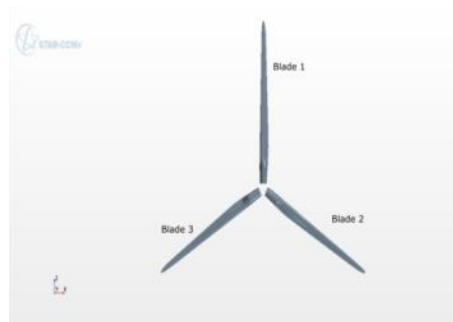
Figure 7.43 Blade position descriptions
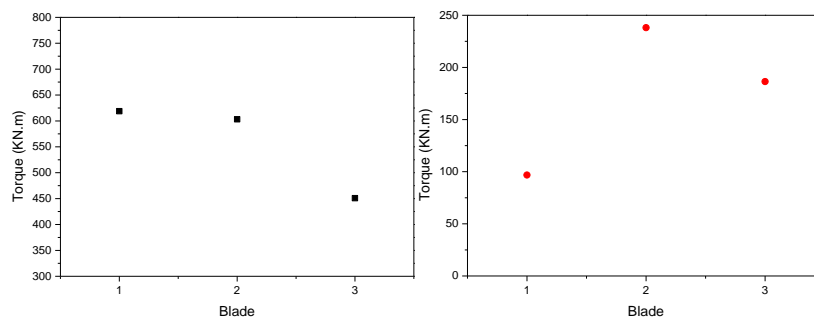
Figure 7.44 Torque at each blade (left: 30 degree, right: 60 degree)
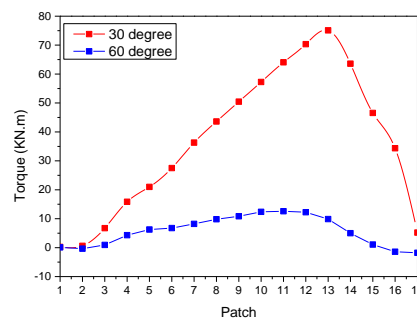
Figure 7.45 Torque along span-wise sections (Blade 1)
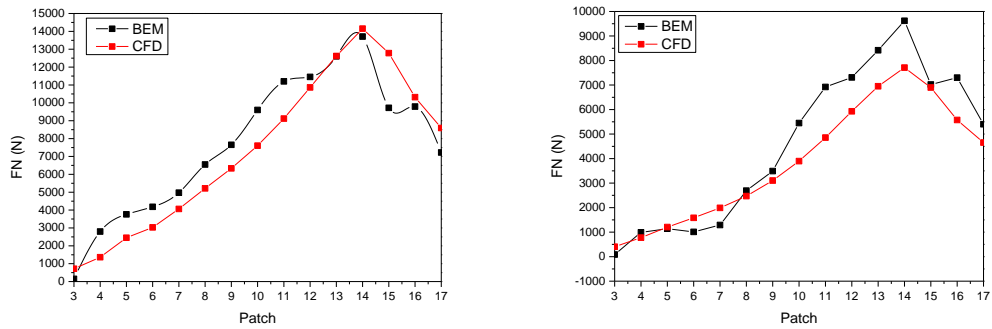
Figure 7.46 Normal force along span-wise sections (left: 30 degree, right: 60 degree)

The velocity relative to the hub velocity for different distances in x direction is displayed in this section. Figure 7.50 shows the clear difference between the various tip speed ratios for yaw angle=0. The velocity deficit is highest near the hub. The axial velocity of the rotor plane is almost similar with the freestream velocity. This indicates that there is little interaction between the airflow and rotor, and most of the air passes through without being disturbed by the wind turbine blades. Since large part of the air flows past the turbine without being affected by the rotor, less energy is extracted from the flow. When tip speed ratios increases, the velocity deficit is more evenly distributed and stronger. This shows that the rotor operates efficiently, and the energy is extracted uniformly from the flow. Near the tip of the blade, there is a sudden drop in a velocity deficit. This is due to the entertainment from the freestream flow due to the tip vortices. There are strong mechanisms acting to make the velocity deficit even out as the wake develops downstream.
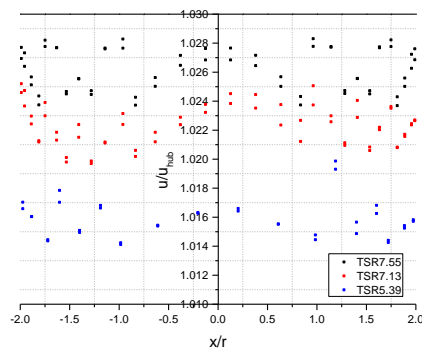
Figure 7.47 Horizontal velocity profiles for X/D=1

The horizontal velocity profiles for several distances behind the rotor plane for a wind turbine with constant operating condition $\lambda = 7.55$ are displayed in figure 7.51.

From this it is possible to see some of the wake development. Wake width increase with streamwise distance from the rotor plane. As the wake width increase downstream, the velocity deficit decrease. Figure 7.52 shows the difference between $\Upsilon=0^o$ and 30° for $\lambda = 7.55$ and different distances behind the rotor. As the yaw angle effects, it becomes asymmetric.

a. Yaw angle =0

b. Yaw angle =30
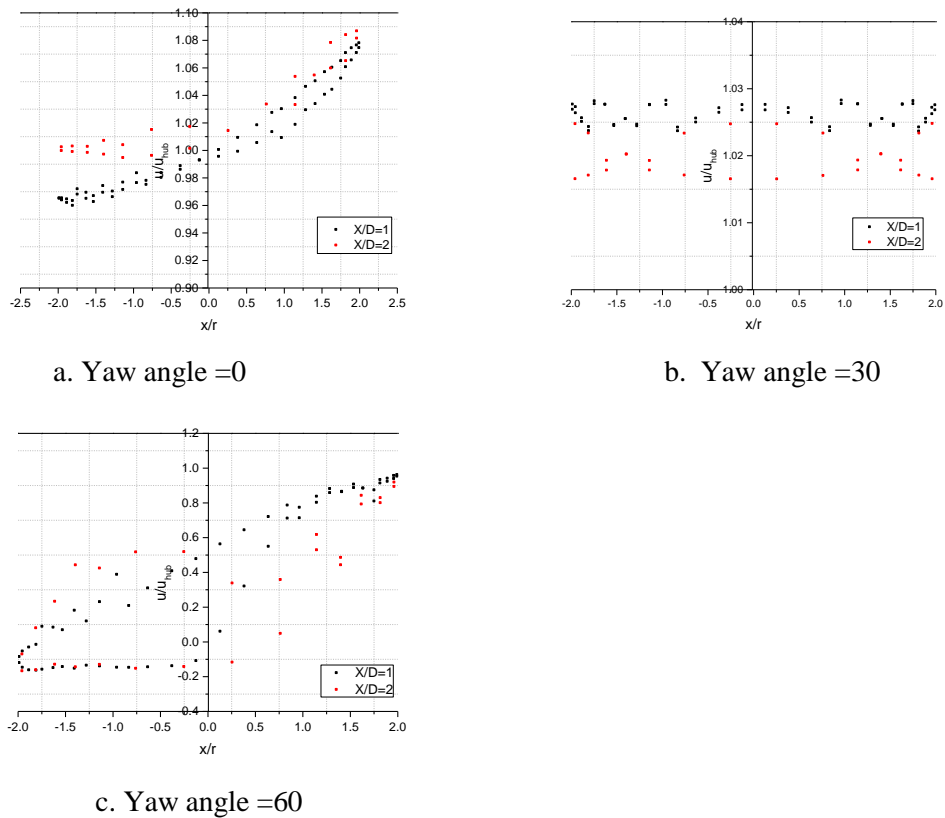
c. Yaw angle =60

Figure 7.48 Horizontal profiles for different distances behind the rotor plane for $\lambda = 7.55$

a. X/D =1

b. X/D =2
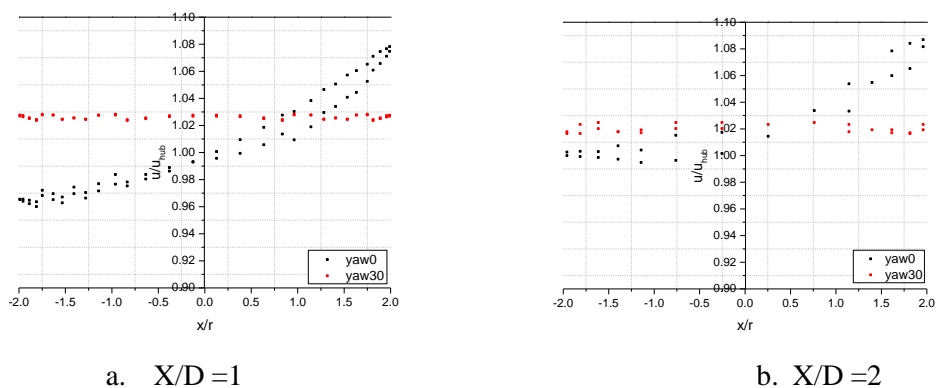
Figure 7.49 Horizontal profiles for different yaw angles for $\lambda = 7.55$

The results of the velocity field behind the wind turbine in the contour plots in this section. The velocity contours for λ=7.55, 7.13 and 5.39 and $\Upsilon=0^o$ are shown in

figures 7.53-7.55. The difference between the velocity field for $\Upsilon=0^o$, 30° and 60° with a tip speed of 7.55 and one diameter behind the rotor plane can be seen in figures 7.53, 7.56 and 7.57. The rotor plane is marked different plots, and for the cases where $\Upsilon=30^o$ and 60° the rotor plane will no longer be a circle. The rotor plane now has an elliptic form. Again the plot for $\Upsilon=30^o$ has a smaller rotor plane area than the one with $\Upsilon=0^o$. The size of the field measurement of X/D=2 was larger than that X/D=1. The reason for this is that the vertical velocity plots indicated that the wake had expanded.
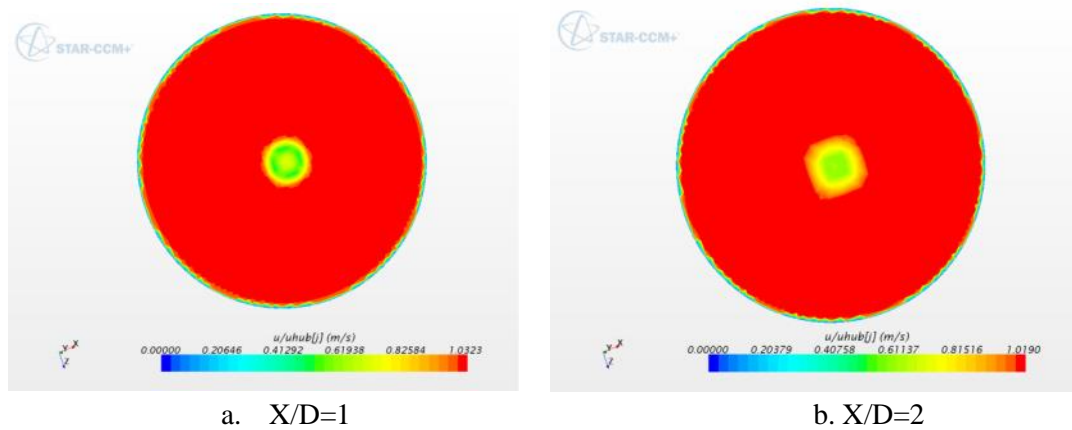
| a. X/D=1 | b. X/D=2 |

Figure 7.50 The velocity field at λ=7.55 and $\Upsilon=0^o$
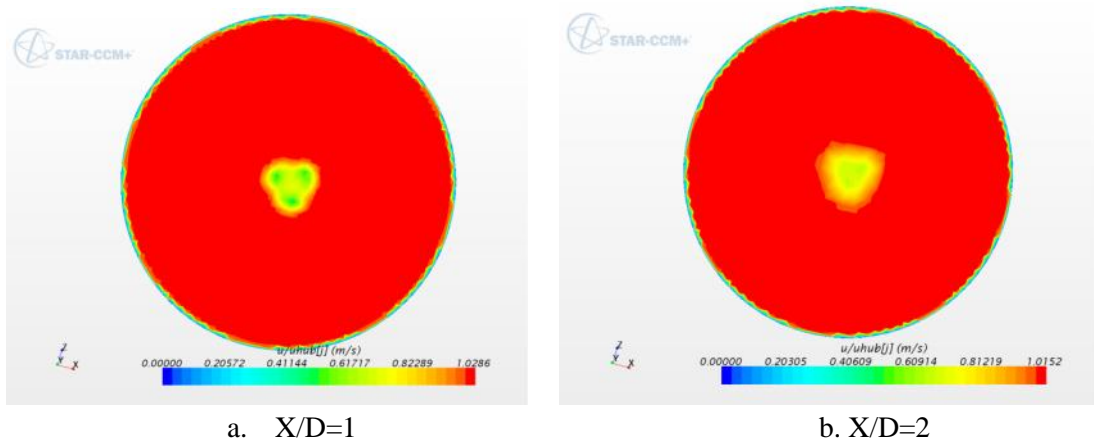
| a. X/D=1 | b. X/D=2 |

Figure 7.51 The velocity field at λ=7.13 and $\Upsilon=0^o$
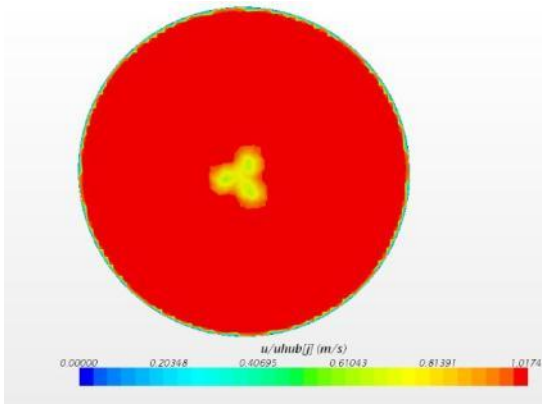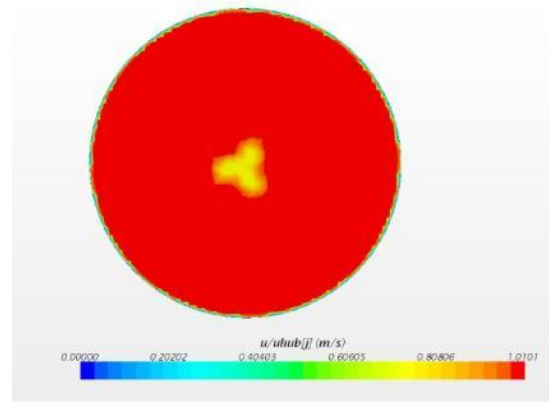
a. X/D=1   b. X/D=2

Figure 7.52 The velocity field at λ=5.39 and $\Upsilon=0^o$
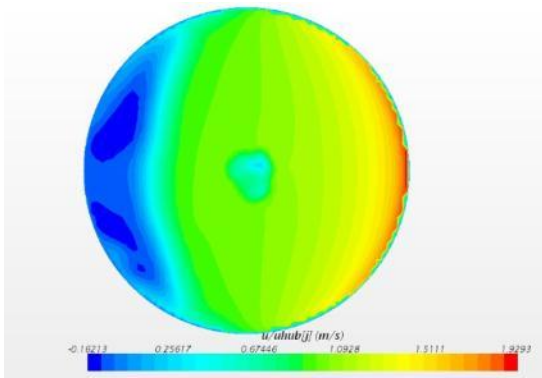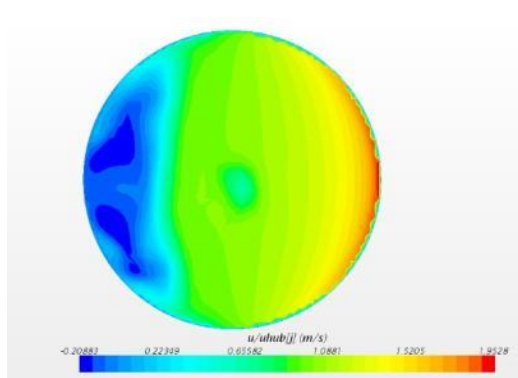
a. X/D=1   b. X/D=2

Figure 7.53 The velocity field at λ=7.55 and $\Upsilon=30^o$
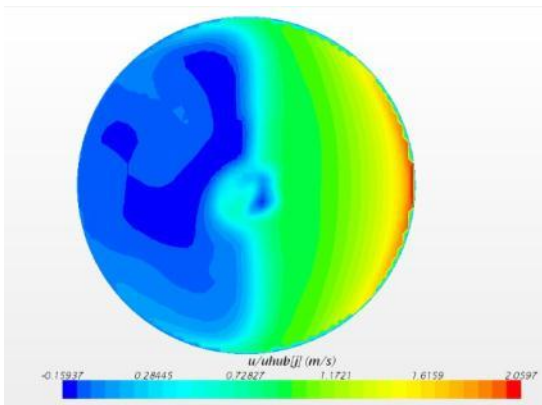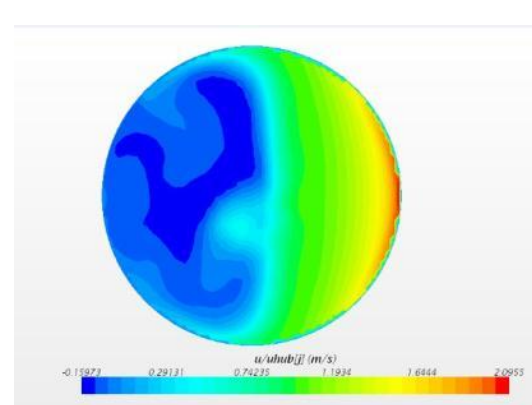
a. X/D=1   b. X/D=2

Figure 7.54 The velocity field at λ=7.55 and $\Upsilon=60^o$

7.4.5 Compare fully turbulent with transition model in CFD

According to 2D aerodynamic simulation shown in Chapter 4, transition model will have a good result compared with the fully turbulent model. STAR CCM+ offers two transition models: Gamma ReTheta model and Turbulence suppression model. Here I chose Gamma ReTheta model to do the transition calculation. Transition calculation is very time consuming which spent about 4 times than fully turbulent calculation. Table 7.9 shows the power and thrust output compared between fully turbulent and transition model using CFD method. Good agreement of results is obtained with these two models. It also can be seen that the transition model results are slightly under-predicted than that of fully turbulent. The relative error is about 9% for low wind speed while for high wind speed where an underestimation of nearly 4.6% occurs. In general, for larger wind turbines, where Reynolds numbers are higher, the advantages of using the Transition model may not be significant.

Table 7.7 Power and Thrust comparison between fully turbulent and transition model

Wind speed (m/s)	RPM	Fully turbulent		Transition model	
		Power (KW)	Thrust (KN)	Power (KW)	Thrust (KN)
8	9.16	1799	359	1637	341
11.4	12.1	4896	667	4672	665

7.4.6 Compare with shear wind condition

The power thrust generated by a wind turbine largely depends on the wind speed. During time periods with identical hub-height wind speeds but different shapes to the wind profile, a turbine will produce different amounts of power and thrust. This variability may be induced by atmospheric stability, which affects profiles of mean wind speed, direction and turbulence across the rotor disk. A number of different flow mechanisms as concerns the rotor aerodynamics and the energy conversion are caused by the sheared flow. The induction varies over the rotor disk; the operational point for the individual airfoil sections varies during one rotor revolution; the wake rotation behind the rotor causes a redistribution of the sheared flow, and the vortex sheets behind the rotor are tilted. These effects will be exemplified and discussed

below in order to come closer to an understanding of how the sheared flow influences the energy conversion and the loading on the rotor.

NWP condition

The current version of AeroDyn accommodates two types of wind files. One type specifies hub-height wind data that also includes wind shears and gusts. I use IECWind to generate these files for standard IEC wind conditions. Figure 7.58 showed velocity distribution along the hub height at the NWP condition using eq 7.5 when the hub wind speed is 8m/s.
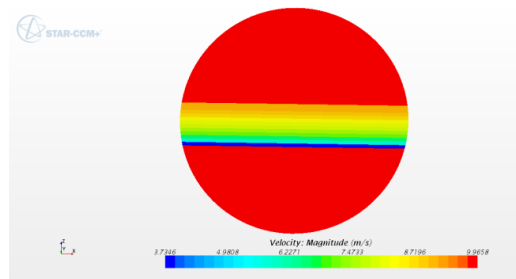
Figure 7.55 Velocity distribution at the NWP condition when the hub wind speed is 8m/s

Figure 7.59 showed the comparison results for aerodynamic thrust and power for a normal wind profile (NWP) condition at 8m/s and 11m/s. Unsteady CFD and BEM methods are used to calculate those results. The results show overall good agreement but approximately 9.3% (8m/s) and 15% (11m/s) differences are seen for the calculated thrust. However, the power described a larger discrepancy about 14.1% (8m/s) and 25% (11m/s), respectively. It can be seen that the analysis results by the BEM seem to predict higher values than those by the CFD. When the velocity increased, the discrepancy became larger. The computational load distributions for inflow with shear are shown in figure 7.60. The tip correction model may causes deviations. Moreover, for the uniform inflow, the computed power was 1799 and 1606 kW for the sheared inflow case, and this should be seen 10.7% lower power in the inflow with shear. Overall, BEM method may not predict the aerodynamic performance accurately in a complex condition.
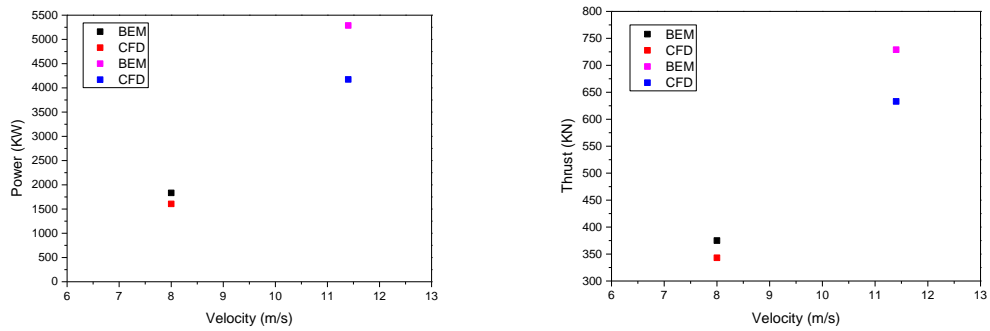
Figure 7.56 Power and thrust at the NWP condition when hub wind speed is 8m/s and 11m/s
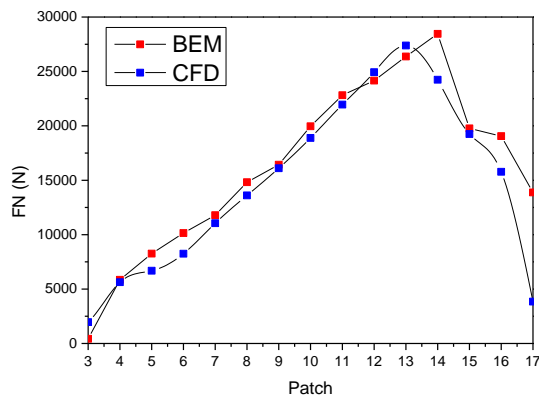
Figure 7.57 Normal force along span-wise sections at 11.4m/s

Extreme coherent gust (ECG) condition

Section 7.2.2.2 above described the ECG condition detailed. The magnitude of the wind speed profile imposed in the CFD analysis was shown in Figure 7.61 according to the theory equations. Figure 7.62 and Table 7.10 showed the comparison results of for aerodynamic thrust and power for an extreme coherent at an average hub wind speed of 8 m/s. As a result, CFD computations predict much higher values of thrust and power for the ECG condition. The results clearly show that the predicted aerodynamic power considering transient wind gust tends to be dominantly changed during the period of extreme wind gust blowing. When the extreme wind gust occurs, there is large variation in the magnitude of power and thrust curve. In addition, there are somewhat differences for high wind speed region which highly dynamic characteristic of flow-field around wind turbine occurs. Figure 7.63 indicated the

normal force along the blade sections. There is a big difference comparing with CFD and BEM. The CFD results showed the maximum forward.
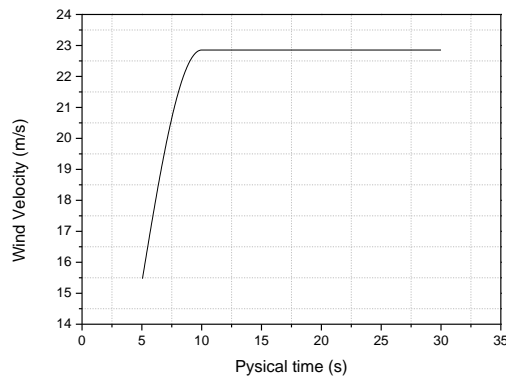
Figure 7.58 Velocity distribution vs time
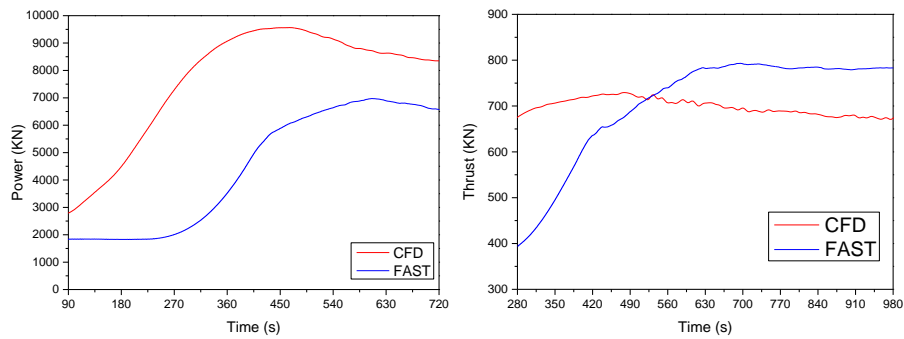
Figure 7.59 Comparison of power and thrust

Table 7.8 Power and thrust comparison with CFD and BEM

	Power (KW)	Thrust (KN)
BEM	6364	787
CFD	7500	867
Difference	15.1%	10.2%
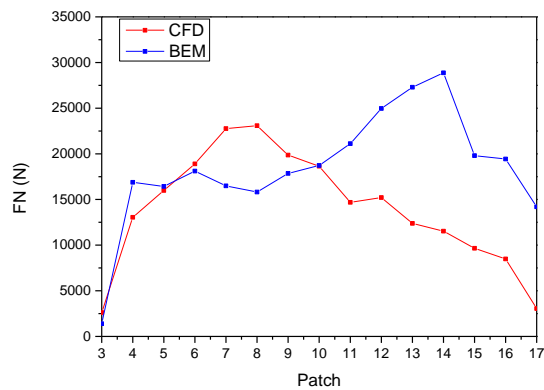
Figure 7.60 Normal force along span-wise sections when the hub wind speed is 8m/s

7.5   Conclusion

Aerodynamic performance of NREL 5MW wind turbine was detected by using STAR CCM+. According to the validations above, I chose k-w SST turbulence model to simulate. For calculating the wind turbine using the CFD software, computational domain and boundary conditions were described detailed. The total cells were about 120 million. To confirm the accuracy, a grid uncertainty analysis was conducted by ITTC guidelines. Reasonably small levels of uncertainty were estimated for power and thrust which identify that this mesh method is suitable for the simulation.

As the literature reviews described, most researchers did CFD simulations using the rotor only wind turbine. Therefore, three different conditions, rotor only, with hub and whole wind turbine, were compared in this chapter. The results of power and thrust were almost same, but the whole model showed a little small. The existing hub and tower separate the flow over the blade which decreases the velocity a little. Inlet and outlet flow is necessary to detect. Tangential velocity, rotation velocity and inflow velocity at every point were described. Rotation velocity at the downstream was close to 1 which defines that constriction of wake flow is not significant.

A transition model from laminar to turbulent flow is modelled using Langtry and Menter correction based Gamma-Theta transition model. This model is a two equations model used in CFD to modify turbulent transport equations. A comparison between turbulent model and transition model was conducted. Good agreement of results was obtained with these two models. The transition model results were slightly under-predicted than that of fully turbulent. However, when Reynolds numbers are higher, the advantages of using the transition model may not be significant.

When compared with FAST results, it can be observed that the results matched well at low, medium and high wind speeds. BEM method got the largest power and thrust about 5800 KW and 800 KN of all. At lower wind speed, the power was small as the blades experience stall. At high wind speed above the design wind speed, the power decreased. As there is no experiment data, we assume that CFD method can predict

the power and thrust accurately at pre-stall, stall and post-stall region. However, at the yaw condition, compared CFD results with BEM, a larger discrepancy was found which means that BEM may not predict the aerodynamic performance accurately in the oblique flow condition.

Analysing the span-wise sectional results, a large difference was found at the tip of the blade. Therefore, the tip loss correction was important to the potential method.

Wind turbine wake was significant to analyse. As the wake extends downstream of the rotor, the centreline velocity deficit decrease, and the width increase. The rotor thrust coefficient has a large influence on the extent of the wake. Moreover, wake rotation will increase the kinetic energy in the wake.

Finally, various critical design load cases (DLC) based on wind turbine design guidelines were considered. As a result, CFD computations predict much higher values of thrust and power for the NWP and ECG conditions. The discrepancy between CFD and BEM is larger than that in a unit wind. That is because BEM cannot predict well under complex conditions.

8. AERODYNAMIC PERFORMANCE OF FLOATING OFFSHORE WIND TURBINE USING CFD METHOD

8.1 Overview

For a floating HAWT, the flow field becomes even more complicated. The chapters above showed that BEM method may not predict accurately in a complex yaw and shear conditions. Therefore, whether BEM method can be used to predict aerodynamic characteristic of FOWT is significant to detect. Translational and rotational motions introduce additional effective wind contributions. Platform pitching and surging motions, will result in the rotor rarely operating in a purely axial flow - the wind will generally appear skewed with respect to the rotor. Another consideration is the change ineffective wind speed across the rotor due to the introduction of an effective wind shear, which is a result of platform pitch and surge. Aside from the changes in effective wind direction and magnitude, the additional DOFs associated with a floating wind turbine introduce additional unsteadiness to the flow, which limits the analysis methods that may be employed. There are very little publicly available data on operational offshore floating wind turbines because of the limited number of deployed systems and their proprietary nature.

8.2 Case Conditions

As discussed in chapter 5, we chose three different platform pitching frequencies and angles, below –rated, rated and sever sea state and two platform types, respectively. Hence the simulation motion can be defined as a simple harmonic platform motion. The simulation of the operating condition is defined by a wind speed of 8 m/s and 11 m/s and a rpm of 9.16 and 12.1, respectively (Thanhtoam, 2014).

The inputs are divided into four distinct regions, corresponding with four quadrants of the wave phase space, for comparison: R1 (wave crest) is at maximum downstream velocity and mean positions, R2 (mean wave height, decreasing) is at zero stream-wise velocity and maximum downstream platform positions, R3 (wave trough) is at maximum upstream velocity and mean position, and R4 (mean wave height, increasing) is at zero stream-wise velocity and maximum upstream position.

The case conditions shown in table 8.1 used to set-up the CFD simulations were computed by FAST. Chapter 5 had a detailed description. The case output values are given in table 8.2 -8.3. Aerodynamic performance with different platform motions was compared with FAST results. Pitch, surge and pitch-surge combined motions were calculated separately to detect the platform motions effect on the rotor blade. The tower, hub and nacelle might cause the flow interference between them and turbine rotors. Therefore, three simulations are performed, each using configuration displayed in figure 8.1. A theoretical maximum configuration utilizes only the rotor. The other two simulations use the full system. The first of these latter two simulations has the rotor set at the 1.912m overhang, referred to as the "1*Overhang" simulation. The final simulation doubles the overhang (3.824m) to determine the effect of moving the rotor farther from the tower. This simulation is referred to as the "2*Overhang" simulation.

Table 8.1 Wind and sea state definitions for FAST simulations

	U_∞ m/s	Ω	H_s (m)	T_p (s)
Below-rated	8	9.16	1.83	12.72
Severe sea condition	8	9.16	5	8
Rated	11.4	12.10	2.54	13.35

Table 8.2 Output from FAST of Spar platform

Wind speed (m/s)	Ω (rpm)	Platform Pitching Amplitude (deg)	Platform Mean Pitch Angle (deg)	Platform Surge Amplitude (m)
8	9.16	0.336	2.5	0.7
8	9.16	0.36	5	0.65
11.4	12.10	0.49	5	1.14

Table 8.3 Output from FAST of TLP platform

Wind speed (m/s)	Ω (rpm)	Platform Pitching Amplitude (deg)	Platform Mean Pitch Angle (deg)	Platform Surge Amplitude (m)
8	9.16	0.0445	0.098	0.656
8	9.16	0.3535	0.0978	0.737
11.4	12.10	0.055	0.186	0.85
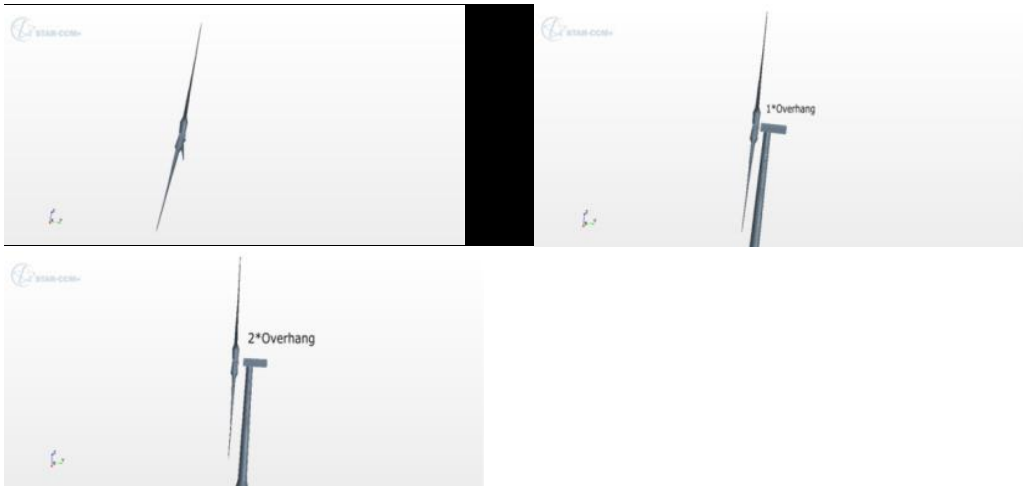
Figure 8.1 Three different configurations used

8.3   Simulation Settings

The specific profiles of NREL 5-MW wind turbine and spar and TLP platforms are described in Chapter 5. As the results compared with the rotor-only and whole (with hub, nacelle and tower) turbine, here, figure 8.2 - 8.4 show the geometric details in the STAR CCM+ software. The simulation setting and grid conception were shown in chapter 7. Figure 8.5 describes the grid design for whole wind turbine. The total number of cells in the numerical grid was approximately 28 million. The motion technique was used to simulate the moving rotor blade and platform motions. Other condition settings were the same as chapter 6 described. The pitching and surging motion due to the pitching and surging DOF modes of a platform is given as the following equation assumes as a sine function with an amplitude (*h*) and frequency (*f*).

$$\theta_{pitch} = h_{pitch}.\sin(2\pi f.t) \tag{8.1}$$

$$\theta_{surge} = h_{surge}.\sin(2\pi f.t + \varphi) \tag{8.2}$$
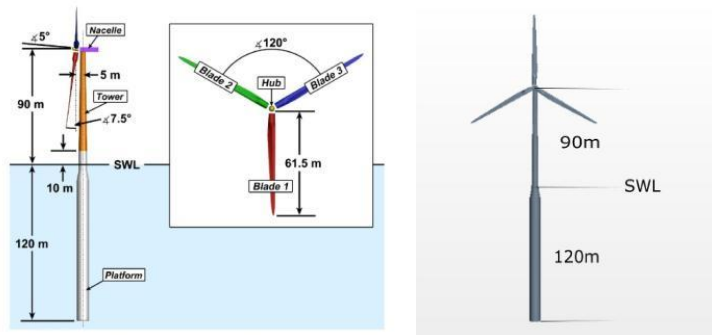
Figure 8.2 Overall OC3-Hywind geometric details
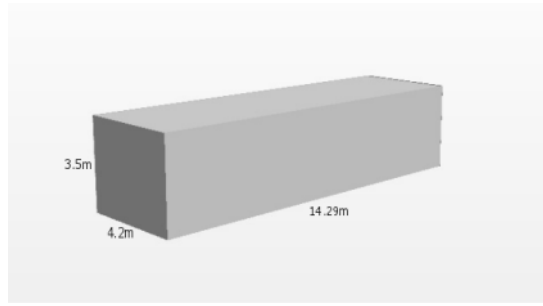
Figure 8.3 Nacelle geometry   Figure 8.4 Hub geometry
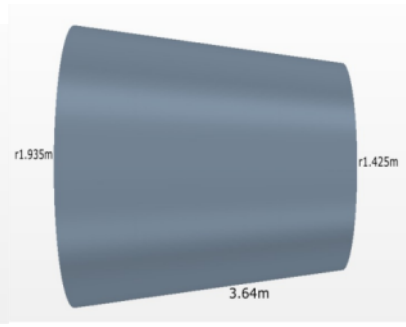
Figure 8.5 Grid design for CFD simulations

8.4   Induction Factors with CFD Results

The axial and the tangential induction factors are two most important factors that a BEM code calculates iteratively. The axial induction factor a_1 and tangential induction factor a_2 are defined as follows:

$$a_1 = 1 - \frac{u_x}{U_\infty} \tag{8.3}$$

$$a_2 = \frac{u_\theta}{r\Omega} \tag{8.4}$$

Where the velocities u_x and u_θ are the velocities which are intrinsically calculated as part of solution iteration.

The CFD based approach to calculate the Induction factors is a first step towards the verification of these values when complex turbine motions are involved. The approach involves the calculation of the forces on the wind turbine blades with high fidelity CFD simulations and extracts the elemental force values. These values are compared with the forces from the BEM equations and the induction factors are derived. The two equations used for the above mentioned approach are the thrust and the torque equations. The elemental torque and the elemental thrust equations used in BEM along with the loss factors are given in equations (8.5) and (8.6) respectively.

$$dM = 4\pi r^3 dr \rho U_\infty F (1 - a_1) a_2 \Omega \tag{8.5}$$

$$dT = 4\pi r dr \rho U_\infty^2 F(1-a_1)a_1 \qquad (8.6)$$

Both axial and tangential induction factors can be evaluated using the two equations. The axial induction factors were calculated by equating the thrust equations with the elemental thrust values obtained with CFD, as given in equation (8.7). There are two solutions possible for the induction factors with the thrust equation. The choice of the solution for the induction factor is quite clear in the thrust equation as one root is <0.5 and the other is > 0.5. All the roots <0.5 were chosen in compliance with FAST. The axial induction factors thus obtained were used with the elemental torque equation and equated with the elemental torque values obtained from CFD data to calculate the tangential induction factors as given by equation (8.8).

$$a_1(1-a_1) = \frac{dF_{CFD}}{4\pi r dr \rho U_\infty^2 F} \qquad (8.7)$$

$$a_2 = \frac{dT_{CFD}}{4\pi r^3 dr \rho U_\infty F(1-a_1)\Omega} \qquad (8.8)$$

F is the total loss factor. $F = F_t \times F_h$

F_t is the Prandtl tip loss.

$$F_t = \left(\frac{2}{\pi}\right) \cos^{-1}(e^{-f_t}) \qquad (8.9)$$

Where $f_t = \frac{B(R-r)}{2rsin\phi}$

F_h is the Hub losses:

$$F_h = \left(\frac{2}{\pi}\right) \cos^{-1}((e^{-f_h}) \qquad (8.10)$$

Where $f_h = \frac{B(r-Rhub)}{2rsin\phi}$

B is the number of blades, R is the rotor radius, r is the elemental radius and φ is the local flow angle.

8.5   Grid Sensitive

The verification is to confirm that we solve the equation correctly by checking if the solutions are consistent with the governing equations and initial and boundary

conditions that have been used. The accuracy of numerical results significantly depends on the number of grids and time step chosen for each problem. Thus, the proper grid system and time step are needed to be verified before large numerical cases to be simulated. The mesh independence was carried out using the grid convergence index (GCI) method which defined in the chapter. The turbine condition at wind speed =8m/s is considered for this study. Three grades of mesh refinement are used. Five interrogation points are arbitrarily used at different locations in the flow field in order to find the GCI at these locations. The axial velocity is considered in this analysis. Table 8.4 shows various quantities of interest including the GCI for all points considered from A to E. The coordinates of the points are also shown in Figure 8.6. Values of the GCI all fall below 6%, which is acceptable for this work. This ensured that the level of grid refinement is enough to ensure that the solution is independent of the grid size.

Table 8.4 Grid convergence analysis results

	A (10m,60m)	B (200m,60m)	C (10m,20m)	D (200m,20m)	E (-30m,70m)
Ux1 increase	4.89	7.38	6.57	6.46	7.66
Ux2 fine	5.05	7.41	6.64	6.50	7.67
Ux3 decrease	5.10	7.52	6.78	6.62	7.70
δ_G^* (%)	3.27	0.41	1.07	0.62	0.13
Fine GCI	5.95	0.20	1.33	0.39	0.08
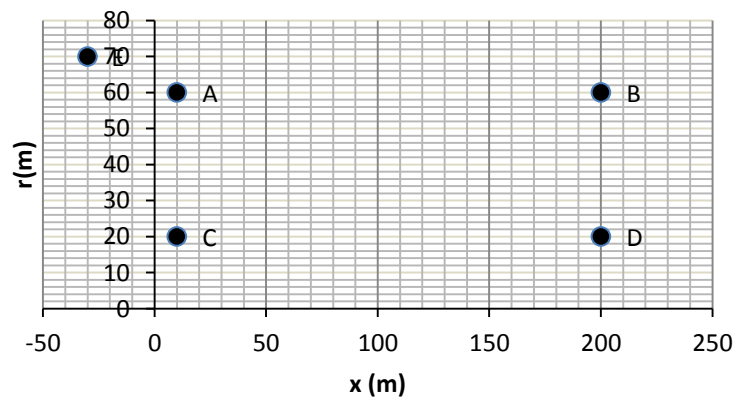
Figure 8.6 Coordinates of the points A to E used in the grid convergence

8.6   Results and Discussion

Classical BEM characterise the airfoil sections in terms of parameters describing local flow and forces. These include the sectional angle of attack (AOA), axial induction factor (a_1) and tangential induction factor (a_2), lift (C_l) and drag (C_d) coefficients, normal (C_n) and tangential (C_t) induction coefficients. CFD results can be inspected to obtain these airfoil parameters, though the definition of some of them makes evaluation somewhat ambiguous.

8.6.1   Unsteady aerodynamic effect with different simulation methods

The flow separation region near the blade root is shown in contour plots in Figure 8.7. The mesh behind the rotor was refined to capture the wake correctly. Figure 8.8 shows the tip vortices. The flow separation of the suction and pressure side by the pressure contour was shown in Figure 8.9. All the contours describe the flow characteristics behind the rotor for a case of 8 m/s wind. The floating wind turbine shows an unsteady flow field, similar to turbulent wake state. We examined the cause of the turbulent wake state. An unsteady flow arises from platform pitching motion in the downward direction. During this movement, the induction factor is very high at the top of the rotor plane.
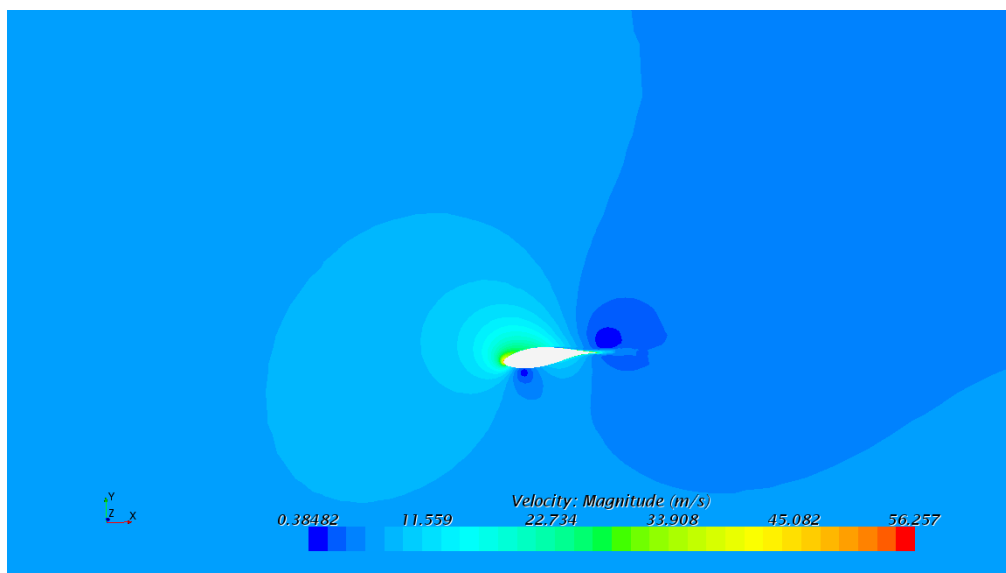
Figure 8.7 Velocity contour plot showing the flow separation
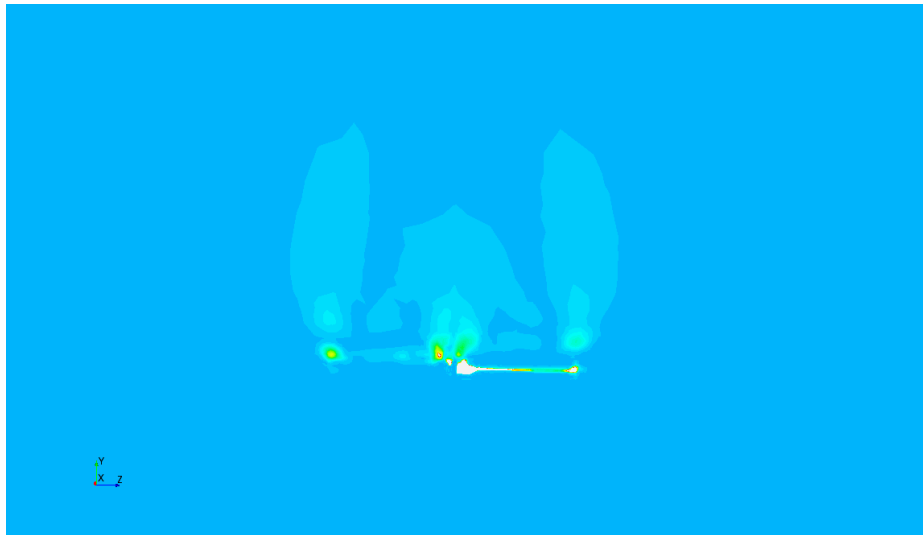
Figure 8.8 Vorticity contour showing the tip vortices
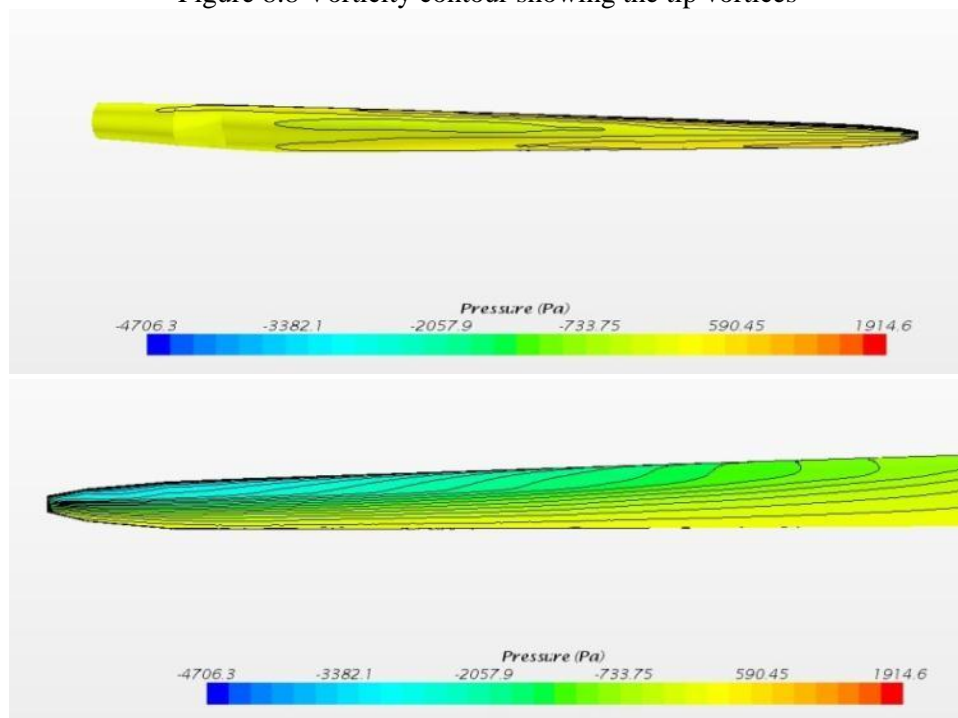
Figure 8.9 Pressure contours show flow separation of suction and pressure side

Figure 8.10-8.12 show the comparison of the unsteady aerodynamic power and thrust responses among the CFD and FAST solvers for the pitch, surge and pitch-surge combined motions at the wind speed of 8m/s and 11.4m/s, respectively. Table 8.5-8.7 described the maximum, mean and minimum power and thrust compared with three different methods at three different platform motions according to the curves. It is observed from these plots that the power calculated with the FAST match quite well with the CFD results. All the differences are smaller than 15%. Compared with three

motions, P-S combined motion reached the maximum divergence. Moreover, FAST with BEM approach underestimated these values compared to the FAST with GDW, especially the peak area of additional velocity. The unsteady CFD can effectively predict the aerodynamic the aerodynamic wake effect better than other numerical approaches. Consider the viscous effect and vortex wake, and real blade rotation about a hub centre can account for the flow field interaction. CFD method produces the lowest estimation of aerodynamic power responses.

At the 1/4T (T means period of platform's pitch oscillation), aerodynamic power tends to increase because the additional velocity increases and make the strong interaction between the rotor blades and wake regime. However, at the 4/4T, the aerodynamic power phenomenon is reversed due to the decreasing of the additional velocity. At the 2/4T and 3/4T, weak wake interactions between the rotor blades and its wake. Therefore, the additional velocity contribution and non-axial angle maintain a key role in the aerodynamic performance.
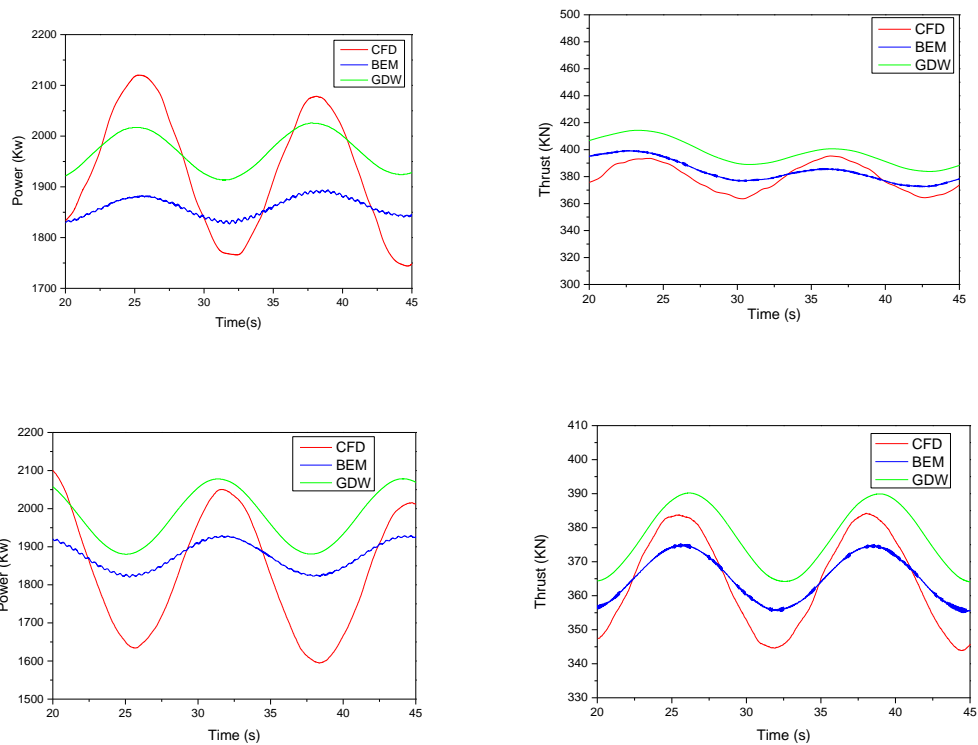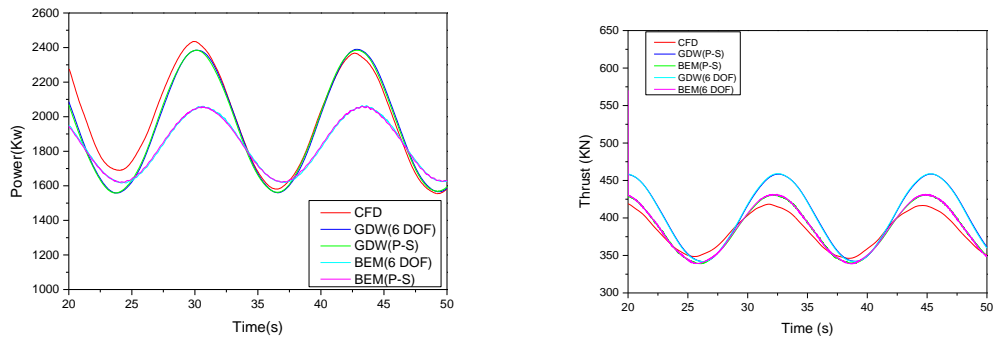
Figure 8.10 Power and thrust curve at below-rated condition (pitch, surge and pitch-surge for row 1, 2, 3)
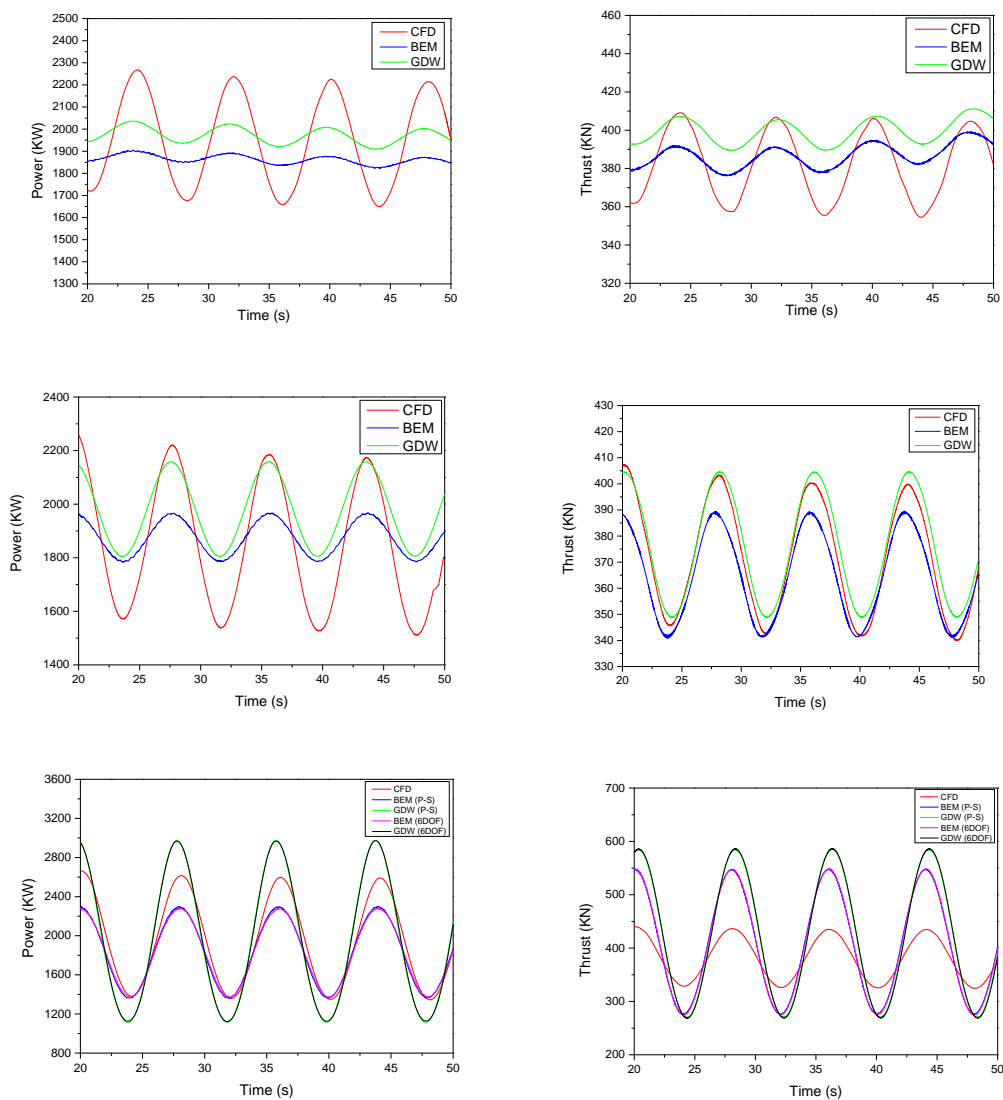
Figure 8.11 Power and thrust curve at sever condition (pitch, surge and pitch-surge for row 1, 2, 3)
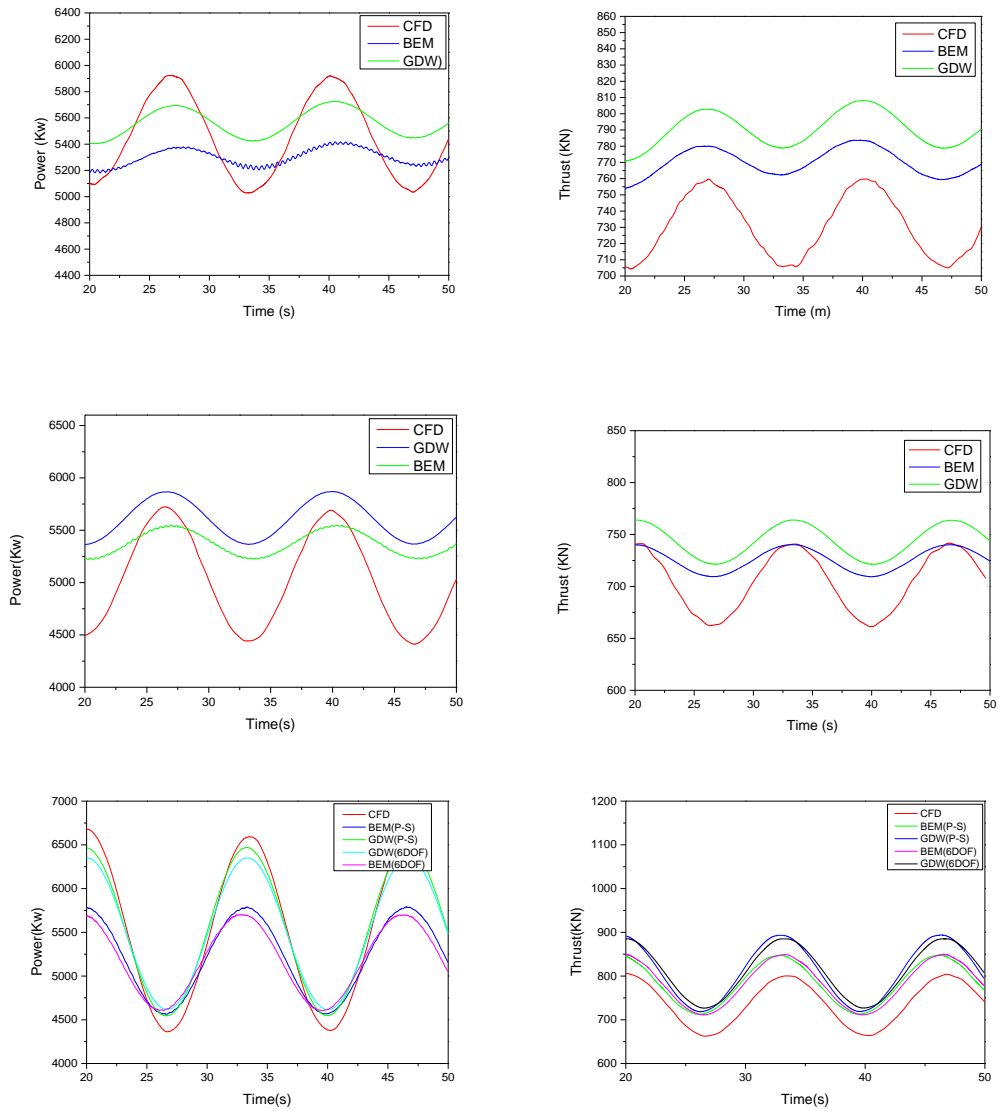
Figure 8.12 Power and thrust curve at rated condition (pitch, surge and pitch-surge for row 1, 2, 3)

Table 8.5 Power and thrust comparison with different methods at pitch condition

Pitch Power (KW)										
	Condition	Maximum			Mean			Minimum		
		CFD	BEM	GDW	CFD	BEM	GDW	CFD	BEM	GDW
1	Below	2077	1890	2020	1914	1860	1970	1750	1828	1914
2	Severe	2238	1904	2023	1960	1875	1950	1965	1849	1936
3	Rated	5955	5417	5726	5464	5325	5581	5035	5231	5449
		Below-rated			Severe sea condition			Rated		
		Max	Mean	Min	Max	Mean	Min	Max	Mean	Min
Difference % (CFD vs BEM)		9.0	2.8	4.5	15	4.3	5.9	9.0	2.5	3.9
Difference % (CFD vs GDW)		2.7	2.9	9.4	9.7	0.5	1.5	3.9	2.1	8.2

Pitch Thrust (KN)									
	Condition	Maximum			Mean			Minimum		
		CFD	BEM	GDW	CFD	BEM	GDW	CFD	BEM	GDW
1	Below	395	399	414	381	388	401	363	372	385
2	Severe	407	399	411	384	383	399	356	372	389
3	Rated	760	780	808	732	772	794	706	760	779
		Below-rated			Severe sea condition			Rated		
		Max	Mean	Min	Max	Mean	Min	Max	Mean	Min
Difference (%) (CFD vs BEM)		1.0	1.8	2.4	2.0	0.3	4.5	2.6	5.5	7.7
Difference (%) (CFD vs GDW)		4.8	5.3	6.1	1.0	4.0	9.3	1.0	8.5	10.3

Table 8.6 Power and thrust comparison with different methods at surge condition

Surge Power (KW)									
	Condition	Maximum			Mean			Minimum		
		CFD	BEM	GDW	CFD	BEM	GDW	CFD	BEM	GDW
1	Below	2015	1929	2078	1780	1878	1981	1578	1822	1881
2	Severe	2183	1965	2158	1865	1892	1992	1527	1788	1807
3	Rated	5692	5870	5547	5012	5620	5393	4415	5368	5229
		Below-rated			Severe sea condition			Rated		
		Max	Mean	Min	Max	Mean	Min	Max	Mean	Min
Difference (%) (CFD vs BEM)		4.3	5.5	15.5	10.0	1.5	17.0	3.1	12.1	21.6
Difference (%) (CFD vs GDW)		3.1	11.3	19.2	1.1	6.8	18.3	2.6	7.6	18.4

Surge Thrust (KN)									
	Condition	Maximum			Mean			Minimum		
		CFD	BEM	GDW	CFD	BEM	GDW	CFD	BEM	GDW
1	Below	384	375	390	364	364	377	344	355	364
2	Severe	400	389	405	373	365	375	342	341	349
3	Rated	742	750	764	700	725	743	661	709	722
		Below-rated			Severe sea condition			Rated		
		Max	Mean	Min	Max	Mean	Min	Max	Mean	Min
Difference (%) (CFD vs BEM)		2.3	0	3.2	2.8	2.2	0.3	1.1	3.6	7.3
Difference (%) (CFD vs GDW)		1.6	3.6	5.8	1.3	0.5	2.1	3.2	6.1	8.5

Table 8.7 Power and thrust comparison with different methods at P-S condition

P-S Power (KW)									
	Condition	Maximum			Mean			Minimum		
		CFD	BEM	GDW	CFD	BEM	GDW	CFD	BEM	GDW
1	Below	2366	2061	2389	1979	1836	1950	1556	1625	1566
2	Severe	2560	2281	2971	1997	1822	2013	1348	1374	1129
3	Rated	6591	5702	6349	5452	5155	5463	4384	4607	4618
		Below-rated			Severe sea condition			Rated		
		Max	Mean	Min	Max	Mean	Min	Max	Mean	Min
Difference (%) (CFD vs BEM)		12.9	7.2	4.4	10.9	8.8	1.9	13.5	5.5	5.1
Difference (%)		1.0	1.5	0.6	16.0	0.8	15.7	3.7	0.2	5.3

(CFD vs GDW)										
P-S Thrust (KN)										
	Condition	Maximum			Mean			Minimum		
		CFD	BEM	GDW	CFD	BEM	GDW	CFD	BEM	GDW
1	Below	417	431	459	379	382	398	346	339	342
2	Severe	435	548	586	379	412	427	326	276	269
3	Rated	800	849	885	735	784	802	664	712	727
		Below-rated			Severe sea condition			Rated		
		Max	Mean	Min	Max	Mean	Min	Max	Mean	Min
Difference (%) (CFD vs BEM)		3.4	0.8	2.0	26.0	8.7	15.3	6.1	6.7	7.2
Difference (%) (CFD vs GDW)		10.1	5.0	1.2	34.7	12.7	17.5	10.6	9.1	9.5

8.6.2 Unsteady aerodynamic effect with different platform motions

Pitch and surge motions will cause a phase difference in a real situation. Figure 8.13 showed power results in different phase angles of pitch and surge. We can find that the times to get the maximum and minimum point are different. Here, 180 degrees was chosen to compare with other platform motions. Figures 8.14-8.16 were the power and thrust curves at different wind speeds.
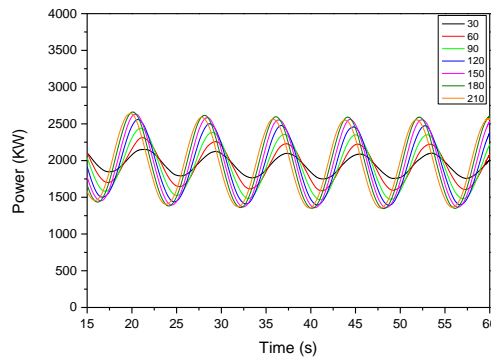
Figure 8.13 Power of different phases
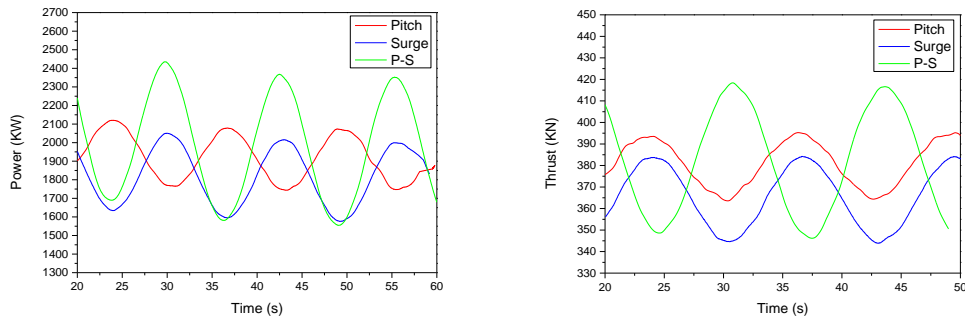
Figure 8.14 Power and thrust curve at below rated condition
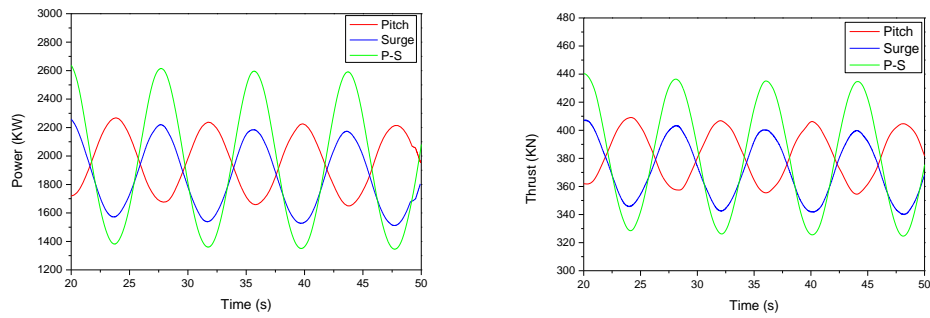
Figure 8.15 Power and thrust curve at sever condition
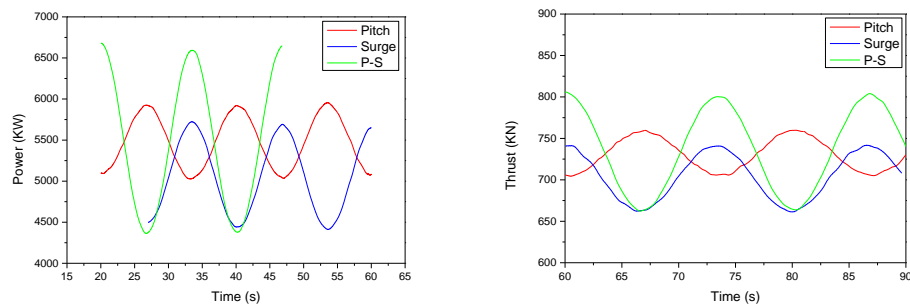
Figure 8.16 Power and thrust curve at rated condition

8.6.3 Unsteady aerodynamic effect compared with onshore and offshore

I investigated the sectional thrust and power compared between the offshore and onshore wind turbine and the CFD approach and FAST code as shown in Fig.8.17-818. As can be shown in figures, the largest forces occurred at the 3/4 blade which was agreed with the theory. Compared the CFD result first, at the low wind speed (8m/s), the platform pitch motion made the flow complex which increasing the aerodynamic load. However, at the high wind speed (11.4m/s), the phenomenon was reversed. The platform motion made the negative effect which decreasing the thrust and power. Then, the data from FAST code showed a big difference. The results did not change a lot when the wind turbine got a pitch motion, because the BEM method cannot predict the platform motion effect on the aerodynamic performance of the rotor accurately. Overall, FAST code underestimated the results than CFD approach, particularly near the blade tip. This may due to the fact that the loads here are influenced significantly by the tip loss factors used along with the BEM equations.

The angle of attack was calculated by the equations introduced in chapter 7. Compared with the onshore results, the biggest difference was shown at 15m of the

blade. Moreover, the difference between CFD and BEM is larger than that of onshore condition. It is proved again that BEM may not predict the aerodynamic performance in a complicated motion condition

The axial induction factors were calculated by equating the BEM based thrust equations with the CFD thrust data for every element. These values were later substituted into the BEM based power equations and equated with the CFD power values at each element to obtain the tangential induction factors for each element. The plots comparing the axial and tangential induction factors are given in figure 8.20 for two different wind cases. The variation in the axial induction factors near the tip arises due to the variation of thrust. It may be due to the tip loss factors included in the BEM code. Also, a small variation in the axial and tangential induction factors is noticed near the hub. This is due to the factor that there is no hub in the CFD based calculations. Overall, further investigations for prediction the validity of the tip loss factors and enhancing the same for FOWT applications are needed.
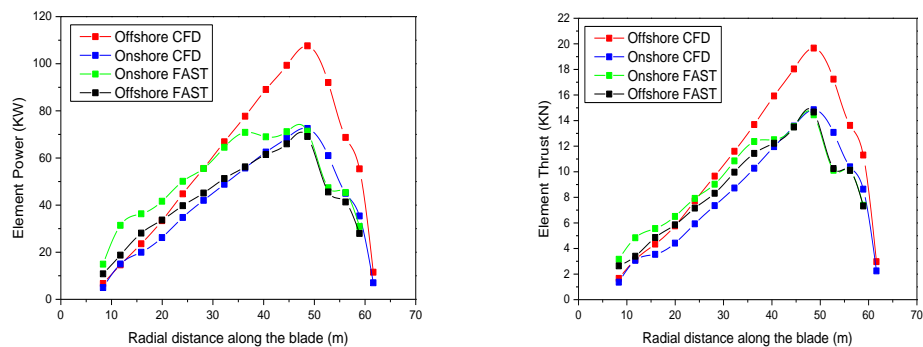
Figure 8.17 Element power and thrust at wind speed 8m/s
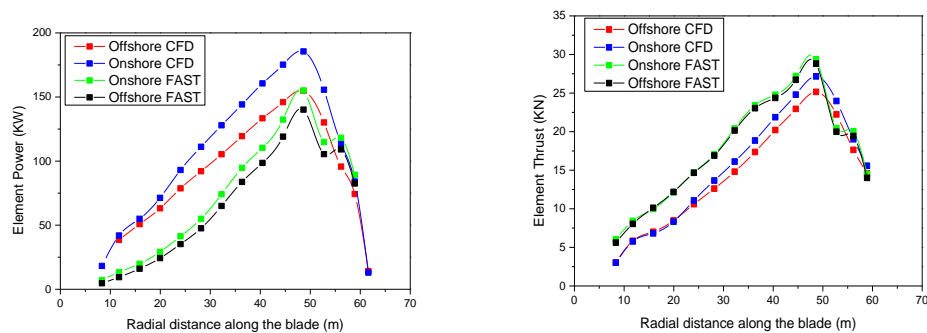
Figure 8.18 Element power and thrust at wind speed 11.4m/s
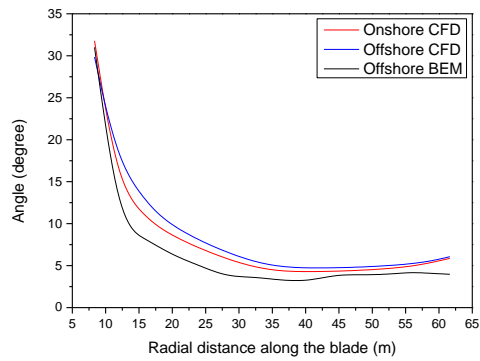
Figure 8.19 Angle of attack along the blade at severe condition
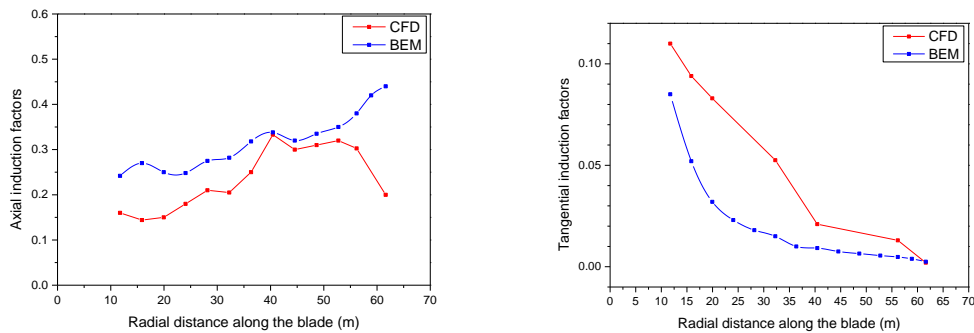
Figure 8.20 Axial and tangential induction factors along the blade

8.6.4 Wake evolution and induction

According to the Figure 8.21, we can find that the wake spreads about two times of radius. Strong tip and hub vortices are shown in figures 8.22-8.23. Notice that the vortices cannot be resolved beyond x/R=1. The trailing vortices exhibit the same characteristics as the tip vortices with very slight radial oscillatory motion. Compared with the onshore vortices, the hub vortices are more clearly. Contour plots of the resulting velocity field at hub and tip during different time instances of 0T, (1/4)T, (1/2)T, and (3/4)T where T is the motion period are shown in figure 8.24. Compared with the onshore wind turbine, the velocity is tilt. The velocity flow varies from different time instances.

Axial velocity on lateral traverses at X/D=1 and 2 of four different times are shown in figure 8.25 which provide insight on the general wake behaviour downstream of the rotor. The variation results arise. It is asymmetric and varies with time which is different from the onshore condition. Figure 8.26 and 8.27 describes the horizontal

profiles. The farther the distance, the bigger the difference of the two sides is. Compared with onshore wind turbine, the axial velocity profiles of offshore condition shows more complicated. The unit axial velocity differs with inflow velocities. The larger the inflow velocity, the larger the wake expansion is.
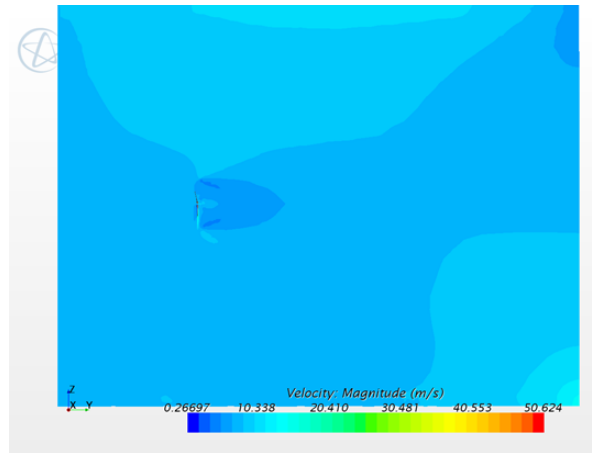
Figure 8.21 Velocity contour of the whole field at severe condition
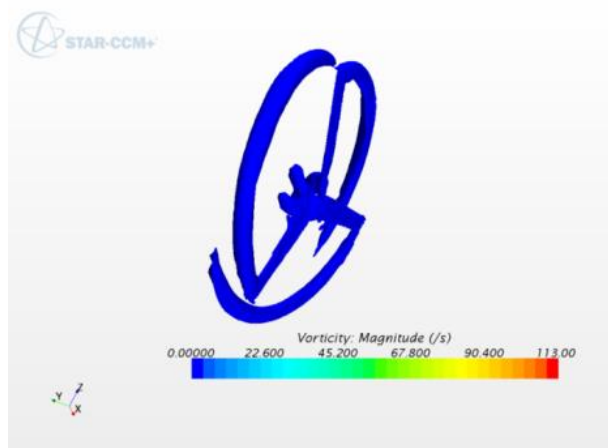
Figure 8.22 Vorticity contour of blade
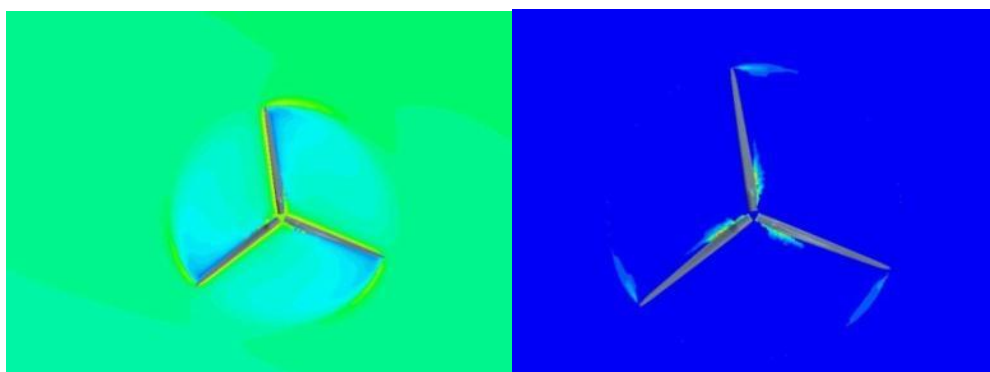
Figure 8.23 Velocity and vorticity contour of blade

0T

1/4T

1/2T

3/4T
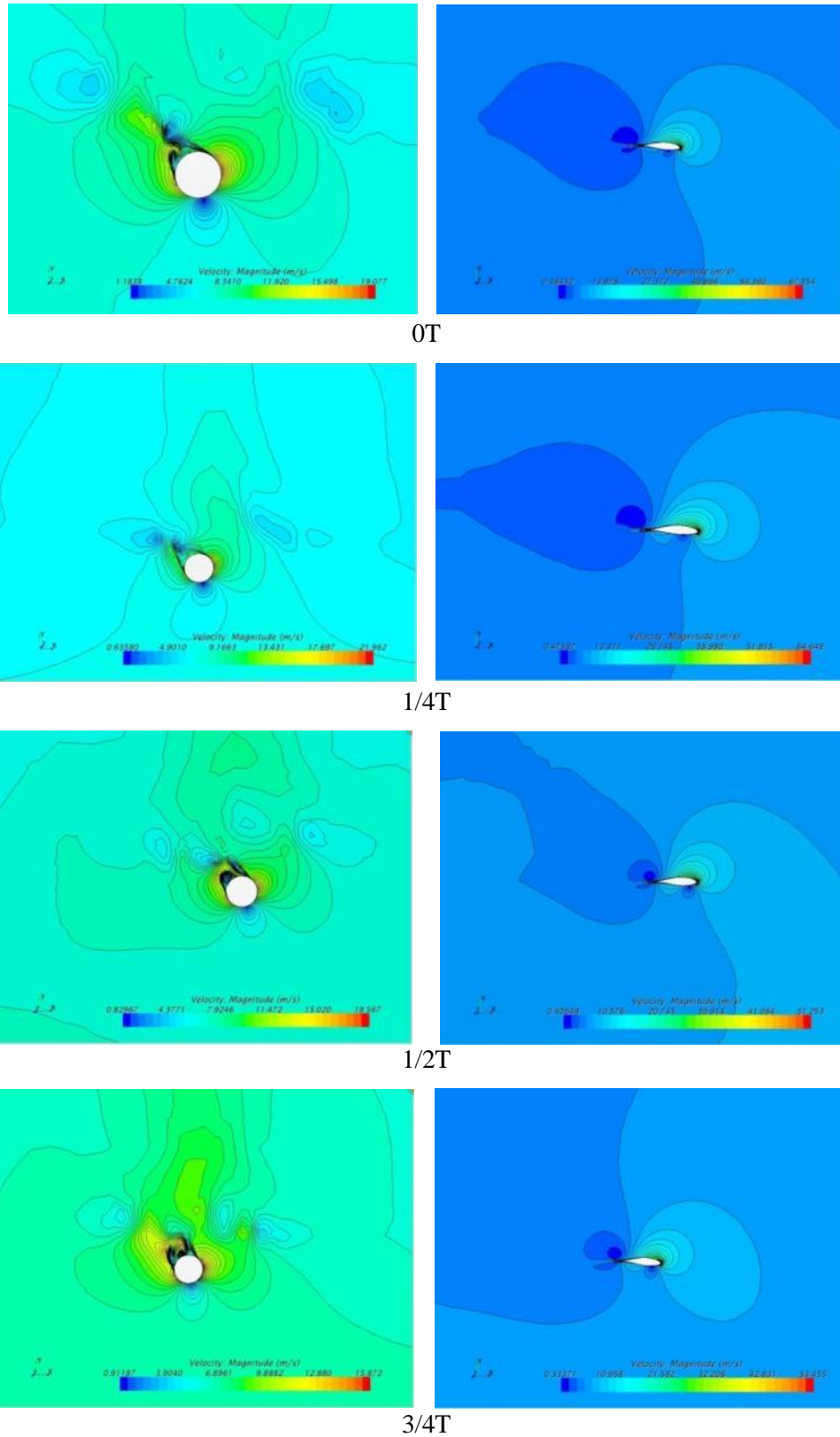
Figure 8.24 Velocity contour at blade root and tip
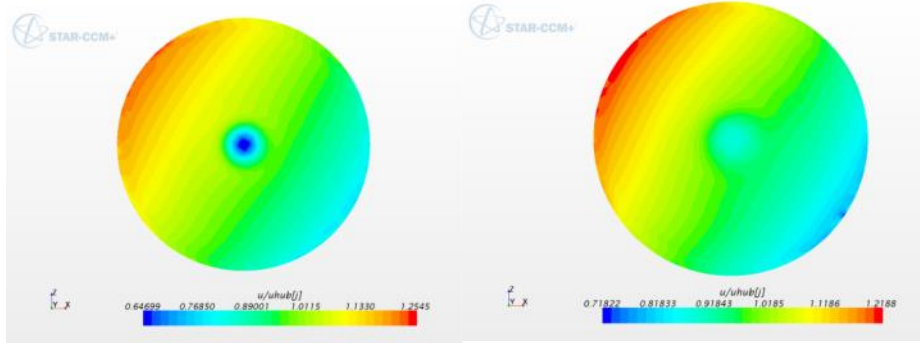
a. X/D=1   b. X/D=2 (0T)
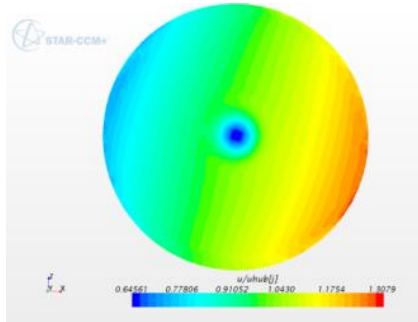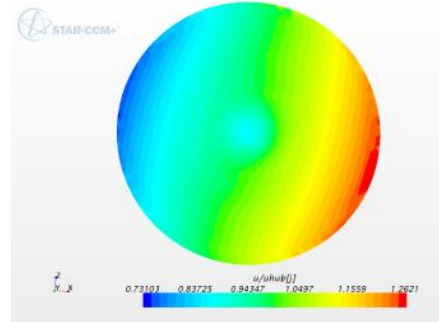
a. X/D=1   b. X/D=2 (1/4T)
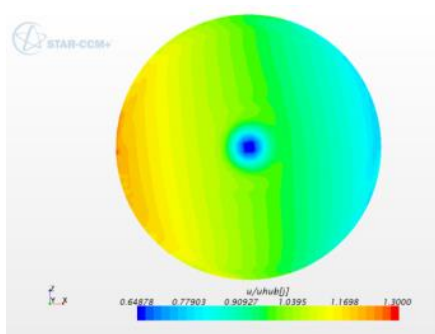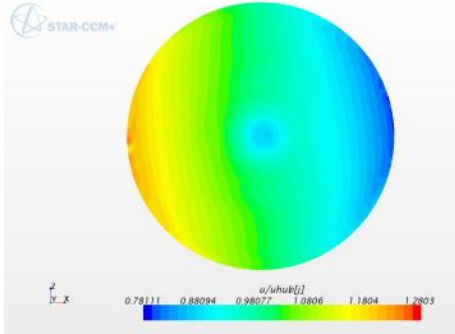
a. X/D=1   b. X/D=2 (1/2T)
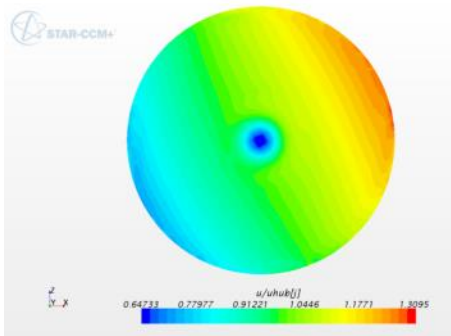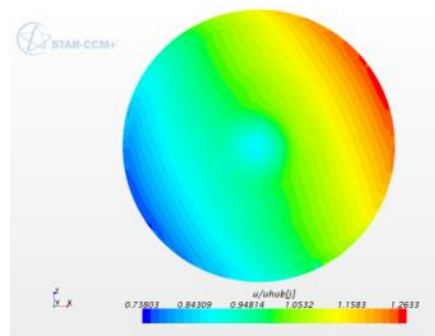
a. X/D=1   b. X/D=2 (3/4T)

Figure 8.25 Axial velocity at different time of X/D=1 and X/D=2
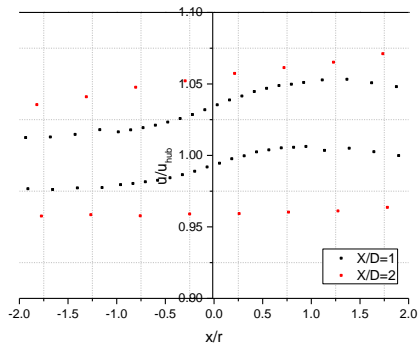
Figure 8.26 Horizontal profiles at X/D=1 and X/D=2
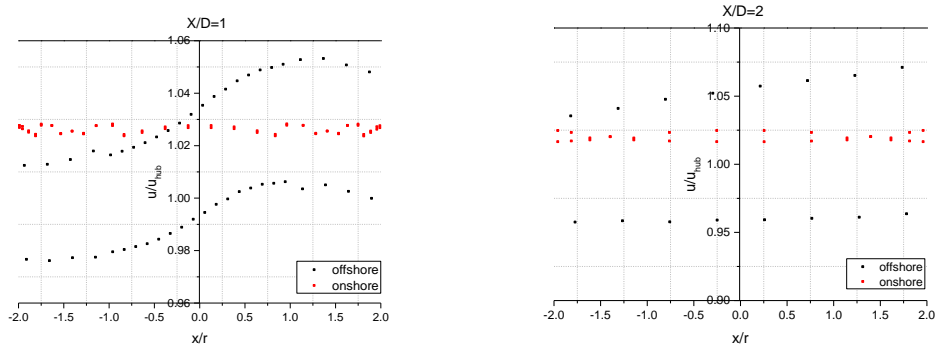
a. X/D=1   b. X/D=2

Figure 8.27 Comparison of horizontal profiles with onshore and offshore

Below Condition
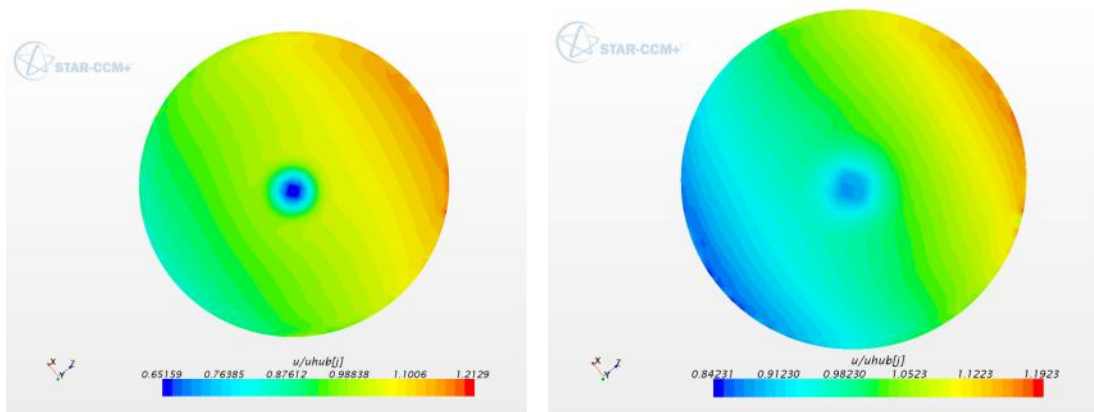
a. X/D=1   b. X/D=2 (0T)

Figure 8.28 Axial velocity at X/D=1 and X/D=2
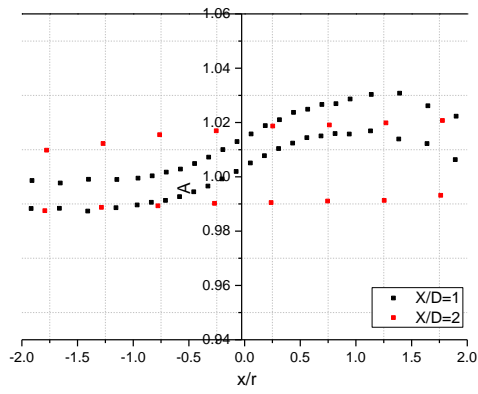
Figure 8.29 Horizontal profiles at X/D=1 and X/D=2

Rated Condition
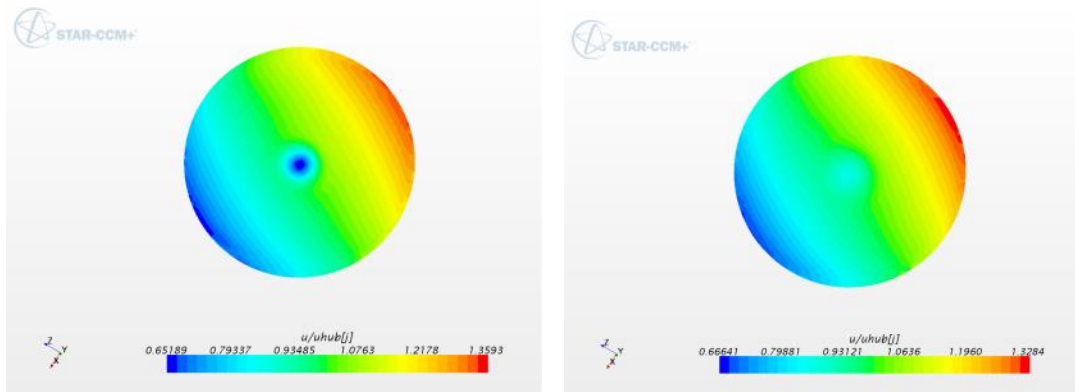
a.   X/D=1   b. X/D=2 (0T)

Figure 8.30 Axial velocity at X/D=1 and X/D=2
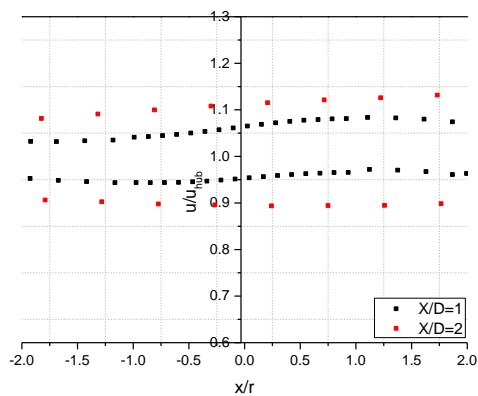
Figure 8.31 Horizontal profiles at X/D=1 and X/D=2

Time history of turbulent velocities for 2 points located at approximately hub height and centre of the turbine (y=0m and z=90m) and at different non-dimensional axial locations including the inlet of the simulation domain. The position at 1m and 5m are chosen to avoid the influence of the rotor and to ensure that the stream tube is not broken down due to viscous dissipation. It can be seen that for all locations the 3 velocities components fluctuate randomly around their expected mean velocities, 11m/s for u and 8m/s for v and w. The figure essentially shows that the turbulent field solved by CFD with the explicit wind turbulence at the inlet is appropriately transported through the whole simulation domain throughout the simulation, but turbulence decay due to viscous losses mentioned previously is observed, as velocities closer to the inlet tend to have larger fluctuations than more downstream locations.
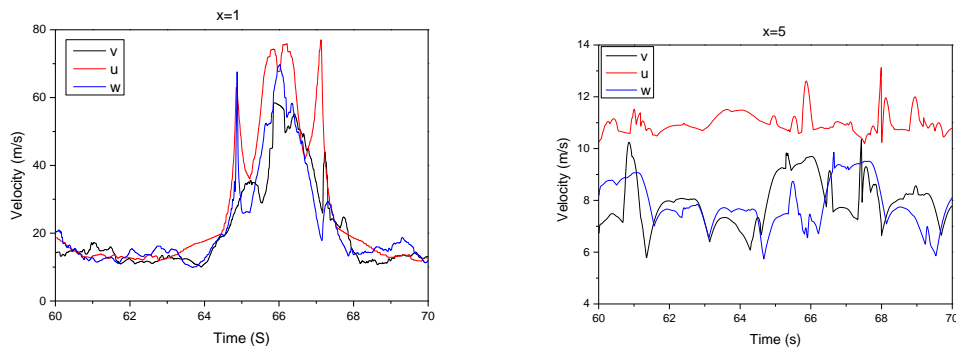
Figure 8.32 Time history of velocity

8.6.5 Rotor-tower effect

Shown from the Figure 8.33, the tower has little effect on the blade. There is almost no difference of power and thrust between the overhang 1 and overhang 2. The hub may influent the aerodynamic performance a little. It shows a 2% lower of power and thrust compared with no hub condition. The power and thrust of rotor only underestimates about 8% compared with the full system which can be explained by the velocity contours. Figure 8.36 indicates an obvious flow effect by the tower especially in the root part.
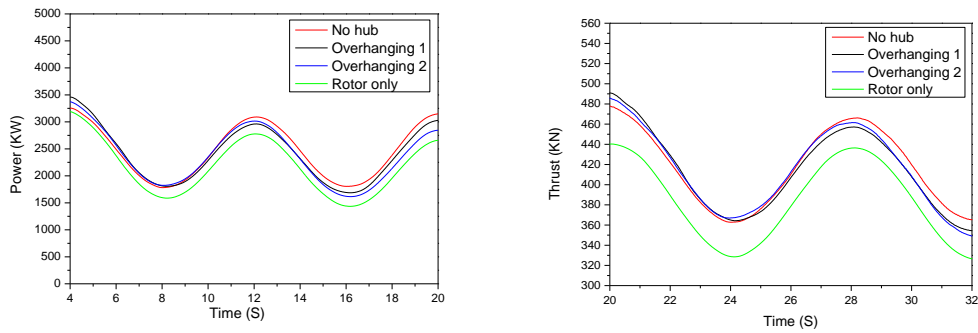
Figure 8.33 Comparison of power and thrust with different simulation models
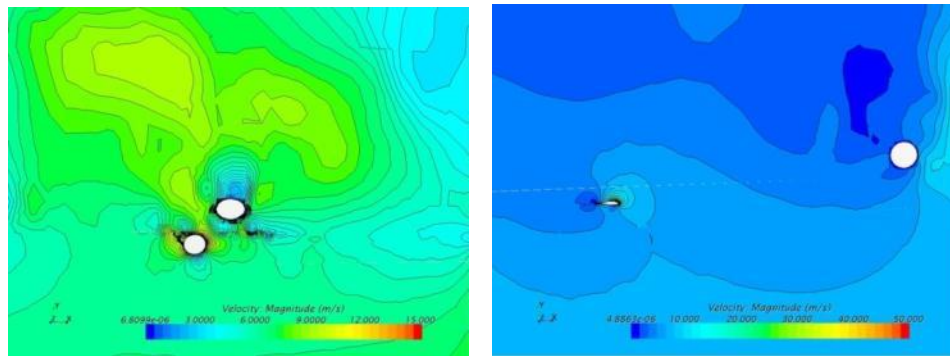
Overhang 1
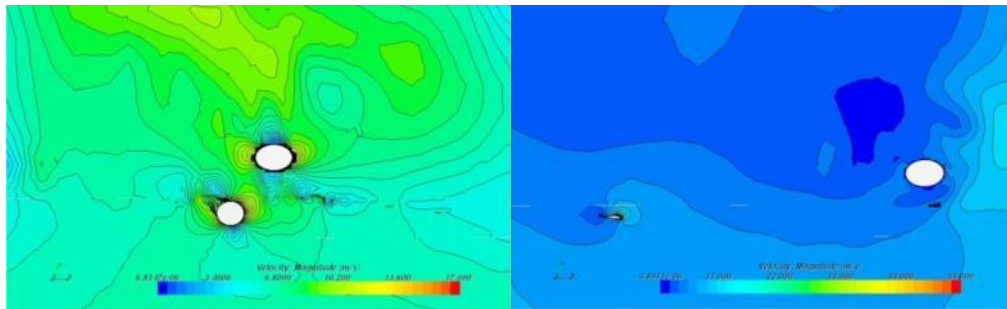
Overhang 2

Figure 8.34 Velocity contours of tip and root

8.6.6 Aerodynamic performance of TLP offshore wind turbine

Figure 8.35-8.37 show power and thrust curve of pitch-surge motions at different conditions. Compared with spar offshore wind turbine, the TLP offshore wind turbine showed smaller motions (pitch and surge combined motion) at the same wave and wind conditions. Therefore, the gap between the maximum and minimum values is relatively small. The TLP wind turbine showed smaller maximum power and thrust which meets the expectation. This indicates that the motions have an advantage effect on the aerodynamic characteristics on the other side. However, the

difference between the FAST and CFD cannot get a consistent discipline. It showed a larger difference in most conditions compared with spar wind turbine.
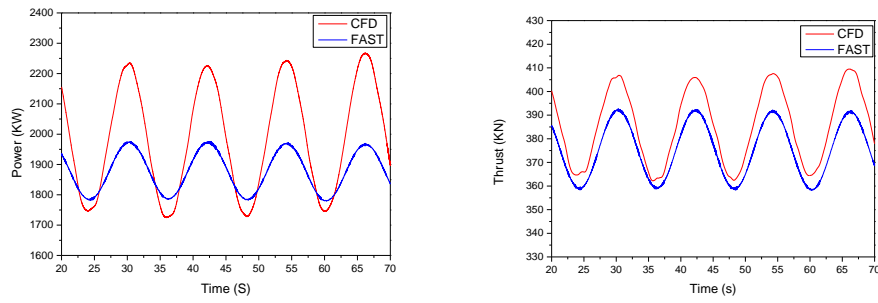
Figure 8.35 Power and thrust curve at below rated condition
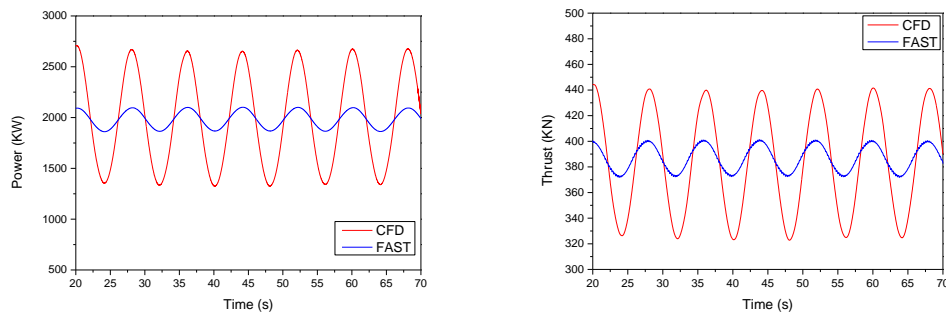
Figure 8.36 Power and thrust curve at severe condition
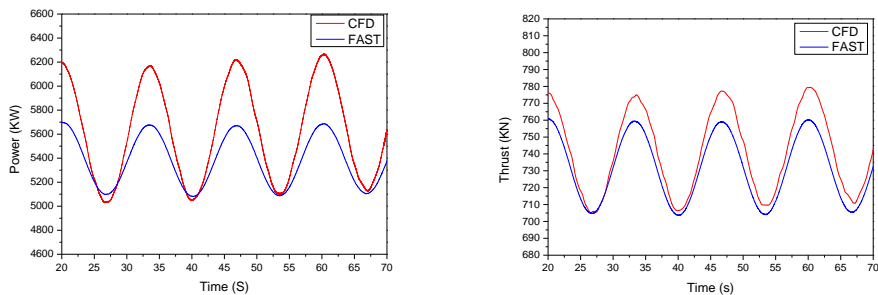
Figure 8.37 Power and thrust curve at rated condition

Table 8.8 Power and thrust comparison of different platform configurations

P-S Power (KW)									
	Max			Mean			Min		
	Below-rated	Severe sea condition	Rated	Below-rated	Severe sea condition	Rated	Below-rated	Severe sea condition	Rated
Spar	2366	2560	6591	1979	1997	5452	1556	1348	4384
TLP	2235	2710	6269	2000	1950	5600	1725	1324	5029
P-S Thrust (KN)									

	Max			Mean			Min		
	Below-rated	Severe sea condition	Rated	Below-rated	Severe sea condition	Rated	Below-rated	Severe sea condition	Rated
Spar	664	735	800	326	379	435	346	379	417
TLP	412	439	779	388	380	742	362	325	705

Table 8.9 Power and thrust comparison of different simulation methods

P-S Power (KW)									
	Max			Mean			Min		
	Below-rated	Severe sea condition	Rated	Below-rated	Severe sea condition	Rated	Below-rated	Severe sea condition	Rated
CFD	2235	2710	6269	2000	1950	5600	1725	1524	5029
FAST	1976	2101	5700	1880	1970	5390	1780	1859	5080
Differ TLP	11.6%	22.5%	9.1%	6.0%	1.0%	3.8%	3.2%	22.0%	1.0%
Differ Spar	1.0%	1.5%	0.6%	16.0%	0.8%	15.7%	3.7%	0.2%	5.3%
P-S Thrust (KN)									
	Max			Mean			Min		
	Below-rated	Severe sea condition	Rated	Below-rated	Severe sea condition	Rated	Below-rated	Severe sea condition	Rated
CFD	412	439	779	388	380	742	362	325	705
FAST	393	401	761	377	387	732	358	372	703
Differ TLP	4.6%	8.7%	2.3%	2.8%	1.8%	1.4%	1.1%	14.5%	0.3%
Differ Spar	10.1%	5.0%	1.2%	34.7%	12.7%	17.5%	10.6%	9.1%	9.5%

8.6.7   Shear effect

The general trends are similar to those with uniform wind shown in figure 8.38, but the mean thrust and power are about 12% upper.

The individual blade behaviour, exhibits a significant increase in normal and tangential force when the blade is at the top and a decrease when the blade is at the bottom, as expected shown in figure 8.39. A logarithmic wind velocity distribution immediately results in higher AOAs when the blade is at the top and the incoming wind speed is higher, with a dramatic decrease when the blade is at the bottom. Figure 8.40 and 8.41 show the velocity contours which indicates a more complex phenomenon. The velocity distribution is not clear. Figure 8.42 and 8.43 indicate time history of point velocities components. The trend is similar, while it fluctuates more complicated.
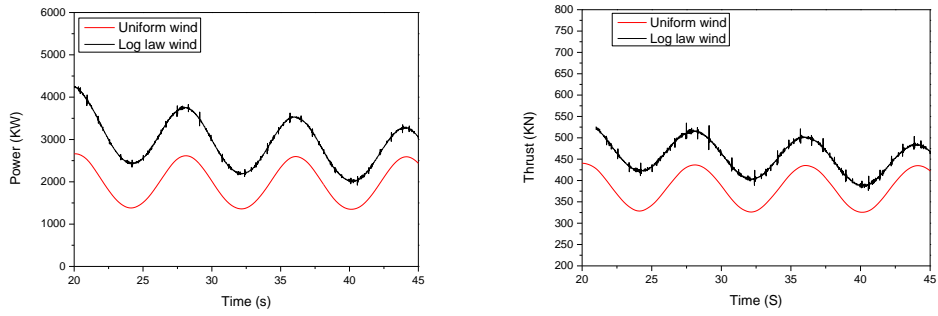
Figure 8.38 Power and thrust
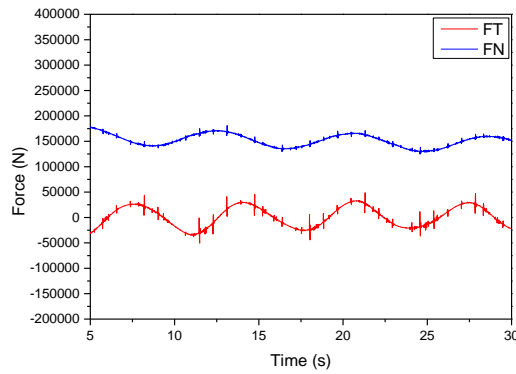
Figure 8.39 Normal and tangential force on blade 1
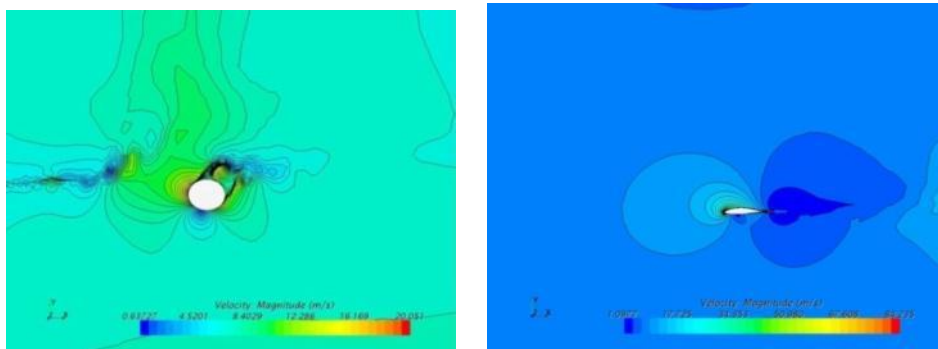
Figure 8.40 Root and tip velocity contours

a. X/D=1   b. X/D=2
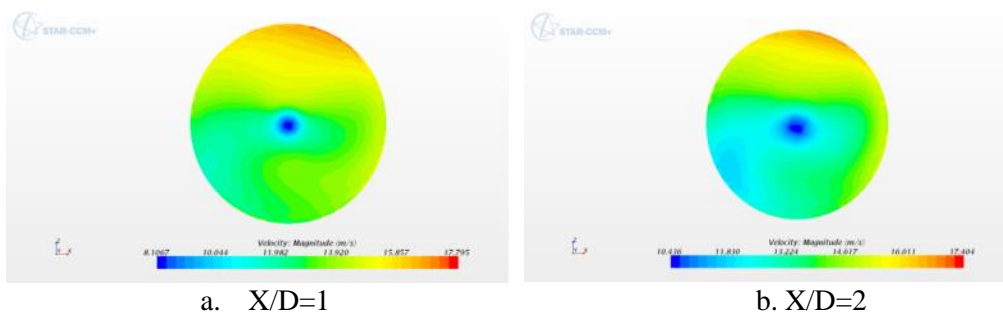
Figure 8.41 Axial velocity contours
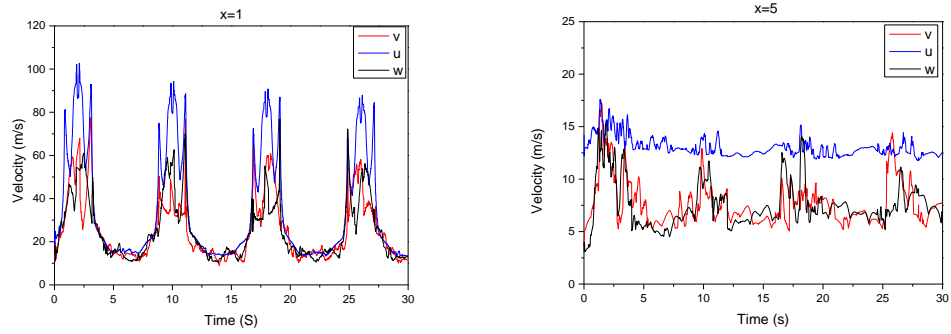
Figure 8.42 Time history of mean velocity
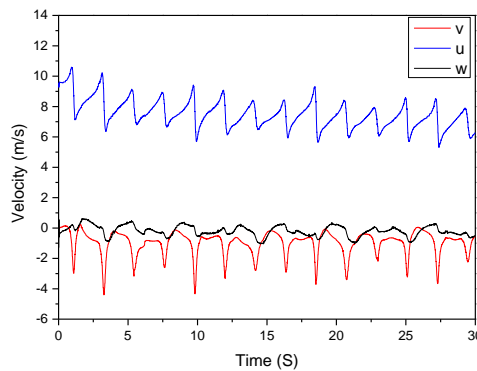
Figure 8.43 Time history of maximum velocity at hub point

8.7   Conclusion

Three different case conditions (below rated, rated and severe) are chosen to simulate and analyse aerodynamic characteristics of FOWT in this chapter. Pitch, surge and pitch-surge combined motions are calculated separately to detect the platform motions effect on the rotor blade. The pitching and surging motions are given as the following equations: $\theta_{pitch} = h.\sin(2\pi f.t)$ and $\theta_{surge} = h.\sin(2\pi f.t + \varphi)$.

The tower, hub and nacelle may cause the flow interference between them and turbine rotors. Therefore, three different configurations are used. After grid sensitive confirmation, several results and conclusions are received.

First, when compared with BEM and GDW solvers, power and thrust match well with CFD results. All the discrepancies are smaller than 15%. Pitch and surge combined motions reach the maximum difference. Moreover, BEM approach underestimate these values compared with GDW, while CFD method produces the lowest estimation. In addition, pitch and surge motions cause a phase difference in a

real situation. Therefore, the times to get the maximum and minimum point are different.

Second, element power and thrust are compared with onshore and offshore wind turbine. The largest forces occur at the 3/4 blade which was agreed with the theory. At the low wind speed (8m/s), the platform pitch motion makes an advantage effect on the aerodynamic load. However, at the high wind speed (11.4m/s), the phenomenon is reversed. In the FAST simulation, the results do not change a lot which may because the BEM method cannot predict the platform motion effect on the aerodynamic performance of the rotor accurately. What's more, the variation in the axial induction and tangential induction factors near the tip and blade arises. Overall, further investigations for prediction the validity of the tip loss factors and enhancing the same for FOWT applications are needed.

Third, strong tip and hub vortices are shown. Compared with the onshore wind turbine, the velocity is tilt. The velocity flow varies from different time instances. Axial velocity is asymmetric and varies with time which is different from the onshore condition. Compared with onshore wind turbine, the axial velocity profiles of offshore condition shows more complicated. The unit axial velocity differs with inflow velocities. The larger the inflow velocity, the larger the wake expansion is. Moreover, the point velocities components fluctuate randomly around their expected mean velocities, 11m/s for u and 8m/s for v and w. velocities closer to the inlet tend to have larger fluctuations than more downstream locations.

Fourth, the tower has little effect on the blade. There is almost no difference of power and thrust between the overhang 1 and overhang 2. The hub may influent the aerodynamic performance a little. Additionally, the TLP offshore wind turbine showed smaller motions at the same wave and wind conditions. Therefore, the gap between the maximum and minimum values is relatively small. The TLP wind turbine showed smaller maximum power and thrust which meets the expectation.

Finally, the general trends of power and thrust using log law wind are similar to those with uniform wind. The individual blade behaviour, exhibits a significant

increase in normal and tangential force when the blade is at the top and a decrease when the blade is at the bottom.

9.   RANS-BEMT APPROACH

9.1   Overall

When making aeroelastic computations of a wind turbine rotor, it is important that the aerodynamics is physically correctly modelled. Since the aerodynamics of a rotating wind turbine rotor is highly unsteady and three-dimensional, this is not a trivial task. BEMT assumes a 2D flow around the blade, only local 3D corrections at the blade root and at the tip are done in FAST. According to chapters described above, BEM method cannot predict aerodynamic performance accurately, especially in the motion condition. Therefore，corrected BEM method using the CFD airfoil results is an interesting thing to find if it can modify the accuracy of the results. Here, choosing pitch and surge combined motion case to validate the accurate of the RANS-BEMT approach.

Many engineering tools rely on pre-calculated 2D force coefficients for the aerodynamic loads. Multiple approaches to obtain these coefficients have been proposed and often these coefficients are simply tuned to better fit the measured thrust and power delivered by the rotor. This chapter looks at a common solution that consists of optimizing the load coefficients of the rotor to reproduce the measured rotor loads. Two variants of optimizations are applied. First, instead of using commonly used 2D airfoil data, 2D CFD RANS data was used. To account for this 3D character, the second proposed method is based on the use of 2D airfoil data obtained by post-processing of 3D flow data coming from 3D CFD computations. How to extract the aerodynamic characteristics from 3D CFD rotor computations is indicated in Session 7.3.4. With the proposed method and a sufficiently accurate CFD computation, it is possible to obtain airfoil characteristics from a give wind turbine design without using empirical stall corrections model.

Coupling method of FAST (a BEMT code of NREL for coupling of rotor aerodynamic and floater hydrodynamics) and STAR CCM+ (a commercial CFD software) is described as follows.

1.   Start point: CFD results

- Obtaining axial and tangential forces from CFD:

- Integration of pressure and shear stress for 2D section

- Calculation of $\{C_L, C_D$ and $\alpha\}$

2. Input for FAST

- Results of FAST:

- Thrust and power coefficient (C_T and C_P)

- Axial and tangential induction factors (a_1 and a_2)

However, as the time limitation, airfoil data are not available for angle of attack over the entire range of $\pm180°$. Therefore, a method was applied to extrapolate the airfoil data from CFD data. Figure 9.1 shows lift and drag coefficients for an example airfoil. Letters A-G across the top of the plot show different regions of angle of attack. Region A is the location of the CFD data for this airfoil. It is quite common to only have reliable data for angles between approximately 0° and 20°. Region B, from a point just beyond stall to 90°, is the region that the Viterna equations are applied in their original form. The equations are taken from a report by Viterna and Janetzke. (Aerodyn User's Guide)

$$C_{D_{max}} = 1.11 + 0.018AR \tag{9.1}$$

$$C_D = C_{D_{max}} \sin^2\alpha + B_2 \cos\alpha \tag{9.2}$$

where

$$B_2 = \frac{C_{D_s} - C_{D_{max}} \sin^2\alpha_s}{\cos\alpha_s} \tag{9.3}$$

and subscript s denotes the value at the stall angle (called the matching point in this User's Guide because it need not be exactly at stall). AR is the blade aspect ratio. The lift is given by

$$C_L = \frac{C_{D_{max}}}{2} \sin 2\alpha + A_2 \frac{\cos^2\alpha}{\sin\alpha} \tag{9.4}$$

Where $A_2 = (C_{L_s} - C_{D_{max}} \sin\alpha_s \cos\alpha_s) \frac{\sin\alpha_s}{\cos^2\alpha_s}$ \tag{9.5}

These equations yield $C_L=0$ and $C_D=C_{Dmax}$ at $\alpha=90°$, and the stall (or matching point values) at α_s. Thus it is important to select α_s carefully.

Regions C, D and E of Figure D1 values are obtained by scaling and reflecting the values from Region B. A scaling factor to C_L to account for the asymmetry of the airfoil is 0.7. That is, all lift values are reduced by 30% from the values shown in Region B. Drag values are not changed, just reflected. In regions F and G, linear interpolation is used to connect the various regions. C_L is forced to zero at $\alpha=\pm180°$.
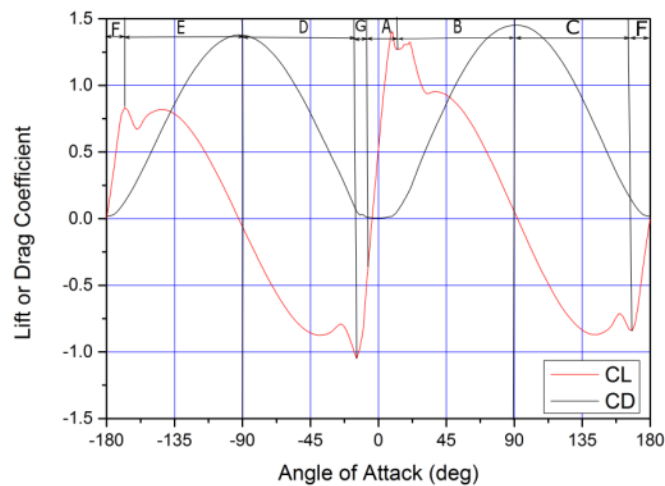
Figure 9.1 Lift and drag coefficient for an example airfoil (Aerodyn User's Guide)

9.2   2D CFD Data

C_L and C_D coefficients by 2D CFD calculations were utilized into FAST to obtain power and thrust. 2D airfoil data based on CFD computations is shown in figure 9.2. The thrust and power coefficient at severe condition computed using BEMT are given in figure 9.3.
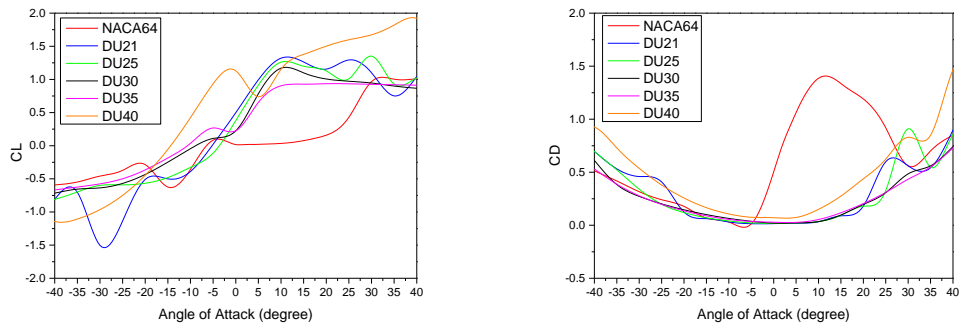
Figure 9.2 2D airfoil data based on CFD
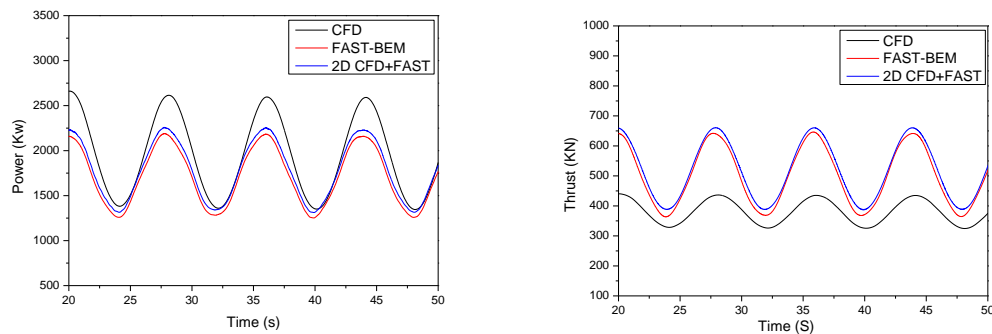
Figure 9.3 Power and thrust comparison

Although the 2D CFD results are expected to give better estimates of the flow features and aerodynamic coefficients, their effect on the BEMT-based wind turbine performance predictions are not satisfactory. A direct approach based on 2D calculations did not give realistic loads on the rotor. The overall effect of using CFD-based input data on power and thrust is small. It is likely that the unsatisfactory BEMT-based performance predictions are due to the radial velocity components as observed in the 3D RANS results. These velocity components are not considered within BEMT using any 2D input data.

9.3   2D Airfoil Data from 3D CFD Computations

Owing to the highly three-dimensional flow, the sectional aerofoil characteristics will deviate from 2D aerofoil characteristics, especially at the inner part of the blade and near the blade tip. Therefore, airfoil data from 3D CFD calculation were fed into FAST.

Lift and drag force can be calculated by the normal and tangential components of force which can be found in the CFD simulation results. To do this, the angle of attack needs to be established by calculating the relative inflow angle to the blade. Since the relative velocity is required, the surge velocity of the rotor u(t) needs to be included.

$$tan\varphi = \frac{u_x - u(t)}{r\Omega + u_\theta} \tag{9.6}$$

$$tan\varphi = \frac{u_\infty(1-a_1)}{r\Omega(1+a_2)} \tag{9.7}$$

The angle of attack is given by

$$\alpha = \varphi - \theta_{pitch} - \theta \tag{9.8}$$

Where θ_{pitch} is the blade pitch and θ is the blade twist which is a function of blade radius. The angle of attack is used to obtain the lift and drag coefficient C_L and C_D respectively. The relative velocity to the blade is given by

$$U_{rel} = \sqrt{(u_x - u(t))^2 + (r\Omega + u_\theta)^2} \tag{9.9}$$

Which gives a lift and drag force per unit span of

$$F_L = \frac{1}{2}\rho U_{rel}^2 C C_L \tag{9.10}$$

$$F_D = \frac{1}{2}\rho U_{rel}^2 C C_D \tag{9.11}$$

Where C is the chord.

The axial and tangential force components can be found by decomposing the lift and drag forces as follows.

$$F_n = F_L cos\emptyset + F_D sin\emptyset \tag{9.12}$$

$$F_t = F_L sin\emptyset - F_D cos\emptyset \tag{9.13}$$

$$So \ F_L = F_n cos\emptyset + F_t sin\emptyset \tag{9.14}$$

$$F_D = F_n sin\emptyset - F_t cos\emptyset \tag{9.15}$$

Overall, extract 2D aerodynamic coefficient from 3D CFD calculation was shown in figure 9.4. Based on the input data which were generated using the proposed 3D

CFD based method, BEMT performance predictions were done. In figure 9.5, C_T and C_P are plotted against velocity.
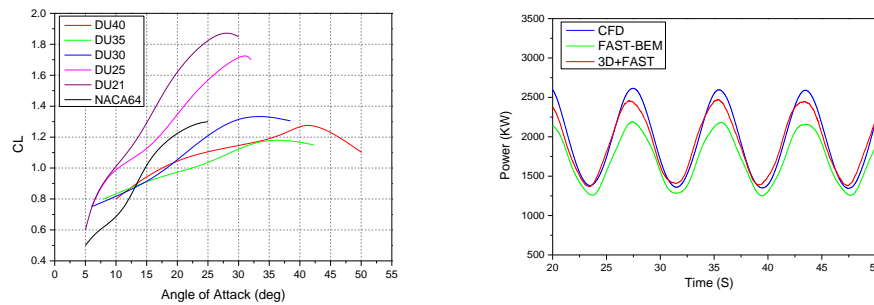
Figure 9.4 2D airfoil data from 3D CFD   Figure 9.5 Power comparison

The results based on 3D CFD calculations came close to the fully CFD results. The predictions based on the post-processed 3D CFD data were in good overall agreement with the fully 3D CFD computations. Especially, the minimum values were almost same.

9.4   Conclusion

This chapter used a link between RANS and BEM calculations of FOWT at severe condition. 2D and 3D RANS results were as input for BEMT computations. Several results are detected as follows:

•Flow around turbine blade more 2D for full scale

•Full scale results more appropriate for this approach

•Similar results for CFD 3D and RANS-BEMT

•RANS-BEMT approach relies on RANS and BEMT results

•Differences are acceptable

Overall, the use of purely 2D data from 2D CFD RANS computations did however not result in the desired improvement due to the highly 3D character of the flow which is not considered with the conventional BEMT. However, the 3D CFD+FAST approach was shown to be successful and can therefore be extremely useful for

future FOWT performance prediction. RANS-BEMT coupled approach is an option to be considered.

10. CONCLUSIONS AND FUTURE RESEARCH

10.1 Overview

The main research objective is to quantify the aerodynamic performance of multi-objective applied to the two main floating platform concepts: the tension leg and spar-buoy platforms. The results and conclusions in this work are intended to be used by designers and developers of floating turbines. Simulations are carried out using FAST, a well-established wind turbine design and simulation tool based on potential flow method, and CFD commercial software, STAR CCM+. The particular focus was on the state-of -the-art unsteady RANS approach. This thesis clearly showed that CFD can be used for predicting aerodynamic performance of FOWT under complicated conditions, in order to obtain more accurate results compared with BEMT and GDW.

10.2 Conclusion

First, the objective in Chapter 2 was shown as below:

- *To review previous works* on *aerodynamic calculation of wind turbines with three different methods, experiment, BEM and CFD.*

For the 2D aifoil, early studies rely on wind tunnel experiments and theoretical analysis. However, in recent years, CFD methods play an increasingly important role to analyse the details flow field characteristics. Reynolds number, roughness, turbulence intensity, angle of attack, dynamic stall and boundary layer transition are significant parameters to affect the aerodynamic performance of airfoil.

For the 3D wind turbine, Blade Element Momentum method (BEM) is the most common used method for engineering design in industry. However, BEM method cannot model a turbulent region behind the rotor, dynamic stall condition and yawed inflow condition. Therefore, several models were developed to improve the aerodynamic performance. This tradition BEM theory with common corrections still has its limitations, especially in complicated simulation condition. Several CFD studies in literature perform 3D rotor flow simulations. It estimates aerodynamic

performance better and can describe the flow field. However, it requires much more computational time and relies on operator's experiences.

Floating offshore wind turbine are combined aerodynamic, hydrodynamic and mooring system dynamic effects. Rotational and transitional motions primarily cause oblique flow conditions. In last years, several wind tunnel based aerodynamic experiments on model FOWTs has been undertaken. Aero-servo-elastic simulation tools like Bladed, FAST or HAWC2 based on BEM method are used to verify the stability and the ability of a FOWT structure. Several studies are conducted compared BEM method and CFD method in different motions.

Second, the objective in Chapter 3 is to give a simple introduction of CFD theory, turbulence models, wall functions, CFD commercial software STAR CCM+ and uncertainty analysis in CFD verification.

Chapter 4 achieves following objectives.

- *To detect a reliable simulation model (grid, turbulence model, time step) in CFD aerodynamic calculation.*
- *To detect aerodynamic characteristics of 2D airfoil in unsteady condition.*

The results of CFD show a good agreement with experimental data. The unsteady state has an obvious hysteresis phenomenon. It means that the upstroke and downstroke values are various. As many potential flow theories rely on the airfoil data (CL and CD) as the input data, the dynamic stall of the airfoil will have a significant influence on the aerodynamic load output. It often uses Beddoes-Leishman theory to describe the dynamic stall. Therefore, getting the accurate airfoil data fed into the potential flow method may be a meaningful way to predict more accurate aerodynamic coefficient of wind turbine.

The next research objectives in Chapter 5 are:

- *To have a good knowledge of BEM theory to recognise its limitations.*
- *To detect the platform motions using FAST.*

NREL gives the detail design of 5MW FOWT using spar platforms and tension leg platforms (TLP). Three different wind and sea conditions were chosen. Surge and pitch DOFs appear to the largest amplitude modes. Others are very small, even close to zero. Moreover, the platform motion of TLP is significantly smaller than that of spar platform. Comparing the bending moment at the tower base and blade root, the change in the wave height and wind speed will affect the bending moments of blade roots and tower base.

The following objectives are obtained in Chapter 6 as follows.

- *To detect an applicable 3D wind turbine CFD simulation model (grid, boundary condition, motion methods).*
- *CFD method can be reliable in a skew flow condition*

At small wind speeds, steady computations are performed more close to the experimental results. However, the results are not as good at high wind speeds. Overall, rigid body motion results compare well at all wind speeds. Moreover, there is no obvious difference of power compared with different boundary conditions. However, the thrust results showed a big difference especially at high wind speeds. In general, whole boundary condition showed better results.

Different fixed yaw angles were simulated to describe the skewed flow phenomena. Detailed flow physics are analysed. Chord wise distributions of the surface pressure coefficient compared with different yaw angles. When the angle increased, the pressure distributions are changed.

The next objectives to be tackled are addressed in Chapter 7.

- *To detect the hub and tower effects*
- *To detect the influence of transition model*
- *To detect the difference with FAST and CFD results*
- *To detect the wake characteristics in dynamic condition*
- *To detect the aerodynamic performance in shear wind condition*

As the literature reviews described, most researchers did CFD simulations using the rotor only wind turbine. Therefore, three different conditions, rotor only, with hub

and whole wind turbine, were compared in this chapter. The results of power and thrust were almost same, but the whole model showed a little small. The existing hub and tower separate the flow over the blade which decreases the velocity a little. Inlet and outlet flow is necessary to detect. Tangential velocity, rotation velocity and inflow velocity at every point were described. Rotation velocity at the downstream was close to 1 which defines that constriction of wake flow is not significant.

A transition model from laminar to turbulent flow is modelled using Langtry and Menter correction based Gamma-Theta transition model. This model is a two equations model used in CFD to modify turbulent transport equations. A comparison between turbulent model and transition model was conducted. Good agreement of results was obtained with these two models. The transition model results were slightly under-predicted than that of fully turbulent. However, when Reynolds numbers are higher, the advantages of using the transition model may not be significant.

When compared with FAST results, it can be observed that the results matched well at low, medium and high wind speeds. BEM method got the largest power and thrust about 5800 KW and 800 KN of all. At lower wind speed, the power was small as the blades experience stall. At high wind speed above the design wind speed, the power decreased. As there is no experiment data, we assume that CFD method can predict the power and thrust accurately at pre-stall, stall and post-stall region. However, at the yaw condition, compared CFD results with BEM, a larger discrepancy was found which means that BEM may not predict the aerodynamic performance accurately in the oblique flow condition.

Analysing the span-wise sectional results, a large difference was found at the tip of the blade. Therefore, the tip loss correction was important to the potential method.

Wind turbine wake was significant to analyse. As the wake extends downstream of the rotor, the centreline velocity deficit decrease, and the width increase. The rotor thrust coefficient has a large influence on the extent of the wake. Moreover, wake rotation will increase the kinetic energy in the wake.

Finally, various critical design load cases (DLC) based on wind turbine design guidelines were considered. As a result, CFD computations predict much higher values of thrust and power for the NWP and ECG conditions. The discrepancy between CFD and BEM is larger than that in a unit wind. That is because BEM cannot predict well under complex conditions.

Following this, 4 main objectives are addressed in Chapter8.

- *To detect the effects of different platform motions (pitch, surge and pitch-surge) on the aerodynamic load of blades*
- *To detect the unsteady aerodynamic performance with different simulation methods*
- *To detect the wake evolution and induction of offshore floating wind turbine*

First, when compared with BEM and GDW solvers, power and thrust match well with CFD results. All the discrepancies are smaller than 15%. Pitch and surge combined motions reach the maximum difference. Moreover, BEM approach underestimate these values compared with GDW, while CFD method produces the lowest estimation. In addition, pitch and surge motions cause a phase difference in a real situation. Therefore, the times to get the maximum and minimum point are different.

Second, element power and thrust are compared with onshore and offshore wind turbine. The largest forces occur at the 3/4 blade which was agreed with the theory. At the low wind speed (8m/s), the platform pitch motion makes an advantage effect on the aerodynamic load. However, at the high wind speed (11.4m/s), the phenomenon is reversed. In the FAST simulation, the results do not change a lot which may because the BEM method cannot predict the platform motion effect on the aerodynamic performance of the rotor accurately. What's more, the variation in the axial induction and tangential induction factors near the tip and blade arises. Overall, further investigations for prediction the validity of the tip loss factors and enhancing the same for FOWT applications are needed.

Third, strong tip and hub vortices are shown. Compared with the onshore wind turbine, the velocity is tilt. The velocity flow varies from different time instances.

Axial velocity is asymmetric and varies with time which is different from the onshore condition. Compared with onshore wind turbine, the axial velocity profiles of offshore condition shows more complicated. The unit axial velocity differs with inflow velocities. The larger the inflow velocity, the larger the wake expansion is. Moreover, the point velocities components fluctuate randomly around their expected mean velocities, 11m/s for u and 8m/s for v and w. velocities closer to the inlet tend to have larger fluctuations than more downstream locations.

Fourth, the tower has little effect on the blade. There is almost no difference of power and thrust between the overhang 1 and overhang 2. The hub may influent the aerodynamic performance a little. Additionally, the TLP offshore wind turbine showed smaller motions at the same wave and wind conditions. Therefore, the gap between the maximum and minimum values is relatively small. The TLP wind turbine showed smaller maximum power and thrust which meets the expectation.

Finally, the general trends of power and thrust using log law wind are similar to those with uniform wind. The individual blade behaviour, exhibits a significant increase in normal and tangential force when the blade is at the top and a decrease when the blade is at the bottom. To detect the shear effect on the floating offshore wind turbine

The final objective is achieved in Chapter 9.

- *RANS-BEMT approach is more appropriate for FOWT*

2D and 3D RANS results were as input for BEMT computations. Overall, the use of purely 2D data from 2D CFD RANS computations did however not result in the desired improvement due to the highly 3D character of the flow which is not considered with the conventional BEMT. However, the 3D CFD+FAST approach was shown to be successful and can therefore be extremely useful for future FOWT performance prediction. RANS-BEMT coupled approach is an option to be considered.

10.3   Future Research

As the limitation of study time, some problems still remain in this thesis.

1. The results show a larger difference between FAST and CFD of FOWT in a complicated condition. It seems that BEM cannot estimate the aerodynamic performance of FOWT accurately. How to modify FAST may be a big problem in the future study.

2. Chapter 4 calculated the aerodynamics of a 2D airfoil. It only chose the angle of attack from 0° to 20°. Here, extrapolating the airfoil data from CFD data by Viterna equations. Therefore, angles of attack over the entire range of ±180 need to be calculated. The airfoil data results (CL, CD and CM) will be fed into FAST. This RANS-BEM approach may be used in other different conditions to confirm the results obtained by this thesis.

3. As the results of chapter 8, there was a big difference in blade tip. Therefore, further investigation of tip loss factor in FOWT is significant.

4. Chapter 9 used 2D airfoil data from 3D CFD results to modify FAST. The dynamic stall phenomenon still be modified by applying Beddoes-Leishman theory. Using the hysteresis phenomenon obtained by CFD results directly sent into FAST may achieve better results. More segmentation may be needed to ignore the tip and hub loss.

5. Though, this thesis is focused on the aerodynamic performance. I did some researches of hydrodynamic simulations of spar platform by now. Next stage may have a research on platform motions using CFD. Moreover, mooring line may be considered.

6. According to the platform studying, an aerodynamic-hydrodynamic coupling CFD simulation method can be established. In this thesis, all the motions applied in the wind turbine are forced motions. Using the coupling simulation method, 6 DOF DFBI motions of FOWT can be detected.

7. In this thesis, the wind turbine is rigid. FAST is an elastic simulation tool. Establishing an elastic CFD model of FOWT is interesting and challenging.

REFERENCE

Abbott I.H, Doenhoff A.V (1949), *Theory of Wind Sections*, McGraw-Hill: London, UK

Ackerman M.C., (1991), *Yaw Modelling of Small Wind Turbines*, in: Wind Energy Technology and Implementation, Elsevier, Amsterdam, 1991, p. 3.

AIAA, (1998), *Guide for the Verification and Validation of Computational Fluid Dynamics Simulations*, G-077-1998

Ainslie J.F.. (1998), *Calculating the Flow-field in the wake of wind turbines*. Journal of Wind Engineering and Industrial Aerodynamics, 27(1-3):213 – 224, 1988.

Anand Bahuguni, Krishnamoorthi Sivalingam, Peter Davies, Johan Gullman-Strand , Vinh Tan NGUYEN (2014), *Implementation of Computational Methods to Obtain Accurate Induction Factors for Offshore Wind Turbines*, the ASME 2014 33rd International Conference on Ocean, Offshore and Arctic Engineering, OMAE2014, June 8-13, 2014, San Francisco, California, USA, OMAE2014-23992

Anderson J.D., (2009), *Computational Fluid Dynamics*, Springer Berlin Heidelberg, 2009, ISBN: 978-3-540-85055-7

Anderson, John D., Jr., *Computational Fluid Dynamics—an Engineering Tool?*, in A.A.

Antoniou I., Asimako Poulos D, Frangoulis A., et al. (1992), *Turbulence Measurements on Top of a Steep Hill*, Journal of Wind Engineering and Industrial Aerodynamics, 1992, 39: 343-355

Bak C, Troldborg N and Madsen H (2011), *DAN-AERO MW: Measured Airfoil Characteristics for a MW Rotor in Atmospheric Conditions* (Proc. of EWEA)

Baldwin B., Lomax H., (1978), *Thin-layer Approximation and Algebraic Model for Separated Turbulent Flows*, 16th Aerospace Sciences Meeting, 1978, (doi: 10.2514/6.1978-257)

BareiB R., Wagner S., (1993), *The Free Wake/Hybrid Wake Code ROVLM*a Tool for Aerodynamic Analysis of Wind Turbines*, EWEC 93, TravemuKnde, Germany, 1993.

Barnsley M, Wellicome J.(1992), *Wind Tunnel Investigation of Stall Aerodynamics for a 10 m Horizontal Axis Roto*r, Journal of Wind Engineering and Industrial Aerodynamics 1992; 39: 11–21.

Bayati, I., Belloli, M. and Facchinetti, A. (2013), *Wind Tunnel Test of Floating Offshore Wind Turbines: A Proposal for Hardware-in-the-loop Approach*, presented at the European Wind Energy Conference, Vienna, 2013.

Bayati, I., Belloli, M., Ferrari, D., Fossati, F. and Giberti, H.(2014), *Design of a 6-DoF Robotic Platform for Wind Tunnel Tests of Floating Wind Turbines*, Energy Procedia Vol. 53, 2014 pp. 313 – 323.

Bazilevs Y., Hsu M.-C., Akkerman I., Wright S., Takizawa K., Henicke B., Spielman T. and Tezduyar T. E., (2011), *3D Simulation of Wind Turbine Rotors at Full Scale Part I: Geometry Modeling and Aerodynamics*, International Journal For Numerical Methods In Fluids, 01/2011, B65(1-3):207-235. DOI: 10.1002/fld.2400

Beddoes, T.S. (1983), *Representation of Airfoil Behaviour*. Vertica 7, 183–197

Bekiropoulus D, Rieb R, Lutz T, Kramer E, Matha D, Werner M, et al. (2011), *Simulation of Unsteady Aerodynamic Effects on Floating Offshore Wind Turbines*. In: 11th German wind energy conference; 2011.

Benjanirat Sarun, (2006) *Computational Studies of Horizontal Axis Wind Turbines in High Wind Speed Condition using Advanced Turbulence Models*, Thesis (Ph.D.), Georgia Institute of Technology, December 2006

Benjanirat Sarun, Sankar Lakshmi, Xu Guanpeng, (2003*), Evaluation of Turbulence Models for the Prediction of Wind Turbine Aerodynamics*, 41st Aerospace Sciences Meeting and Exhibit, 6-9 January 2003, Reno, Nevada. AIAA 2003-517 (doi: 10.2514/6.2003-517)

Bertagnolio F., Sorensen N., Johansen J., et al. (2001), *Wind Turbine Airfoil Catalogue*, RisO-R-1280, 2001.

Boussinesq Approximation:
https://en.wikipedia.org/wiki/Boussinesq_approximation_(buoyancy)

Boussinesq Eddy Viscosity Assumption: http://www.cfd-online.com/Wiki/Boussinesq_eddy_viscosity_assumption

Brian Launder, D.E.Spalding, (1974), *The Numerical Computation of Turbulent Flow Computer Methods,* Computer Methods in Applied Mechanics and Engineering, 03/1974; 3(2):269-289. DOI: 10.1016/0045-7825(74)90029-2

Brodeur R.R., van Dam C.P.(2001), *Transition Prediction for a Two-Dimensional Reynolds-averaged Navier-Stokes Method Applied to Wind Turbine Airfoils*, Wind Energy, 2001, 4(15): 61-75

Buhl, M.L., Jr. (2004), *A New Empirical Relationship between Thrust Coefficient and Induction Factor for the Turbulent Windmill State*, NREL/TP-500-36834. Golden, CO: National Renewable Energy Laboratory, September.

Bulder, B. H., et al, (2002), *Study to Feasibility of and Boundary Conditions for Floating Offshore Wind Turbines*, Novem 2002-CMC-R43, ECN, MARIN, Lagerway the Windmaster, TNO, TUD, MSC, December 2002.

Burton T. (2011), *Wind Energy Handbook*, John Wiley & Sons Ltd.: Chichester, UK

Butterfield Sandy, Musial Walt, Jonkman Jason (2005), *Engineering Challenges for Floating Offshore Wind Turbines,* 2005 Copenhagen offshore wind turbine conference, Copenhagen, Denmark, October 25-28, NREL/CP-500-38776

Cebeci T., Clark R. W., Chang K. C., Halsey N.D., and Lee K., (1986), *Airfoils with separation and the resulting wakes,* J. Fluid Mech. (1986), vol. 163, pp. 323-347

Chattot Jean-Jacques, (2009), *Effects of Blade Tip Modifications on Wind Turbine Performance using Vortex Model*, Computers & Fluids, Volume 38, Issue 7, August 2009, Pages 1405–1410

Chen K. K., Thyson N.A. Extension of Emmons, (1971), *Spot Theory to Flows on Blunt Bodies*, AIAA Journal of Propulsion and Power, 1971, 9(5):821-825

Chen Yen-Pin, *A study of the aerodynamic behavior of a NREL phase VI wind turbine using the CFD methodology*, Master Thesis, Wright State University, 2011

Cheng, P. W. (2002), *A Reliability Based Design Methodology for Extreme Responses of Offshore Wind Turbines*, Ph.D. Dissertation, Wind Energy Research Institute, Delft University of Technology, Delft, The Netherlands, 2002.

Chih-Hua Wu, Nguyen Vinh-Tan, Jing Lou, Krishnamoorthi Sivalingam, (2015), *A Computational Fluid Dynamics Model for Aerodynamics Analysis of Offshore Wind Turbines Rotor under Floating Platform Induced Motion*, Proceedings of the ASME 2015 34th International Conference on Ocean, Offshore and Arctic Engineering, OMAE2015, May 31-June 5, 2015, St. John's, Newfoundland, Canada, OMAE2015-41742

Christensen H.F., Sorensen N.N. (1994), *A Comparative Study between a Dynamic Stall Model and Experiments on a HAWT*, Greece: European Wind Energy Association Conference, 1994

Coleman, H. W., and Steele, W. G., (1999), *Experimentation and Uncertainty Analysis for Engineers*, 2nd Edition, Wiley, New York, NY

Coleman, H. W., and Stern, F., (1997), *Uncertainties in CFD Code Validation*, ASME J. Fluids Eng., 119, pp. 795–803.

Corten G.P., Veldkamp H.F. (2002), *Insects can Halve Wind Turbine Power*, Nature, 2002, 412:42-43.

Cummins, W. E., (1962), *The Impulse Response Function and Ship Motions*, Schiffstechnik, Vol. 9, October 1962, pp. 101–109.

Daniel Micallef, Tonio Sant, (2015), *Loading Effects on Floating Offshore Horizontal Axis Wind Turbines in Surge Motion*, Renewable Energy, 83 (2015) 737-748

David Hartwanger, Dr Andrej Horvat, (2008), *3D Modelling of a Wind Turbine using CFD*, NAFEMS UK Conference 2008 "Engineering simulation: effective use and best practice" Cheltenham, UK, June 10-11, 2008

David J. Laino, A. Craig Hansen, Jeff E. Minnema, (2002), *Validation of the AeroDyn Subroutines using NREL Unsteady Aerodynamics Experiment Data*, Wind Energy, Volume 5, Issue 2-3, April - September 2002, Pages 227–244

Dexin He. (2006), *Wind Engineering and Industrial Aerodynamics*, Beijing: National Defense Industry Press, 2006.

Dinyavari, M.A.H., Friedmann, P.P. (1984), *Unsteady Aerodynamics in Time and Frequency Domains for Finite Time Arbitrary Motion of Rotary Wings in Hover and Forward Flight*, AIAA Paper 84–0988, 1984.

Dominique Roddier, Christian Cermelli, Alexia Aubault, Alla Weinstein (2010), *WindFloat: A Floating Foundation for Offshore Wind Turbines*, Journal of Renewable and Sustainable Energy, 2, 033104

Dong Ok Yu, Ju Yeol You, Oh Joon Kwon, (2013), *Numerical Investigation of Unsteady Aerodynamics of a Horizontal-axis Wind Turbine under Yawed Flow Conditions*, Wind Energy, Volume 16, Issue 5, July 2013, Pages 711–727

Dowell, E.H. (1980), *A Simple Method for Converting Frequency Domain Aerodynamics to the Time Domain*, NASA TM-81844, 1980.

Drela M (1989), *XFOIL: An Analysis and Design System for Low Reynolds Number Airfoils*, Conference on Low Reynolds Number Airfoil Aerodynamics, University of Notre Dame: 1989

Duque EPN, Burklund MD, Johnson W. (2003), *Navier–Stokes and Comprehensive Analysis Performance Predictions of the NREL Phase VI Experiment*, Journal of Solar Energy Engineering 2003; 124: 457–467, DOI: 10.1115/1.1624088

Earl Duque, C. van Dam, Shannon Hughes, (1999), *Navier-Stokes Simulations of the NREL Combined Experiment Phase II Rotor*, 37th Aerospace Sciences Meeting and Exhibit, AIAA-99-0037.

Eastman J.N, (1932), *The Aerodynamic Characteristics of Eight Very Thick Airfoils from Tests in the Variable Density Wind Tunnel*, NACA Report No.391, 1932.

Ecaf L, Hoekstra M. (2000), *On the Application of Verification Procedures in Computational Fluid Dynamics,* 2nd MARNET Workshop, Barcelona, Spain, 2000

Edwards, J.W., Breakwell, J.V., Bryson Jr., A.E., (1989), *Reply by Authors to Vepa*. Journal of Guidance and Control, 2, 447–448, 1989

Eecen, P. J., (2003), *Wind Waves: Forces Due to Waves on Offshore Wind Turbines*, ECN-C--03-097, Petten, The Netherlands: Energy Research Centre of The Netherlands, September 2003.

EPPler R. (1990), *Airfoil Design and Data*, Berlin: SPringer一Verlag, 1990.

Erich Hau. (2006), *Wind Turbines - Fundamentals, Technologies, Application, Economics*, Springer-Verlag Berlin Heidelberg, second edition, 2006

European Wind Energy Association (2013), *Deep Water-The Next Step for Offshore Wind Energy*, a report by the European Wind Energy Association

Farrugia, R., Sant, T. and Micallef, D.,(2014), *Investigating the Aerodynamic Performance of a Model Offshore Floating Wind Turbine*, Renewable Energy, Vol. 70, 2014, pp. 24-30.

Fernandes, G., Make, M., Gueydon, S., and Vaz, G., (2014), *Sensitivity to Aerodynamic Forces for the Accurate Modelling of Floating Offshore Wind Turbines*, In 1st

International Conference on Renewable Energies Offshore, 24–26 Nov 2014, Lisbon, Portugal, RENEW2014

Firooz A., Gadami M., (2006), *Turbulence Flow for NACA4412 in Unbounded Flow and Ground Effect with Different Turbulence Models and Two Ground Conditions: Fixed and Moving Ground Conditions*, Int. Conference on Boundary and Interior Layers, BAIL 2006

Fluent 14.0 Users' Guide

Franck Bertagnolio, Niels Sorensen, Jeppe Johansen and Peter Fuglsang, (2001), *Wind Turbine Airfoil Catalogue*, Riso National Laboratory, Roskilde, Denmark, August 2001, Riso-R-1280(EN)

Freitas, C. J., (1993), *Editorial Policy Statement on the Control of Numerical Accuracy*, ASME J. Fluids Eng., 115, pp. 339–340.

Freudenreieh K, Kaiser K, Sehaffarczyk A. P. (2004), *Reynolds Number and Roughness Effects on Thick Airfoils for Wind Turbine,* Wind Engineering, 2004, 28(5):529—546.

Freymuth P. (1988), *Three-dimensional Vortex Systems of Finite Wings*, Journal of Aircraft 1988; 25: 971–972

Fuglsang P, Bak C. (2004), *Development of the Riso Wind Turbine Airfoils*, Wind Energy 2004, 7, 145–162

Fulton, G. R., Malcolm, D. J., and Moroz, E., (2006), *Design of a Semi-Submersible Platform for a 5MW Wind Turbine*, 44th AIAA Aerospace Sciences Meeting and Exhibit, 9–12 January 2006, Reno, NV, AIAA Meeting Papers on Disc [CD-ROM], Reston, VA: American Institute of Aeronautics and Astronautics, January 2006, AIAA-2006-997.

Garrel A (2003), *Development of a Wind Turbine Aerodynamics Simulation Module*, Report ECN-C-03-079, 01/2003;

Garrick, I.E. (1938), *On Some Reciprocal Relations in the Theory of No-stationary Flows*, NACA Report 629, 1938

Germanischer Lloyd, (2010), *Guidelines for the Certification of Wind Turbines*, 2010th edn., Hamburg

Gharbi N.EI, Absi R. (2009), *Effect of Near-wall Treatments on Airflow Simulations*. International Conference on Computational Methods for Energy Engineering and Environment: CCM3E. Sousse, Tunisia, 185-189

Glauert, H. (1926), *A General Theory of the Autogyro*, ARCR R&M No. 1111.

Glauert, H. (1935), *Airplane propellers*, Aerodynamic Theory (W. F. Durand, ed.), Div. L, Chapter XI, Berlin:Springer Verlag

Global Wind Energy Council, (2015), *Global wind statistics 2014*

Gonzalez A, Munduate X, (2007), *Unsteady Modelling of the Oscillating S809 Aerofoil and NREL Phase VI Parked Blade using the Beddoes–Leishman Dynamic Stall Model*, Journal of Physics: Conference Series, 75:012020-1–0-8.

Gould J., Fiddes S.P., (1991), *Computational Methods for the Performance Prediction of HAWTs*, in: Wind Energy Technology and Implementation, Elsevier, Amsterdam, 1991, p. 29.

Graves, R.A., (1982), *Computational Fluid Dynamics: The Coming Revolution*, Astronautics and Aeronautics, Vol. 20, No. 3, March 1982, pp. 20–28.

Gross A., Fasel H. F., Friederieh T., et al. (2010), *Numerical Investigation of S822 Wind Turbine Airfoil*, AIAA-2010-4478, 2010.

Guntur S, Bak C and Sorensen N (2011), *Analysis of 3D Stall Models for Wind Turbine Blades Using Data from the MEXICO Experiment*, Proc. of the 13th International Conference on Wind Engineering (Amsterdam, the Netherlands)

Gupta S, Leishman J. (2006), *Dynamic Stall Modelling of the S809 Aerofoil and Comparison with Experiments*, Wind Energy 2006;9:521–47.

Gupta S. (2006), *Development of a Time-accurate Viscous Lagrangian Vortex Wake Model for Wind Turbine Applications*, Doctoral Dissertation, University of Maryland, 2006.

Gupta, Abhishek, *Prediction of Aerodynamic Forces on Wind Turbine Blades using Computational Fluid Dynamics*, ISBN/ISSN 9780494291344

Hand M, Simms D, Fingersh L, (2001), *Unsteady Aerodynamics Experiment Phase VI: Wind Tunnel Test Configurations and Available Data Campaigns*. United States, NREL Report No. TP-500-29955

Hansen M, Sorensen N, Sorensen J and Mikkelsen J, (1997), *Extraction of Lift, Drag and Angle of Attack from Computed 3D Viscous Flow around a Rotating Blade*, Proc. of the European Wind Energy Conference (Dublin) pp 499-501

Hansena M. O. L, Sφensena J. N, Voutsinasb S, et al., (2006), *State of the Art in Wind Turbine Aerodynamics and Aeroelasticity*, Progress in Aerospace Sciences, 2006, 42: 285-330

Hassig, H.J. *An Approximate True Damping Solution of the Flutter Equations by Determinant Iteration*, Journal of Aircraft 8, 825–889, 1971

Hau E. (2006), *Wind Turbines, Fundamentals, Technologies, Application, Economics*, 2nd ed. Springer: Berlin, Germany

Hess J L, (1990), *Panel Methods in Computational Fluid Dynamics*, Annual Review of Fluid Mechanics Vol. 22: 255-274, January 1990, DOI: 10.1146/annurev.fl.22.010190.001351

Ishihara, T., et al., (2007b), *A Study on the Dynamic Response of a Semi-submersible Floating Offshore Wind Turbine System Part 1: A Water Tank Test*, Proceedings of the 12th International Conference on Wind Engineering, Cairns, Australia

Ishihara, T., Phuc, P.V., and Sukegawa, H., (2007a), *Numerical Study on the Dynamic Response of a Floating Offshore Wind Turbine System due to Resonance and Nonlinear Wave*, Proceedings of 2nd EOW, Berlin, Germany

ITTC, (1996), 21st ITTC Proceedings, *Report of the Resistance Committee*, Bergen/Trondheim, Norway, September

ITTC, (1999), 22nd ITTC Proceedings, *Report of the Resistance Committee*, Seoul, Korea/Shanghai, China, Sept

ITTC, (1999), *General Uncertainty Analysis in CFD Guidelines for RANS Codes*, ITTC – Recommended Procedures and Guidelines, 7.5-03 -01-02, 1999

ITTC, (1999), *Resistance and Flow Uncertainty Analysis in CFD Examples for Resistance and Flow*, ITTC – Recommended Procedures and Guidelines, 7.5-03 -02-01, 1999

ITTC, (2008), *Uncertainty Analysis in CFD Verification and Validation Methodology and Procedures*, ITTC – Recommended Procedures and Guidelines, 7.5-03 -01-01, 2008

Jens N. Sørensen and Shen WZ, (2002), *Numerical Modeling of Wind Turbine Wakes,* Journal of Fluids Engineering, volume 124, issue 2, 393-399, June 2002,

Jens N. Sørensen, Niels Troldborg, Robert Mikkelsen, (2007), *Simulation and Modelling of Turbulence in Wind Farms*, EWEC 2007-European wind energy conference and exhibition. MIC, Milan, Italy

Jeon, M., Lee, S., Lee, S. (2014), *Unsteady Aerodynamics of Offshore Floating Wind Turbines in Platform Pitching Motion using the Vortex Lattice Method*, Renewable Energy, vol. 65, 2014, pp. 207-212.

Jeppe Johansen, Niels N. Sørensen, (2004), *Aerofoil Characteristics from 3D CFD Rotor Computations*, Wind Energy, Volume 7, Issue 4, October/December 2004, Pages 283–294

Jeppe Johansen, Niels N. Sørensen, (2006), *Numerical Analysis of Winglets on Wind Turbine Blades using CFD*, Risø-R-1543(EN) February 2006.

Johansen J. (1999), *Unsteady Airfoil Flows with Application to Aeroelastic Stability,* Riso R 1116(EN). Tech. Rep., Risoe National Laboratory; 1999

Johansen J., Sørensen N. N., Michelsen J. A., Schreck S., (2002), *Detached-eddy Simulation of Flow around the NREL Phase VI Blade*, Wind Energy, Volume 5, Issue 2-3, April - September 2002, Pages 185–197

Johansen, J., Sørensen, N. N., Michelsen, J. A., and Schreck, S., (2002), *Detached-Eddy Simulation of Flow around the NREL Phase-VI Rotor,* Wind Energy, Vol. 5, No. 2-3, 2002, pp. 185-197.

Jones, R.T. (1939), *The Unsteady Lift of a Wing of Finite Aspect Ratio*. NACA Report 681, 31–38, 1939.

Jones, W.P. (1945), *Aerodynamic Forces on Wings in Non-Uniform Motion*, British Aeronautical Research Council, R & M 2117, 1945.

Jonkman J. and Musial W., (2010), *Offshore Code Comparison Collaboration (OC3) for IEA Task 23 Offshore Wind Technology and Deployment,* Technical Report, NREL/TP-5000-48191, December 2010

Jonkman J., (2007), *Dynamics Modeling and Loads Analysis of an Offshore Floating Wind Turbine*, Technical Report, NREL/TP-500-41958, November 2007

Jonkman J., (2008), *Influence of Control on the Pitch Damping of a Floating Wind Turbine*, Presented at the 2008 ASME Wind Energy Symposium, Reno, Nevada, January 7–10, 2008, NREL/CP-500-42589

Jonkman J., (2010), *Definition of the Floating System for Phase IV of OC3*, Technical Report NREL/TP-500-47535, May 2010

Jonkman J., Butterfield S., Musial W., and Scott G., (2009), *Definition of a 5-MW Reference Wind Turbine for Offshore System Development*, Technical Report, NREL/TP-500-38060, February 2009

Jonkman Jason M., Marshall L. Buhl Jr., (2005), *FAST User's Guide*, Technical Report NREL/EL-500-38230, August 2005

Joslin R.D., Viken S.A., (2001), *Baseline Validation of Unstructured Grid Reynolds-Averaged Navier-Stokes toward Flow Control*, Journal of Aircraft Vol.38 number 2, 2001, pages 389-393

Julia Layton, *How Wind Power Works*, HowStuffWorks.com http://science.howstuffworks.com/environmental/green-science/wind-power3.htm

Kaimal J.C., Finnigan J.J. (1994), *At mospheric Boundary Layer Flows: Their Structure and Measurement,* Oxford University Press, New York, 1994

Kari Med, (2011), *Wind Turbine in Yawed Operation*, Master of Science in Energy and Environment, Norwegian University of Science and Technology, June 2011

Khalfallah M.G., Koliub A.M. (2007), *Effect of Dust on the Performance of Wind Turbines*, Desalination, 2007, 209-220.

Kim DH, Yu DO, Kwon OJ, Fletcher TM, Scheurich F, Brown RE. (2010), *Predicting Unsteady Blade Loads of a Wind Turbine using RANS and Vorticity Transport Methodologies*, EWEC 2010, Warsaw 2010; 2010: 33–37.

Knight M, Wenzinger C.J (1929). *Wind Tunnel Tests on a Series of Wing Models through a Large Angle of Attack Range Part 1 Force Tests* .Virginia, United States, NACA Report No. 317.

Kobra Gharali, David A. Johnson, (2012), *Numerical Modelling of an S809 Airfoil under Dynamic Stall, Erosion and High Reduced Frequencies*. Applied Energy, 93 (2012), 45-52.

Kress Christian, Chokani Ndaona, Abhari Reza, (2013), *Aerodynamic Effectiveness and Blade Loading of a Multi-Megawatt Wind Turbine*, EWEC 2013, European Wind Energy Conference, Vol. 2, Wien, AT, Feb 4-7, 2013

Kristian S. Dahl, Peter Fuglsang. (1998), *Design of the Wind Turbine Airfoil Family RISØ-A-XX,* Risø National Laboratory, Roskilde, Denmark, December 1998, Risø-R-1024(EN).

Krogstad P.-Å. Adaramola, M.S., (2011), *Experimental Investigation of Wake Effects on Wind Turbine Performance*, Renewable Energy, 36(8):2078–2086, 2011.

Kühn, M., (2001), *Dynamics and Design Optimization of Offshore Wind Energy Conversion Systems*, Ph.D. Dissertation, Wind Energy Research Institute, Delft University of Technology, Delft, The Netherlands, 2001.

Landahl M. T. and Stark V. J. E., (1968), *Numerical Lifting-surface Theory - Problems and Progress.* AIAA Journal, November, 1968, Vol. 6, No. 11 : pp. 2049-2060 (doi: 10.2514/3.4936)

Lanzafame R., Mauro S., Messina M., (2013), *Wind Turbine CFD Modelling using a Correlation-based Transitional Model*, Renewable Energy, 52 (2013) 31-39

Larsen A, Walther J H. (1998), *Discrete Vortex Simulation of Flow Around Five Generic Bridge Deck Sections*, Journal of Wind Engineering and Industrial Aerodynamics, 1998, 77- 78: 591- 602.

Larsen, T. J. and Hanson, T. D., (2007), *A Method to Avoid Negative Damped Low Frequent Tower Vibrations for a Floating, Pitch Controlled Wind Turbine*, Journal of Physics: Conference Series, The Second Conference on The Science of Making Torque From Wind, Copenhagen, Denmark, 28–31 August 2007, [online journal], Vol. 75, 2007, 012073.

Larsson, L., Stern, F., Bertram, V., (2000), *Gothenburg 2000 A Workshop on Numerical Ship Hydrodynamics*, Chalmers University of Technology, Gothenburg, Sweden

Laursen J, Enevoldsen P, Hjort S, (2007), *3D CFD Quantification of the Performance of a Multi-Megawatt Wind Turbine*, Journal of Physics: Conference Series 75 (2007) 012007

Le Maitre OP, Scanlan R H, Knioc O M. (2003), *Estimation of the Flutter Derivatives of an NACA Airfoil by Means of Navier–Stokes Simulation*, Journal of Fluids and structures, 2003, 17: 1- 28.

Lee Fingersh, Dave Simms, Maureen Hand, Dave Jager, Jason Cotrell, Mike Robinson, Scott Schreck, Scott Larwood, (2001), *Wind Tunnel Testing of NREL's Unsteady*

Aerodynamics Experiment , 20th 2001 ASME Wind Energy Symposium,AIAA-2001-0035, doi: 10.2514/6.2001-35

Lee, K. H., (2005), *Responses of Floating Wind Turbines to Wind and Wave Excitation*, M.S. Dissertation, Department of Ocean Engineering, Massachusetts Institute of Technology, Cambridge, MA, USA, January 2005.

Leishman J. G., Beddoes T. S. (1989), *A Semi-Empirical Model for Dynamic Stall, Journal of the American Helicopter Society*, Volume 34, Number 3, 1 July 1989, pp. 3-17(15)

Leishman J. Gordon, (2000), *Principles of Helicopter Aerodynamics*, ISBN 0-521-66060-2 University of Cambridge

Leishman J. Gordon, (2002), *Challenges in Modeling the Unsteady Aerodynamics of Wind Turbines*, 21st ASME Wind Energy Symposium and the 40th AIAA Aerospace Sciences Meeting, Reno, NV, AIAA 2002-0037

Leishman JG, Beddoes TS., (1986), *A Generalized Method for Unsteady Airfoil Behavior and Dynamic Stall Using the Indicial Method*, Proceedings of 42nd Annual Forum of the American Helicopter Society, Washington, DC, 1986; 243-265

Leonardo Chamorro, Fernando Porté-Agel, (2009), *A Wind-tunnel Investigation of Wind-turbine Wakes: Boundary-layer Turbulence Effects*. Boundary-Layer Meteorology, 132:129–149, 2009. 10.1007/s10546-009-9380-8

Li Yuan, Kang Shun, Fan Zhongyao, et al., (2012), *Aerodynamics Performance for Wind Turbine Airfoil of Full Angle of Attack*, Chinese Society of Engineering Thermophysics Conference, Fluid Mechanical, 092100, 2012

Liebeck R.H. (1978), *Design of Subsonic Airfoils for High Lift*, Journal of Aircraft, 15(9), 547-561

Lindenburg C, (2003), *Investigation into Rotor Blade Aerodynamics: Analysis of the Stationary Measurements on the UAE Phase-VI Rotor in the NASA-Ames Wind Tunnel,* Tech. Rep. ECN-C03-025 ECN, The Netherlands

Lindenburg, C., (2005), *PHATAS Release "NOV-2003" and "APR-2005" USER'S MANUAL: Program for Horizontal Axis wind Turbine Analysis and Simulation*, ECN-I--05-005, Petten, the Netherlands: Energy Research Center of the Netherlands, May 2005.

Loewy, R.G. (1957), *A Two-Dimensional Approximation to Unsteady Aerodynamics in Rotary Wings*, Journal of the Aeronautical Sciences 24, 81–92, 1957

Loftin L. A. (1954), *Airfoil Section Characteristics at High Angle of Attack*, NACA-TN-3241, 1954.

Lorber P, Carta F, Covino A. (1992), *An Oscillating Three-dimensional Wing Experiment: Compressibility, Sweep, Rate, Waveform, and Geometry Effects on Unsteady Separation and Dynamic Stall*. UTRC Report R92-958325-6, 1992.

Madsen H. Aa., Riziotis V., Zahle F., Hansen M.O.L., Snel H., Grasso F., Larsen T.J., Politis E., Rasmussen F., (2012), *Blade Element Momentum Modelling of Inflow with Shear in Comparison with Advanced Model Results*, Wind Energy, Volume 15, Issue 1, January 2012, Pages 63–81

Madsen Helge, Sørensen Niels N., Schreck Scott, (2003), *Yaw Aerodynamics Analyzed with Three Codes in Comparison with Experiment*, 41st Aerospace Sciences Meeting and Exhibit, 6-9 January 2003, Reno, Nevada. AIAA 2003-519.

Make, M., (2014), *Predicting Scale Effects on Floating Offshore Wind Turbines: A Numerical Analysis of Modeland Full-scale Wind Turbines using a RANS CFD Solver*, Master thesis, Technical University Delft

Manish K.Singh, K.Dhanalakshmi, S.K.Chakrabartty, (2007), *Navier-Stokes Analysis of Airfoils with Gurney Flap,* Journal of Aircraft, Vol.15, No.9, 978, 547-561.

Manwell J. F., McGowan J. G., and Rogers A. L., (2003), *Wind Energy Explained -Theory*, Design and Application. John Wiley & Sons Ltd, 2003

Manwell, J.F.; McGowan, J.G.; Rogers, A.L., (2002), *Wind Energy Explained: Theory, Design and Application*, New York: John Wiley & Sons.

Marco Masciola, Amy Robertson, Jason Jonkman, Frederick Driscoll, (2011) *Investigation of a FAST-OrcaFlex Coupling Module for Integrating Turbine and Mooring Dynamics of Offshore Floating Wind Turbines*, the 2011 International Conference on Offshore Wind Energy and Ocean Energy, Beijing, China, October 31 – November 2, 2011

Mark Potsdam, Dimitri Mavriplis, (2009), *Unstructured Mesh CFD Aerodynamic Analysis of the NREL Phase VI Rotor*, 47th AIAA Aerospace Sciences Meeting including The New Horizons Forum and Aerospace Exposition, DOI: 10.2514/6.2009-1221

Martin Johannes KUHN. (2001), *Dynamic and Design Optimisation of Offshore Wind Energy Conversion Systems*, DUWIND Delft University Wind Energy Institute, Report 2001.002

Martin O. L. Hansen, Jeppe Johansen, (2004), *Tip Studies using CFD and Comparison with Tip Loss Models*, wind energy, Volume 7, Issue 4, October/December 2004, Pages 343–356

Martin O. L. Hansen., (2008), *Aerodynamics of wind turbines*, Earthscan, second edition

Martin Steven, Day Sandy, Conor B. Gilmour, (2015), *Rotor Scaling Methodologies for Small Scale Testing Of Floating Wind Turbine Systems*, Proceedings of the ASME 2015 34th International Conference on Ocean, Offshore and Arctic Engineering, OMAE2015, May 31-June 5, 2015, St. John's, Newfoundland, Canada

Martin, H., Kimball, R., Viselli, A., and Goupee, A., (2012), *Methodology for Wind/Wave Basin Testing of Floating Offshore Wind Turbines,* In Proceedings of the 31st International Conference on Ocean, Offshore and Arctic Engineering (OMAE) Rio de Janeiro, Brazil June.

Matha D., Schlipf M., Cordle A., Pereira R., Jonkman J.,(2011), *Challenges in Simulation of Aerodynamics, Hydrodynamics, and Mooring-Line Dynamics of Floating Offshore Wind Turbines*, Presented at the 21st Offshore and Polar Engineering Conference, Maui, Hawaii , June 19-24, 2011, NREL/CP-5000-50544, October 2011

Matha Denis, Fabian Wendt, Werner Manuel, Cheng Po Wen, Thorsten Lutz, (2012), *Aerodynamic Inflow Conditions on Floating Offshore Wind Turbine Blades for Airfoil Design Purposes*, Proceedings of the Twenty-second International Offshore and Polar Engineering Conference, Rhodes, Greece, June 17–22, 2012, pp480-488

Matha Denis, Fischer Sven-Alan, Hauptmann Stefan and Cheng Po Wen, (2013), *Variations in Ultimate Load Predictions for Floating Offshore Wind Turbine extreme Pitching Motions applying different Aerodynamic Methodologies*, the Twenty-third International Offshore and Polar Engineering Anchorage, Alaska, USA, June 30–July 5, 2013

Matha Denis, Fischer Tim, Kuhn Martin, Jonkman Jason, (2009), *Model Development and Loads Analysis of a Wind Turbine on a Floating Offshore Tension Leg Platform*, Presented at the 2009 European Offshore Wind Conference and Exhibition Stockholm, Sweden, September 14-16, 2009, NREL/CP-500-46725, February 2010

MeCroskey W.J (1981), *The Phenomenon of Dynamic Stall*, United States, NASA Technical Report No. TM-81264

Mehta, U. B., (1998), *Credible Computational Fluids Dynamics Simulations*, AIAA J., 36, pp. 665–667.

Menter, F.R., (1993), *Zonal Two-equation K-ω Turbulence Model for Aerodynamic Flows*. AIAA Paper 1993-2906, 1993, 2

Menter, F.R., (1994), *Two-equation Eddy-viscosity Turbulence Models for Engineering Applications*. AIAA-Journal, 32(8), pp. 269-289, 1994

Micallef D, Kloosterman M, Ferreira CSa, Sant T, van Bussel G. (2010), *Validating BEM, Direct and Inverse Free Wake Models with the Mexico Experiment*, 48th AIAA Aerospace Sciences Meeting and Exhibit, American Institute of Aeronautics and Astronautics: Orlando, FL, 2010; 1–10.

Michel Make, Guilherme Vaz, Gerson Fernandes, Simon Burmester, Sebastien Gueydon, (2015), *Analysis of Aerodynamic Performance of Floating Wind Turbines Using CFD and BEMT Methods*, Proceedings of the ASME 2015 34th International Conference on Ocean, Offshore and Arctic Engineering, OMAE2015, May 31-June 5, 2015, St. John's, Newfoundland, Canada, OMAE2015-42086

Miehel R., et al. (1984), *Stability Calculations and Transition Criteria on Two-or-Three-Dimensional Flows*, Laminar-Turbulent Transition, 1984, (7):455－461

Mikkelsen, R. F., Sørensen, J. N., (2003), *Actuator Disc Methods Applied to Wind Turbines*, MEK-FM-PHD; No. 2003-02

Miley S.J. (1982), *A Catalog of Low Reynolds Number Airfoil Data For wind Turbine Applications*, Spring field: National Technical Information Service, U. S. Dept. of Commerce, 1982

Ming-Chen Hsu, Ido Akkerman, Yuri Bazilevs, (2014), *Finite Element Simulation of Wind Turbine Aerodynamics: Validation Study Using NREL Phase VI Experiment*, Wind Energy, Volume 17, Issue 3, March 2014, Pages 461–481

Minu Jeon, Seungmin Lee and Soogab Lee, (2014), *Unsteady Aerodynamics of Offshore Floating Wind Turbines in Platform Pitching Motion using Vortex Lattice Method*, Renewable Energy, 2014, vol. 65, issue C, pages 207-212

Mish P.F., Deven Port W.J. (2001), *Mean Loading Effects on the Surface Pressure Fluctuations on an Airfoil in Turbulence*, Proceedings of the 7th AIAA/CEAS Aeroacousties Conference, Maastricht, Netherlands: 2001

Monier A. Elfarra, Nilay Sezer-Uzol, I. Sinan Akmandor, (2014), *NREL VI Rotor Blade: Numerical Investigation and Winglet Design and Optimization using CFD*, Wind Energy, Volume 17, Issue 4, April 2014, Pages 605–626

Montgomerie B. (2004), *Methods for Root Effects Tip Effects and Extending the Angle of Attack Range ∓180 deg with Application to Aerodynamics for Blades on Wind Turbines and Propellers*, FOI-R-1305-SE, 2004.

Moriarty P.J., Hansen A.C., (2015), *AeroDyn Theory Manual*, NREL/TP-500-36881, January 2005

Mukesh M .Yelmule, EswaraRao Anjuri VSJ, (2013), *CFD Predictions Of NREL Phase VI Rotor Experiment in NASA/AMES Wind Tunnel*, International Journal of Renewable Energy Research, Vol 3, No.2, 2013

Munk M.M, Miller E.W. (2011), *The Variable Density Wind Tunnel of The National Advisory*, NACA Report No.227

Musial W., Butterfield S., and Boone A., (2004), *Feasibility of Floating Platform Systems for Wind Turbines*, the 23rd ASME Wind Energy Symposium Reno, Nevada January 5–8, 2004, NREL/CP-500-34874

Myose, R. Heron, Papadakis M. (2006), *The Effect of Gurney Flaps on a NACA0011 Airfoil*, AIAA Paper96-0059, Jan 2006.

Niels N. Sørensen, (2009) *CFD Modelling of Laminar-turbulent Transition for Airfoils and Rotors using The γ- Model*, Wind Energy, Volume 12, Issue 8, November 2009, Pages 715–733

Niels N. Sørensen, Scott Schreck, (2012), *Computation of the National Renewable Energy Laboratory Phase-VI Rotor in Pitch Motion during Standstill*, wind energy, Volume 15, Issue 3, April 2012, Pages 425–442

Nielsen, F. G., Hanson, T. D., and Skaare, B., (2006), *Integrated Dynamic Analysis of Floating Offshore Wind Turbines*, Proceedings of OMAE2006 25th International Conference on Offshore Mechanics and Arctic Engineering, 4–9 June 2006, Hamburg, Germany [CD-ROM], Houston, TX: The American Society of Mechanical Engineers (ASME International) Ocean, Offshore and Arctic Engineering (OOAE) Division, June 2006, OMAE2006-92291.

Nilay Sezer-Uzol, Lyle N. Long, (2006), *3-D Time-Accurate CFD Simulations of Wind Turbine Rotor Flow Fields*, 44th AIAA Aerospace Sciences Meeting and Exhibit 9-12 January 2006, Reno, Nevada, AIAA 2006-0394

Noda M, Flay R. G. J, (1999), *A Simulation Model for Wind Turbine Blade Fatigue Loads*. Journal of Wind Energy and Industrial Aerodynamics, 1999, 83: 527-540.

Ogilvie, T. F. (1964), *Recent Progress toward the Understanding and Prediction of Ship Motions*, Fifth Symposium on Naval Hydrodynamics, September, 1964, pp. 3–128.

Ouahiba Guerri, Khadidja Bouhadef, Ameziane Harhad. (2006), *Turbulent Flow Simulation of the NREL S809 Airfoil*, Wind Engineering, 2006, 30(4): 287-302.

Passon, P. and Kühn, M., (2005), *State-of-the-art and Development Needs of Simulation Codes for Offshore Wind Turbines*, Copenhagen Offshore Wind 2005 Conference and Expedition Proceedings, 26–28 October 2005, Copenhagen, Denmark [CD-ROM], Copenhagen, Denmark: Danish Wind Energy Association, October 2005.

Peter J.Schubel , Richard J. Crossley. (2012), *Wind Turbine Blade Design*, Energies, 5, 3425-3449

Pitt, D.M.; Peters, D.A. (1981), *Theoretical Prediction of Dynamic-Inflow Derivatives*, Vertica, 5(1), March

Piziali R. (1994), *2-D and 3-D Oscillating Wing Aerodynamics for A Range of Angles of Attack Including Stall*, NASA TM 4632, 1994

Pouring (ed.), (1976), *Numerical Laboratory Computer Methods in Fluid Dynamics*, ASME, New York, 1976, pp. 1–12

Qian Weiqi, Leung Randolph C.K. (2008). *Numerical Simulation Considering the Transition Effects of Airfoil Dynamic Stall,* Journal of Aerodynamics, 26(1), 50-55

Qian Weiqi, Zhan Hao, Bai Junqiang. (2006), *Transition Prediction Method Based on the Turbulence Model,* Journal of Aerodynamics, 2006, 24(4):502−507.

Ramsay R, Homan M, Gregorek G (1995), *Effects of Grit Roughness and Pitch Oscillation on the S809 Airfoil*, NREL/TP-442-7817

Raymond Chow, C. P. van Dam, (2012), *Verification of Computational Simulations of the NREL 5 MW Rotor with a Focus on Inboard Flow Separation*, Wind Energy, Volume 15, Issue 8, November 2012, Pages 967–981

Ridder de E.-J., Otto, W., Zondervan, G.-J., Huijs, F., and Vaz, G., (2014), *Development of a Scaled-Down Floating Wind Turbine for Offshore Basin Testing*, Proceedings of OMAE2014 33rd International Conference on Offshore Mechanics and Arctic Engineering, 8–13 June 2014, San Francisco, California, USA

Roache P. (1994), *Perspective: A Method for Uniform Reporting of Grid Refinement Studies*. Journal of Fluids Engineering, (ASME) 1994; 116:405–413

Roache, P. J., (1998), *Verification and Validation in Computational Science and Engineering*, Hermosa Publishers, Albuquerque, New Mexico

Roache, P.J., (2003), *Criticism of the Correction Factor Verification Method*, ASME J. Fluids Eng., Vol. 125, July 2003.

Robert D. Preuss, Emil O. Suciu, and Luigi Morino, (1980), *Unsteady Potential Aerodynamics of Rotors with Applications to Horizontal-Axis Windmills*, AIAA Journal, April, 1980, Vol. 18, No. 4 : pp. 385-393 (doi: 10.2514/3.50769)

Robertson AN, Jonkman JM, Goupee AJ, Coulling AJ, Prowell I, Browning J. (2013), *Summary of Conclusions and Recommendations Drawn from the Deepcwind Scaled Floating Offshore Wind System Test Campaign*, In: Conference: ASME 2013 32nd International Conference on Ocean, Offshore and Arctic Engineering; 2013.

Robin Langtry, Janusz Gola, Florian Menter, (2006), *Predicting 2D Airfoil and 3D Wind Turbine Rotor Performance using a Transition Model for General CFD Codes,* 44th AIAA Aerospace Sciences Meeting and Exhibit 9-12 January 2006, Reno, Nevada, AIAA 2006-395 (doi: 10.2514/6.2006-395)

Robinson M, Wissler J. (1988), *Unsteady Surface Pressure Measurements on a Pitching Wing*, AIAA 88-0328, 26th Aerospace Sciences Meeting, January 1988.

Robinson M.C., Hand M.M., Simms D.A., Schreck S.J., (1999), *Horizontal Axis Wind Turbine Aerodynamics: Three-Dimensional, Unsteady, and Separated Flow Influences*, the 3rd ASME/JSME Joint Fluids Engineering Conference San Francisco, California July 18-23, 1999, NREL/CP-500-26337

Rockel, S. Camp, E., Schmidt, J., Peinke, J., Cal R.B. and Holling, M., (2014), *Experimental Study on Influence of Pitch Motion on the Wake of a Floating Wind Turbine Model*, Energies 2014, Vol. 7, pages 1954-1985.

Ronsten G. (1992), *Static Pressure Measurements on a Rotating and a Non-Rotating 2.375m Wind Turbine Blade Comparison with 2D Calculations*, Journal of Wind Engineering and Industrial Aerodynamics, 1992; 39: 105–118

Rood, E. P., (1996), *Validation Strategy for RANS Computational Ship Hydrodynamics*, 2nd International Conference on Hydrodynamics, Hong Kong

Rooij R.P.J.O.M., Timmer W. *Roughness Sensitivity Considerations for Thick Rotor Blade Airfoils* [J]. Solar Energy Eng. Trans. ASME 2003, 125, 468–478.

Rosen A., Lavie I., Seginer A., (1990), *A General Free Wake Efficient Analysis of Horizontal Axis Wind Turbines*, Wind Eng. 14 (6).

Sant T, Bonnici D, Farrugia R, Micallef D. (2015), *Measurements and Modelling of the Power Performance of a Model Floating Wind Turbine under Controlled Conditions*. Wind Energy 2015; 18 (5):811e34.

Schaffarczyk A.P., Stahl B., (2004), *Experimental and Numerical Deduced Performance Properties of A 30% Thick Roughness Profile at High Reynolds Number for Use on Multimegawatt Blades*, 7th German Wind Energy Conference, DEWEK 2004, October 2004

Schreck S, Addington G, Luttges M. (1991), *Flow Field Structure and Development near the Root of a Straight Wing Pitching at Constant Rate*, AIAA 91-1793, 22nd Fluid Dynamics, Plasma Dynamics and Lasers Conference, June 1991

Schreck S, Helin H. (1994), *Unsteady Vortex Dynamics and Surface Pressure Topologies on a Finite Pitching Wing*, Journal of Aircraft, 1994; 31: 899–907

Schreck S. (guest ed.). (2002), *Special issue: Analysis and Modelling of the NREL Full-scale Wind Tunnel Experiment*, Wind Energy 2002; 5: 77–257

Schreck S., Robinson M., Hand M. and Simms D., (2000), *HAWT Dynamic Stall Response Asymmetries under Yawed Flow Condition*s, Wind Energy, 2000; 3:215–232 (DOI: 10.1002/we.40)

Sclavounos, P. D., (2007), *Surface Waves and Their Interaction with Floating Bodies,* Lecture Notes, Massachusetts Institute of Technology (MIT) OpenCourseWare [online publication], URL: http://ocw.mit.edu/OcwWeb/Ocean-Engineering/13-022Surface-Waves-and-their-Interaction-With-Floating-BodiesSpring2002/CourseHome/index.htm, [cited 27 September 2005].

Scott J. Schreck, Michael C. Robinson, M. Maureen Hand, David A. Simms, (2001), *Blade Dynamic Stall Vortex Kinematics for a Horizontal Axis Wind Turbine in Yawed Conditions*, Transactions of the ASME, Vol. 123, November 2001

Sean Quallen, Tao Xing, Pablo Carrica, Yuwei Li, Jun Xu, (2014), *CFD Simulation of a Floating Offshore Wind Turbine System Using a Quasi-static Crowfoot Mooring-Line Model Journal of Ocean and Wind Energy*, Vol. 1, No. 3, August 2014, pp. 143–152

Sears, W.R. (1940), *Operational Methods in the Theory of Airfoils in Non-Uniform Motion*, Journal of the Franklin Institute 230, 95–111, 1940

Sebastian T., Lackner M.A., (2012), *Development of a Free Vortex Wake Method Code for Offshore Floating Wind Turbines*, Renewable Energy, Volume 46, October 2012, Pages 269–275

Sébastien Gueydon, Guillaume Venet, Gerson Fernandes, (2015), *Influence of the Rotor Characterization on the Motion of a Floating Wind Turbine*, Proceedings of the ASME 2015 34th International Conference on Ocean, Offshore and Arctic Engineering, OMAE2015, May 31-June 5, 2015, St. John's, Newfoundland, Canada

Sheng W, Galbraith R, Coton F (2009). *On the S809 Airfoil's Unsteady Aerodynamic Characteristics*, Wind Energy, 12(7), 52–67

Sheng W, Galbraith R, Coton F. (2007), *A Modified Dynamic Stall Model for Low Mach Numbers*, Sol Energy Eng 2007;130:031013-1–031013-10

Sieot C., Aubrun S.,Loyer S.,et al. (2006), *Unsteady Characteristics of the Statics Tall of an Airfoil Subjected to Free Stream Turbulence Level Up to 16%*, Experiments in Fluids, 2006, 41: 641-648

Simms, D. A., Schreck, S., Hand, M., and Fingersh, L., J., (2001), *NREL Unsteady Aerodynamics Experiment in the NASA Ames Wind Tunnel: A Comparison of Predictions to Measurements*, NREL/TP-500-29494, June 2001

Simoes F.J., Graham J.M.R., (1991), *Prediction of Loading on a Horizontal Axis Wind Turbine using a Free Vortex Wake Model*, BWEA Conference, 1991, p. 247.

Simon-Philippe Breton, Geir Moe Status (2009), *Plans and technologies for offshore wind turbines in Europe and North America*, Renewable Energy, 34, 646–654

Skaare, B., Hanson, T. D., and Nielsen, F. G., (2007), *Importance of Control Strategies on Fatigue Life of Floating Wind Turbines*, Proceedings of OMAE2007 26th

International Conference on Offshore Mechanics and Arctic Engineering, 10–15 June 2007, San Diego, CA [CD-ROM], Houston, TX: The American Society of Mechanical Engineers (ASME International) Ocean, Offshore and Arctic Engineering (OOAE) Division, June 2007, OMAE2007-29277.

Snel H., Schepers J.G., (1993), *Investigation and Modelling of Dynamic Inflow Effects,* The Ecwec'93 Conference, Traveminde, 8~12 March, 1993 Rx--93-029

Snel, H.; Schepers, J.G. (ed.) (1995), *Joint Investigation of Dynamic Inflow Effects and Implementation of an Engineering Method*, ECN-C-94-107, Petten: Energy Research Centre of the Netherlands April.

Soltani M.R, Marzabadi F.R (2009), *Effect of Reduced Frequency on the Aerodynamic Behaviour of an Airfoil Oscillating in a Plunging Motion*, Scientia Iranica, 16(1), 40-52.

Somers D (1997), *Design and Experimental Results for the S809 Airfoil*, United States, NREL Technical Report No. SR-440-6918

Song, Y. and Perot, J.B., *CFD simulations of the NREL phase VI rotor*, Wind Engineering, 39(3), pp. 299-310, 2014

Song, Y., *CFD simulations of the flow around NREL phase VI wind turbine*, Master Thesis, University of Massachusetts Amherst, 2014

Sørensen J. N., Shen W. Z., Munduate X., (1998), *Analysis of Wake States by a Full-Field Actuator Disc Model,* Wind Energy, Volume 1, Issue 2, December 1998, Pages 73–88

Sorensen N., Michelsen J., (2002), *Aerodynamic predictions for the Unsteady Aerodynamics Experiment Phase-II rotor at the National Renewable Energy Laboratory*, 2000 ASME Wind Energy Symposium, AIAA-2000-0037.

Sørensen, N. N., Michelsen, J. A., and Schreck, S., (2002), *Navier-Stokes Predictions of the NREL Phase VI Rotor in the NASA AMES 80ft x120ft Wind Tunnel*, Wind Energy, Vol. 5, No. 2-3, 2002, pp. 151-169.

Spezial C. G., Abid R., Anderson E. C., (1992), *Critical Evaluation of Two-equation Models for Near-wall Turbulence*, AIIA Journal, 30(2), 324-331.

Srinivas Guntur, Niels N Sørensen, (2014) *Evaluation of Several Methods of Determining the Angle of Attack on Wind Turbine Blades*, Journal of Physics: Conference Series (Online), Vol. 555, 012045, 2014.

Stack J. (1931), *Tests in the Variable Density Wind Tunnel to Investigate the Effects of Scale and Turbulence on Airfoil Characteristics*, NACAT.N.No.364, 1931

STAR CCM+ users' guide

Stern, F., Paterson, E. G., and Tahara, Y., (1996), *CFDSHIP-IOWA: Computational Fluid Dynamics Method for Surface-Ship Boundary Layers and Wakes and Wave Fields*, Iowa Institute of Hydraulic Research, The University of Iowa, IIHR Report No. 381.

Stylianos D Pesmajoglou, J.M.R Graham, *Prediction of aerodynamic forces on horizontal axis wind turbines in free yaw and turbulence*, Journal of Wind Engineering and Industrial Aerodynamics, Volume 86, Issue 1, May 2000, Pages 1–14

Sun D K, Owen J S, Wright N G, (2008), *Total Fluid Structure Interaction of Prismatic Line Like Structures Using LES and Block Iterative Coupling*, Journal of Wind Engineering and Industrial Aerodynamics, 2008, 96: 840- 858

Suzuki A. (2000), *Application of Dynamic Inflow Theory to Wind Turbine Rotors*, Doctoral dissertation. University of Utah; 2000

Suzuki, H., et al., (2009). *Progressive Drifting Of Floating Wind Turbines In A Wind Farm*, Proceedings of the ASME 28th International Conference on Ocean, Offshore and Arctic Engineering, Honolulu, Hawaii, OMAE2009-79634

Tangler J. L., Somers D. M., (1995), *NREL Airfoil Families for HAWTs*, updated AWEA 1995.doc.

Thanhtoan Tran, Donghyun Kim, Jinseop Song, (2014), *Computational Fluid Dynamic Analysis of a Floating Offshore Wind Turbine Experiencing Platform Pitching Motion*, Energies 2014, 7, 5011-5026; doi:10.3390/en7085011

Thanh-Toan Tran, Dong-Hyun Kim, Kang-Sik Bae, (2013), *Extreme Load Estimation for a Large Wind Turbine Using CFD and Unsteady BEM*, Computational Science and Its Applications – ICCSA 2013, Volume 7975 of the series Lecture Notes in Computer Science pp 127-142

Theodorsen T., (1935), *General Theory of Aerodynamic Instability and the Mechanism of Flutter*, NACA Report, NO 496, 1935

Thomas Sebastian, Matthew Lackner, (2011), *Offshore Floating Wind Turbines - An Aerodynamic Perspective,* 49th AIAA Aerospace Sciences Meeting including the New Horizons Forum and Aerospace Exposition 4-7 January 2011 Orlando, Florida AIAA 2011-720 (doi: 10.2514/6.2011-720)

Thomas Sebastian, Matthew Lackner, (2011), *A Comparison of First-Order Aerodynamic Analysis Methods for Floating Wind Turbines,* 48th AIAA Aerospace Sciences Meeting Including the New Horizons Forum and Aerospace Exposition 4-7 January 2011 Orlando, Florida AIAA 2010-998 (doi: 10.2514/6.2010-998)

Timmer W. A., Van Rooij R. P. J. O. M. (2001) *Some Aspects of High Angle-of-Attack Flow on Airfoils for Wind Turbine Application*, Proceedings of EWEC, Copenhagen 2-6 ,July, 2001.

Timmer W.A, van Rooij R.P.J.O.M. (2003), *Summary of the Delft University Wind Turbine Dedicated Airfoils*, Sol. Energy Eng. Trans. ASME 2003, 125, 488–496

Timmer W.A., Schaffarczyk A.P. (2004), *The Effect of Roughness at High Reynolds Number on the Performance of DU97-w-300mod,* Wind Energy, Volume 7, Issue 4, October/December 2004, Pages 295–307

Tokuyama H.b Nakajo Y.a Ushiyama I.c Nishizawa, Y.a. (2009), *Yaw Behavior of Horizontal-Axis Small Wind Turbines in an Urban Area*. Wind Engineering, 33(1):19–30, 2009

Tongchitpakdee C, Benjanirat S, Sankar LN. (2005), *Numerical Simulation of the Aerodynamics of Horizontal Axis Wind Turbines under Yawed Flow Conditions*, Journal of Solar Energy Engineering 2005; 127: 464–474

Tonio Sant, Kurt Cuschieri, (2015), *Numerical Modelling of the Aerodynamic Characteristics of a Floating Offshore Wind Turbine under Yawed Rotor Conditions,* ASME 2015 34th International Conference on Ocean, Offshore and Arctic Engineering, Volume 9: Ocean Renewable Energy, St. John's, Newfoundland, Canada, May 31–June 5, 2015

Tracy, C. (2007), *Parametric Design of Floating Wind Turbines*, M.S. Thesis. Cambridge, MA: Massachusetts Institute of Technology, 2007.

Vaal JB de, Hansen MOL, Moan T. (2014), *Effect of Wind Turbine Surge Motion on Rotor Thrust and Induced Velocity*, Wind Energy 2014; 17(1):105e21.

van Garrel A. (2003), *Development of a Wind Turbine Aerodynamics Simulation Module,* Technical Report ECN-C–03-079, ECN, 2003.

van Rooij R. p. J. O. M. (1996), *Modification of the Boundary Layer Calculation in RFOIL for Improved Airfoil Stall Prediction*, Netherlands: Delft, Rapport IW 一 96087R,1996.

Veldkamp, H. F., van der Tempel, J., (2005), *Influence of Wave Modelling on the Prediction of Fatigue for Offshore Wind Turbines*, Wind Energy, Vol. 8, No. 1, January/March 2005, pp. 49–65.

Vepa, R. (1976), *Approximants to Represent Unsteady Aerodynamic Loads for Arbitrarily Small Motions of Wings*. AIAA Paper, pp. 7–17, 1976

Verelst D.R.S. and Larsen T.J., (2010), *Yaw stability of a free-yawing 3-bladed downwind wind turbine,* Wind Energy Research. http://windenergyresearch.org/?p=398

Vijfhuizen W. J. M. J, (2006), *Design of a Wind and Wave Power Barge*, M.S. Dissertation, Department of Naval Architecture and Mechanical Engineering, Universities of Glasgow and Strathclyde, Glasgow, Scotland, September 2006.

Voutsinas S., Belessis S.G., Rados K.G., (1994*), Investigation of the Yawed Operation Wind Turbines by Means of a Vortex Particle Method*, AGARD CP-552, Aerodynamics and Aeracoustics of Rotorcraft, 1994

Wang C. M., Utsunomiya T., Wee S. C., Choo Y. S. (2010), *Research on Floating Wind Turbines: A Literature Survey*, The IES Journal Part A: Civil & Structural Engineering, Vol. 3, No. 4, 267–2

Wayman, E. N., Sclavounos, P. D., Butterfield, S., Jonkman, J., and Musial, W., (2006), *Coupled Dynamic Modelling of Floating Wind Turbine Systems*, Offshore Technology Conference, 1–4 May 2006, Houston, TX [CD-ROM], Richardson, TX: Offshore Technology Conference, May 2006, OTC 18287, NREL/CP-500-39481, Golden, CO: National Renewable Energy Laboratory.

Wayman, E., (2006), *Coupled Dynamics and Economic Analysis of Floating Wind Turbine Systems*, M.S. Dissertation, Department of Mechanical Engineering, Massachusetts Institute of Technology, Cambridge, MA, USA, June 2006

Wen Zhong Shen, Jens Nørkær Sørensen, Jianhui Zhang, (2007), *Actuator Surface Model for Wind Turbine Flow Computations*, 2007 European Wind Energy Conference and Exhibition, EWEC 2007 01/2007; 2.

Wen Zhong Shen, Robert Mikkelsen, Jens Nørkær Sørensen, Christian Bak, (2005), *Tip Loss Corrections for Wind Turbine Computations*, Wind Energy, Volume 8, Issue 4, October/December 2005, Pages 457–475, DOI: 10.1002/we.153

Whale J., Fisichella C. J., Selig M. S., (2000), *Correcting Inflow Measurements from Wind Turbines Using a Lifting-Surface Code*, Transactions of the ASME Vol. 122, NOVEMBER 2000 196-202.

Wilson, R. and Stern, F., (2002), *Verification and Validation for RANS Simulation of a Naval Surface Combatant*, Standards for CFD in the Aerospace Industry, 2002 AIAA Aerospace Sciences Meeting, Reno, Nevada, 14-17 January 2002.

Wilson, R., Shao, J. and Stern, F., (2004), *Discussion: Criticism of the Correction Factor Verification Method,* ASME J. Fluids Eng., Vol. 126, July 2004.

Wind Energy Association (2013), *2030: The Next Steps for EU Climate and Energy Policy*, a report by wind Energy Association

Withee, J. E., (2004), *Fully Coupled Dynamic Analysis of a Floating Wind Turbine System*, Ph.D. Dissertation, Department of Ocean Engineering, Massachusetts Institute of Technology, Cambridge, MA, USA, 2004.

Wolfe W. P, Ochs S.S., (1997), *CFD Calculations of S809 Aerodynamic Characteristic*s, United States, AIAA Report No. 97-0973.

Xie Zhengtong. (2009), *Wind Turbine Blade Flow in Abnormal Environments* [EB/OL] (2009-10-15) httP://emg.soton.ae.uk/researeh/ProjeetS/Wind-turbine-blade-flow-in-abnormal-environments/

Xu Guanpeng, (2001), *Computational Studies of Horizontal Axis Wind Turbines*, Thesis (Ph.D.)--Georgia Institute of Technology, 2001; Publication Number: AAI3015701; ISBN: 9780493265797.

Yunus A. Çengel, John M. Cimbala, (2006), *Fluid Mechanics: Fundamentals and Applications*, McGraw-HillHigher Education, December 2006

Yuwei Li, Kwang-Jun Paik, Tao Xing, Pablo M. Carrica, (2012), *Dynamic overset CFD simulations of wind turbine aerodynamics*, Renewable Energy 37 (2012) 285-298

Zambrano, T., MacCready, T., Kiceniuk, T., Jr., Roddier, D. G., and Cermelli, C. A., (2006), *Dynamic Modeling of Deepwater Offshore Wind Turbine Structures in Gulf of Mexico Storm Conditions*, Proceedings of OMAE2006 25th International Conference on Offshore Mechanics and Arctic Engineering, 4–9 June 2006, Hamburg, Germany [CD-ROM], Houston, TX: The American Society of Mechanical Engineers (ASME International) Ocean, Offshore and Arctic Engineering (OOAE) Division, June 2006, OMAE2006-92029.

Zambrano, T., MacCready, T., Roddier, D. G., and Cermelli, C. A., (2007), *Design and Installation of a Tension Moored Wind Turbine*, Proceedings of OMAE2007 26th International Conference on Offshore Mechanics and Arctic Engineering, 10–15 June 2007, San Diego, CA [CD-ROM], Houston, TX: The American Society of Mechanical Engineers (ASME International) Ocean, Offshore and Arctic Engineering (OOAE) Division, June 2007, OMAE2007-29587

Zhang Shiang. (2009), *Design Methods of Wind Turbine Airfoil Based on Panel Method*. China Lanzhou, Lanzhou University of Technology, 2009

Zhang Yan, Igarashi T, Hu Hui. (2011), *Experimental Investigations on the Performance Degradation of a Low Reynolds Number Airfoil with Distributed Leading Edge Roughness,* 49th AIAA Aerospace Sciences Meeting, Orlando: 2011: 18

Zhong S., Infield D.G., (1991), *Prediction of Wind Turbine Performance in Axial and Non-axial Flows by a Prescribed Wake Model*, BWEA Conference, 1991, pp. 261

APPENDIX A: GEOMETRY OF NREL 5-MW WIND TURBINE WITH OC3-HYWIND SPAR PLATFORM

Basic physical properties of the NREL 5MW are given in Table 1 (Jonkman, 2009). Under the definition of the floating system of OC3 by Jonkman, a modified version of the UpWind 5MW reference wind turbine (Jonkman, et al., 2007) on the OC3 Hywind spar buoy floating support structure has been chosen. Table 2 summarizes the floating platform properties (Jonkman, 2010).

Table A-1 Properties of the NREL 5-MW baseline wind turbine

Rating	5MW
Rotor Orientation, Configuration	Upwind, 3 Blades
Control	Variable Speed, Collective
Drivetrain	High Speed, Multiple-Stage
Rotor, Hub Diameter	126 m, 3 m
Hub Height	90 m
Cut-In, Rated, Cut-Out Wind Speed	3 m/s, 11.4 m/s, 25 m/s
Cut-In, Rated Rotor Speed	6.9 rpm, 12.1 rpm
Rated Tip Speed	80 m/s
Overhang, Shaft Tilt, Precone	5 m, 5°, 2.5°
Rotor Mass	110,000 kg
Nacelle Mass	240,000 kg
Tower Mass	347,460 kg
Coordinate Location of Overall CM	(-0.2 m, 0.0 m, 64.0 m)

Table A-2 Floating platform structural properties

Depth to Platform Base Below SWL (Total Draft)	120 m
Elevation to Platform Top (Tower Base) Above SWL	10 m
Depth to Top of Taper Below SWL	4 m
Depth to Bottom of Taper Below SWL	12 m
Platform Diameter Above Taper	6.5 m
Platform Diameter Below Taper	9.4 m
Platform Mass, Including Ballast	7,466,330 kg
CM Location Below SWL Along Platform Centreline	89.9155 m
Platform Roll Inertia about CM	4,229,230,000 kg•m^2
Platform Pitch Inertia about CM	4,229,230,000 kg•m^2
Platform Yaw Inertia about Platform Centreline	164,230,000 kg•m^2

APPENDIX B: GEOMETRY OF NREL 5-MW WIND TURBINE WITH OC3-HYWIND TLP PLATFORM

The MIT/NREL TLP is shown in Figure 1 and its basic properties are listed in Table 1. Detailed information regarding the modification and TLP design is provided in Matha (2009).
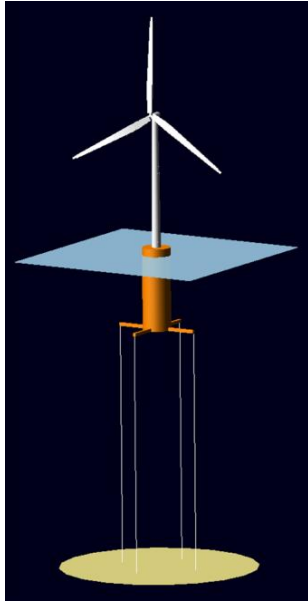
Figure B-1 MIT/NREL TLP (Matha, 2009)

Table B-1 Basic Properties of MIT/NREL TLP

Static Properties	Value
Platform diameter	18 m
Platform draft	47.89 m
Total displacement	12,179 m3
Platform mass	8,600,000 kg
Distance between fairleads	54 m
Concrete (ballast) mass	8,216,000 kg
Concrete height (from bottom of platform)	12.6 m
Water depth	200 m

APPENDIX C: GEOMETRY OF NREL PHASE VI WIND TURBINE

The geometry and operating parameters were summarized in Table 1. The blade of NREL VI consists of 19 sections. Each section has different chord lengths and twist angles as shown in Table 2:

• at r = 0 m: centre of the hub;

• at r = 0.508 m: the start of the blade root, the blade section is circular;

• between r = 1.343m and r = 5.029 m: the blade sections are of S809 airfoil.

The blade geometry is developed by software Gambit as shown in Figure 6.1.

Table C-1 Geometry and operating parameters of NREL Phase VI rotor (Monier, 2014)

Number of blades	2
Rotor diameter	10.058 m
RPM	71.63 rpm
Cut-in wind speed	5 m/s
Rated power	19.8 kw
Rotor location	Upwind
Power regulation	Stall regulated
Blade tip pitch angle	3 degree
Blade profile	S809
Blade chord	0.358-0.728 m

Table C-2 Chord and twist variations along the NREL VI rotor blade23 (Monier, 2014)

Section	Radial distance r (m)	Span station r/5.029 (m)	Chord length (m)	Twist degree
1	0.508	0.101	0.218	0
2	0.66	0.131	0.218	0
3	1.343	0.267	0.728	18.074
4	1.51	0.3	0.711	14.292

5	1.648	0.328	0.697	11.909
6	1.952	0.388	0.666	7.979
7	2.257	0.449	0.636	5.308
8	2.343	0.466	0.627	4.715
9	2.562	0.509	0.605	3.425
10	2.867	0.57	0.574	2.083
11	3.172	0.631	0.543	1.15
12	3.476	0.691	0.512	0.494
13	3.781	0.752	0.482	-0.015
14	4.023	0.8	0.457	-0.381
15	4.086	0.812	0.451	-0.475
16	4.391	0.873	0.42	-0.920
17	4.696	0.934	0.389	-1.352
18	4.78	0.95	0.381	-1.469
19	5.029	1	0.358	-1.775

APPENDIX REFERENCE

Jonkman J., (2010), *Definition of the Floating System for Phase IV of OC3*, Technical Report NREL/TP-500-47535, May 2010

Jonkman J., Butterfield S., Musial W., and Scott G., (2009), *Definition of a 5-MW Reference Wind Turbine for Offshore System Development*, Technical Report, NREL/TP-500-38060, February 2009

Jonkman J., (2007), *Dynamics Modeling and Loads Analysis of an Offshore Floating Wind Turbine*, Technical Report, NREL/TP-500-41958, November 2007

Matha Denis, Fischer Tim, Kuhn Martin, Jonkman Jason, (2009), *Model Development and Loads Analysis of a Wind Turbine on a Floating Offshore Tension Leg Platform*, Presented at the 2009 European Offshore Wind Conference and Exhibition Stockholm, Sweden, September 14-16, 2009, NREL/CP-500-46725, February 2010

Monier A. Elfarra, Nilay Sezer-Uzol, I. Sinan Akmandor, (2014), *NREL VI Rotor Blade: Numerical Investigation and Winglet Design and Optimization using CFD*, Wind Energy, Volume 17, Issue 4, April 2014, Pages 605–626